TUNL LI

PROGRESS REPORT

1 SEPTEMBER 2011 – 31 AUGUST 2012

Triangle Universities Nuclear Laboratory

Duke University
North Carolina State University
University of North Carolina at Chapel Hill

Box 90308, Durham, North Carolina 27708-0308, USA

Work described in this Progress Report is supported by the United States Department of Energy, Office of High Energy and Nuclear Physics, under:

Grant No. DE-FG02-97ER41033 (Duke University),
Grant No. DE-FG02-97ER41042 (North Carolina State University), and
Grant No. DE-FG02-97ER41041 (University of North Carolina).

Contents

Introduction

The Triangle Universities Nuclear Laboratory (TUNL) is a center for nuclear physics consisting of three consortium universities: Duke University, North Carolina State University (NCSU), and the University of North Carolina at Chapel Hill (UNC). There are currently 19 faculty members, approximately 50 graduate students and 15 postdoctoral fellows from the consortium universities conducting research at TUNL on a broad range of topics that include fundamental symmetries, neutrino physics, nuclear astrophysics, and strong interaction physics (hadron structure, light nuclei and many-body systems). Progress in fundamental science often requires technological advances. To this end, TUNL groups are conducting R&D on particle detectors, signal processing electronics, data acquisition, production and evaluation of ultra low radioactivity materials, and accelerator systems. In addition to the fundamental nuclear physics research program at TUNL, groups are applying nuclear-physics techniques in the areas of national nuclear security, homeland security and biology.

TUNL operates three accelerator facilities: the High Intensity Gamma-Ray Source (HIγS), the Laboratory for Experimental Nuclear Astrophysics (LENA) and the tandem accelerator laboratory. There is an accelerator physics group that supports HIγS operations and conducts accelerator physics research focused on γ-ray source development. The tandem accelerator and LENA are maintained by technicians and students, while R&D to create new capabilities on the low-energy accelerators is carried out by research groups in collaboration with the technical staff. In addition to the accelerator facilities, the research infrastructure includes non-accelerator research facilities (e.g., project R&D laboratories and low-background counting facilities) as well as technical and administrative staff that support research and accelerator operations. Laboratory materials and supplies and a pool of research equipment are available for use by the research groups.

The research program is a mixture of in-house experiments, which are conducted at the local accelerator and research facilities, and international collaborative projects such the neutron Electric Dipole Moment experiment (nEDM) and Majorana Demonstrator, which are carried out at national user laboratories. Both types of projects use the research infrastructure (technical and administrative support, material and supplies, and equipment) at TUNL. Coordination of the efforts of research groups within the consortium combined with the strategic use of the infrastructure resources at TUNL enables groups to take significant responsibilities on the international collaborative projects.

The Low-Energy Program in the Office of Nuclear Physics (ONP) at the Department of Energy (DOE) supports the collaborative research at TUNL through three grants, one to each consortium university. The grants to NCSU and UNC support the activities of the research groups at these institutions. The budgets for these awards include student and postdoctoral-fellow support, travel, senior investigator salaries, and modest funding for laboratory materials and supplies. The UNC grant also includes support for one research-scientist staff position for neutrino physics research. The Duke grant has two components: (1) support for the shared research infrastructure at TUNL (including operation of accelerator facilities, technical and engineering support for research, special research facilities, materials, supplies, and equipment) and (2) support for the Duke research group.

This document is a compilation of status reports of research projects conducted by TUNL groups during the period of **September 1, 2011 to August 31, 2012**. It covers the second half of the final year (March 1, 2011 to February 29, 2012) of the previous grant and first half of year-one (March 1, 2012 to February 28, 2013) of the new grant (March 1, 2012 to February 28, 2015) to the three consortium universities from the DOE ONP Low-Energy Program.

During this reporting period research groups at TUNL published 48 papers in refereed journals of which 6 were letter articles. Consortium members delivered 60 invited talks at APS meetings, conferences, workshops, and department colloquia and seminars. In addition, the consortium groups

published 28 papers in conference proceedings and gave 30 contributed talks at APS meetings and conferences. About 50% of the journal papers and 40% of the invited talks were based on work done at the on-site accelerator and research facilities. Summaries of accomplishments made during this reporting period in the five main research areas, including the nuclear physics research program at HIγS, are given below. In addition, some of the instrumentation and equipment R&D that is associated with the research projects is reported in the Nuclear Instrumentation and Methods section of this report. At the beginning of the summary for each research area, the faculty who devote more than 25% of their research effort and the graduate students conducting their thesis research in that area are listed. Only students enrolled at one of the consortium universities are included. The number in parenthesis is the number of students working in this area. The younger graduate students who have not committed to a thesis project are listed according to the area of their main contributions. Also, students who received their Ph.D. degree during this reporting period with a thesis topic in this area are listed. Finally, the number of journal articles published during this reporting period is given for each area.

1. **Fundamental Symmetries in the Nucleus:**
   The main experiments in this research area include the search for violation of time-reversal invariance via measurement of the neutron electric dipole moment (nEDM), tests of the long-term stability of coupling constants, non-unitarity tests of the CKM matrix, and measurement of the neutron lifetime. Progress on the nEDM project, interaction coupling constant experiments, and the neutron lifetime measurements are summarized below.

   Faculty: Haase, Huffman, Gao, Golub, Gould, Ahmed, and Young
   Graduate Students (10): Huffer (NCSU), Kendellen (NCSU), Medlin (NCSU), Palmquist (NCSU), Pattie (NCSU), Reid (NCSU), Schelhammer (NCSU), VornDick (NCSU), Zeck (NCSU), and Zhang (Duke)
   Ph.D. Degrees Awarded: Broussard (Duke), Holley (NCSU), Swank (NCSU), and Zheng (Duke)
   Number of published papers: 8

   (a) **nEDM Project:**

   - A system for measuring helium diffusion through materials used in the nEDM apparatus has been constructed, and characterization of a variety of materials is underway.
   - Reliable thermal modeling of the nEDM experiment requires quantitative knowledge of the main mechanisms for heat transfer within and external to the central volume of the apparatus. The NCSU group has developed a technique for measuring the heat deposited in the dilution refrigerator (DR) via superfluid helium film flow and vapor reflux back to the DR volume.
   - Construction of the ultra-cold neutron source (UCN) at the PULSTAR reactor at NCSU is proceeding on a schedule to have its first beam in late 2013. Concurrent with this work the group at NCSU is designing apparatuses for studying systematic effects in the nEDM experiment.

   (b) **Coupling Constants and Unitarity Tests of the CKM Matrix:**

   - The Oklo natural nuclear reactors have proven to be one of the more sensitive terrestrial testing grounds for studying the time variation of the fine structure constant. However, this requires that the operating temperature of the reactors be known. Analysis by a group at NCSU of recent cross-section measurements of neutron capture on ^{175}Lu indicates an operating temperature of the Oklo reactors that is a factor of more than three lower than the recommended value. Neutron capture cross-section measurements have been initiated at the PULSTAR reactor with the aim of providing data to help resolve this discrepancy.
   - The UCNA collaboration has made significant progress in reducing systematic errors in their polarization and energy calibrations. These improvements make possible β-asymmetry measurements with a precision of better than 0.5%. In addition, the collaboration collected data for about 34×10^6 decays during this reporting period, increasing the total number of accumulated decays to 65×10^6.
   - An important quantity for the CKM matrix is the weak mixing parameter V_{ud} between the up and down quarks. The most precise determination of this parameter

is provided by measurements of the lifetime for superallowed $0^+ \rightarrow 0^+$ Fermi decays in nuclei. Analysis was completed of ^{19}Ne lifetime data recently measured at Kernfysisch Versneller Institut (KVI) in Groningen by a TUNL group. A paper is being prepared for publication.

(c) **Neutron Lifetime Measurements:**

- The collaboration for the neutron-lifetime measurement at NIST has commissioned an upgrade to their apparatus and has collected decay data on trapped neutrons for several months. This experiment applies a technique that has very different sources of systematic uncertainties than previous measurements. Ultra-cold neutrons are confined in a three-dimensional magnetic trap in a liquid helium bath. The β particles emitted by the neutron decays are measured via detection of the scintillation light from ionization by the β particles in the liquid helium. Analysis of these initial data is underway.

2. **Neutrino Physics:**
A major theme in this research area is the search for violation of lepton-number conservation through the observation of neutrinoless double-beta decay ($0\nu\beta\beta$). The MAJORANA DEMONSTRATOR (MJD) is the main project at TUNL in this pursuit. The MJD project uses p-type point-contact, high-purity, and isotopically enriched (^{76}Ge) germanium crystals as both the sample and the detector in the search for $0\nu\beta\beta$ decay. The MJD experiment is located at the 4850-foot level in the Sanford Underground Research Facility (SURF) in Lead, SD. Other activities in this research area include KATRIN (determination of the absolute mass of neutrinos via studies of tritium decay); $2\nu\beta\beta$ decay to excited 0^+ states; and measurements of nuclear reaction data important for guiding calculations related to $0\nu\beta\beta$ decay and dark-matter-detection experiments. Progress on the projects in this area is summarized below.

Faculty: Henning, Howell, Karwowski, Tornow, Wilkerson, and Young
Graduate Students (13): Combs (NCSU), Corona (UNC), Finch (Duke), Finnerty (UNC), Giovanetti (UNC), Leviner (NCSU), MacMullin (UNC), Silano (UNC), Snavely (UNC), Strain (UNC), Ticehurst (UNC), Vorren (UNC), and Wierman (UNC)
Ph.D. Degrees Awarded: none
Number of published papers: 10 + 1 special report

(a) **Majorana Demonstrator Project:**

- **CD 2/3 stage approval**
The MJD collaboration achieved the major milestone of being approved for CD 2/3 activities. The CD 2/3 review was held in May 2012. This accomplishment marked the transition of the project to the construction and experiment installation stage.
- In addition to the major CD 2/3 milestone review, several site readiness reviews were conducted at SURF this year:
  - Oxygen Deficiency Hazards
  - Structural Analysis
  - SURF Cryo-Committee Review
  - Germanium Reduction and Refinement
  - MJD Laboratory Readiness Review and Inspection
- Underground component fabrication is a key protocol for minimizing radiological backgrounds in the MJD. The underground cleanroom-machine-shop was brought into operation this year. The results of gas analysis of the outgas from electroformed copper pieces placed in an ultra-high vacuum system indicate that the machining process does not contaminate the surface of the material at the level of sensitivity of our tests.
- The cleaning procedures for parts to be used in the DEMONSTRATOR and test assemblies were developed at Pacific Northwest National Laboratory (PNNL). This year, these procedures were implemented in a dedicated cleanroom (maintained at class 1000 or better) at UNC to clean copper, plastic, and stainless steel parts of the MJD detector modules. These cleaned parts were packaged and shipped to the MJD laboratory space at SURF. In addition to cleaning hardware for the first detector module,

this work provided training for the TUNL group in the cleaning procedures that will be carried out underground starting in the coming year.

(b) **Other Low-Background Counting Activities:**

- **MALBEK**
  The Majorana Low-Background Broad-Energy Germanium Detector at KURF (MALBEK) is an R&D project for developing p-type point-contact germanium detectors for applications in searches for weakly interacting massive particles (WIMPs). This application requires operating the detector at an ultra-low energy threshold to detect the recoil germanium nuclei in the event of a WIMP interaction in the detector. This year, modifications to materials in the detector cryostat reduced the background by about a factor of 10 in the region of the energy spectrum below 140 keV. This background reduction will significantly improve the signal-to-noise ratio in the 5 to 10 keV region of the energy spectrum, where signals from recoil nuclei are expected.
- Measurements of $2\nu\beta\beta$ decay to excited states provide information important for assessing calculations of nuclear matrix elements for $0\nu\beta\beta$ decay. Currently data exist for two nuclei only. Though ^{96}Zr is a good candidate for $2\nu\beta\beta$ decay, the process has never been observed in this nucleus. This year a new setup to search for the $2\nu\beta\beta$ of ^{96}Zr was installed at KURF, and measurements are underway.
- **KATRIN**
  The Karlsruhe Tritium Neutrino (KATRIN) experiment is a measurement of the kinematic mass of the electron antineutrino through the analysis of the spectral shape of the endpoint region of tritium β decay. Commissioning of the main spectrometer will start in 2013, and the TUNL group reports significant progress on items important for the commissioning. These include modeling processes that are potential sources of backgrounds in the main spectrometer, performing large-scale electromagnetic simulations of the main spectrometer, simulating electron transport and field-induced backgrounds (*e.g.*, Penning traps) in the focal-plane detector (FPD), and optimizing the FPD veto system.

(c) **Nuclear Reaction Measurements Important for Low-Background Counting Measurements:**

- Neutron-induced reactions are a source of background in low-background counting experiments that search either for $0\nu\beta\beta$ decay or for dark-matter particles. Groups at TUNL are measuring cross sections of nuclear reactions important for modeling the neutron-induced backgrounds in $0\nu\beta\beta$-decay experiments and dark-matter particle detectors. These reactions include ^{136}Xe$(n,2n)^{135}$Xe, ^{136}Xe$(n,n'\gamma)^{136}$Xe, ^{40}Ar$(n,n'\gamma)^{40}$Ar, ^{20}Ne$(n,n'\gamma)^{20}$Ne, Ge$(n,x\gamma)$, Cu$(n,x\gamma)$, ^{40}Ar$(n,p)^{40}$Cl, and neutron elastic scattering on Ne and Ar.
- Two-nucleon transfer reactions provide a mechanism for validating assumptions made in quasiparticle random-phase-approximation calculations about the ground-state configuration of nuclei involved in $0\nu\beta\beta$ decay. To this end, TUNL groups are constructing an experiment to carryout (^{3}He,n) two-proton-transfer reactions on nuclei used in $0\nu\beta\beta$ decay searches. The designs of the experiment and the ion-source ^{3}He gas recirculation system (see the Accelerator Physics section) are reported.

3. **Nuclear Astrophysics:**
The focus in this research area is on measurements and data evaluations that are important for resolving element abundance anomalies in globular clusters and for modeling stellar evolution, nucleosynthesis, and classical novae. A key part of this program is the measurement of reactions, such as ^{12}C$(\alpha,\gamma)^{16}$O, which are relevant to the evolution of massive stars. This research is primarily carried out at LENA and HIγS. The nuclear astrophysics experiments done at HIγS are reported in the Photonuclear Reactions section. Progress in this area is summarized below.

Faculty: Champagne, Iliadis, and Kelley
Graduate Students (7): Buckner(UNC), Cooper(UNC), Daigle (UNC), Downen (UNC), Hunt (UNC), Kelly (UNC), and Rich (UNC)

Ph.D. Degrees Awarded: none
Number of published papers: 4 + 1 special report

- Depletion of ^{18}O has been observed in low-mass asymptotic giant branch stars and certain presolar oxide grains. The $^{18}\mathrm{O}(p,\gamma)^{19}\mathrm{F}$ reaction could potentially contribute to this depletion. A search for an alleged resonance in this reaction at 95 keV was carried out at LENA. These measurements were used to set a new upper limit on the strength of such a resonance. This new limit is a factor of about eight lower than previous determinations. Based on these results, the $^{18}\mathrm{O}(p,\gamma)^{19}\mathrm{F}$ reaction does not contribute significantly to the depletion of ^{18}O in the above astrophysics environments.
- **STARLIB**
  The key ingredient of any realistic stellar computer model is a set of nuclear reaction probabilities, called reaction rates. A group at TUNL has created a novel method for estimating the rates for a large number of nuclear reactions. The newly devised method provides the first statistically meaningful values of reaction rates at all desired stellar temperatures. This work was published in Nuclear Physics **A841**, 31 (2010), but significant improvements to the library were made in this reporting period. In addition, the STARLIB website `http://www.tunl.duke.edu/~astro/ReactionRates/Rates.html` was completed and upgraded.
- Most meteorites are fragments of larger meteoroids that formed at about the same time as our solar system. Thus the study of meteorites can provide important information about the origin and early history of our solar system. In the summer of 2011, the North Carolina Museum of Natural Sciences loaned a TUNL group a fragment of the meteorite that landed in Farmville, NC on December 4, 1934. The isotopic abundances in the meteorite are being characterized using the $\gamma\gamma$ spectrometer at LENA.

4. **Nuclear Structure and Reactions:**
This area broadly covers two topics, few-nucleon systems and many-body physics of strongly interacting particles. The main aim of the few-nucleon experiments is to provide data important for refining few-nucleon calculations and developing the theoretical framework for describing systems of strongly interacting hadrons that have the structure and symmetries of QCD. The major thrusts in the many-nucleon systems research are the study of collective responses of nuclei to electromagnetic waves and the description of nuclear structure attributes with statistical models. The on-site accelerator facilities used for this research are the tandem accelerator laboratory and HIγS. Some of this work is also done at the Los Alamos Neutron Science Center. The experiments in this area done at HIγS are reported in the Photonuclear Reactions section. Progress in this area is summarized below.

Faculty: Ahmed, Howell, Karwowski, Kelley, Mitchell, Tornow, and Weller
Graduate Students (3): Gooden (NCSU), Kafkarkou (Duke), and Walker (NCSU)
Ph.D. Degrees Awarded: Esterline (Duke)
Number of published papers: 3 + 1 special report

- Reaction data on light nuclei are important for developing *ab initio* calculations based on effective nucleon-nucleon interactions. In addition, the fusion of light nuclei has applications in nuclear energy research. Examples are proton- and α-particle-induced reactions on isotopes of boron. These reactions are key processes in the design of aneutronic fusion reactors for energy production. To contribute to basic and energy research, groups at TUNL are making cross-section measurements of the $^{10}\mathrm{B}(p,\alpha)$, $^{10}\mathrm{B}(\alpha,n)$ and $^{11}\mathrm{B}(\alpha,n)$ reactions.
- In addition to testing nuclear reaction models, the $(n,2n)$ reaction is used in techniques for diagnosing high neutron fluxes, *e.g.*, assessing the performance of nuclear devices, and measuring the radiation released during fusion events at the National Ignition Facility. Cross sections for the $(n,2n)$ reaction on ^{181}Ta and ^{64}Zn were measured for incident neutrons from 8 to 14.5 MeV.
- A recent review of fission data suggests an unexpected dependence of the yields from neutron-induced fission on the incident neutron energy. To study this effect, fission prod-

uct yields were measured for neutron-induced fission on ^{235}U, ^{238}U, and ^{239}Pu at incident neutron energies between 4 and 15 MeV.

- For reactions induced by light nuclei ($A \leq 4$) at incident energies from about 15 to 200 MeV, the semiclassical exciton model of preequilibrium nuclear reactions provides a simple way to describe the continuum energy and angular distributions of the light nuclei emitted during energy equilibration. The TUNL pre-equilibrium code, PRECO, is based on this model. Recently a phenomenological projectile-breakup model was developed to make the PRECO code more complete. This year the main focus was on updating code parameters important for validating the breakup model for incident α particles. To this end, fits to 100 experimental (α, p) angular distributions were performed.
- Neutron capture data provides information about low-energy collective excitations in nuclei, namely the scissors mode and pygmy resonances. The DANCE collaboration at LANSCE uses γ-ray cascade measurements of isolated neutron resonances to determine resonance properties and to characterize the photon strength function. This year the collaboration published descriptions of a new analysis method that was developed for obtaining multiplicity distributions from the γ-ray-cascade data. Analyses of data on several nuclei were completed this year.

5. **Photonuclear Reactions at HIγS:**
The HIγS facility provides polarized photon beams for a broad research program in nuclear physics, including nuclear structure, nuclear astrophysics, and nucleon structure. The main nuclear structure program is studies of the collective responses of nuclei. Nuclear resonance fluorescence (NRF) is used to study collective modes of excitation at energies below the giant dipole resonance (GDR), and polarized Compton-scattering measurements map out coherent nuclear responses above the GDR. An example is the isovector giant quadrupole resonance. Compton scattering from unpolarized and polarized targets at energies above 60 MeV reveals information about the collective electromagnetic response of the internal degrees of freedom of nucleons. The specific goals of the nuclear physics program at the HIγS include: (1) measuring the astrophysical S-factor for the ^{12}C$(\alpha,\gamma)^{16}$O reaction at energies important to astrophysics, (2) studying collective nuclear excitations using NRF and Compton scattering, (3) determining the electric and magnetic polarizabilities of nucleons, and (4) measuring the spin polarizabilities of nucleons. Proposals for nuclear physics experiments requesting beam time at HIγS are reviewed by a Program Advisory Committee (PAC) consisting of members external to the TUNL consortium. The HIγS PAC meets once a year, normally in June. This year the PAC meeting was delayed until November because of a shutdown to install a new wiggler switchyard. Progress on PAC-approved experiments is summarized below.

Faculty: Ahmed, Clegg, Gao, Howell, Karwowski, Kelley, Iliadis, Tornow, and Weller
Graduate Students (8): Friesen (Duke), Hammond (UNC), Huang (Duke), Laskaris (Duke), Mueller (Duke), Peng (Duke), Tompkins (UNC), and Ye (Duke)
Ph.D. Degrees Awarded: Hammond (UNC)
Number of published papers: 12

(a) **Nuclear Astrophysics:**

- The ^{16}O$(\gamma,\alpha)^{12}$C reaction cross section has been measured at HIγS at γ-ray beam energies between 9.1 and 10.7 MeV using an optical time-projection chamber (OTPC) with CO_2 as the target gas. These data have been fully analyzed. The E1-E2 relative phase angles determined from these data agree with predictions based on elastic-scattering phase shifts. Additional data have been taken using N_2O as the target gas at γ-ray energies between 9.3 and 9.8 MeV. Analysis of these new data is underway.
- The second $J^\pi = 2^+$ state in ^{12}C, predicted to exist over fifty years ago, has been directly observed in the photodisintegration of ^{12}C into three α-particles at HIγS using the OTPC. The measured angular distributions were used to confirm the existence of a 2^+ state in ^{12}C at 10.06(4)MeV with a width of 800(60) keV. A paper to report this result is being prepared.

(b) **Few-nucleon Systems:**

- The goal of the experiments on the three- and two-body photodisintegration of ^{3}He with double polarizations is to test state-of-the-art three-body calculations and to make measurements towards the first investigation of the GDH sum rule on ^{3}He below the pion-production threshold. The first measurements of three-body photodisintegration on ^{3}He with double polarization (polarized beam and target) were performed this year. These measurements were made with circularly polarized γ-ray beams at 12.8 and 14.7 MeV. A new experiment has been designed for two-body ^{3}He photodisintegration with detection of the emitted protons using an array of silicon surface-barrier detectors.
- High-accuracy data for the reactions ^{4}He(γ,p)^{3}H and ^{4}He(γ,n)^{3}He have been measured at HIγS in the energy range between 20 and 30 MeV. These new data contradict recent measurements that reported large discrepancies between data and theoretical calculations. These new data taken at HIγS are in agreement with few-nucleon calculations and with the results of the pioneering experiments performed about 50 years ago, while ruling out most of the data obtained during the past 40 years. The results were published during this reporting period.

(c) **Nuclear Structure:**

- The dominant electromagnetic resonances in nuclei are the electric dipole and the electric quadrupole modes. The isovector giant quadrupole resonance (IVGQR) is of special interest today because the restoring force between the neutrons and protons, which are oscillating out of phase, is a result of the symmetry energy term in the nuclear matter equation of state, which describes the macroscopic behavior of nuclear matter. A knowledge of the strength and density-dependence of this term is crucial to understanding nuclear matter with a large neutron excess, including neutron stars. The parameters of the IVGQR have been poorly determined, until now. A group at TUNL has developed a new technique for making precise determinations of the energy, width, and strength for the IVGQR using Compton scattering of linearly polarized γ-rays at energies above the giant dipole resonance. A systematic survey of nuclei as a function of mass-number is presently underway. Measurements were made on ^{209}Bi and ^{89}Y this year.
- Nuclear resonance fluorescence (NRF) is used to study collective excitations in nuclei at energies below the giant dipole resonance. The pygmy resonance is of particular interest. This year NRF measurements were made on ^{96}Zr and ^{206}Pb. New $J = 1$ states were discovered in both nuclei.

6. **Accelerator Physics**
   TUNL operates three accelerator facilities: the High Intensity Gamma-Ray Source (HIγS), the Laboratory for Experimental Nuclear Astrophysics (LENA), and the tandem accelerator laboratory. Operation, maintenance and R&D activities for each accelerator facility are reported in this section.

7. **Instrumentation R & D**
   Developments in technology and instrumentation are vital to our research and training program. Our current instrumentation development activities include:

   - Instrumentation for characterizing the γ-ray beam at HIγS
   - Polarized target development
   - Detector development for nuclear-reaction measurements
   - Development of infrastructure facilities needed for research using ultra-cold neutrons and for low-background counting (*e.g.*, neutrinoless double-beta decay and dark-matter searches)

8. **Education**

   These activities include:

(a) **Research Experience for Undergraduates**
During this reporting period sixteen undergraduate students conducted research with groups at TUNL. Each summer, TUNL runs a Research Experience for Undergraduates (REU) program in nuclear physics, supported by the National Science Foundation (NSF). This year fourteen students participated in this ten-week program. Twelve of them were supported by the NSF REU grant and the other two by grants to TUNL faculty. Four of the students conducted research with the Duke High-Energy Physics group and spent the second half of their summer at the CERN Large Hadron Collider. The inclusion of the high-energy physics students adds an international component to the TUNL REU program.

(b) **TUNL Seminar Program**
The TUNL seminar program continues with characteristic vigor—this year with fourteen invited speakers. This series is augmented by the TUNL Informal Lunch Talks (TILT), where graduate students and postdoctoral fellows present their research projects; by the TUNL Astrophysics Journal Club; and by a special lecture series given by local speakers on Advances in Physics as part of the REU program during the summer. A related series of talks, the Triangle Nuclear Theory Colloquia, is also beneficial to TUNL faculty and students.

9. **Broader Impact Activities**

In addition to the above research in the frontier areas of nuclear physics, we run a nuclear data program and are conducting research important for applications of nuclear physics in national nuclear security, homeland security, and biology.

(a) **Nuclear Data Program**

- Nuclear data evaluation for $A = 3$ to 20, for which TUNL is the international center
- Web dissemination of nuclear structure information for $A = 3$ to 20

(b) **Applications**
The focus of these activities includes:

- γ-ray-induced reactions for homeland security and national nuclear security
- Neutron-induced reactions for national nuclear security
- Plant physiology using accelerator-produced $^{11}CO_2$ and $^{13}NO_3$

The success of our research program is largely attributable to the talents and enthusiasm of the faculty members, postdoctoral associates, research staff, and graduate students from the three Triangle universities. Also essential to our research program are long-term collaborations with research groups from Gettysburg College, North Carolina A&T State University, North Carolina Central University, North Georgia College and State University, Penn State Altoona, Tennessee Technological University, University of Connecticut at Avery Point, All-Russian Research Institute of Technical Physics (Snezhinsk), Istituto Nazionale di Fisica Nucleare (Pisa), Jagiellonian University (Cracow), Joint Institute for Nuclear Research (Dubna), Technische Hochschule Darmstadt, University of Cologne, and University of Mainz.

In our applications and interdisciplinary research program we collaborate with scientists from several national laboratories, including Lawrence Livermore National Laboratory, Thomas Jefferson National Accelerator Facility, Los Alamos National Laboratory, and Pacific Northwest National Laboratory, and with scientists from private companies, such as, Accelerator Driven Neutron Applications Corporation and Tri Alpha Energy, Inc.

Personnel

Department of Physics, Box 90308, Duke University,
Durham, NC 27708-0308
Department of Physics, Box 8202, North Carolina State University,
Raleigh, NC 27695-8202
Department of Physics and Astronomy, University of North Carolina,
Chapel Hill, NC 27599-3255

Faculty

Ahmed, M. W. (Adjunct Associate Professor)	NCCU/Duke
Bilpuch, E. G. (Professor Emeritus)	Duke
Champagne, A. E. (Professor)	UNC
Clegg, T. B. (Professor)	UNC
Gao, H. (Professor)	Duke
Golub, R. (Professor)	NCSU
Gould, C. R. (Professor)	NCSU
Haase, D. G. (Professor)	NCSU
Henning, R. (Assistant Professor)	UNC
Howell, C. R. (Director, Professor)	Duke
Huffman, P. R. (Associate Director, Professor)	NCSU
Iliadis, C. (Professor)	UNC
Karwowski, H. J. (Professor)	UNC
Kelley, J. H. (Research Associate Professor)	NCSU
Ludwig, E. J. (Professor Emeritus)	UNC
Merzbacher, E. (Professor Emeritus)	UNC
Mitchell, G. E. (Professor Emeritus)	NCSU
Roberson, N. R. (Professor Emeritus)	Duke
Tilley, D. R. (Professor Emeritus)	NCSU
Tonchev, A. P. (Adjunct Associate Professor)	Duke
Tornow, W. (Professor Emeritus)	Duke
Walter, R. L. (Professor Emeritus)	Duke
Weller, H. R. (Assoc. Dir. for Nuclear Physics at HIγS, Professor Emeritus)	Duke
Wilkerson, J. F. (Associate Director, Professor)	UNC
Wu, Y. K. (Associate Director for Light Sources, Associate Professor)	Duke
Young, A. R. (Professor)	NCSU

TUNL Advisory Committee

Aprahamian, A.	University of Notre Dame
Balantekin, A. B.	University of Wisconsin
Garvey, G. T.	Los Alamos National Laboratory
Vigdor, S. E.	Brookhaven National Laboratory
Wiescher, M. C.	University of Notre Dame

HIγS Program Advisory Committee

Beise, E. J.	University of Maryland
Garvey, G. T. (Chair)	Los Alamos National Laboratory
Griesshammer, H.	George Washington University
Rehm, K. E.	Argonne National Laboratory
Sherrill, B. M.	National Superconducting Cyclotron Laboratory
Chen, J. P.	Thomas Jefferson National Laboratory
Donnelly, T. W.	Massachusettes Institute of Technology

Associated Faculty

Crawford, B. E.	Gettysburg College
Crowe, B. J.	North Carolina Central University
Dutta, D.	Mississippi State University
Engel, J.	University of North Carolina
Gai, M.	University of Connecticut at Avery Point
Keeter, K. J.	Idaho State University
Korobkina, E.	North Carolina State University
Markoff, D. M.	North Carolina Central University
McLaughlin, G. C.	North Carolina State University
Norum, B.	University of Virginia
Pedroni, R. S.	North Carolina A&T State University
Prior, R. M.	North Georgia College and State University
Purcell, J.E.	Georgia State University
Shriner, J. F.	Tennessee Technological University
Spraker, M. C.	North Georgia College and State University
Stephenson, S. L.	Gettysburg College
Weisel, G. J.	Penn State Altoona

Accelerator Physics Staff for Operations

Li, J.	Senior Research Scientist (at HIγS)
Mikhailov, S. F.	Senior Research Scientist (at HIγS)
Popov, V. G.	Senior Research Scientist (at HIγS)
Westerfeldt, C. R.	Research Scientist (low energy accel.) & Rad. Safety Manager

Research Staff

Baramsai, B.[1] (Research Associate)	NCSU
Bhatia, C. (Research Associate)	Duke
Bhike, M.[2] (Research Associate)	Duke
Cesaratto, J. M.[3] (Research Associate)	UNC
Chu, P.[4] (Research Associate)	Duke
Crowell, A. S. (Research Scientist)	Duke
Dashdorj, D.[1] (Research Associate)	NCSU
Fränkle, F.M. (Research Associate)	UNC
Green, M.P. (Research Associate)	UNC
Hao, H. (Research Associate)	Duke
Howard, C. (Research Associate)	UNC
Howe, M. A. (Senior Research Scientist)	UNC
Jawalkar, S. [5] (Research Associate)	Duke
Kalbach Walker, C. (Senior Research Scientist)	Duke
Malace, S. (Research Scientist)	Duke
Mazumdar, I.[5] (Senior Visiting Research Scientist)	Duke
Mehta, V.[6] (Research Associate, part time)	NCSU
Meziane, M. (Research Associate)	Duke
Myers, L. S. (Research Associate)	Duke
Parikh, N. (Research Associate)	UNC
Phillips II, D. G. (Research Associate)	UNC/NCSU[2]
Sallaska, A. (Research Associate)	UNC
Seo, P.-N. (Research Associate)	UVA
Sikora, M. H. (Research Associate)	GWU

Technical and Nuclear Data Support Staff

Addison, J. H.[7]	Lab Apparatus Designer
Busch, M.	Mechanical Engineer
Carlin, B. P.	Electronics Supervisor
Carter, E. P.[8]	Accelerator Technician
Dunham, J. D.	Accelerator Technician
Emamian, M.	Mechanical Engineer (at HIγS)
Faircloth, J.	Project and Building Maint. Coordinator (at HIγS)
Johnson, M.	Vacuum Technician (at HIγS)
Mulkey, P. H.	Electronics Technician
Oakley, O.[8]	Electronics Technician (at HIγS)
O'Quinn, R. M.	Accelerator Supervisor
Pentico, M.	Accelerator Technician (at HIγS)
Rathbone, V.	Accelerator Technician (at HIγS)
Sheu, G.	Project Coordinator, Nuclear Data
Swift, G.[9]	Vacuum Engineer (at HIγS)
Wallace, P.[9]	Electrical Engineer and Safety Manager (at HIγS)
Walsh, B.[10]	Accelerator Technician
Wang, P.	RF Engineer (at HIγS)

[1] Supported by NNSA/DOE
[2] As of 6/12
[3] Departed 9/11
[4] As of 10/11
[5] As of 1/12
[6] Supported by NSF/DOE
[7] Deceased 2/12
[8] Part-time
[9] Supported by DHS
[10] As of 6/12

Graduate Students

Agbeve, K. A.	NCCU	Lin, L.	UNC
Attayek, P.	UNC	MacMullin, S.	UNC
Broussard, L. J.[1]	Duke	Medlin, G.[5]	NCSU
Buckner, M.[2]	UNC	Meier, N.	NCSU
Combs, D.	NCSU	Meyer, E.	UNC
Cooper, A.L.	UNC	Mueller, J. M.	Duke
Corona, T. J.	UNC	Palmquist, G.	NCSU
Cumberbatch, L. C.	Duke	Pattie, R. W.,Jr.[4]	NCSU
Daigle, S.	UNC	Peng, C.	Duke
Davis, B. J.	NCCU	Reid, A.	NCSU
Downen, L. N.	UNC	Rich, G.	UNC
Esterline, J. H.[1]	Duke	Schelhammer, K.	NCSU
Fallin, B. A.	Duke	Silano, J.	UNC
Finch, S. W.	Duke	Strain, J.	UNC
Finnerty, P.	UNC	Snavely, K.	UNC
Friesen, F. Q.	Duke	Swank, C. M.	NCSU
Gooden, M. E.	NCSU	Swindell, A. G.	U. Conn
Giovanetti, G. K.	UNC[3]	Ticehurst, D. R.	UNC
Hammond, S. L.[1]	UNC	Tompkins, J. R.	UNC
Harrell, A.	NC A&T	Vorren, K.	UNC
Holley, A. T.[1,4]	NCSU	VornDick, B.[4]	NCSU
Huang, M.	Duke	Walker, C.[6]	NCSU
Hunt, S.	UNC	Wierman, K.	UNC
Huffer, C.	NCSU	Wu, W. Z.[1]	Duke
Kafkarkou, A.	Duke	Ye, Q. J.	Duke
Kelley, J. A.	UNC	Yan, X.	Duke
Kelly, K.	UNC	Zeck, B.[7]	NCSU
Kendellen, D. P.	NCSU	Zhang, Y.	Duke
Laskaris, G.	Duke	Zheng, W. Z.[1]	Duke
Leviner, L.	NCSU	Zimmerman, W. R.	U. Conn

Visiting Scientists

Witała, H.	7/12 - 8/12	Jagiellonian University, Cracow, Poland

Administrative Support Personnel

Strope, J.[8]	Staff Assistant
West, B.	Staff Assistant

[1]Graduated with Ph.D. Degree between 9/11 and 8/12
[2]Supported by DOE NSSA Fellowship
[3]Supported by DOE Office of Science Fellowship
[4]Supported by NSF/DOE
[5]Supported in part by a GAANN Fellowship
[6]Supported by NNSA/DOE
[7]Supported in part by LANL
[8]Partially supported by the Duke University Physics Department

Undergraduates

Student	*Institution*	*Faculty Advisor*
Anderson, N.[1]	University of Michigan	A. E. Champagne
Bascetta, J.	Duke University	C. R. Howell
Beaumont, B.	NCSU	P. R. Huffman
Bradt, J.[1]	University of Rochester	W. Tornow
Charles, A.[1]	University of Virginia	J. Engel (UNC)
Collins, M.	NCSU	D. G. Haase
Daniel, Q.	Florida A&M University	C. R. Howell
Fisher, B.[1]	Richard Stockton College	M. W. Ahmed and H. R. Weller
Frame, D.	NCSU	D. G. Haase
Greene, W.[1]	University of Evansville	H. Gao
Hardin, J.	UNC Chapel Hill	H. J. Karwowski
Havener, L.	UNC Chapel Hill	H. J. Karwowski
Huff, A.[1]	Florida State University	A. Arce (Duke)
Hughes, A.[1]	Rensselaer Polytechnic Inst.	H. Gao
Johnson, C.	UNC Chapel Hill	J. F. Wilkerson
Koufalis, P.[1]	Kutztown University	S. Bass and B. Mueller (Duke)
Le, K.	Duke University	C. R. Howell and C. D. Reid (Duke)
Malone, R.[1]	Gettysburg College	S. Bass and B. Mueller (Duke)
Mauney, A.	NCSU	A. R. Young
Miller, O.[1]	East Tennessee State Univ.	M. Kruse and A. Arce (Duke)
Moore, P.	NCSU	A. R. Young
Muslim, S.	NCCU	D. M. Markoff, H. J. Karwowski, and J. F. Wilkerson
Nash, L.	UNC Chapel Hill	H. J. Karwowski
Nguyen, C.	UNC Chapel Hill	H. J. Karwowski
Raudabaugh, J.	NCSU	D. G. Haase
Rowland, J.	NCSU	D. G. Haase
Royce, C.	NCSU	P. R. Huffman
Sanford, N.[1]	High Point University	K. Scholberg (Duke)
Tripp, N.	Grand Valley State Univ.	C. R. Howell
Zander, C.	NCSU	A. R. Young
Zawisza, I.[1]	Moravian College	C. R. Howell
Zitin, A.	UNC Chapel Hill	J. F. Wilkerson

[1]Supported by the TUNL NSF REU Program

Fundamental Symmetries in the Nucleus

Chapter 1

- **Time-Reversal Violation: The Neutron Electric Dipole Moment**
- **Fundamental Coupling Constants**

1.1 Time-Reversal Violation: The Neutron Electric Dipole Moment

1.1.1 Search for the Neutron Electric Dipole Moment

M.W. Ahmed, H. Gao, R. Golub, C.R. Gould, D.G. Haase, P.R. Huffman, D.P. Kendellen, E. Korobkina, A.R. Reid, C.M. Swank, A.R. Young, Y. Zhang, W.Z. Zheng, *TUNL*; the nEDM collaboration

TUNL plays a major role in the program to develop a new technique to search for a neutron electric dipole moment. This effort offers the promise of a sensitivity up to two orders of magnitude greater than in existing measurements. During the past year, researchers at TUNL have taken data on the geometric phase effect; measured heat flow in superfluid films; collaborated on efforts at LANL to measure the high-voltage breakdown in liquid helium; developed measurement-cell coating and assembly techniques; and are developing an apparatus to study systematic effects using polarized ^{3}He and ultracold neutrons.

The 2007 NSAC Long Range Plan lists the search for an electric dipole moment of the neutron (nEDM) as a key component of a program in fundamental science with neutrons, which in turn is a key piece of a larger program testing fundamental symmetries and interactions. A report from a recent NSAC subcommittee on fundamental physics with neutrons re-endorsed the nEDM search as the top priority. The nEDM collaboration is developing a proposal around the novel technique proposed by Golub and Lamoreaux. The proposed technique uses superthermal capture of cold neutrons in superfluid ^{4}He to create trapped ultracold neutrons (UCNs) and introduces a trace amount of polarized ^{3}He to act as co-magnetometer [Gol94].

Searches for a possible nEDM have a long history, stretching back to Smith, Purcell, and Ramsey's 1957 paper [Smi57] on an experiment performed at the old graphite reactor at ORNL. Significant advances in limits on the nEDM have been tied to qualitative improvements in experimental concept and technique. This experiment would be no exception and would place particular emphasis on the control of experimental uncertainties. The goal of the present effort is an nEDM observation or limit at 4×10^{-28} e·cm. The collaboration received DOE CD-1 funding in 2006 and is working towards an operating experiment. The required beam line, Flight Path 13, has recently started operations at the Spallation Neutron Source at ORNL, where the experiment will be located on the cold neutron line. This is estimated to improve the ultimate number of trapped UCNs by a factor of five over the number possible using the originally planned 0.89 nm monochromator line at Flight Path 13.

The top priority for the experimental effort is understanding the high-voltage breakdown at our operating temperature in liquid helium. Work is presently underway on a new, smaller cryostat, that will reach temperatures below 0.5 K and allow both rapid cool-down and changes on a short timescale. The R&D focus is on open HV issues and the operation of a (scaled) cell with all key features in the electrode gap. The design enables tests at the expected values for operating parameters such as temperature, pressure, and field strength. These efforts are primarily going on at LANL, but TUNL has provided significant guidance in the design of the new cryogenic apparatus.

The primary effort at TUNL is to develop a small-scale test apparatus for use with the UCN source at the PULSTAR reactor facility located on the campus of NC State University. This apparatus will mimic the nEDM cryostat, but with a single, full-sized measurement cell and no provision for establishing a high electric field across the cell. It will be utilized to investigate and elucidate the various interactions between UCNs, ^{3}He, and ^{4}He that will be encountered during the nEDM experiment. These include:

- loading and heat-flush removal of ^{3}He in the measurement cell;

- ^{3}He scintillation monitoring of the relative precessions of UCNs and ^{3}He;
- demonstration of the dressed-spin technique; and
- measurement of the trajectory correlation function, in an effort to reduce the systematic uncertainty due to the geometric-phase effect.

Construction of the UCN source is currently underway at NCSU. We aim to have initial tests of UCN production in the measurement cell in late 2013. Longer-term tests will follow and continue to be performed up to, and perhaps even in parallel with, the commissioning of the full nEDM apparatus.

In addition to the research outlined above and described in subsequent sections of this report, TUNL faculty serve in leadership roles in the project. Golub serves as one of the two principal scientists; Golub and Huffman co-chair the internal technical committee; Gao, Golub, and Huffman serve on the project's executive committee; Haase and Huffman serve as subsystem managers for the construction of the cryovessel and for the assembly and commissioning of the subsystems, respectively; and Huffman serves on the federal project team as the project's technical coordinator and deputy project manager. Several others serve as work-package managers for components of the subsystems. An overview of the nEDM apparatus is shown in Fig. 1.1.

[Gol94] R. Golub and S. K. Lamoreaux, Phys. Rep., **237**, 1 (1994).

[Smi57] J. H. Smith, E. M. Purcell, and N. F. Ramsey, Phys. Rev., **108**, 120 (1957).

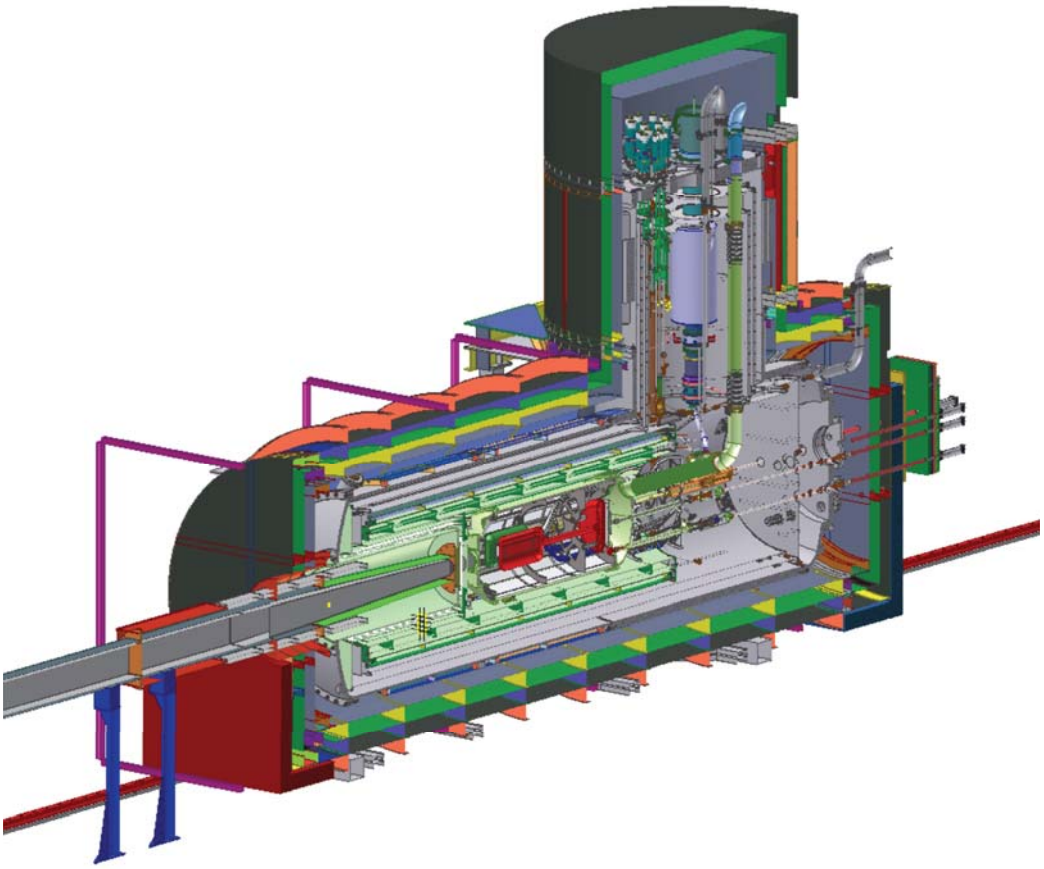

Figure 1.1: (Color online) Cross sectional view of the nEDM apparatus. The approximate dimensions are 7.5 m long, 5.5 m tall, and 2.2 m wide. The neutron beam enters the central volume from the right and is down-scattered in liquid helium to produce ultracold neutrons that are confined within the measurement cells. The cells are positioned within a strong electric field and weak magnetic field. The cells are surrounded by roughly 1,000 l of liquid helium housed in a composite vessel. The ^{3}He system and central volume are cooled to below 500 mK with a ^{3}He/^{4}He dilution refrigerator.

1.1.2 Gas Diffusion and Cryogenic Tests for the nEDM Project

D.P. Kendellen, D.G. Haase, P.R. Huffman, *TUNL*; M.C. Collins, D.K. Frame J.R. Rowland, *North Carolina State University, Raleigh, NC*

A multi-institution collaboration is designing an experiment for a new measurement of the neutron electric dipole moment. It will be mounted on a dedicated beam line at the Spallation Neutron Source at ORNL. In the past year we have focused on cryogenic design and construction issues, on the testing of component materials, and on strategies for removing ^{3}He from liquid ^{4}He during the measurement cycle.

1.1.2.1 Diffusion of Helium Gas through Plastics and Epoxy-Fiber Composites

The proposed measurement of the neutron electric dipole moment (nEDM) at the ORNL Spallation Neutron Source will require a large cryogenic device capable of cooling 1000 liters of liquid helium to 0.45 K. Unfortunately much of the system must be made of materials that are non-metallic, non-electrically conductive, non-magnetic, and not activated by neutrons.

The 1000-liter central volume will be constructed of an epoxy-fiber composite, of a type similar to G-10. The most effective way to cool such a device is by using helium gas for heat exchange from room temperature to 4 K. However, permeation of helium through the composite material reduces the insulation volume and produces a large helium-gas background that frustrates leak detection with a helium mass-spectrometer leak detector. To quantify the diffusion of helium through materials, we have constructed a diffusion-measurement device and measured room-temperature diffusion in thin membranes of Kapton, G-10 and molded dicyclopentadiene from Spencer Composites. The Kapton results compare well with published values [Sch10]. This method can now be used to test other candidate materials.

The permeability K of a particular specimen is a measure of the volume of gas passing through a unit area per unit time under a unit pressure difference; its diffusivity D refers to the speed at which individual atoms pass through it; and its solubility S is the volume of gas that it can contain per unit of applied pressure divided by total volume of the specimen. The permeability, diffusivity, and solubility are related by the equation $K = DS$. Thus measurement of any two of these parameters automatically determines the third.

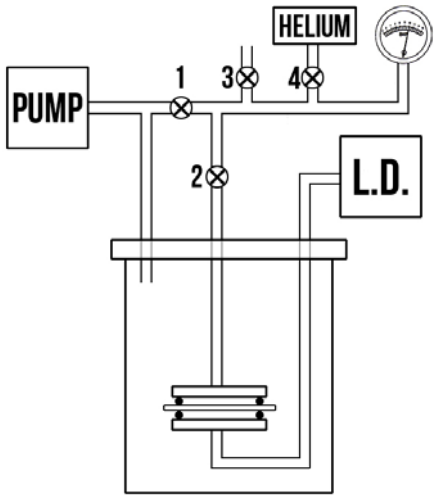

Figure 1.2: Diagram of the experimental configuration. Circles with X's indicate gas valves that may be opened or closed, and L.D. stands for "leak detector". A compound pressure/vacuum gauge is seen in the upper right.

A device, diagramed in Fig. 1.2, was constructed to measure the diffusion of ^{4}He through thin circular plates of material. Helium gas is pumped through a tube that enters the sealed container via one of three quick-couple tube connections on the lid. Inside, the helium gas flows to the sample material sandwiched between a brass flange sealed with rubber O-rings. Helium that diffuses through the sample exits the container through a second connection on the lid and goes to a leak detector that measures the diffusion rate. A third connection leads to a mechanical pump so that any helium that escapes through the edges of the testing flange will be transported away from the leak detector.

Helium is allowed to diffuse through the sam-

ple until the leak detector shows a constant flow rate, indicating that the system has reached equilibrium and the material is fully saturated with helium. Once the material is in equilibrium, its permeability can be determined using the equation

$$K = \frac{L_0 d}{A\Delta P}, \tag{1.1}$$

where L_0 is the steady-state leak rate, d is the sample thickness, A is the sample area, and ΔP is the pressure difference across the sample.

The diffusivity can be extracted using the rate at which the flow increases before reaching steady-state, or, alternatively, the rate at which the flow decays from steady-state. Once the helium input has been removed, the decrease in the flow rate can be fit to an exponential decay

$$L = L_0 e^{-t/t_0} \tag{1.2}$$

with

$$t_0 = \frac{d^2}{D\pi^2} \tag{1.3}$$

from which one can extract the diffusivity constant, D. Such a fit is shown in Fig. 1.3.

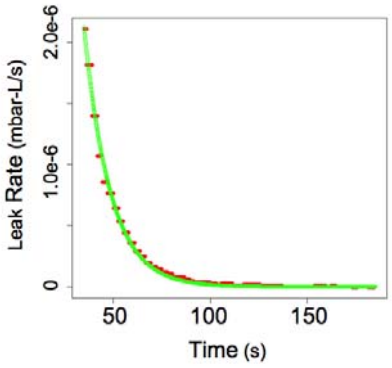

Figure 1.3: Plot for diffusion of helium through a 5 mil Kapton film at room temperature. The red points are the original data points minus background. The green line is the fitting function.

1.1.2.2 Construction and Operation of the 4 K Cryocooler Test Facility

We have completed construction and testing of a chamber in which large pieces of equipment—up to 20 inches diameter and 18 inches high—can be cooled to 4 K for vacuum leak testing. The chamber is cooled by a Sumitomo RDK-415D cryocooler that has reached 3.5 K. We have mounted large flange-pairs made of G-10 and dicyclopentadiene to test gas diffusion and vacuum seals made from 5 mil Kapton film. Large area copper foils were greased to the tops of the fixtures and connected to the RDK-415D cooling head. We attached thermometers at the top and bottom of the fixtures and are analyzing the temperature data to learn how to optimize the cooling process. A helium liquefaction and recirculation circuit is under construction to mount on the RDK-415D and provide cooling to 1.5 K to test superfluid helium film flow.

1.1.2.3 Construction and Testing of Etched Silicon Superfluid Helium Film Suppressors

An nEDM test facility will be constructed at the PULSTAR reactor at NCSU. The facility will be used to study the trapping of neutrons in a superfluid helium container and to measure the interaction of the neutrons with polarized ^{3}He dissolved in the superfluid. In the process, atoms of polarized ^{3}He will be introduced from a room temperature gas cell into the superfluid helium container at low temperature. The initial ^{3}He concentration will be 10^{-10}. Upon completion of the neutron measurement the depolarized ^{3}He must be removed to reduce the concentration to about 10^{-12} in a period of 16 hours.

The ^{3}He is to be removed by preferential evaporation from the ^{4}He. This can be accomplished at temperatures of 0.3 to 0.7 K. However, the process is complicated by a superfluid ^{4}He film flowing out of the container and rapidly filling up the charcoal adsorber used to pump the gas. We are investigating ways to reduce this effect and to optimize the pumping cycle. We are fabricating etched silicon film suppressors [Shi98, Ish10] at the NCSU Nanofabrication Facility and are developing a theoretical model of the helium film-flow and heat-exchange through these suppressors. The suppressors will be tested at 1.5 K on the cryocooler.

[Ish10] K. Ishikawa *et al.*, Cryogenics, **50**, 507 (2010).

[Sch10] S. J. Schowalter, C. B. Connolly, and J. M. Doyle, Nucl. Instrum. Methods A, **615**, 267 (2010).

[Shi98] P. J. Shirron and M. J. DiPirro, Adv. Cryogenic Eng., **43**, 949 (1998).

1.1.3 Superfluid Helium Film Flow and Vapor Reflux

D.P. Kendellen, D.G. Haase, P.R. Huffman, *TUNL*

In each volume of liquid helium connected by a tube to a warmer container, a superfluid film will flow up the tube walls and vaporize. The warm vapor will then be driven back to the cold liquid surface, transporting heat. We measured this effect at 0.3 K in a closed thermal column, in order to assess the validity of an existing model at the operating temperature for the nEDM experiment and to guide the design of heat sinks in the apparatus.

In the nEDM apparatus, a series of liquid helium volumes and connecting tubes will move polarized ^{3}He into the measurement cells and remove the depolarized ^{3}He. The nEDM dilution refrigerator (DR) will cool the ^{3}He volumes to a temperature T of about 0.3 K. In each volume, there is a free surface of liquid and a tube leading to warmer parts of the apparatus. A superfluid film coats the tube and flows up the walls in response to the temperature gradient. The film eventually vaporizes, creating a pressure gradient that drives the warm vapor back to the 0.3 K liquid, where it recondenses. This reflux effect transports heat to the low temperature stage of the DR, where it is costly to remove.

Heat transport from the refluxing vapor has been modeled [Nac94] with a "cold" volume of liquid helium at the base, connected by a thin-walled tube to an upper "hot" volume, which is heated electrically. All heat is assumed to be transported by refluxing vapor. Conduction down the walls of the tube or through the film itself are neglected. No atoms are exchanged between the film and the vapor along the length of the tube. Combining Poiseuille's equation, which describes the pressure gradient in a tube with diameter d, with the chemical potential of an ideal gas, the model gives the pressure and temperature gradients in the cell:

$$\nabla_z P = \frac{128\eta}{\pi d^4}\frac{\dot{Q}R}{L}\frac{T}{P} \quad (1.4)$$

$$\left(\frac{5}{2} - \frac{\mu_4}{kT}\right)\nabla_z T = \frac{128\eta}{\pi d^4}\frac{\dot{Q}R}{L}\frac{T^2}{P^2} \quad (1.5)$$

where η is the viscosity of the helium gas, k is Boltzmann's constant, μ_4 the chemical potential, R the gas constant, L the latent heat of the bulk liquid, and $\dot{Q}$ is the heater power applied to the top of the cell. We can solve these equations for $P(z)$ and $T(z)$. At temperatures above 0.8 K, the cell has a high thermal conductance, and temperature gradients are small. Below 0.5 K, however, the rapidly decreasing saturated vapor pressure has become low enough that the thermal conductance of the cell is about that of a Pyrex tube.

A previous experiment [Hay94] verified the model at $T \geq 0.9$ K for pure ^{4}He in tubes with $d \leq 3.1$ mm. We have now tested the model at 0.3 K using a cell with $d = 6.53$ mm to match the lower temperatures and larger tubes in the proposed nEDM apparatus.

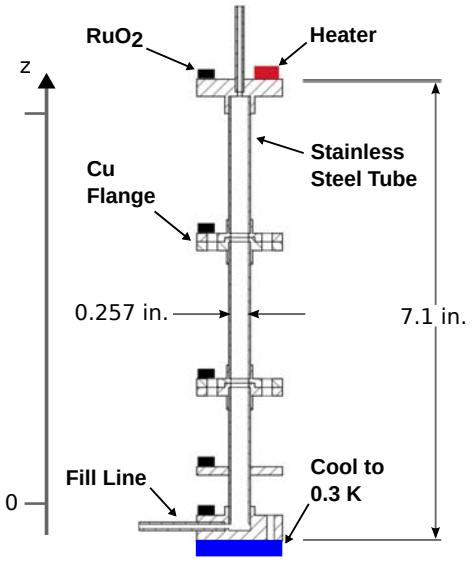

Figure 1.4: (Color online) Film Flow Apparatus

Our apparatus, shown in Fig. 1.4, is a series of stainless steel tubes separated by copper flanges. The tube walls are 0.79 mm thick. We attached a 500 Ω resistive heater at the top and RuO_2 thermometers at five points along the cell. We cooled the base to 0.3 K with a DR. After activating the heater at the top, we recorded the temperature profile.

Figure 1.5 displays the empty-cell equilibrium temperature profiles. Stainless steel is a poor thermal conductor, and modest heater powers produced temperature differences of a few degrees. The measured points agree with curves calculated using the thermal conductivity of stainless steel [Lou74]. As the heater was turned on and off, the cell responded with a time constant of around three minutes.

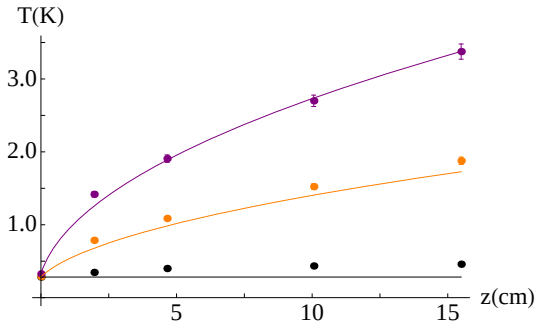

Figure 1.5: (Color online) Empty cell: Temperature vs. vertical height for different heater powers. From top to bottom, $\dot{Q}$ = 100, 25, and 0 μW. The curves are calculated values.

After adding a small amount of liquid to the cell, the temperature gradients were greatly reduced, and the cell's time constant decreased to 20 seconds. Figure 1.6 shows measured profiles with sufficient liquid to form a saturated film. The curves for each heater power were calculated from the reflux model. The bottom curve has $\dot{Q}$ set to 4 μW in the model to match the temperatures measured with the heater turned off (i.e $\dot{Q} = 0$), suggesting that the background heat is on the order of a few microwatts. The measured points should not match the model curve precisely since all of the background heat is not deposited at the top of the cell, as the model assumes.

In Fig. 1.6, there is a considerable rise in the temperature at the top of the tube for only a few microwatts of power, but the rise tends to saturate as the heater power is increased. Refluxing vapor carries off the heat more efficiently as the temperature and vapor pressure rise. The thermal conductance of the cell increases with heater power.

The profiles for 25 and 100 μW agree with the reflux model. In fact, the curves shown in Fig. 1.6 are from a modified version of the model that includes the heat transferred through both the reflux effect and the walls of the tube. This modification mainly affects the profile near the cold end of the tube, where the vapor pressure is low. We have confirmed that the model, with this slight modification, accurately describes heat transport due to the reflux effect in a larger diameter tube at $T = 0.3$ K.

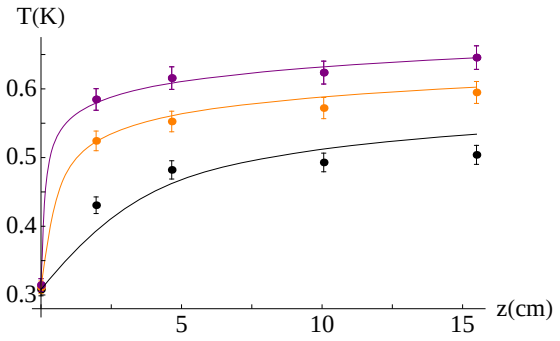

Figure 1.6: (Color online) Liquid in cell: Temperatures vs. vertical height for different heater powers. From top to bottom, $\dot{Q}$ = 100, 25, and 0 μW. The curves are calculated using the reflux model, with $\dot{Q}$ = 4 μW for the bottom curve.

We also measured the breakdown of the reflux in the cell when the base is at 0.75 K. As the heater power is increased, more film will evaporate in the top of the tube than can be replenished by film flowing up the walls. At this critical heater power, the temperature at the top of the cell rose rapidly, as reported in past experiments on unsaturated films [Bow51].

An orifice inside the tube could reduce the amount of heat transferred to the low temperature stage of the DR. The orifice's perimeter reduces film flow to the upper part of the tube and restricts the refluxing vapor. The orifice would be heat sunk at some intermediate temperature to reduce heating to 0.3 K. We will use the model to find the optimal orifice diameters, locations, and temperatures for the nEDM apparatus tubes.

[Bow51] R. Bowers, D. F. Brewer, and K. Mendelssohn, Philos. Mag. Series 7, **42**, 1445 (1951).

[Hay94] M. E. Hayden, M. Cornut, and P. J. Nacher, Physica B, **194-196**, 677 (1994).

[Lou74] O. V. Lounasmaa, *Experimental Principles and Methods Below 1K*, Academic Press, New York, 1974.

[Nac94] P. J. Nacher, M. Cornut, and M. E. Hayden, J. Low Temp. Phys., **97**, 417 (1994).

1.1.4 Systematic Studies for the nEDM Experiment at the PULSTAR Ultracold Neutron Facility

R. Golub, H. Gao, D.G. Haase, P.R. Huffman, A.R. Reid, C.M. Swank, *TUNL*; A. Hawari, E. Korobkina, *North Carolina State University, Raleigh, NC*; the nEDM collaboration

A TUNL program to explore key systematic effects for the nEDM experiment is being developed at the PULSTAR ultracold-neutron source at NCSU. This world-class source of UCNs, coupled with the existing polarized-^{3}He capabilities at TUNL, is enabling the development of a test-bed for investigating many UCN-^{3}He interactions at cryogenic temperatures. This past year, we have focused primarily on the engineering design of the apparatus.

A program at TUNL is being developed with the primary goal of exploring key systematic effects for the nEDM (neutron electric-dipole-moment) experiment. The PULSTAR ultracold neutron (UCN) source at NCSU will soon come online as a world-class source, comparable in intensity to those at the Institut Laue Langevin and LANL. This source, coupled with the existing polarized-^{3}He capabilities at TUNL, allows the development of a test-bed for studying many UCN-^{3}He interactions at cryogenic temperatures.

The goal is to develop an apparatus for testing five key scientific areas in a single nEDM measurement cell. The cell will be filled with liquid helium, reside in a uniform magnetic field (without an electric field), and be cooled to the nEDM experiment's operating temperature. It will use both polarized ^{3}He and polarized UCNs.

The concept is to have a measurement-cell filled with liquid ^{4}He at a temperature of about 450 mK and to place it within a uniform magnetic field, denoted as the B_0 coil. Cryogenic conventional and superconducting magnetic shields will surround this geometry, as will thermal radiation shields and a series of external, conventional magnetic shields. UCNs from the PULSTAR source will be transported to the cell through a series of guides and then introduced into the cell through a valve similar in design to the nEDM "V1" valve. Polarized ^{3}He will be produced using an external system and introduced into the cells alongside the polarized UCNs.

Interactions of the UCNs with the ^{3}He will be monitored using the spin-dependent neutron-capture rate. Light from the neutron-capture events produces scintillations in the liquid helium. The light will be wavelength shifted to the visible region using deuterated fluors and will then be transported away from the cell through acrylic light-guides for detection by photomultiplier tubes. Pulses will be digitized and analyzed offline.

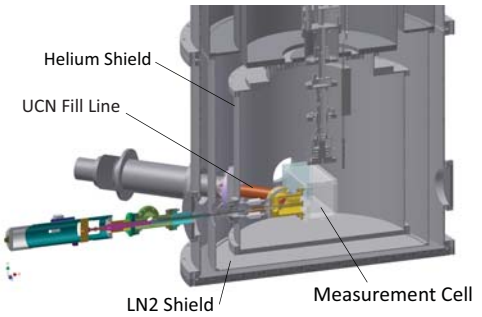

Figure 1.7: (Color online) Engineering cross-sectional schematic of phase I of the nEDM-systematic-studies apparatus. UCNs from the external source enter through a horizontal port, via a vestibule attached to the side of the cell. Polarized ^{3}He enters through a tube (not shown) extending vertically alongside the dilution refrigerator and through the same vestibule.

At the end of a measurement cycle, the unpolarized ^{3}He must then be removed from the liquid. This will be performed using the heat flush technique to concentrate the ^{3}He into a small volume that can be removed from the cryostat.

A schematic of the present experimental design for phase I of the testing is shown in Fig. 1.7. The initial phase will measure UCN and ^{3}He storage times in the measurement cell and will investigate the removal of ^{3}He from the ^{4}He. Phase II will add the B_0 coil and external magnetic shields.

The five areas where studies at TUNL will provide significant advances to the development and implementation of the nEDM project are as follows:

(1) *Measurement of scintillations due to the relative UCN and ^{3}He precession frequencies; demonstration of the critical-dressing technique.* The motion of a spin under the application of static and non-resonant oscillating magnetic fields is quite complicated. Without the new apparatus, the measurements necessary to establish working parameters for the double resonance of UCNs and ^{3}He must occur on the project's critical path during the commissioning phase. The proposed apparatus will allow the critical-dressing parameters to be established and the techniques for providing the critical dressing to be experimentally vetted in parallel with the construction and commissioning of the main apparatus. This will reduce both the time to data collection and the overall risk to the project.

(2) *Measurement of the trajectory correlation function for systematic-error quantification.* Differences between the actual trajectory correlation function in the measurement cells and those predicted by theory may result in a mishandling of the geometric-phase systematic error, leading to a false nEDM result. The proposed apparatus will allow these functions to be measured in order to establish, for example, the effect of wall collisions on the correlation function prior to measurements in the main apparatus.

(3) *Detection of the ^{3}He pseudomagnetic field in search of possible double-resonance effects.* This field results from the spin-dependent coherent-scattering cross section, which leads to an energy shift for the UCNs that is spin-dependent and thus appears as a magnetic field. The pseudomagnetic field is not directly affected by the application of an electric field, but it can be the source of fluctuations in the precession frequency and hence extra noise in the system. The magnitude of the pseudomagnetic field can be reduced by ensuring that the ^{3}He spins have no component along the static magnetic field. This is possible by careful control of the spin-flip pulses.

(4) *Development of techniques for NMR imaging of ^{3}He.* Inhomogeneities in the ^{3}He distribution can couple with field gradients and/or detection non-uniformities to produce a false nEDM signal. The proposed apparatus will enable us to develop imaging techniques to map the uniformity of the ^{3}He distribution and to study inhomogeneities that might arise as a result of effects such as polarity-dependent heat currents that drive the ^{3}He distribution in different directions.

(5) *Study of techniques for reversing $\sigma_{^3He}$, σ_{UCN} and B_0.* Establishing the experimental parameters for reversing the spins and magnetic fields will take considerable time during the commissioning phase of the apparatus. Developing these techniques in parallel in the new apparatus will provide an environment for performing a more complete study of these reversals without the external time constraints imposed by the critical path. This will reduce both the risk to the project and the time to data collection.

Given the infrastructure that will be in place, we note for reference that the apparatus can also be used for additional tests on actual measurement cells that could later be installed in the main apparatus. These items include UCN and/or ^{3}He storage and depolarization studies to optimize measurement-cell materials and fabrication techniques, as well as testing new cell designs and/or trouble shooting cells that don't work in the main apparatus.

A complete cost/benefit analysis has shown that this apparatus is cost-neutral to the project as a whole, while reducing the overall duration of the project by at least six months. Having this apparatus available for dealing with unexpected problems that may arise during commissioning reduces the project risk and could save significant time and cost contingencies.

Measurements using this apparatus will be able to mitigate several project risks identified in the project's risk log: the spin-dressing feedback electronics needed to properly modulate both measurement cells; due to long cool-down/warm-up cycles and complicated geometry, the main apparatus is not an ideal environment in which to debug issues that may arise; the displacement or non-uniformity of ^{3}He atoms relative to the UCNs can result in systematic errors; and the geometric-phase systematic error can lead to a false nEDM.

This program of studies will occur in parallel with the construction and commissioning of the main nEDM apparatus. We estimate that the entire program will last four to five years.

1.2 Fundamental Coupling Constants

1.2.1 Lutetium Thermometry and the Oklo Natural Nuclear Reactors

C.R. Gould, *TUNL*; E.I. Sharapov, *Joint Institute for Nuclear Reactions, Dubna, Russia*

Lutetium thermometry has been used to analyze Oklo natural nuclear-reactor zones but leads to widely varying and puzzling predictions for their operating temperatures $T_{\rm O}$. These, in turn, impact bounds on time variation of the fine structure constant α. We revisit results for reactor zone RZ10 in light of new measurements of the isomer branching ratio $B^{\rm g}$ in ^{175}Lu neutron capture. We conclude that a better measurement of $B^{\rm g}$ with thermal neutrons is needed for reliable temperature predictions.

The Oklo natural reactors have proven to be one of the more sensitive terrestrial testing grounds for studying the time variation of the fine structure constant α. The position of the first neutron resonance in ^{149}Sm strongly influences the effective cross section $\hat{\sigma}$ for neutron capture leading to burnup of ^{149}Sm. The present day resonance energy $E_0 = 97.3$ meV is well known, but in the past it may have been different, leading to a change (through $\hat{\sigma}$) in the isotopic abundances of the various samarium isotopes in Oklo reactor wastes. From modeling the reactor parameters and, in particular, from knowing the reactor temperature, thermal and epithermal neutron spectra can be derived. These can be used to predict whether the ^{149}Sm cross section has changed since the reactors stopped operating. While the majority of Oklo analyses have been consistent with no change [Gou06], astronomical observations continue to argue for a positive effect.

Oklo analyses all reveal that the bounds on variation of α depend significantly on the assumed reactor operating temperature $T_{\rm O}$, and three studies have attempted to bound the temperatures more directly using ^{176}Lu/^{175}Lu thermometry. However, for reactor zone RZ10, one of the best-characterized zones, Hidaka and Holliger [Hid98] succeeded in getting a result ($T_{\rm O} = 380$ C) for only one sample, while for the other three samples they achieved only a surprisingly high lower bound, of $T_{\rm O} > 1000$ C.

In reviewing the data we came to the conclusion that a key parameter in previous analyses may not, in fact, be that well determined. The parameter in question is the branching ratio $B^{\rm g}$ for neutron capture on ^{175}Lu to the isomeric state in ^{176}Lu.

The determination of $B^{\rm g}$ has been the subject of considerable experimental effort in connection with astrophysical studies of the s-process in stars. The difficulty in making a precise determination arises from the fact that its value is obtained by taking the difference between two cross sections of similar magnitude. To address this problem, two precision measurements of the ^{175}Lu total capture and partial activation cross sections at 5 and 25 keV were recently carried out. The conclusions of these studies [Hei08] were that $B^{\rm g} = 0.117 \pm 0.046$ at 5 keV and $B^{\rm g} = 0.143 \pm 0.020$ at 25 keV. These values are about a factor of two less than the value for thermal neutrons, which is 0.28. Such a big difference looks rather puzzling, even taking into consideration a partial contribution of p-wave neutrons. This difference raises the question of whether the thermal value is actually correct.

In our paper [Gou12], we use the 25 keV value and find $T_{\rm O} = 100 \pm 30$, in contrast to $350 < T_{\rm O} < 500$ C using the evaluated value of $B^{\rm g}$ at thermal energy. We conclude that lutetium thermometry can be applicable to analyses of Oklo reactor data, but better measurements of the total and partial capture cross sections on ^{175}Lu are needed at thermal energy to confirm the reliability of temperature predictions. A measurement has been initiated at the NC State PULSTAR reactor to confirm the value of the isomer capture cross section.

[Gou06] C. R. Gould, E. I. Sharapov, and S. K. Lamoreaux, Phys. Rev. C, **74**, 024607 (2006).

[Gou12] C. R. Gould and E. I. Sharapov, Phys. Rev. C, **85**, 024610 (2012).

[Hei08] M. Heil *et al.*, Astrophys. J., **673**, 434 (2008).

[Hid98] H. Hidaka and P. Holliger, Geochimica et Cosmochimica Acta, **62**, 891 (1998).

1.2.2 Gamma-Ray Fluxes in Oklo Natural Nuclear Reactors

C. R. Gould, *TUNL*; E. I. Sharapov, *Joint Institute for Nuclear Research, Dubna, Russia*; A.A. Sonzogni, *Brookhaven National Laboratory, Upton, NY*

We model the prompt, delayed, and equilibrium γ-ray fluxes in Oklo reactor zone RZ10 in order to estimate the rate of burning of ^{176}Lu via photo-excitation of the isomeric state ^{176m}Lu. This channel provides an alternate path for ^{176}Lu depletion and potentially complicates the use of lutetium for determining the reactor operating temperatures. We find the γ-ray fluxes for pulsed mode operation of RZ10 and derive values for the coefficients $\lambda_{\gamma,\gamma'}$ that describe the burn-up of ^{176}Lu. We find the contribution of these channels to be small relative to neutron burn-up, and therefore lutetium thermometry is valid for RZ10.

All Oklo analyses make assumptions about the operating temperatures of the reactors. But there is as yet no agreement on what these temperatures actually were. Utilizing the ^{176}Lu/^{175}Lu isotope-ratio method to determine temperatures was recently revisited by Gould and Sharapov [Gou12]. As concluded there, the degree of depletion of ^{176}Lu will be a reliable indicator of the temperature only if alternate explanations for depletion are ruled out.

One alternate explanation for ^{176}Lu depletion is photo-excitation of the isomeric state in ^{176m}Lu by ^{176}Lu(γ,γ') fluorescence. The isomeric state decays to ^{176}Hf with a half-life of 3.6 hr, and therefore its excitation provides an alternate path for removing ^{176}Lu. Such a process is known in astrophysics and has recently been shown [Thr10, Moh09] to be an important channel for burning ^{176}Lu in stellar environments. Here we explore whether this could have been be an effect in the γ-ray fluxes present in the reactors. The work takes advantage of newly developed data libraries for fission decay chains.

In thermal-neutron-induced fission of ^{235}U, about 6.6 MeV is released in the form of prompt γ rays, about 6.5 MeV as β rays, and about 6.3 MeV as delayed γ rays following β emission. In Oklo, the neutrons also contribute to the prompt γ-ray flux through capture reactions on the material of the reactor. The reactor is thought to have operated for hundreds of thousands of years in a pulsed mode, as water flowed in and then boiled off. We modeled this operation with pulses having a reactor-on time of 0.5 hr and a reactor-off time of 2.5 hr. Calculations are for a pulse occurring after a very long period of reactor operation. There are then three contributions to the flux over a 3 hr period: (1) prompt γ rays occurring during the 0.5 hr the reactor is on at 18 kW power (this is called reactor pulse number N); (2) delayed γ rays emitted during the 2.5 hr the reactor is off but due to fission occurring during pulse N; and (3) equilibrium γ rays emitted over the whole 3 hr period and due to activity built up from the vast number of previous pulses.

The resulting fluxes are shown in Fig. 1.8. The prompt flux is generally much larger than the average delayed flux, as expected, but at a few energies the two are comparable. From these fluxes, and using photo-excitation cross sections at 800 keV and 4 MeV from the literature [Moh09, Car91], we can compute the transformation coefficients $\lambda_{\gamma,\gamma'}$ for Oklo reactor zone RZ10. In both cases the coefficients lead to mean lives that are six or more orders of magnitude larger than those for neutron burn up. We conclude that destruction of ^{176}Lu while the reactor is on is not influenced by the photon flux. These results have been submitted for publication.

[Car91] J. J. Carroll *et al.*, Phys. Rev. C, **43**, 1238 (1991).

[Gou12] C. R. Gould and E. I. Sharapov, Phys. Rev. C, **85**, 024610 (2012).

[Moh09] P. Mohr *et al.*, Phys. Rev. C, **79**, 045804 (2009).

[Thr10] K. Thrane *et al.*, Astrophys. J, **717**, 861 (2010).

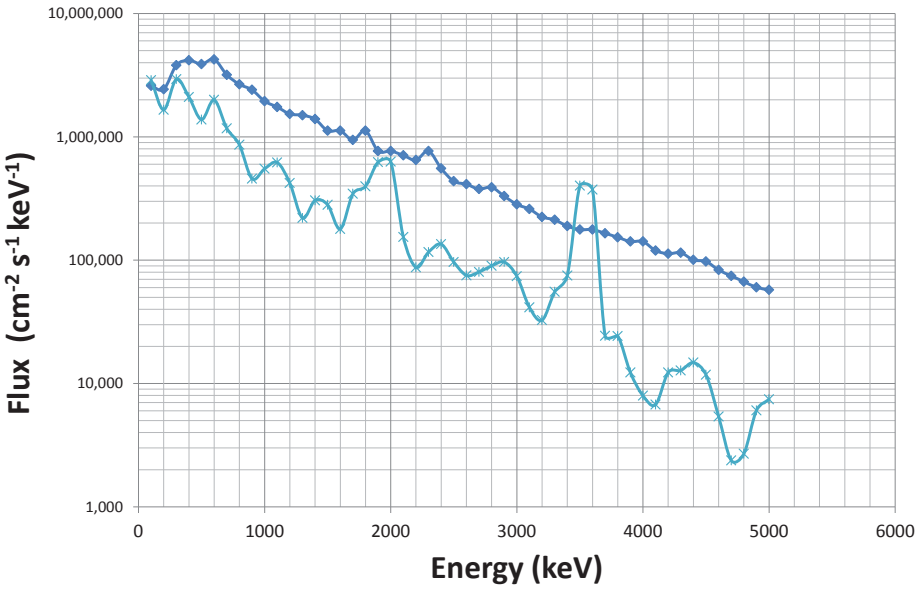

Figure 1.8: (Color online). Prompt and delayed γ-ray fluxes in Oklo reactor zone RZ10 during the period the reactor is on. The fluxes are calculated for an 18 kW reactor cycling on for 0.5 hr and off for 2.5 hr. The prompt flux is the upper line. The lower line is the delayed flux for one 0.5 hr fresh-core reactor-on pulse, multiplied by 1.31 to take into account the equilibrium flux associated with the $N-1$ previous reactor-on pulses, where $N \gg 1$.

1.2.3 Determination of the Neutron Lifetime Using Magnetically Trapped Neutrons

C. Huffer, P.R. Huffman, K. Schelhammer, *TUNL*; K.J. Coakley, M.S. Dewey, M. Huber, H.P. Mumm, A.K. Thompson, A. Yue, *National Institute of Standards and Technology, Gaithersburg, MD*;

We are undertaking an experimental program to measure the neutron lifetime using a new technique with a completely different set of systematic uncertainties than those of previous measurements. Our method uses ultracold neutrons confined by a three-dimensional magnetic trap. We have completed and commissioned an upgrade to our apparatus and have collected several months worth of neutron-trapping data. Analysis of the data is continuing.

We are undertaking an experimental program to measure the neutron lifetime, τ_n, using a new technique with a completely different set of systematic uncertainties than those of previous measurements [Doy94]. Ultracold neutrons (UCNs) are produced by inelastic scattering of cold (0.89 nm) neutrons in a reservoir of superfluid ^{4}He. This is called the "superthermal" process [Gol75]. The neutrons are then confined by a three-dimensional magnetic trap. As the trapped neutrons undergo β decay, the energetic electrons produced in the decay generate scintillations in the liquid He [McK03, McK99], and each decay is detectable with nearly 100% efficiency. The lifetime τ_n can be directly determined by measuring the scintillation rate as a function of time.

Figure 1.9: (Color online) The neutron lifetime apparatus on the NCNR beamline.

The energy dissipation of the trapped UCNs must occur within the trapping region due to the conservative nature of the trap. This occurs when 12 K neutrons (0.89 nm) downscatter in superfluid ^{4}He to near rest via single phonon emission [Gol75]. The UCNs then interact with the magnetic field $\vec{B}$ via their magnetic moment. The neutron's magnetic moment is anti-aligned with its spin direction, and when the neutron's spin is parallel to the magnetic field, it will seek to minimize its potential energy by moving towards low field regions. As the neutron moves in the magnetic field, its spin direction adiabatically follows the direction of the magnetic field. Thus UCNs with energies below the trap depth and in the low-field-seeking state will become trapped.

The UCN population is thermally detached from the helium bath, allowing accumulation of UCNs to a density as high as $P\tau$, where P is the superthermal production rate and τ is the UCN lifetime in the source. Neutron-decay events are detected by turning off the cold neutron beam and observing the scintillation light created by the β-decay electrons. When an electron moves through liquid helium, it ionizes helium atoms along its track. These helium ions quickly recombine into metastable He_2^* molecules that are in excited states. About 35% of the initial electron energy goes into the production of extreme ultraviolet (EUV) photons from singlet decays, corresponding to approximately 22 photons/keV. These EUV photons are frequency down-converted to blue photons using the organic fluor tetraphenyl butadiene coated onto a diffuse reflector (Goretex) surrounding the trapping region. This light is transported via optics to room temperature and detected by two photomultiplier tubes operating in coincidence. Our detection method allows us to observe neutron decay events *in situ*, and therefore directly measure the full exponential decay curve.

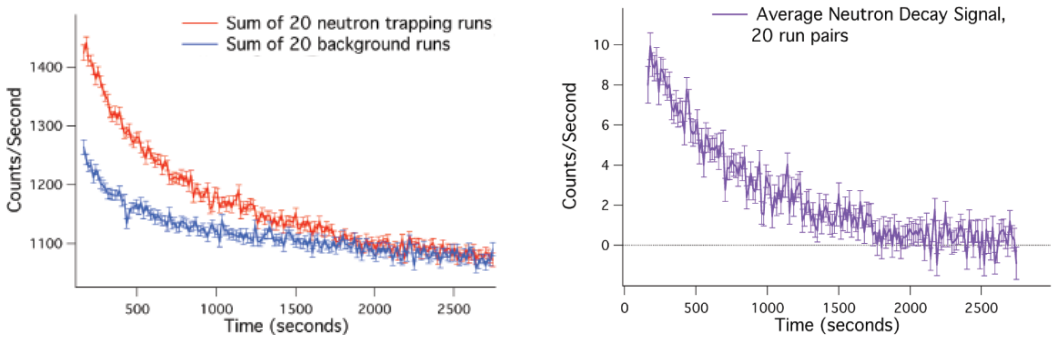

Figure 1.10: (Color online) Neutron trapping and non-trapping data after all background cuts (left) and the neutron decay signal after subtraction of trapping and non-trapping data runs (right).

We have completed and fully-commissioned an upgrade to our apparatus (see Fig. 1.9). The overall conceptual design and composition of the new apparatus has not changed significantly; the cell construction, detection system, cooling system, and neutron optics are essentially scaled versions of the previous design. This approach gave us high confidence in predictions of the number of neutrons trapped, as well as the detection efficiency for the new apparatus. The primary changes that now allow us to trap about twenty times more neutrons are a combination of a stronger magnetic trap and a larger measurement cell.

We collected several months worth of neutron trapping data under various configurations and have began to analyze many of the systematic effects. In general, two kinds of runs are performed: neutron trapping runs, where the magnetic field remains energized during both the trapping and observation periods, and background runs, where the magnetic field is energized only during the observation period so that neutrons are not trapped during the loading phase. The neutron lifetime is extracted by taking the difference between the data from the trapping and non-trapping runs. This allows us to isolate the events that arise solely from neutron decay. Figure 1.10 depicts the result of this subtraction for a representative data set. In principle, these data are then fit with an exponential decay to extract the neutron lifetime.

A significant benefit of the new apparatus is that the increased count-rates will give us time to perform a series of systematic checks, such as measuring the neutron loss due to phonon upscattering, eliminating the above-threshold neutrons, and doing a careful characterization of imperfect background subtraction. Once these systematic studies are successful, we will pursue measuring the neutron lifetime.

[Doy94] J. M. Doyle and S. K. Lamoreaux, Europhys. Lett.), **26**, 253 (1994).

[Gol75] R. Golub and J. Pendlebury, Phys. Lett., **A53**, 133 (1975).

[McK99] D. N. McKinsey *et al.*, Phys. Rev. A, **59**, 200 (1999).

[McK03] D. N. McKinsey *et al.*, Phys. Rev. A, **67**, 062716 (2003).

1.2.4 The UCNA Experiment

L.J. Broussard, B.M. VornDick, J.C. Hoagland, A.T. Holley, R.W. Pattie, Jr., A.R. Young, B.A. Zeck, *TUNL*

This year the UCNA collaboration made improvements in the control of key systematic errors: polarization and energy calibration. A shutter was implemented to improve the statistical precision of polarimetry measurements by an order of magnitude. The uncertainty in the energy calibration and linearity corrections for β detection were also improved by at least a factor of two. Measurements at and below the 0.5% level in the β-asymmetry are now possible. In addition, 34 million decays were observed, pushing the total sample over 65 million events.

Measurements of neutron decay provide fundamental information on parameters (such as the axial form factor for the charged weak interaction of the nucleon) that characterize the weak interaction. These parameters impact predictions of the solar neutrino flux, Big-Bang nucleosynthesis, the spin content of the nucleon, and tests of the Goldberger-Treiman relation. They also place constraints on standard-model extensions such as supersymmetry and left-right symmetric models.

The UCNA experiment is the first attempt to utilize ultracold neutrons (UCNs) for an angular correlation measurement in neutron decay. The use of UCNs for angular-correlation measurements provides a different and powerful approach to the systematic errors characteristic of traditional cold or thermal neutron-beam experiments. In particular, UCNs provide significant advantages for determining the neutron polarization and for controlling neutron-generated backgrounds. Historically, the neutron density in cold neutron beams has been much higher than available UCN densities, making beam experiments the favored method to perform angular correlations, but systematic errors have increasingly driven the ultimate uncertainty of angular correlation measurements, providing impetus to explore the use of UCNs. The magnitude of the β-asymmetry is parameterized by the A coefficient. Our first experimental results (a 4.5% measurement of A from the 2007 run period) were published in 2009 [Pat09]. The results of our 2008/2009 runs were published in 2010 [Liu10], and a long paper has just been accepted for publication [Pla12].

UCNA is located at the Los Alamos Neutron Science Center and utilizes a solid deuterium ultracold neutron source developed for this project. During the last run period, we produced a publication detailing the performance of this source, quantitatively confirming that it is comparable to or stronger than the rotor source at Institut Laue-Langevin, which has served as the standard for UCN sources for the past 35 years [Sau11]. UCNs are coupled to the decay volume through a 15 m guide system that incorporates a 7 T polarizer magnet, a spin-flipper system, and finally the bore of a 1 T spectrometer magnet where decays are observed (see Fig. 1.11).

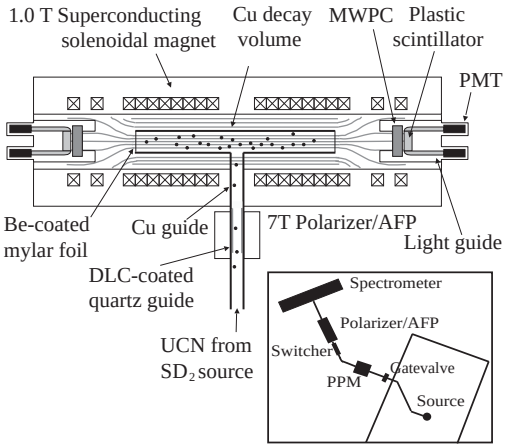

Figure 1.11: Schematic diagram of the UCNA polarizer and β-spectrometer. The inset depicts the layout of the source and guides.

The $\boldsymbol{\mu}\cdot\mathbf{B}$ interaction of the neutron with magnetic fields produces an energy change of ± 60 neV/T, depending on the whether the neutron spin is parallel or antiparallel to the applied field.

The extremely low kinetic energy of UCNs—below 180 neV for our experiment—makes possible a method unique to UCNs for producing highly polarized neutron samples. The $\boldsymbol{\mu} \cdot \mathbf{B}$ interaction produces a 420 neV barrier to the neutrons with spin parallel to the field (the neutron's magnetic moment is negative) in our 7 T polarizer magnet, completely blocking the transmission of this spin state through the high-field system. There is therefore an essentially 100% polarized sample of UCNs after traversing this region. The UCNs then pass through a high-power, radio-frequency adiabatic spin-flipper, which permits the preparation of a UCN sample polarized either parallel or antiparallel to the field. The spin-flipper region is then coupled by our guide system to a decay volume within the uniform 1 T field of the β spectrometer. In the last run period, we published a detailed characterization of the adiabatic fast passage (AFP) spin-flipper [Hol12].

One of the central developments for 2011 was the implementation of a UCN shutter at the entrance of the decay spectrometer. The equilibrium depolarized-UCN fraction in the spectrometer was measured by closing the shutter (storing the UCNs in the decay trap), stopping UCN flow into the polarizer magnet, and redirecting flow from the guide system out of the spectrometer into a "switcher" UCN detector (see Fig. 1.11). After the guide system is emptied of UCNs, the flipper state is changed, permitting only depolarized UCNs to travel to the switcher detector, and the shutter is opened so that depolarized UCNs can be measured in the depolarized-UCN detector. The shutter improved the statistics of our depolarized UCN measurements by an order of magnitude and eliminated a significant correction which had to be applied to the previous polarimetry procedure.

UCNs were confined to a 12.5-cm diameter, 3-m long Cu decay trap, coaxial with a 1 T uniform field at the center of the spectrometer. The inner surface of the decay trap is coated with diamond-like carbon. The ends of the decay trap were sealed with Be-coated Mylar windows. β particles were recorded in detector assemblies situated at either end of the solenoidal spectrometer, where the field has fallen to 0.6 T. Each detector assembly is composed of a position-sensitive multi-wire proportional counter (MWPC) with aluminum-coated entrance and exit windows, backed by a plastic scintillator to measure the full energy of the β particles.

Over 34×10^6 decays were observed during the 2011 run cycle. Although these data, when combined with the 2010 runs, will permit a sub-0.5% measurement of the β-asymmetry, we also implemented an LED pulser and improved characterization of the calibration sources. These improvements, together with the development of new, ultrathin decay-trap windows, with a total thickness less than 0.3 microns, set the stage for a push to below 0.4% in precision in the 2012 run cycle. Analysis of existing data is in progress, with unblinding of the 2010 runs planned before October, 2012.

A final, significant development project for UCNA was carried out at TUNL. Measurements were performed of the proton response for large, segmented silicon detectors developed specifically for β-decay experiments with neutrons. This project utilized a low energy proton accelerator built by previous TUNL student Seth Hoedl [Hoe06]. It provided critical support for proposed experiments at the Spallation Neutron Source and the LANL UCN facility, measuring β-decay angular correlations through the detection of recoil protons in delayed coincidence with decay β particles.

[Hoe06] S. Hoedl *et al.*, J. Appl. Phys., **99** (2006).

[Hol12] A. T. Holley *et al.*, Rev. Sci. Instrum., **83** (2012).

[Liu10] J. L. Liu *et al.*, Phys. Rev. Lett., **105** (2010).

[Pat09] R. W. Pattie *et al.*, Phys. Rev. Lett., **102** (2009).

[Pla12] B. Plaster *et al.*, Phys. Rev. C, **(accepted for publication)** (2012).

[Sau11] A. Saunders *et al.*, Rev. Sci. Instrum., **(submitted)** (2011).

1.2.5 Results of the Measurement of the Half-Life of ^{19}Ne

L.J. Broussard, H.O. Back, M.S. Boswell, A.S. Crowell, M.F. Kidd, C.R. Howell, R.W. Pattie, Jr., A.R. Young, *TUNL*; P.G. Dendooven, G.S. Giri, D.J. Van der Hoek, K. Jungmann, W.L. Kruithof, C.J.G. Onderwater, P.D. Shidling, M. Sohani, O.O. Versolota, L. Willmann, H.W. Wilschut, *Kernfysich Versneller Instituut, Groningen, The Netherlands*

The ^{19}Ne half-life is an important parameter in precision tests of the Standard Model. Researchers at TUNL have collaborated with the Trapped Radioactive Isotopes Microlaboratories for fundamental Physics (TRIμP) group at the Kernfysich Versneller Instituut (KVI) to perform a measurement of the half-life of the ^{19}Ne positron decay to ^{19}F. The data was taken during the spring 2009, and the analysis was completed this year. The value for the ^{19}Ne half-life obtained in this work is 17.2832 $\pm$ 0.0077 seconds. This result is substantially larger than previous high-precision measurements. The experiment is summarized and details of the analysis are given in this report.

The half-lives and angular correlations of the T=$\frac{1}{2}$ mirror transitions can be used to extract V_{ud} at a similar precision to that obtained by superallowed $0^+ \rightarrow 0^+$ Fermi decays. Also, the T=$\frac{1}{2}$ system can be used in cross checks of the accuracy of the nuclear models used in calculations of theoretical corrections which are applied to the corrected $\mathcal{F}$t values.

We made high-precision measurements of the half-life of ^{19}Ne. These measurements were carried out using the TRIμP facility at KVI in 2009. The ^{19}Ne was created via the (p,n) reaction from a ^{19}F beam produced by the AGOR cyclotron incident on a H_2 gas target cell that was developed by the TUNL group. The resulting particle beam was purified in the TRIμP dual-stage magnetic isotope separator and implanted into an aluminum tape. The tape drive system was designed and built at TUNL. Silicon detectors in the TRIμP separator were used to identify contaminants using the unique energy and timing correlations of each isotope. The concentration levels of isotopes such as ^{15}O was estimated from correlations in the value of the extracted lifetime with the implantation time. Each ^{19}Ne sample deposited in the tape was transported to a shielded enclosure for γ-ray counting by two HPGe clover detectors used to detect in coincidence the collinear 511-keV γ-rays from the annihilation of the positions from the ^{19}Ne decays.

The data were collected using a data acquisition system developed by TUNL consisting of a CAEN V1724 14bit 100MS/s waveform digitizer and MIDAS-based software. A pulser signal with a constant repetition rate of 120 Hz was fed into the clover preamps for online checks of rate-dependent effects. The shaped detector signal waveforms from the eight clover segments were digitized and stored. Gain fluctuations affecting the signal pulse height were monitored online using the digitized pulser signal. Long-term gain changes due to the detector cooling cycle were monitored using the peak in the energy spectrum at 511 keV.

The data collection was divided into four sets: background measurements, a contamination study, a diffusion study, and the high precision decay measurement. The typical measurement cycle consisted of a beam-on implanting period, a sample positioning period, then a beam-off counting period. During background measurements, the cycle was the same except that the sample was not moved to the detectors. During the contamination study, the implanting time was significantly lengthened to increase the relative levels of long-lived contaminants. During the diffusion study, a degrader was placed in front of the tape to enhance the fraction of nuclei implanted near the surface of the tape.

In each measurement cycle, coincidence events which passed the energy-threshold and deadtime filters were histogrammed into decay plots. The histogrammed data were fitted using the Maximum-Likelihood method to a function corrected for the measured background and deadtime. To evaluate sensitivies to systematic effects, each decay data set was processed using different analysis conditions including the beginning and ending times of the fitting window, the length of the applied deadtime period, the width

Table 1.1: Summary of the most important systematic effects in this measurement. The relative size of the effect on the half-life determination and the relative uncertainty in the size of the effect are given in columns two and three.

Systematic Effect	Correction (%)	Uncertainty (%)
Clock Accuracy	-	1.0×10^{-3}
Statistical bias	$+1.30 \times 10^{-2}$	8.3×10^{-6}
Deadtime	-3.03×10^{-2}	5.6×10^{-3}
Accidental coincidences	$+6.85 \times 10^{-2}$	1.7×10^{-3}
Energy determination	-4.30×10^{-2}	6.0×10^{-3}
Diffusion	$+4.82 \times 10^{-4}$	7.8×10^{-5}
Backgrounds	-5.20×10^{-2}	1.2×10^{-3}
Contamination	-	2.9×10^{-2}

of the coincidence acceptance window, and the energy thresholds.

A blind analysis was performed on the data by applying a random multiplicative factor to the actual clock period used to bin the data into time histograms. The factor differed from unity by up to ±5%. A half-life value for ^{19}Ne was determined for each data set. The fitting function used to determine the half life was studied in detail using Monte-Carlo simulations. A small bias was observed for small sample sizes and due to the limited fitting window. The systematic uncertainty introduced by rate-dependent effects, such as accidental coincidences, deadtime, and pile-up, were also estimated using these simulations. A Monte-Carlo simulation was developed to model the effect of diffusion on the extracted half-life value. The uncertainty caused by contaminant radioactive isotopes was estimated using multi-exponential fits and the variation in the half-life determined from data sets with different implantation times.

The non-sample related background rate was 0.2878 ± 0.0064Hz, which gave an average signal to background ratio of about 1000 : 1. An upper limit for the diffusion coefficient of ^{19}Ne in aluminum of $1.00 \pm 0.52 \times 10^{-2} \mu m^2 s^{-1}$ was obtained from the diffusion studies, making diffusion effects negligible at the implanted depths used in our measurements. The largest systematic corrections applied in the analysis were to account for ambient backgrounds and rate dependent effects. The largest source of uncertainty was due to the radioactive contamination in the implanted sample, which was difficult to characterize due to the limited time of flight information in the separator. The corrections and uncertainties due to these effects are summarized in Table 1.1.

The half-life determined in this experiment was $17.2832(51)_{stat}(58)_{sys}$ seconds. Previous determinations of the half-life are shown in Fig. 1.12. A new global average for the ^{19}Ne half-life is determined using the statistical procedure adopted by the Particle Data Group [Ber12] and is found to be 17.2619 ± 0.0094 seconds.

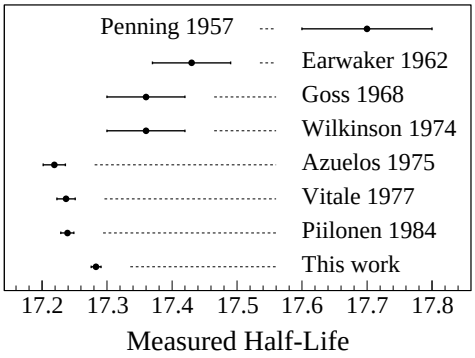

Figure 1.12: Previous measurments of the half-life of ^{19}Ne, including the result from this work. The global average is 17.2619(94) **seconds.**

[Ber12] J. Beringer *et al.*, Phys. Rev. D, **86**, 010001 (2012).

Neutrino and Dark Matter Physics

Chapter 2

- **$\beta\beta$-Decay Experiments**
- **Tritium β Decay**
- **Dark Matter Search**

2.1 $\beta\beta$-Decay Experiments

2.1.1 The Majorana Demonstrator Neutrinoless Double-Beta Decay Experiment

J.F. Wilkerson, M. Busch, D. Combs, P. Finnerty, F.M. Fränkle, G.K. Giovanetti, M.P. Green, R. Henning, M.A. Howe, L. Leviner, S. MacMullin, D.G. Phillips, B. Shanks, K. Snavely, J. Strain, G. Swift, W. Tornow, K. Vorren, A.R. Young, *TUNL*

The Majorana collaboration[1] is searching for neutrinoless double-beta decay using ^{76}Ge. The observation of neutrinoless double-beta decay would show that lepton number is violated, and that neutrinos are Majorana particles. It would also provide information on neutrino mass. Attaining sensitivities for neutrino masses in the inverted hierarchy region, 25 to 50 meV, requires large, tonne-scale detectors with extremely low backgrounds. The collaboration is constructing the Demonstrator in a clean room laboratory facility at the 4850-foot level at the Sanford Underground Research Facility in Lead, SD. The primary aim of the Demonstrator is to show the feasibility for a future tonne-scale measurement.

Neutrinoless double-beta decay ($0\nu\beta\beta$) is the only viable method to search for lepton number violation and, correspondingly, to determine the Dirac-Majorana nature of the neutrino [Cam08, Avi08]. Reaching the neutrino mass scale associated with the inverted mass hierarchy, 25 to 50 meV, will require a half-life sensitivity on the order of 10^{27} y, corresponding to a signal of a few counts or less per tonne-year in the $0\nu\beta\beta$peak. To observe such a small signal, one will need to construct tonne-scale detectors with backgrounds in the region of interest at or below about one count t^{-1} y^{-1} (corresponding to 2.5×10^{-4} counts keV^{-1} t^{-1} y^{-1}). A convincing discovery that neutrinos are Majorana particles and that lepton number is violated will require the observation of $0\nu\beta\beta$in multiple experiments using different $0\nu\beta\beta$isotopes.

The sensitivity of a $0\nu\beta\beta$search increases with the exposure of the experiment, but ultimately depends on the achieved background level. This relationship is illustrated in Fig. 2.1, where we have used the Feldman-Cousins definition of sensitivity in order to transition smoothly between the background-free and background-dominated regimes. Although this figure is drawn using experimental parameters relevant for $0\nu\beta\beta$searches using ^{76}Ge, the situation for other isotopes is not qualitatively different. It may be concluded that achieving sensitivity to the entire parameter space for inverted-hierarchical Majorana neutrinos would require about 10 tonne-years of exposure with a background rate of less than one count t^{-1} y^{-1}. Higher background levels would require significantly more mass to achieve the same sensitivity within a similar counting time.

The Majorana collaboration is searching for $0\nu\beta\beta$using ^{76}Ge, which utilizes the demonstrated benefits of enriched high-purity germanium (HPGe) detectors. These include intrinsically low-background source material, understood enrichment chemistry, excellent energy resolution, and the ability to apply sophisticated event reconstruction. The primary technical challenge is the reduction of environmental ionizing-radiation backgrounds by about a factor of a hundred below what has been previously achieved. Specific goals of the Majorana Demonstrator are:

- Demonstrate a path forward to achieving a

[1] Majorana collaboration institutions: Black Hills State Univ., Spearfish, SD; Duke Univ., Durham, NC; Institute for Theoretical and Experimental Physics, Moscow, Russia; Joint Institute for Nuclear Research, Dubna, Russia; Lawrence Berkeley National Laboratory, Berkeley, CA; Los Alamos National Laboratory, Los Alamos, NM; Oak Ridge National Laboratory, Oak Ridge, TN; Osaka Univ., Osaka, Japan; North Carolina State Univ., Raleigh, NC; Pacific Northwest National Laboratory, Richland, WA; South Dakota School of Mining and Technology, Rapid City, SD; Triangle Universities Nuclear Laboratory, Durham, NC; Univ. of Alberta, Edmonton, Alberta, Canada; Univ. of Chicago, Chicago, IL; Univ. of North Carolina, Chapel Hill, NC; Univ. of South Carolina, Columbia, SC; Univ. of South Dakota, Vermillion, SD; Univ. of Tennessee, Knoxville, TN; Univ. of Washington, Seattle, WA.

background rate at or below one count t^{-1} y^{-1} in the 4 keV region of interest (ROI) around the 2039 keV Q-value of the ^{76}Ge $0\nu\beta\beta$.

- Show technical and engineering scalability toward a tonne-scale instrument.
- Field an array that provides sufficient sensitivity to test the Klapdor-Kleingrothaus claim [KK06] while having comparable sensitivity with alternate approaches.

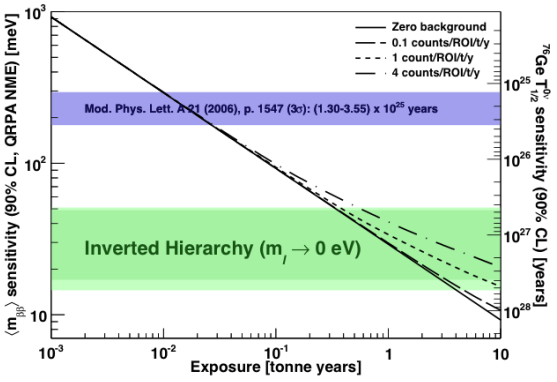

Figure 2.1: 90% C.L. sensitivity as a function of exposure for $0\nu\beta\beta$searches in ^{76}Ge under different background scenarios.

To this end, the collaboration is building the DEMONSTRATOR, a modular instrument composed of two cryostats built from ultra-pure electroformed copper, each of which can house over 20 kg of HPGe detectors [Sch12, Wil12, Agu11]. The individual p-type point-contact (PPC) detectors have masses in the range of 0.6-1.0 kg. The baseline plan calls for two thirds of the detectors to be grown from 86% enriched material, resulting in a ^{76}Ge mass of 30 kg enriched detectors and 10 kg of natural detectors. This enriched material is sufficient to achieve the physics goal while still optimizing cost and providing a systematic check of enriched vs. natural Ge. The modular approach will allow us to assemble and optimize each cryostat independently, providing step-wise deployment with minimum interference on already operational detectors. The cryostats sit within a graded shield where the inner passive shield will be constructed of electroformed and commercial high-purity copper, surrounded by high-purity lead, which itself is surrounded by an active muon veto and neutron moderator (see Fig. 2.2). The experiment is being assembled in underground clean-room laboratories at the 4850-foot level (1478 m) of the Sanford Underground Research Facility.

A prototype module, built using high purity commercial copper, is scheduled to be commissioned near the start of 2013. It will be populated with two strings of natural PPC detectors and mounted on a monolith transporter. Cryostat 1, fabricated using ultra-clean electroformed Cu, will contain seven strings of both enriched and natural Ge detectors and is scheduled to be commissioned in 2013. Cyostat 2, which will contain all enriched detectors, is scheduled to be be completed in 2014. The DEMONSTRATOR will be operated for three to four years, in order to collect about 100 kg-years of exposure.

Support for this project is provided by the DOE Office of Nuclear Physics and NSF Particle Astrophysics.

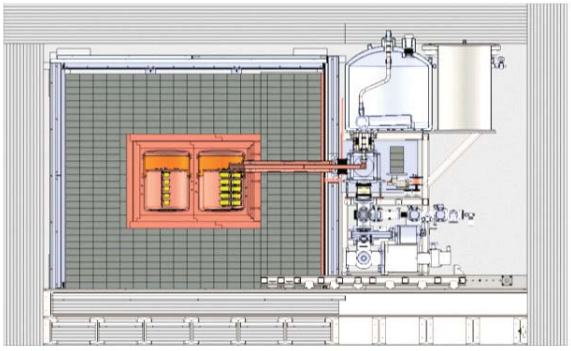

Figure 2.2: Cross-sectional view of the MAJORANA DEMONSTRATOR. Strings of detectors are visible in the two cryostats. Cryostats are mounted in moveable transporters allowing independent assembly and testing. The cryostat vacuum system and thermosyphon cooling system is visible for the cryostat on the right. For scale, the inner Cu dimensions where the cryostats are inserted is 20 in. high and 30 in. in length.

[Agu11] E. Aguayo *et al.*, AIP Conf. Proc., **417**, 95 (2011).

[Avi08] F. T. Avignone III, S. R. Elliott, and J. Engel, Rev. Mod. Phys., **80**, 481 (2008).

[Cam08] L. Camilleri, E. Lisi, and J. F. Wilkerson, Annu. Rev. Nucl. Part. Sci. **58**, 343 (2008).

[KK06] H. Klapdor-Kleingrothaus and I. Krivosheina, Mod. Phys. Lett., **A21**, 1547 (2006).

[Sch12] A. Schubert *et al.*, AIP Conf. Proc., **1441**, 480 (2012).

[Wil12] J. Wilkerson *et al.*, J. Phys. Conf. Ser., **375**, 042010 (2012).

2.1.2 Project Engineering for the MAJORANA DEMONSTRATOR Project

M. BUSCH, J.F. WILKERSON, R. HENNING, *TUNL*

Project engineering for the MAJORANA DEMONSTRATOR project is being managed by engineers at TUNL. The primary responsibility of the project engineer is to provide design and fabrication guidance and coordination for all MAJORANA DEMONSTRATOR hardware. This includes developing and chairing design reviews in accordance with the engineering strategy; coordinating all engineering, design, and fabrication activities required to complete the project; and communicating and archiving all design content to the collaboration.

2.1.2.1 Engineering design reviews

Project engineering for the MAJORANA DEMONSTRATOR project (see Sect. 2.1.1) is being managed by engineers at TUNL. The engineering strategy outlines the design review process for the project. There are three major review stages: conceptual design, preliminary design, and final design. Each design review clearly demarks and documents milestones in the design process. The conceptual design review establishes a baseline configuration that allows engineers and designers to complete the necessary analysis and to specify all of the components of the system. The preliminary design review serves as a way to lock in the configuration and specifications for a final configuration. The final design review brings together the final engineering calculations, safety analysis, fabrication drawings, and assembly procedures to ensure a quality finished product.

The past year was a major design review milestone for the MAJORANA DEMONSTRATOR. In preparation for CD2/3 review with the DOE, held in May 2012, a series of independent external preliminary design reviews were held to finalize the design and operation of the DEMONSTRATOR. These reviews involved inviting subject-matter experts from outside of the collaboration to evaluate the function and safety of the DEMONSTRATOR design. In addition to the major DOE CD2/3 review, site-safety readiness reviews were held by the host laboratory, Sanford Underground Research Facility or SURF. These reviews are summarized below:

- Pressure Safety: August 2011
- Oxygen Deficiency Hazards: Dec 2011
- Structural Analysis: Dec 2011
- SURF Cryo-Committee Review: Dec 2011
- Germanium Reduction and Refinement: fall 2011
- MJD Laboratory Readiness Review and Inspection

The contents and results of these reviews were summarized and archived in the preliminary design report for CD2/3, which is in preparation. Final design reviews continue as elements of the design are released for fabrication.

2.1.2.2 Coordination of design activities

The MAJORANA DEMONSTRATOR engineering team consists of over twenty design contributors at seven institutions around the country. The project engineer is responsible for providing clear design, fabrication, and installation guidance for all contributors.

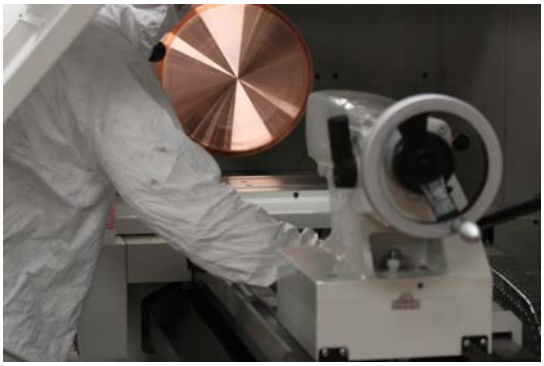

Figure 2.3: (Color online) Electroformed copper on the lathe in the underground cleanroom machine shop

This past year has been particularly exciting from an engineering and design perspective, as the DEMONSTRATOR transitions from design to fabrication. The project engineer oversaw the

installation of the underground cleanroom machine shop at the 4850-foot-level Davis Campus Laboratory at SURF, and machining is underway now (see Figs. 2.3 and 2.4). The purpose of the underground cleanroom machine shop is to produce ultra-low-radioactive-background components from copper that has been electroformed in cleanroom conditions underground, shielded from the cosmic-ray activation and environmental contamination normally introduced in the material processing and fabrication chain. In preparation for this work, a contract was put in place with a local machine shop—Adams ISC of Rapid City, SD—to train a machinist in cleanroom techniques. This training was carried out in a temporary cleanroom installation at Adams ISC and in a cleanroom machining facility at UNC.

Figure 2.4: (Color online) A completed bottom lid for one of the Demonstrator **cryostats**

2.1.2.3 Communicating Design status

A series of weekly conference calls are utilized as a way to communicate and coordinate the design status and near-term goals of the Majorana Demonstrator. Documents and images of the design are posted to a central website for conference calls and collaboration meetings. They are in file formats that are readable by the entire collaboration.

All fabrication drawings, including prototypes and test parts, are assigned unique part numbers and posted in pdf format to the MJ Twiki website. The drawing numbers follow a convention devised and managed by the project engineer. This convention is documented on the MJ Twiki. All 3D design content for the Majorana Demonstrator is produced using Solidworks. A server-based archive and product-development management software tool called Solidworks Enterprise PDM is used to coordinate design efforts across the collaboration. This system allows designers at any collaborating institution to update their model to the current version, check in and check out design content, manage version and revision control, and have an automated mirrored archiving system. The software implementation, training, and maintenance required for this system is managed by the project engineer.

2.1.3 Electroformed Copper Outgassing Studies for the MAJORANA DEMONSTRATOR

K. VORREN, R. HENNING, J.F. WILKERSON, *TUNL*

The cryostat and detector assemblies within the MAJORANA DEMONSTRATOR will be machined using highly radiopure electroformed copper and held at ultra high vacuum (UHV). It is important that nothing that could affect detector characteristics outgasses from the copper. Samples of machined electroformed copper were placed in a vacuum chamber attached to a residual gas analyzer and held at UHV to test for outgassing products. It was found that air constituents made up the bulk of the ions detected.

2.1.3.1 Introduction

The MAJORANA DEMONSTRATOR is an ultra-low-background experiment designed to determine whether a tonne-scale neutrinoless double-beta-decay experiment can achieve backgrounds of less than 1 count per tonne-year within a 4 keV region of interest around 2039 keV. For this reason, it is important that all components of the DEMONSTRATOR detector are well characterized.

Significant steps have been taken by the MAJORANA collaboration to ensure cleanliness and radiopurity. A clean room and clean machine shop have been built underground at the 4850 ft level of the Homestake mine in Lead, SD for the manufacture and machining of radiopure electroformed copper. This copper will be used for the detector assembly and cryostat, and also for the inner shield of the DEMONSTRATOR. Because of the sensitive location of these components, multiple studies, including outgassing studies, have been performed on the electroformed copper to understand any backgrounds that it may contribute.

During the elctroforming process, copper is electroplated on stainless steel mandrels in an underground cleanroom. The underground environment reduces cosmogenic isotopes, such as ^{60}Co, that form within the copper when it is exposed to cosmic rays on the earth's surface. The copper used in the electroplating process comes from a sacrificial anode made of oxygen free, high conductivity (OFHC) copper. Copper ions from the anode travel through a plating bath consisting of sulfuric acid and copper sulfate and are deposited on the mandrel, which also serves as the cathode. Once the copper growth is sufficient, the electroformed copper is removed from the bath for machining [Hen10]. The machining process is shown in Fig. 2.5

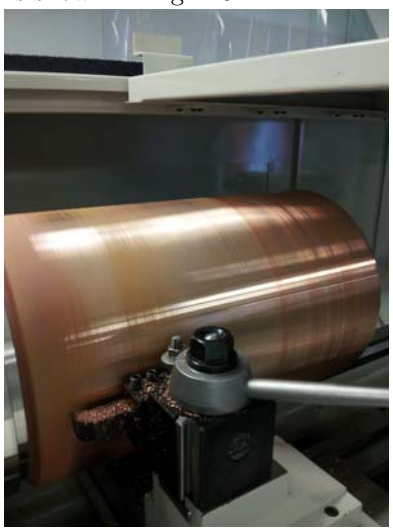

Figure 2.5: (Color online) Machining of electroformed copper on the lathe

2.1.3.2 Experimental Setup

Samples of copper chips were placed in a vacuum chamber and pumped down to ultra high vacuum using a Pfeiffer turbomolecular pump ("turbopump"). A cart designed for portable use of a Pfeiffer Prisma Plus residual-gas analyzer (RGA) was attached to the sample station. The cart also has a dedicated turbopump. Heat tape and aluminum foil were wrapped around the sample chamber, completely covering it for baking. A separate roll of heat tape was used to bake some of the pumping cart to try to reduce water vapor in the system.

The copper sample that was used was shipped from the above ground machine shop in Rapid City, SD on March 23, 2012. The chips were from copper waste produced during machining.

They arrived bagged, having previously been in a class 10,000 cleanroom environment. Some runs were done with the sample taken right out of the bag. Later on, the sample was cleaned with 1% micro-90 in the ENPA electronics lab sonicator at UNC, in case contamination from grease on the machines was present.

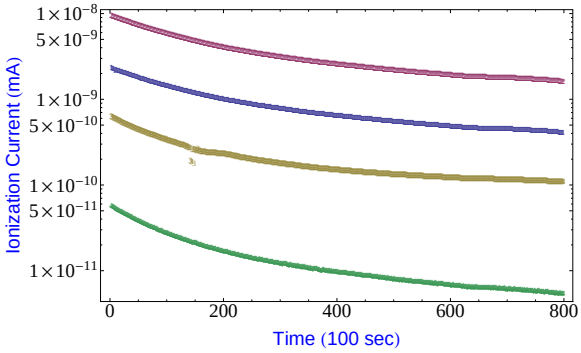

Figure 2.6: (Color online) Total ionization current over time. Counts within three sigma of the peak's mean amu were summed to get the total. The top two traces are from water vapor (18 and 17 amu respectively); The bottom two traces are from N_2 and N (28 and 14 amu respectively).

2.1.3.3 Sample Analysis

The Pfeiffer Prisma Plus RGA comes with the data acquisition software package Quadera, which was used to collect data from the RGA. The data were displayed in a plot of ionization current vs. amu in real time. The RGA scans a user-specified range of masses, collecting charge per each amu for a user-specified amount of time. Each run was set to scan mass numbers from zero to one hundred for 1.0 s per amu. The runs were repeated for three days. During this time, the pressure in the chamber would drop form 10^{-6} Torr to 10^{-9} Torr. This effect can be seen in the plots of individual ion currents vs. time in Fig. 2.6. The data were exported to an ASCII file and plotted with Mathematica. A sample coarse spectrum can be seen in Fig. 2.7.

Fragments of ions accompany parent ions within the spectrum and provide a good signature for determining which substances are present in the chamber. For example, the fragment OH^+ (17 amu) is found with water vapor [YT107]. Doubly ionized molecules were also used to help identify substances in the chamber. Since the RGA is measuring a charge to mass ratio, doubling the charge generates a signal at half the mass.

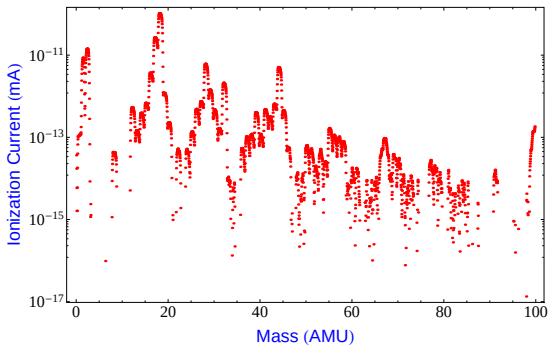

Figure 2.7: (Color online) RGA spectrum.

2.1.3.4 Conclusion

All of the ions identified in the spectrum were consistent with air constituents. Water vapor had the most intense peak in the spectrum, followed by hydrogen and nitrogen. Sulfates which were used in the electroforming process, and propylene glycol which was used during machining were not found in the outgassing spectrum. Other, more exotic, ions were also not present.

[Hen10] R. Henning *et al.*, TUNL Progress Report, **XLIX**, 22 (2010).

[YT107] *RGA Spectra Data, Interpretation Guide*, Technical report, YTI Thin Film Products and Services, `www.ytionline.com/techinfo/rgaspectrainterguide.html`, 2007.

2.1.4 Parts Cleaning for the MAJORANA DEMONSTRATOR

J. STRAIN, D. COMBS, G.K. GIOVANETTI, M. GREEN, S. MACMULLIN, *TUNL*; E.W. HOPPE, *Pacific Northwest National Laboratory, Richland, WA*

The parts for the prototype cryostat and detector strings for the MAJORANA DEMONSTRATOR project have been fabricated, cleaned, and are being shipped to the Sanford Underground Laboratory at Homestake, SD for assembly. A cleanroom was built at the University of North Carolina at Chapel Hill to clean all the copper, plastic and stainless steel parts. Details on the work performed in the cleanroom and the procedures used for cleaning are discussed.

The MAJORANA collaboration is constructing the MAJORANA DEMONSTRATOR to determine the feasibility of a tonne-scale ^{76}Ge-based neutrinoless double-beta decay experiment (see Sect. 2.1.1). To meet the ultra-low-background level required for the DEMONSTRATOR, and ultimately for a tonne-scale experiment, special care must be taken in acquiring low-radioactivity materials. Furthermore, the parts made from the low-radioactivity materials must be properly handled during the machining and cleaning processes.

The first step of the MAJORANA DEMONSTRATOR is to construct a prototype cryostat with two strings of germanium detectors. Each string will first be characterized in its own test cryostat. Parts for the prototype cryostat and string-test cryostats were cleaned in a soft-walled clean room at the University of North Carolina at Chapel Hill. The cleanroom is equipped with a hood, proper air filtration and HEPA filters. Cleanroom vinyl flooring was installed prior to building the soft-walled cleanroom.

The cleanroom is 200 ft^2 with an additional anteroom, a curtained off section with 100% HEPA coverage for drying clean parts, and an exit for drums of hazardous waste. The room is also equipped with a large stainless steel cleanroom sink, ultrasonic cleaners, a high-purity water system producing 18.2 MΩ·cm water, and purified liquid nitrogen boil-off that can be accessed with a PTFE (polytetrafluoroethylene) spray gun.

The sample-preparation cleanroom at UNC has been maintained at a class 1000 or better. The curtained off area for clean parts only (no personnel) has been maintained at a class 10 or better.

Proper cleaning procedures for parts to be used in the DEMONSTRATOR and any test assemblies were developed at Pacific Northwest National Laboratory. These procedures have been implemented at the UNC clean room and are discussed below.

Figure 2.8: (Color online) Etching a copper part in the cleanroom hood. A copper part is being scrubbed in the sulfuric acid bath. The bath is initially clear; the blue color is from copper sulfate. To the immediate right of the sulfuric acid bath is the first rinse bath, followed by the citric acid bath. Not pictured is the second rinse bath.

2.1.4.1 Etching Copper

The DEMONSTRATOR crystals will be assembled in strings and housed in copper cryostats. The copper cryostats and the copper parts that make up the strings will be etched to remove surface contaminants. The test-string assemblies plus the copper parts for the prototype and string-test cryostats have been etched at the UNC cleanroom.

In the current etching procedure, copper pieces are initially cleaned with 2% Micro-90 de-

tergent and then thoroughly rinsed with high-purity water. Each copper part is then submerged in an etchant bath of 1% sulfuric acid, 3% hydrogen peroxide and high-purity water; followed by a passivation bath of 1% (by weight) citric acid and high-purity water. Furthermore, between each step, each copper part is thoroughly rinsed with high-purity water. The etchant is most effective when agitated, so it is important that during the etching the copper parts are scrubbed by someone wearing clean gloves (see Fig. 2.8). It is also important to transfer the copper parts quickly from one bath to another to prevent oxidation in the air. After removing a part from the final high-purity water rinse, it is immediately dried with liquid nitrogen boil-off (see Fig. 2.9), placed in a laminar flow hood for a few hours and double bagged in anti-static nylon tubing. The nylon tubing used is known to be relatively impermeable to radon and is made and packaged in a cleanroom environment. A collection of copper parts, both before and after cleaning, is shown in Fig. 2.10.

Figure 2.9: (Color online) A copper part being dried with purified liquid nitrogen boil-off after it had been etched and passivated.

2.1.4.2 Leaching Plastic

The strings that will hold the DEMONSTRATOR crystals contain small plastic pieces that need to be leached. Furthermore all bins, beakers, tweezers and other general lab supplies used in the etching and leaching process must be made of plastic and leached.

In the current leaching procedure, plastic pieces are initially cleaned with 2% Micro-90 detergent and then thoroughly rinsed with high-purity water. Each plastic part is then leached for 24 hours in 6 M nitric acid three times, with each nitric acid bath followed by a high-purity water rinse. After removing a part from the final nitric acid bath, it is rinsed with high-purity water, dried with liquid nitrogen boil-off and double bagged in anti-static nylon tubing.

Figure 2.10: (Color online) To the left are copper parts after they have been etched, passivated and dried. To the right are copper parts before any cleaning.

In the future, most parts that need to be cleaned for the DEMONSTRATOR will be cleaned at the 4850-foot level of the Sanford Underground Research Facility (SURF), where the MAJORANA DEMONSTRATOR is being constructed. The materials and equipment that were used to clean parts for the DEMONSTRATOR at the sample-preparation cleanroom at UNC were sent to the MAJORANA laboratory space at SURF for future cleaning to be done underground. The sample-preparation cleanroom at UNC will continue to clean some small parts that will be used for the DEMONSTRATOR and relevant testing. Future work will also involve continually checking cleaning procedures developed by the MAJORANA collaboration and helping to make these procedures both efficient and cost effective.

2.1.5 Testing the Thermal-Interference Fit for the MAJORANA DEMONSTRATOR Detector Unit

D.C. COMBS, M. BUSCH, M.P. GREEN, R. HENNING, J.F. WILKERSON, *TUNL*

The MAJORANA collaboration plans to use an array of high purity germanium diodes to search for neutrinoless double-beta decay in ^{76}Ge. Each of the detectors will be housed in a copper mount that utilizes a thermal interference fit. A test assembly of a detector unit has been conducted at UNC.

The MAJORANA collaboration plans to search for neutrinoless double-beta decay in ^{76}Ge. The MAJORANA DEMONSTRATOR is a 40 kg array of semiconductor diodes constructed out of high purity germanium enriched in the isotope ^{76}Ge. Each diode is housed in a detector unit made primarily of electroformed copper. The design of the detector unit utilizes a thermal interference fit between the copper detector mounting plate and three copper hollow hexagonal rods to make a mechanically strong and thermally conductive joint. Here we describe the process of testing the interference fit of those pieces.

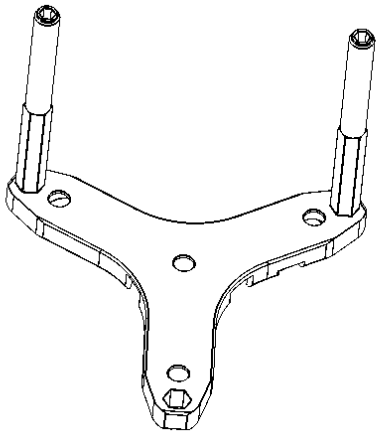

Figure 2.11: Drawing of the detector mounting plate and hollow hexagonal rods. The front rod is removed to show the hexagonal hole in the mounting plate.

An interference fit takes advantage of thermal expansion or contraction. The thermal interference in the MAJORANA DEMONSTRATOR detector unit is achieved with the use of liquid nitrogen to cool and contract the hollow hexagonal rods so that they will fit into the hexagonal holes in the detector mounting plate.

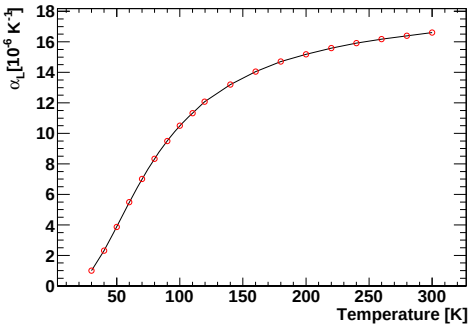

Figure 2.12: (Color online)The coefficient of linear thermal expansion for copper as a function of temperature. The points are calculated values and the curve is a linear interpolation.

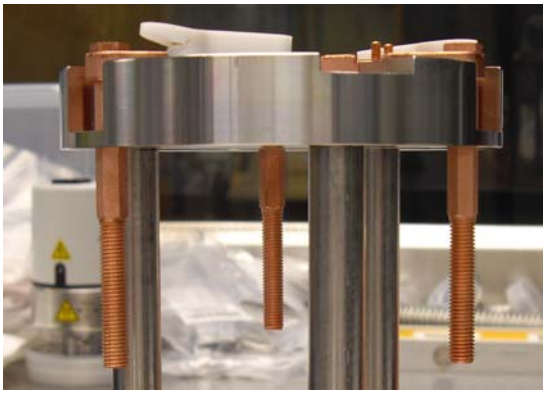

Figure 2.13: (color online) Detector mounting plate with the hex rods in the mounting fixture.

Fig. 2.11 shows an engineering drawing of the detector mounting plate and the rods. Each rod is specified to have a dimension across the shank of 0.251±0.0002 in, and the hole in the mounting plate is specified to be 0.250±0.0002 in from face to face. The pieces are machined in two stages.

The first stage is done in a CNC (computer numerical control) mill and lathe. The precision machining is done using a wire-EDM (electric discharge machining) machine. The coefficient of linear thermal expansion $\alpha_{\rm L}$ for copper as a function of temperature is shown in Fig. 2.12 using data from [Whi73]. Integrating $\alpha_{\rm L}$ from 77 K to 298 K yields a contraction of 0.3%. After cooling, the rods should have a dimension across the hexagonal shank of 0.250 in.

A test unit for one detector was assembled in a class 1000 cleanroom at UNC. The goals of the test were to determine if any of the dimensions required adjustment and to check the procedure. Before assembling the detector unit, the copper pieces were etched and passivated according to a procedure developed at Pacific Northwest National Laboratory [Hop07]. After cleaning, the detector plate was placed in a custom fixture designed to hold it on the table, allowing the rods to be inserted from above. The rods were dipped in a bath of liquid nitrogen and quickly dropped into the mounting plate. In the initial attempt, none of the three hollow hexagonal rods could be inserted all the way into the crystal mounting plate. After an aggressive re-etching of the rods and the mounting plate, all of the rods were seated, and one of the three was too loose. Future work on this project will involve attempting to quantify precisely the amount of material removed in the etching process.

[Hop07] E. Hoppe *et al.*, Nucl. Instrum. Methods A, **579**, 486 (2007).

[Whi73] G. White, J. Phys. D, **6**, 2070 (1973).

2.1.6 The Majorana Low-Background Broad-Energy Germanium Detector at KURF (MALBEK): Low-Energy Program Status

P. Finnerty, G.K. Giovanetti, R. Henning, J.F. Wilkerson, *TUNL*; A.G. Schubert, *University of Washington, Seattle, WA*

Previously, MALBEK had an energy threshold of about 550 eV and a significant low-energy continuum due to slow signals originating near the n^+ contact. A source of low-energy γ rays from ^{210}Pb near the n^+ contact of the detector was found to have been the origin of these slow signals. We have removed the source of ^{210}Pb from within the cryostat, and the slow signal backgrounds have been reduced by about 95% in the 5 to 10 keV region.

Since the development of the first germanium detectors, the observation of slow-rise-time signals and pulse-height-deficit effects have been reported extensively in the literature [Ale64, Str67, Tam67, Sak71]. Due to the recent interest in low-threshold p-type point-contact (PPC) germanium detectors for use in searches for low-mass weakly-interacting massive particles (WIMPs) [Bar09, Aal08, Aal11a, Mar10, Aal11b, Sch05, Ell09], determining the cause of these slow-signals has become an important research topic. The leading hypothesis claims that these signals arise from interactions near the boundary between the lithium-diffused n^+ contact (dead layer). The lithium concentration is thought to follow a sigmoidal function more closely than a step-function. This results in a transition layer, in which the lithium concentration gradually falls off to zero. Therefore the electric fields in this region are weak. The weak electric fields cause charge carriers in this region to move much more slowly, with their movement dominated by thermal diffusion.

For example, if a charge cloud is created in the transition layer, the cloud will diffuse due to the slower drift velocity, so that the probability for charge trapping is increased. Charge trapping results in one of two scenarios: either (1) the charge will subsequently be released, or (2) the charge will become trapped for a period longer than the integration time of the electronics. Scenario (1) results in slow-signals, while (2) results in energy degradation.

It is clear that with a source of γ rays with energies below 100 keV, there is a higher probability that the γ ray will interact within the outer 1-2 mm of the detector, in the dead+transition layer, thus resulting in a low-energy excess, potentially mimicking a WIMP signal. We should note that there is a non-zero probability that a higher energy γ ray will interact in this layer, but for the sake of this argument, it is a reasonable assumption to ignore it.

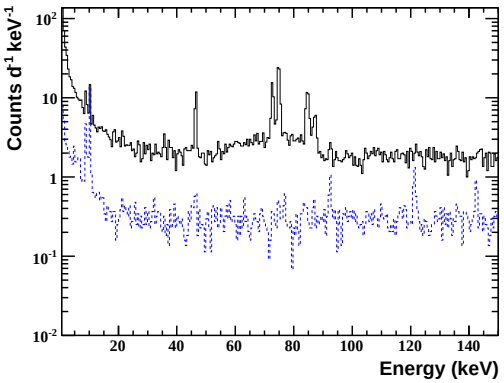

Figure 2.14: (Color online) Measured γ-ray spectra. The upper curve has the lead shims in place and includes cosmogenic peaks from K-shell electron capture in ^{65}Zn (8.99 keV), ^{68,71}Ge (10.36 keV), and ^{210}Pb (46.5 keV), plus Pb x-rays (72-90 keV). The lower curve was measured after the lead shims were removed. Notice the lack of ^{210}Pb (46.5 keV) and Pb X-rays (72-90 keV). Several peaks are now visible: ^{67}Ga (93.31 keV), ^{57}Co (122.06 keV) and ^{57}Co γ-ray + x-ray summing (136.47 + 7.06 keV).

After several months of steady-state operation in an underground environment, we observed a background due to the ^{210}Pb 46.5 keV γ-ray line. (The mean free path of such a γ ray in germanium is 0.4721 mm.) This spectrum is the upper curve in Fig. 2.14. We concluded that the source of ^{210}Pb had to be internal to the

cryostat, namely the lead shims used to position the germanium crystal within the cryostat. These shims were supposed to be "ancient" and therefore radio-pure. However the backgrounds observed were not consistent with ancient lead shims. We opened the cryostat and removed the lead foils that were used to shim the germanium crystal inside the detector holder (see Fig. 2.15), replacing the lead shims with teflon. This change reduced the 46.5 keV peak intensity by a factor of 10.4 (see Fig. 2.14) and reduced the slow-signal contamination by about 95% (see Fig. 2.16).

Figure 2.15: (Color online) The two aluminized non-low-background lead shims that were removed from MALBEK. They were located between the high-voltage copper foil and the germanium crystal. Together the shims contain 3.013 g of lead.

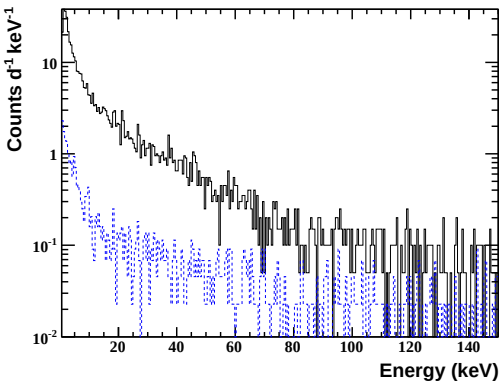

Figure 2.16: (Color online) The energy spectrum corresponding to slow-signals. The upper curve was taken with the lead shims in place; for the lower curve they were replaced with teflon.

We have shown that the removal of a source of low-energy γ-rays adjacent to a PPC germanium crystal results in a significant reduction in both low-energy and slow-signals. We have accumulated over 130 live-days of background data with MALBEK since the removal of the lead shims. We will continue to acquire data at least until December 2012.

[Aal08] C. E. Aalseth *et al.*, Phys. Rev. Lett., **101**, 251301 (2008), Erratum: *ibid.* 102 (2009) 109903.

[Aal11a] C. E. Aalseth *et al.*, Phys. Rev. Lett., **106**, 131301 (2011).

[Aal11b] C. E. Aalseth *et al.*, Phys. Rev. Lett., **107**, 141301 (2011).

[Ale64] T. K. Alexander *et al.*, Phys. Rev. Lett., **13**, 86 (1964).

[Bar09] P. S. Barbeau, Ph.D. thesis, University of Chicago, 2009.

[Ell09] S. R. Elliott *et al.*, J. Phys. Conf. Ser., **173**, 012007 (2009).

[Mar10] M. G. Marino, Ph.D. thesis, University of Washington, 2010.

[Sak71] E. Sakai, IEEE Trans. Nucl. Sci., **18**, 208 (1971).

[Sch05] S. Schönert *et al.*, Nucl. Phys. B, Proc. Suppl., **145**, 242 (2005).

[Str67] M. Strauss and R. Larsen, Nucl. Instrum. Methods, **56**, 80 (1967).

[Tam67] U. Tamm, W. Michaelis, and P. Coussieu, Nucl. Instrum. Methods, **48**, 301 (1967).

2.1.7 Research and Development for the MALBEK Data-Acquisition System

G.K. Giovanetti, P. Finnerty, R. Henning, M.A. Howe, J.F. Wilkerson, *TUNL*

We describe efforts to improve performance of a data-acquisition system for the Majorana low-background broad-energy germanium detector at KURF.

As part of the research and development efforts for the Majorana Demonstrator (see Sect. 2.1.1), we have deployed a prototype 450-g broad-energy germanium (BEGe) detector at the Kimballton Underground Research Facility (KURF) in Ripplemeade, VA. The Majorana low-background broad-energy germanium detector at KURF (MALBEK) is investigating point-contact, modified-BEGe detector performance, exploring the sub-keV energy spectrum in a search for light, weakly interacting massive particles (WIMPs) [Gio12], and serving as a test-bed for electronics, software, and data-analysis techniques for the Majorana Demonstrator (see Sect. 2.1.6).

The MALBEK data-acquisition system, shown in Fig. 2.17, uses the object-oriented real-time control and acquisition (ORCA) system, an object-oriented data-acquisition application that provides an easy-to-use, graphical interface for manipulation of experimental hardware and data streams. ORCA, which is discussed in Sect. 8.4.1, provides a catalog of fully encapsulated objects representing hardware, data-readout tasks, data-analysis modules, and control modules. The ORCA application includes ORCAScript, a small interpreted programming language that can be used to implement data-stream filtering, real-time event building and data plotting, and the automation of run control and run-time experimental parameters.

A central challenge in the design of the MALBEK and Demonstrator DAQ is the wide energy spectrum of the events of interest, ranging from the sub keV region for WIMP-nucleus scattering, to energies above 2 MeV for neutrinoless double-beta decay. To meet this requirement, each detector is digitized in a high-gain and a low-gain channel. This scheme roughly doubles the number of triggers from a single detector. In addition, at energies below 100 keV, contributions to the energy spectrum from slow pulses originating near the germanium-crystal dead layer become significant. These slow pulses do not contain the full event energy and create a continuum in the energy spectrum that can mask low-energy x rays and dark-matter signals. (The source and reduction of slow pulses are discussed in Sect. 2.1.6). It is therefore important to digitize events at high resolution to determine the rise times of physics events and eliminate any slow pulses. These two requirements greatly increase the expected data rate of the Demonstrator.

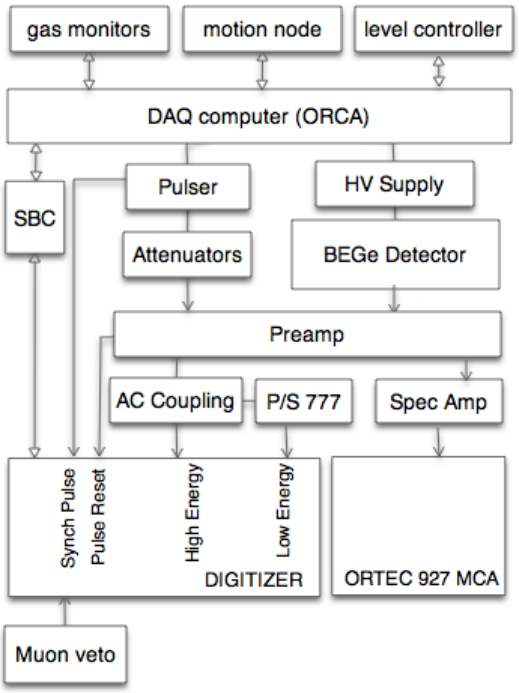

Figure 2.17: Block diagram of the MALBEK DAQ

We have made two modifications to the Struck Innovative Systeme 3302 ADC, a VME-based, eight-channel, sixteen-bit digitizer capable of digitization rates up to 100 MHz. The first change is the addition of a high trigger thresh-

old. Any event that is larger than a configurable high-energy-suppress threshold will not cause a trigger. This allows high-energy events to be eliminated in the high-gain channel. They will now only be digitized in the low-gain channel. The second change is the addition of a feature allowing for variable digitization rates within a single channel. This is accomplished by adding a second raw-data buffer to the card. Data saved in this buffer is pre-summed from 4 to 256 clocks. Now, instead of capturing the entire 100-microsecond event at 100 MHz, we can digitize the few-microsecond region that contains the rising edge of the event at 100 MHz and use the pre-summed data buffer to save the remainder of the event. These two changes reduce the size of the events while maintaining the wide energy response and high resolution required for analysis.

The MALBEK DAQ has been running stably since February of 2009. We will continue to use it as a test-bed for DAQ improvements relevant to the MAJORANA DEMONSTRATOR.

[Gio12] G. K. Giovanetti *et al.*, J. Phys.: Conf. Ser., **375**, article 012014 (2012).

2.1.8 Underground Low-Background Assay at KURF

K. Vorren, R. Henning, S. MacMullin, J.F. Wilkerson, *TUNL*

Two HPGe detectors are in operation at the Kimballton Underground Research Facility, located inside a mine near Ripplemead, VA. The detectors are being used for materials assay in a low-background environment. A status update of the low-background counting facility is provided.

2.1.8.1 Facility Overview

The Kimballton Underground Research Facility (KURF) is located about 25 miles from Virginia Polytechnic and State University in the Kimballton mine owned by Lhoist North America. The facility is located in a building on the 14th level of the mine at a depth of 520 meters, providing 1450 meters of water-equivalent shielding. The low-background counting (LBC) facility is operated by UNC/TUNL and housed within a Naval Research Laboratory (NRL) modified shipping container.

The LBC facility has two HPGe detectors used exclusively for low-background assay work. The first detector,"Melissa," is a 1.1kg, 50% RE (relative efficiency compared to NaI) Canberra LB (low-background) detector. Melissa is oriented vertically and is cooled using a dipstick cryostat. Melissa's shield consists of 15 cm of Doe-run lead and 2.54 cm of OFHC (oxygen-free high conductivity) copper. The FWHM at 1.33 MeV is 1.70 keV, and the threshold is around 20 keV. The other detector, "VT-1," is a 0.956 kg, 35% RE ORTEC LLB Series detector in a J-type configuration. VT-1's shield consists of a 10.1 cm ORTEC commercial lead shield and 0.3 cm of OFHC copper. VT-1 has a FWHM of 1.80 keV at 1.33 MeV, and the threshold is also about 20 keV.

A liquid nitrogen boil-off system is in place for both VT-1 and Melissa, in order to purge ^{222}Rn from the detector volumes. The boil-off is collected from a separate 30 L Dewar of liquid nitrogen and piped to the detector region. The result is a decrease of radon by a factor of approximately 3.5 [Fin11]. Radon reduction in Melissa was improved recently by increasing the boil-off flow rate into the detector volume via a hole drilled through the copper shield. For more technical details regarding the facility and detector setup, see Ref. [Fin11]. Photographs of samples in each of the detectors are given in Figs. 2.18 and 2.19.

Figure 2.18: (Color online) Mineral Oil sample inside VT-1.

2.1.8.2 Routine Operation

All monitoring and data acquisition is controlled by orca, which is run on a small Mac Mini in the NRL trailer [How08]. From within the orca interface, it is possible to stop and start runs, control the liquid nitrogen (LN) levels in the detector Dewars, and monitor the data in real time. In case of power failure in the mine, data collection is segmented into hour long runs, and transferred offsite for backup. All of the operations performed with orca can be done remotely.

Due to the low operating temperature necessary for HPGe detector operation, constant monitoring of liquid nitrogen is required. The level in the detector Dewars is controlled by an AMI 286 liquid-level controller. The controller is programmed to automatically fill the detector Dewars whenever the LN decreases beyond a user-determined threshold, which is usually 10% of

capacity. The threshold levels and fill levels can easily be set within ORCA, so that the user simply has to check that everything is functioning correctly.

2.1.8.3 Sample Analysis

The preamplifier output from each detector is fed into a spectroscopy amplifier for shaping. The unipolar output is then forwarded to an ORTEC 927 ASPEC multi-channel analyzer (MCA). All data from the MCA is handled by ORCA. The ORCA output is then processed using ORCAROOT which fills ROOT trees with the MCA spectra and other useful information for analysis, such as the live time, real time, and channel information. Finally, a program which reads the ROOT trees is used for spectrum analysis. The spectrum-analysis code was designed for batch processing of different sets of data, making it possible to simultaneously analyze different samples. This can be useful when comparing sample-run and background-run data or when determining count rate as a function of source position within the detector region.

For analysis, a sample spectrum is compared to the background. Background and sample spectra are normalized by dividing out the counting time. A library of common γ-ray lines is used to search for peaks and determine the activity of the sample. A Gaussian plus a linear background function is fit to each peak used for analysis. The peak area is then extracted by subtracting the linear background determined in the fitting procedure from the integral of the peak. The net peak area is found by subtracting the peak area of a background peak from the corresponding sample peak. If there is no peak in the background spectrum, the background peak area is set to zero.

The activity is determined using the equation,

$$A_\gamma = \frac{N}{\epsilon_\gamma m} \tag{2.1}$$

where N is the net peak area, ϵ_γ is the peak efficiency, and m is the mass of the sample. Peak efficiency is determined using a MAGE [Bau06] Monte Carlo simulation. The Monte Carlo has been validated by checking peak efficiencies against calibrated samples [Fin11].

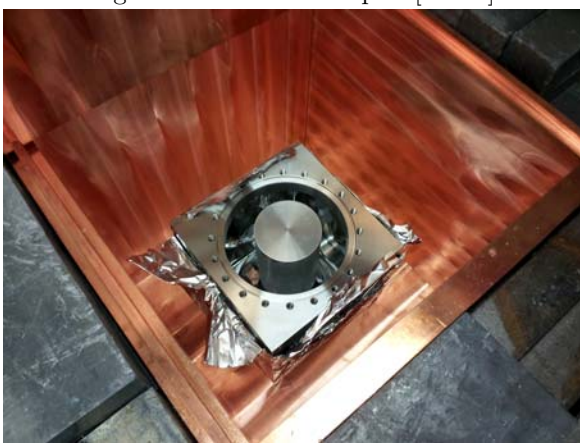

Figure 2.19: (Color online) Service body cube inside Melissa.

2.1.8.4 Conclusion

The LBC at KURF has been in operation for over four years. With sufficient notice, samples can be assayed fairly quickly. While most of the assayed samples come from the MAJORANA collaboration, samples from other institutions have also been assayed. Activities of selected recent samples is given in Table 2.1.

Table 2.1: Sample Activities ($\frac{mBq}{kg}$)

Sample	Source	U	Th
Service Body	MAJORANA	< 4	< 14
Mineral Oil	MAJORANA	<30	<38
Tungsten	VT	<4	<40

[Bau06] M. Bauer *et al.*, J. Phys. Conf. Ser., **39** (2006).

[Fin11] P. Finnerty *et al.*, Nucl. Instrum. Methods A, **642**, 65 (2011).

[How08] M. Howe, M. Marino, and J. F. Wilkerson, In *IEEE Nuclear Science Symposium, NSS-08*, pp. 3562–3667, 2008.

2.1.9 The ^{136}Xe$(n,2n)^{135}$Xe Cross Section between 9 and 15 MeV

C. Bhatia, S.W. Finch, M.E. Gooden, W. Tornow, *TUNL*

The cross section for the reaction ^{136}Xe$(n,2n)^{135}$Xe to both the isomeric and ground states was measured at 14.5 MeV to help resolve inconsistencies in the existing database. Additionally, the cross section for the isomeric-state transition was measured for neutron energies down to 9 MeV—the first measurements below 14.5 MeV.

Among the three currently operating searches for neutrinoless double-beta ($0\nu\beta\beta$) decay, two use ^{136}Xe as the target medium. Very recently, the EXO [Aug12] and KamLAND-Zen [Gan12] collaborations reported lower limits for the half-life $T_{1/2}$ of ^{136}Xe. From these limits, an upper bound on the effective Majorana neutrino mass can be deduced. Although these experiments are mounted underground, muon-induced spallation neutrons are of concern, because they could potentially cause events that are indistinguishable from the ones of interest at 2458 keV, the Q-value for $0\nu\beta\beta$.

The ^{136}Xe$(n,2n)^{135}$Xe reaction ($Q = -8.1$ MeV) is of special interest, because the $(n,2n)$ cross sections for nuclei with large $(N-Z)/A$ values are typically many hundreds of mb. The reaction on ^{136}Xe either feeds directly to the ground state of ^{135}Xe or it populates the isomeric $11/2^-$ state at 526.6 keV. The isomeric state decays with $T_{1/2} = 15.3$ min to the $3/2^+$ ground state ($> 99.4\%$ isomeric transition, $< 0.6\%$ β decay). The ^{135}Xe ground state β-decays to ^{135}Cs with $T_{1/2} = 9.14$ h.

Although there is no decay radiation from ^{135}Xe and ^{135}Cs which interferes with the signal for $0\nu\beta\beta$ decay, the creation of two, mostly low-energy neutrons is of concern. These neutrons can capture on ^{136}Xe, producing ^{137}Xe which β decays ($T_{1/2} = 3.82$ min), resulting in a variety of deexcitaion γ rays. These include one at 2474.8 keV. Given the 1.67% energy resolution of the EXO detector, this γ ray could produce a single-site event that would be indistinguishable from a potential $0\nu\beta\beta$ signal centered at 2458 keV. The ^{137}Xe γ rays at 2444.0 keV and 2452.4 keV are accompanied by other γ rays, and therefore, are of less concern for EXO. However, the KamLAND-Zen detector's energy resolution is about 4.2% in the region of interest, and the detector cannot distinguish single-site from multi-site events occurring within a spatial separation 20 to 25 cm. Therefore up to five levels in ^{137}Xe can potentially produce events in the signal region. On the other hand, the overburden and external shielding of the KamLAND-Zen detector should substantially reduce the frequency of neutron-induced reactions in the detector material relative to the EXO detector.

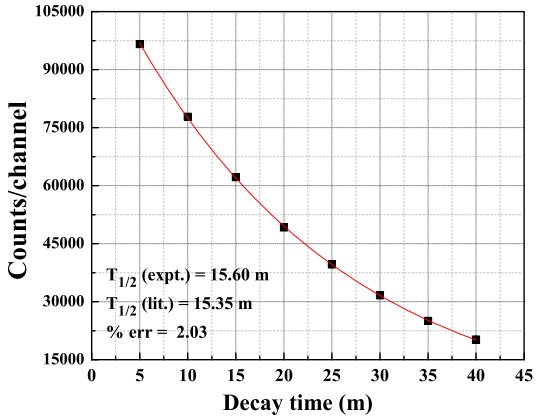

Figure 2.20: (Color online) Measured decay half-life of ^{136}Xe$(n,2n)^{135m}$Xe reaction.

The ^{136}Xe$(n,2n)^{135m}$Xe reaction cross section was measured using the activation technique. The ^{2}H$(d,n)^3$He reaction, initiated with a pulsed deuteron beam, was used to produce quasi-monoenergetic neutrons between 9 and 14.5 MeV. A titanium sphere [Rup09] of 10 mm outer diameter and 0.2 mm wall thickness, loaded to about 250 atm (725 mg) with ^{136}Xe (isotopically enriched to 99.9%) was positioned 2.9 cm from the end of a deuterium gas cell. The deuterium gas pressure was adjusted to keep the neutron energy spread below ±200 keV. As described in Sect. 2.3.3, a neutron monitor in com-

bination with a Monte-Carlo simulation was used to determine the neutron flux at the position of the xenon sphere. The irradiation time was 45 min. The HPGe detector, the data-acquisition system, and the data analysis used to determine the yield of the 526.6 keV line were identical to those referred to in Sect. 2.3.3. Figure 2.20 shows the decay curve for the 526.6 keV γ-ray line obtained after irradiation with 12 MeV neutrons. There is good agreement between the measured and literature half-life values. Runs were also taken with an identical but empty titanium sphere to check for background events in the relevant energy region. Our measured cross sections for the ^{136}Xe$(n,2n)^{135m}$Xe reaction are shown in Fig. 2.21. The error bars include counting statistics plus uncertainties in the neutron flux determination, the amount of ^{136}Xe, and the absolute HPGe efficiency. All these uncertainties were added in quadrature. Previous data [Kon68, Sig76, Reg82] exist only at 14.5 MeV. As seen in Fig. 2.21, they show consistently smaller values than found in the present work.

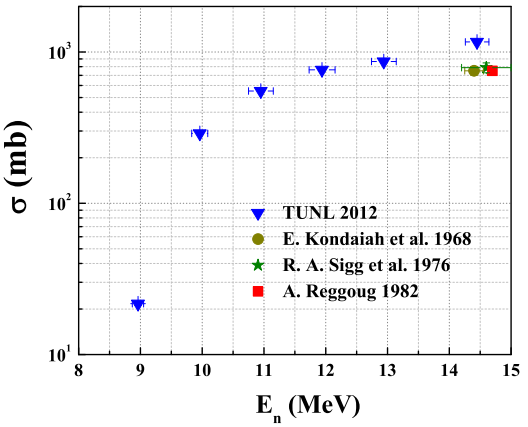

Figure 2.21: (Color online) Measured cross-section data of ^{136}Xe$(n,2n)^{135m}$Xe reaction between 9 and 15 MeV.

At E_n = 12.0 and 14.5 MeV we recorded the decay curve of the 249.8 keV γ ray resulting from the β decay of the ^{135}Xe ground state to the first excited state in ^{135}Cs, which has $T_{1/2}$ = 9.10 h. Figure 2.22 shows the extracted cross section for this transition in comparison to previous data [Kon68, Sig76, Reg82], which are quite scattered. The two curves are the ENDF/B-VII.1 and TENDL-2011 predictions [Kon05]. In the future we will extend our ground-state transition measurements to lower energies.

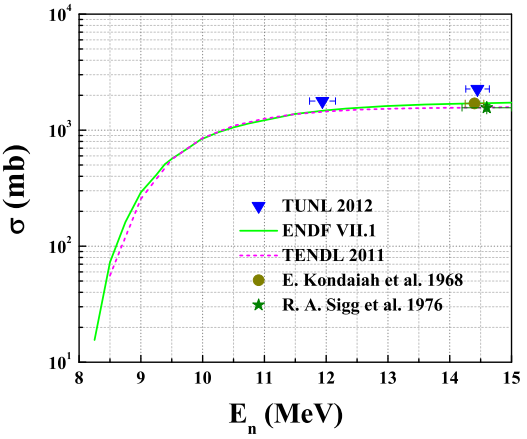

Figure 2.22: (Color online) Measured cross-section data of ^{136}Xe$(n,2n)^{135}$Xe reaction at E_n = 12.0 and 14.5 MeV.

Our results show that the ^{136}Xe$(n,2n)^{135}$Xe cross section is very large, peaking at more than 2000 mb at about E_n = 15 MeV. Therefore, experiments searching for the $0\nu\beta\beta$ of ^{136}Xe should be operated very deep underground where, the muon-induced spallation-neutron flux will not cause a problem. Of course, the required depth depends on details of the experimental technique and the shielding arrangement used.

[Aug12] M. Auger *et al.*, Phys. Rev. Lett., **109**, 032505 (2012).

[Gan12] A. Gando *et al.*, Phys. Rev. C., **85**, 045504 (2012).

[Kon68] E. Kondaiah *et al.*, Nucl. Phys., **A120**, 337 (1968).

[Kon05] A. J. Koning, S. Hilaire, and M. C. Duijvestjin, AIP Conf. Proc., **769**, 1154 (2005).

[Reg82] A. Reggoug *et al.*, Mohammad V University, Morocco, Annual Report, **5**, 14 (1982).

[Rup09] A. Rupp *et al.*, Nucl. Instrum. Methods A, **608**, 152 (2009).

[Sig76] R. A. Sigg and P. Kuroda, Nucl. Sci. Eng., **60**, 235 (1976).

2.1.10 The ^{136}Xe(n,$n'\gamma$)^{136}Xe Reaction at 8 MeV

J.W. Bradt, *University of Rochester, Rochester, NY*; J.H. Esterline, B. Fallin, S.W. Finch, M.E. Gooden, W. Tornow, *TUNL*

For the first time, a search was performed for γ-ray lines in neutron inelastic scattering from ^{136}Xe. Such scattering could interfere with the potential neutrinoless double-beta decay signal at 2458 keV. Evidence for two weak lines at 2443 keV and 2464 keV has been found.

The EXO [Aug12] and KamLAND-Zen [Gan12] collaborations use ^{136}Xe as a target medium in their ongoing search for neutrinoless double-beta ($0\nu\beta\beta$) decay. Although these experiments are operating underground, muon-induced spallation neutrons and neutrons from (α,n) reactions are of concern because they could potentially mimic the signal expected from the $0\nu\beta\beta$ decay at 2458 keV. Therefore, a program has been initiated at TUNL to measure neutron-induced cross sections on ^{136}Xe in the energy range between 4 and 16 MeV. These can then be used to guide theoretical calculations for these important reactions at lower and higher energies.

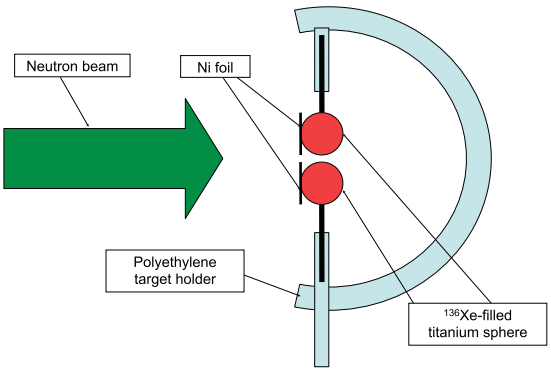

Figure 2.23: (Color online) Arrangement of ^{136}Xe gas cells

Here we report on our first measurements of the reaction ^{136}Xe(n,$n'\gamma$)^{136}Xe at E_n = 8.0 MeV using four 60% HPGe detectors to record γ-ray spectra at 80°, 90°, 110°, and 120°. The xenon gas, enriched to 99.9% in ^{136}Xe, was contained in two 10 mm outer diameter titanium spheres [Rup09] with wall thickness of 0.2 mm, and pressurized to about 250 atm (725 mg in either cell). A nickel foil, 9.5 mm in diameter and 0.5 mm thick, was attached to each titanium sphere for neutron flux determination. Figure 2.23 shows how the two xenon cells were arranged. The center-to-center distance between the neutron production gas cell and the xenon sphere was 280 cm, and the distance between the xenon sphere and the front face of the HPGe detectors varied between 51 mm at 80° and 100 mm at 120°. The HPGe detectors were surrounded by an inner cylinder made of copper (2.8 mm wall thickness and 250 mm long) and an outer cylinder made of lead (20 mm wall thickness and 100 mm long). See Sect. 2.1.11 for additional experimental details.

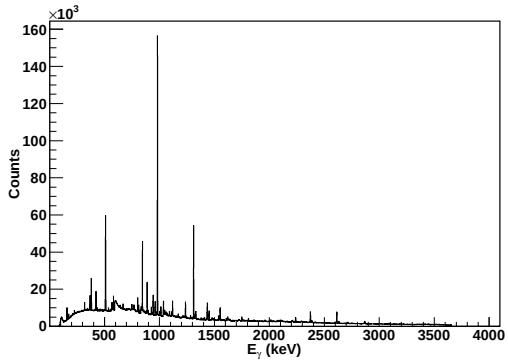

Figure 2.24: An HPGe detector spectrum

A γ-ray spectrum measured with an HPGe detector is shown in Fig. 2.24. A large number of discrete peaks can be seen. Most of them are from neutron inelastic scattering on the five titanium isotopes (^{48}Ti: 73.7%, ^{46}Ti: 8.3%, ^{47}Ti: 7.4%, ^{49}Ti: 5.4%, and ^{50}Ti: 5.2% natural abundance). Unfortunately, the $2^+ \rightarrow 0^+$ transition energy in ^{136}Xe (1313.0 keV) overlaps almost entirely with the $4^+ \rightarrow 2^+$ transition energy in ^{48}Ti (1312.1 keV). Nevertheless, cross-section information for the $2^+ \rightarrow 0^+$ transition in ^{136}Xe was obtained by taking runs with an identical but empty titanium sphere. Because only one empty titanium cell was available, half of the runs were taken with it mounted in the

bottom position, and the other half with it in the top position. These runs are also helpful to make sure that the results reported in the present work are only from ^{136}Xe-related γ-ray transitions, and not from misidentified peaks.

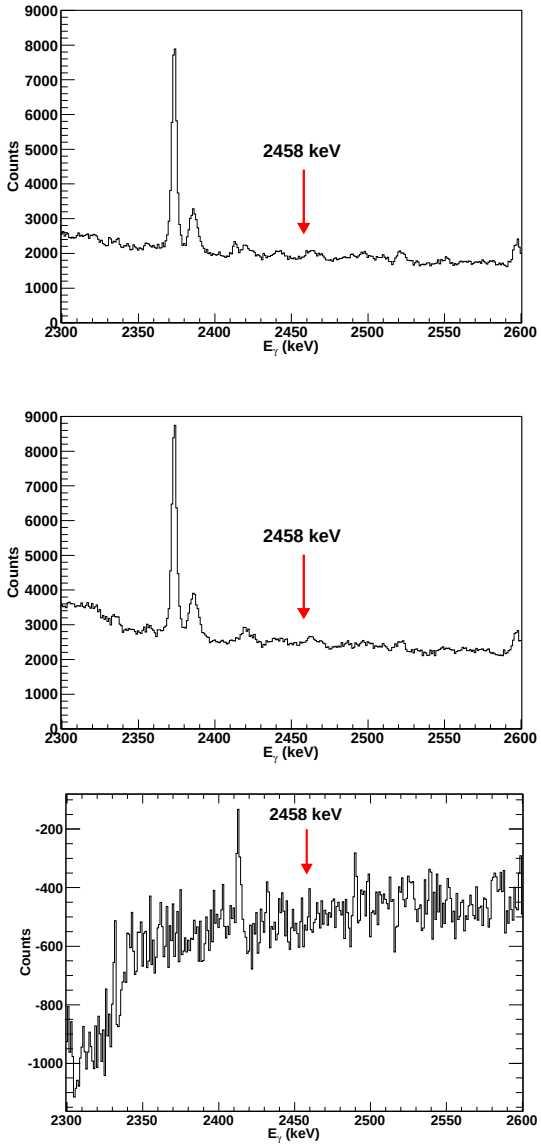

Figure 2.25: (Color online) Enlargement of the portion of the γ-ray energy spectra between 2300 and 2600 keV. The expected $0\nu\beta\beta$ energy of 2458 keV is labeled with a red arrow. The top panel shows the spectrum when ^{136}Xe is present, the second panel shows the spectrum for an empty sphere, and the bottom panel shows the difference spectrum.

Within the 1.67% energy resolution of the EXO detector, the known level scheme of ^{136}Xe does not show any γ-ray transitions which could cause single-site events in the energy region centered at 2458 keV. The closest level is at 2414.7 keV. However there are levels at 2444.4 keV and 2465.0 keV that decay through a sequence of γ-ray emissions to the ground state. The individual γ rays from each of these sequences would be recorded together in the KamLAND-Zen detector. Given the detector's 4.2% energy resolution, these events cannot be distinguished from the $0\nu\beta\beta$ signal of interest at 2458 keV. The EXO detector, however, would recognize them as multi-site events.

Figure 2.25(a) exhibits a small peak centered at 2414.4 keV, which is not present in Fig. 2.25(b). This peak is due to the deexcitation of the 2414.7 keV level referred to above. The γ-ray lines at 2375.1 keV and 2387.2 keV are due to neutron inelastic scattering from ^{48}Ti. The difference spectrum in Fig. 2.25(c) shows the 2414.7 keV peak more clearly. As expected from information in the literature, Fig. 2.25(c) does not show any indication of the two ^{136}Xe lines at 2444.4 keV and 2465.0 keV because the associated states do not decay directly to the ground state. However, as noted above, the γ-ray cascades may be a potential problem for KamLAND-Zen. We will estimate the importance of the 2444.4 keV and 2465.0 keV states from the observed yield of the 2414.7 keV transition in the KamLAND-Zen experiment.

The cross sections for the observed transitions in ^{136}Xe will be determined in the near future, once the associated yield analyses—including those of the ^{58}Ni and ^{60}Ni isotopes used for neutron flux determination—have been completed. Then the number of background events in the energy region of interest for the $0\nu\beta\beta$ decay of ^{136}Xe can be calculated using estimates for the neutron flux at the location of the KamLAND-Zen detector.

[Aug12] M. Auger, Phys. Rev. Lett., **109**, 032505 (2012).

[Gan12] A. Gando, Phys. Rev. C, **85**, 045504 (2012).

[Rup09] G. Rupp, Nucl. Instrum. Methods A, **608**, 152 (2009).

2.1.11 The ^{X}Ge$(n, x\gamma)$ Reactions at $E_n = 8$ MeV

J.H. Esterline, B. Fallin, S.W. Finch, M.E. Gooden, C.R. Howell, J.H. Kelley, W. Tornow, *TUNL*

We resumed an investigation of neutron-induced transitions that could potentially contribute background to the region of interest for neutrinoless double-beta ($0\nu\beta\beta$) decay of ^{76}Ge. Observed γ-ray lines in close proximity to this region, $\pm$ 3 keV around the decay energy of 2039 keV, were identified as originating from the decay of ^{74}Ge.

After initial studies of ^{76}Ge$(n, x\gamma)$ performed in 2006 [Kwa07] at incident neutron energies of 8 and 12 MeV, we performed additional measurements at 8 MeV using the same sample, which is enriched to 86% in ^{76}Ge. The existing data had indicated γ rays with energies of 2005, 2023, 2035, and 2074 keV [Kwa08], all of which are in the vicinity of the 2039 keV Q-value for the neutrinoless double-beta ($0\nu\beta\beta$) decay of ^{76}Ge. These lines were identified with transitions between levels of ^{74}Ge, which has an abundance of 14% in both our sample and the enriched HPGe detectors used in the GERDA and Majorana experiments. They may be of interest in evaluating the Compton background in the $0\nu\beta\beta$ region of interest (ROI). The background that survives the requirement that no energy be deposited in adjacent detectors results in the inclusion of only so-called "single-site events." Furthermore, in the case of the 2035 keV transition, the finite energy resolution means that there is a potential, small direct contribution of full-energy deposition in a single-site event to the background in the ROI.

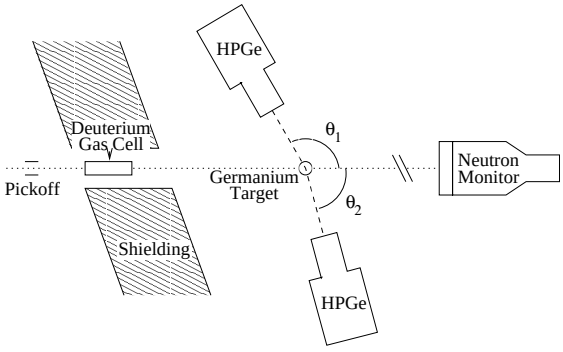

Figure 2.26: A schematic diagram of the setup in the SNSA between the time pickoff of the pulsed deuteron beam and the neutron monitor downstream of the germanium sample.

In addition to ^{74}Ge, the other naturally occurring isotopes of germanium are of possible relevance because of the anticipated presence in the Majorana experiment of unenriched germanium (with isotopic abundances of 20.6% ^{70}Ge, 27.4% ^{72}Ge, 7.8% ^{73}Ge, 36.5% ^{74}Ge, and 7.7% ^{76}Ge). This prompted measurements on natural germanium to be initiated. Such measurements are also needed to correct the ^{76}Ge data for γ-ray events not originating from the sample, but created by neutrons scattered by the sample into the HPGe detectors.

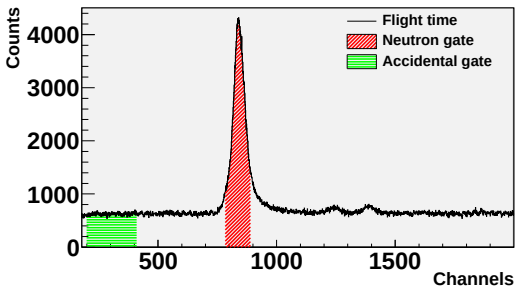

Figure 2.27: (Color online) A spectrum of pickoff-to-detector flight time. The times shown correspond to detected energies above 800 keV, since the lower-energy signals were of little interest in the present work. The time resolution is 0.1ns/channel. The peak due to 8.0 MeV neutrons features prominently around channel 850. Both the neutron gate and the accidental gate are indicated.

The measurements were performed at TUNL's Shielded Neutron Source Area (SNSA). The first set of data was obtained with two clover HPGe detectors located at 100° and 125° relative to the incident neutron beam; a second set was obtained with four 60% HPGe detectors located at various times at 45°, 60°, 80°, 90°, 110° and

120°. A gas cell filled to 6 atm with deuterium was bombarded with a deuteron beam pulsed at 2.5 MHz to produce a mononergetic and likewise pulsed neutron beam with an energy of 8.0 ± 0.35 MeV via the ^{2}H$(d,n)^3$He reaction. This beam irradiated a 10.2 cm^2 ^{76}Ge target with a thickness of 0.2 cm. Two thin iron monitor foils were affixed to the front and back of the target for neutron flux determination. These foils were also irradiated separately for background determination. Figure 2.26 shows a schematic of the experimental setup with two of the four 60% HPGe detectors.

A typical time-of-flight-time (TOF) spectrum between the capacitive time-pickoff located upstream of the deuterium gas cell and an HPGe detector is shown in Fig. 2.27. In addition to the energy spectrum corresponding to the peak of interest, there is a locally uniform background preceding γ rays from the gas cell's beam stop. This indicates the presence of a distinct energy spectrum uniquely identifiable with pervasive "accidental" coincidences. The subtraction of these accidentals from the spectrum associated with the peak of interest yielded a more accurate representation of neutron-induced events. Figure 2.28 presents the energy spectrum around the $0\nu\beta\beta$ ROI at 2039 keV, obtained from a partial analysis of data from the 100° clover HPGe detector data with the ^{76}Ge sample. Also shown are spectra obtained with only the iron monitor foils in the beam (presented as "background" data). The transitions identified in [Kwa08] are noted to be present in the ^{76}Ge spectra but not in the iron background (with the possible exception of 2035 keV).

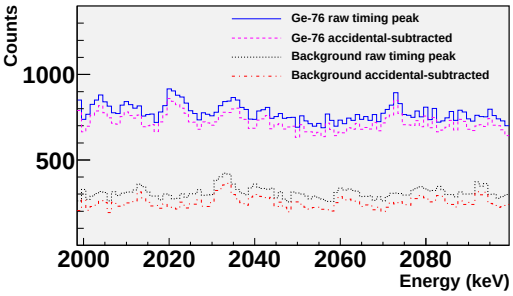

Figure 2.28: (Color online) Energy spectra around the $0\nu\beta\beta$ ROI corresponding to the neutron peaks for both the ^{76}Ge sample and Fe background (monitor foils), with the effect of accidental subtraction shown for each.

The determination of cross sections for the γ-ray lines related to either ^{76}Ge or ^{74}Ge (and the iron monitor foil) is in progress, as is the data analysis of the more complicated (and, potentially, edifying) spectra obtained with the natural germanium sample.

[Kwa07] E. Kwan *et al.*, TUNL Progress Report, **XLVI**, 25 (2007).

[Kwa08] E. Kwan *et al.*, TUNL Progress Report, **XLVII**, 26 (2008).

2.1.12 Partial Cross Sections of Neutron-Induced Reactions on ^{nat}Cu for $0\nu\beta\beta$-Decay Background Studies

M.E. Gooden, B.A. Fallin, S.W. Finch, C.R. Howell, J.H. Kelley, G. Rusev, A.P. Tonchev, W. Tornow, *TUNL*

Partial-cross-section measurements of $(n, x\gamma)$ reactions on ^{nat}Cu were carried out at TUNL using monoenergetic neutrons at six energies from 6 to 16 MeV. These studies were performed to provide accurate cross-section data on materials abundant in experimental setups using HPGe detectors to search for rare events such as the neutrinoless double-beta decay of ^{76}Ge. Spallation and (α,n) neutrons are expected to cause the largest source of external background in the energy region of interest. Our cross-section data will be compared to theoretical calculations and to data recently obtained at LANL.

Because of the extreme rarity of neutrinoless double-beta ($0\nu\beta\beta$) decay, extreme care must be taken to understand and reduce background in searches for such events. In this effort, most external sources can be eliminated by various means, and therefore one of the largest sources of background comes from neutrons generated in cosmic-ray interactions. These neutrons interact with the surrounding materials and produce signals in the detector by $(n, x\gamma)$ reactions. Most of the shielding material is lead, and studies of lead have already been done. However, copper is also widely used as a shielding material and is a component of the detector itself [Agu11]. Thus careful studies of the reaction ^{nat}Cu$(n, x\gamma)$ are vital to understanding this possible background.

To this end, measurements were carried out at the TUNL FN tandem accelerator using pulsed neutron beams with energies of E_n = 6, 8, 10, 12, 14, and 16 MeV. The beams were produced via the ^{2}H(d,n)^{3}He reaction. Two high-purity germanium (HPGe) clover detectors, positioned at 100° and 130° relative to the beam direction, were used to measure the γ-ray yields in the energy range of 500 to 3500 keV. The neutron flux on target was determined [Hut08] using the known cross section of the ^{56}Fe 846.7 keV transition. The iron used as a flux monitor consisted of two thin ^{nat}Fe foils that sandwiched the copper target. At each beam energy, approximately 36 hours of beam time were used for the sample-in measurement. An equal amount of time was spent with no copper target, so that only the iron monitor foils were in the beam. Similar studies have been carried out at LANL using a white neutron source, and results from our measurements will be compared to those from the LANL group, once they are published.

The data-acquisition system used was SpecTcl, which records event by event, allowing timing cuts to be made. The energy spectra were then analyzed using the ROOT code. Timing cuts were applied for the prompt neutrons from the ^{2}H(d,n)^{3}He reaction, and accidental background was subtracted, resulting in spectra with only beam-correlated events. These final spectra were integrated to determine the yields. An example of such a spectrum can be seen in Fig. 2.29.

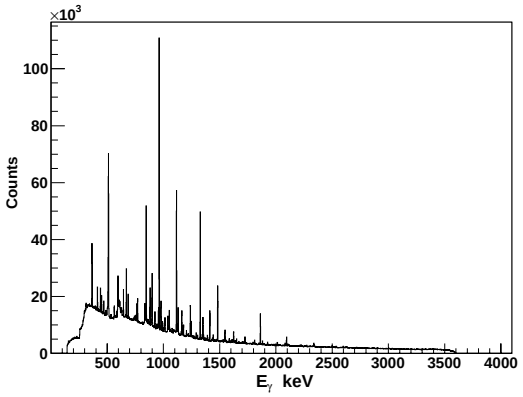

Figure 2.29: γ-ray energy spectrum from HPGe Clover 1 for E_n = 10 MeV.

Partial cross sections are being obtained for the most significant peaks in the γ-ray energy spectra. The two main isotopes of copper are ^{63}Cu and ^{65}Cu, with abundances of 69.2 and 30.8%, respectively. The most intense transitions for which we want to determine cross-sections are shown in Table 2.2.

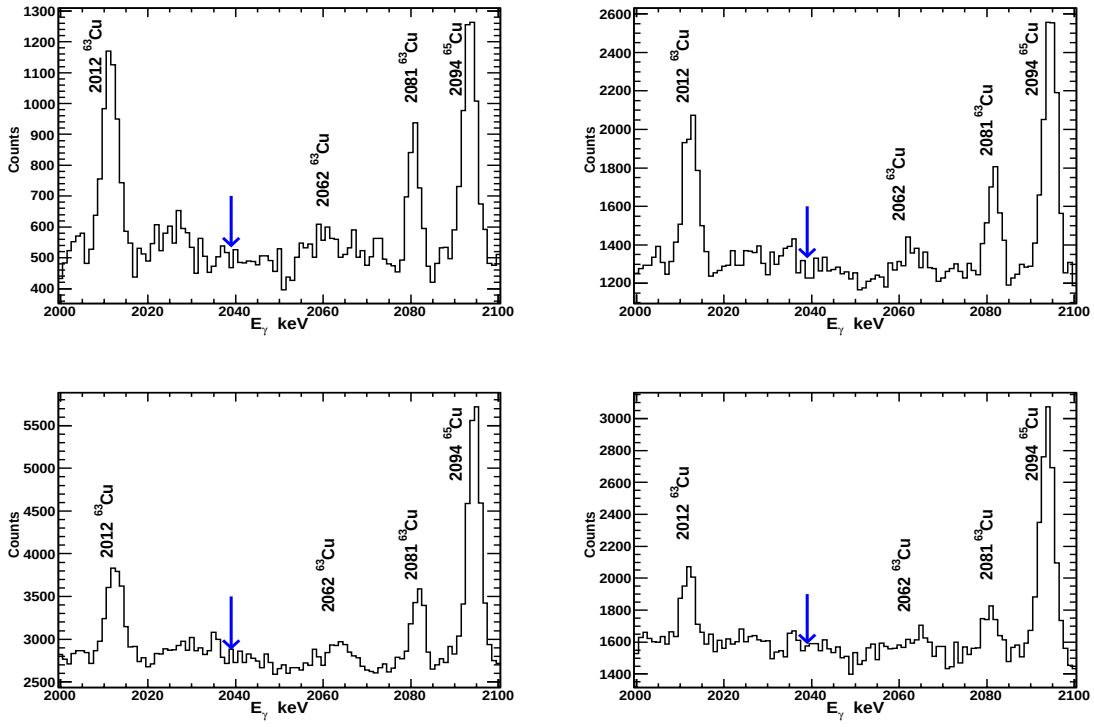

Figure 2.30: (Color online) A portion of the γ-ray spectra from HPGe Clover 1. Prominent peaks are labeled and the Q value of 2039 keV for the $0\nu\beta\beta$ decay is marked with a blue arrow. The plots shown correspond to: top left E_n = 6 MeV, top right E_n = 8 MeV, bottom left E_n = 10 MeV, and bottom right E_n = 12 MeV.

Table 2.2: The most intense transitions seen from the two most abundant copper isotopes.

^{63}Cu	^{65}Cu
669.6 keV	770.6 keV
962.1 keV	1115.5 keV
1412 keV	1481.8 keV
1547 keV	1623.4 keV
2081 keV	1725 keV

For $0\nu\beta\beta$ decay, the Majorana collaboration's isotope of interest is ^{76}Ge, which has a Q-value of 2039 keV. The main goal of this study is to determine if there are lines created by neutron reactions in copper that would interfere in the region of interest around the expected signal energy.

As seen in Fig. 2.30, there are strong lines above 2039 keV, at 2081 keV and 2094 keV, which will lead to Compton scattering events. There is also a signal at 2035 keV due to neutrons scattered into the HPGe detectors and interacting with ^{74}Ge.

Future work includes processing the data for E_n = 16 MeV. The code GEANT4 will be used to determine γ-ray absorption in the copper target at the relevant energies, and corrections will be made to account for feeding from higher-energy states into the levels of interest. Comparisons will also be made between our cross-section data and the results of theoretical Hauser-Feshbach–statistical-model calculations from the TALYS code.

[Agu11] E. Aguayo *et al.*, In *Proceedings of the DPF-2011 Conference*, 2011, `http://arxiv.org/pdf/1109.6913v1.pdf`.

[Hut08] A. L. Hutcheson, Ph.D. thesis, Duke University, 2008.

2.1.13 Double-Beta Decay of ^{96}Zr to an Excited Final State

S.W. Finch, W. Tornow, *TUNL*

A search for the first observation of ^{96}Zr's double-beta decay to an excited final state is currently underway at KURF. Two germanium detectors observe the two coincident γ rays from the resulting cascade. Preliminary results using an isotopically enriched ^{96}Zr sample are presented.

Observation of neutrinoless double-beta ($0\nu\beta\beta$) decay would identify the neutrino as a Majorana particle and allow a measurement of the neutrino mass to be made. The $0\nu\beta\beta$ decay rate is proportional to the neutrino mass and a nuclear matrix element (NME). This means the NME must be theoretically calculated. Such calculations are very difficult at the present time, and the $2\nu\beta\beta$ decay rate is used to calibrate them. By measuring $2\nu\beta\beta$ to an excited final state (see Fig. 2.31) we can provide additional information which may be used to help fine tune these NME calculations.

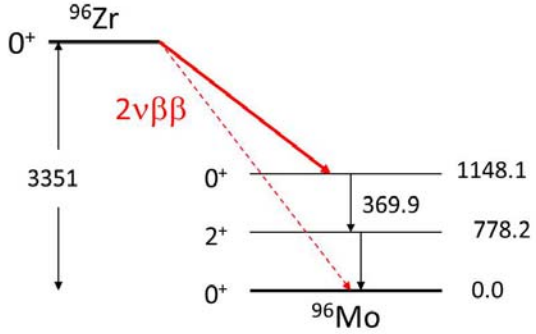

Figure 2.31: (Color online) The $\beta\beta$ decay scheme for ^{96}Zr. The ground-state decay is shown by the dashed line, with the excited-state decay represented by the solid line.

The measurements are being made underground at KURF, which has 1450 meters-water-equivalent of overburden. The experimental apparatus consists of two coaxial HPGe detectors, with the isotope of interest sandwiched between them. This arrangement is inside a NaI annulus which is used as an active veto. The two HPGe detectors record the two coincident γ rays from the $0^+ \rightarrow 2^+ \rightarrow 0^+$ decay sequence. Passive shielding includes 3/4 in. of copper and 6 in. of lead.

This apparatus was previously used to measure the double-beta ($\beta\beta$) decay half life of ^{100}Mo and ^{150}Nd to their excited 0_1^+ states [Kid09, Kid12]. The goal of this experiment it to extend those measurements—decay to the first excited 0^+ state—to ^{96}Zr. The NEMO-3 collaboration has already measured the half-life of the $2\nu\beta\beta$ decay of ^{96}Zr to the ground state and found $T_{1/2}^{2\nu} = [2.35 \pm 0.14(stat) \pm 0.16(syst)] \times 10^{19}$ y [Arg10].

^{96}Zr differs from the other $\beta\beta$ decay isotopes in that single-beta decay is energetically allowed, but only by a long-lived "fourth-forbidden decay." This half life has been estimated theoretically at 2.4×10^{20} y [Hei07]. The daughter nucleus, ^{96}Nb, decays with a half life of 23.35 hours to the 5^+ level of ^{96}Mo, emitting a cascade of γ rays as it de-excites to the 0^+ ground state (see Fig. 2.32). In this cascade, the 2^+ level of interest for $\beta\beta$-decay to excited final states is excited, however, the 0_1^+ state is not. Previous attempts to measure ^{96}Zr's $\beta\beta$ decay to an excited final state have produced only a lower limit of 3.3×10^{19} years for the half-life [Arp94]. These searches only looked for a single 778.2 keV γ ray from the $2^+ \rightarrow 0^+$ part of the decay. Because this 778.2 keV γ ray also appears in the γ-ray cascade resulting from ^{96}Nb, single detection experiments are only sensitive to $T_{1/2}^{\beta+\beta\beta}$. With our coincidence technique, we can independently measure both the β and $\beta\beta$ decay modes.

An estimate of the background present in our apparatus may be found by analyzing the data collected during the ^{150}Nd and background runs. In the 778.2 + 369.7 keV coincidence for ^{96}Zr there are no coincidence events within a ±2-keV-wide window (see Fig. 2.33 (c) and (d)) and four events within ±3 keV after 722 days of data collection. It should be noted that this analysis does not include any radioactive contamination that may be present in the zirconium sample.

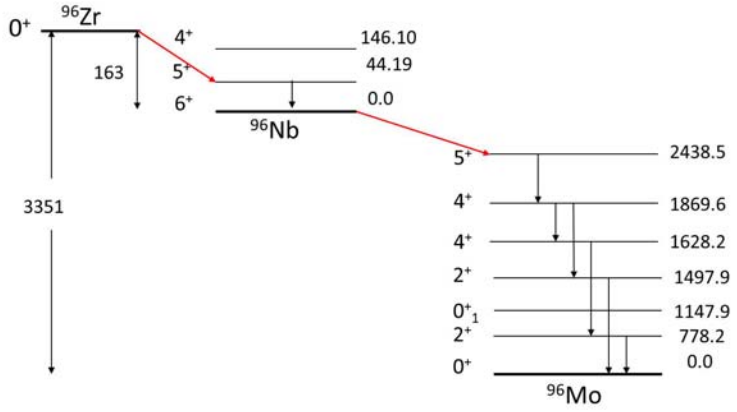

Figure 2.32: Decay scheme for ^{96}Zr in the case of two successive single-beta decays.

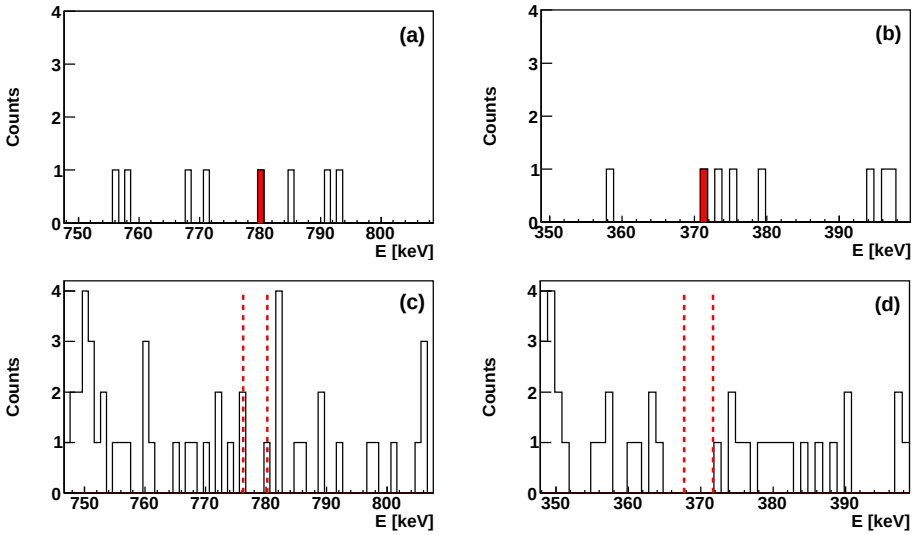

Figure 2.33: (Color online) Plots (a) and (b) show the ^{96}Zr region of interest after 104.8 days of data acquisition with the enriched sample; the one event passing all cuts is highlighted. Plots (c) and (d) show the same region after 722 days with no ^{96}Zr present; there are no events passing all cuts. Plots (a) and (c) are events in coincidence with 369.9 keV, while (b) and (d) are in coincidence with 778.2 keV, both use a ±2-keV-wide window.

Our ^{96}Zr source consists of two ZrO_2 samples: 7.2835 g enriched to 91.39% ^{96}Zr and 26.9688 g enriched to 64.15%, giving a total of 17.914 g ^{96}Zr. After 104.8 days with the ^{96}Zr sample in place we have one candidate event matching our selection critera. This event is shown in Fig. 2.33 (a) and (b).

[Arg10] J. Argyriades *et al.*, Nucl. Phys., **A847**, 168 (2010).

[Arp94] C. Arpesella *et al.*, Nucl. Phys., **B35**, 375 (1994).

[Hei07] H. Heiskanen *et al.*, J. Phys. G, **34**, 837 (2007).

[Kid09] M. F. Kidd, J. H. Esterline, and W. Tornow, Nucl. Phys., **A821**, 251 (2009).

[Kid12] M. F. Kidd *et al.*, Submitted to Phys. Rev. C, (2012).

2.1.14 Measurement of the (^{3}He,n) Reaction on Candidates for Neutrinoless Double-Beta Decay

D.R. Ticehurst, D. Combs, C.R. Howell, A.R. Young, *TUNL*

This experiment will measure the strength to 0^+ excited states for the ^{76}Ge(^{3}He, n)^{78}Se and ^{74}Ge(^{3}He, n)^{76}Se reactions relative to the strength for the transition to the 0^+ ground state in selenium. The goal is to test the validity of the BCS approximation in QRPA calculations of the nuclear matrix elements for neutrinoless double-beta decay ($0\nu\beta\beta$). The conceptual design of the experiment has been developed, and background levels have been assessed.

If neutrinoless double-beta decay is observed, its measured half-life will allow determination of the effective Majorana neutrino mass using calculated nuclear matrix elements for the transition [Vog08]. The experiment described here provides a test of the method used to calculate the matrix elements by determining the strength to 0^+ excited states in the two-proton stripping reactions ^{76}Ge(^{3}He,n)^{78}Se and ^{74}Ge(^{3}He,n)^{76}Se [Blo10].

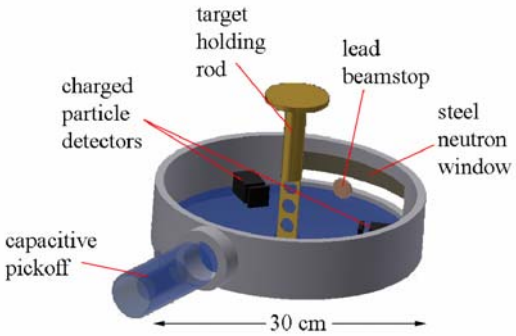

Figure 2.34: (Color Online) A schematic diagram of the target chamber. A similar chamber already exists and may be modified for this experiment.

This experiment will be carried out on the FN-tandem accelerator at TUNL. The germanium target will be placed in a thin-walled scattering chamber (see Fig. 2.34) and bombarded with a pulsed beam of 20 MeV ^{3}He nuclei [Tic11]. Neutrons emitted from the target will be measured in Target Room 1 using 12.7-cm-diameter, 5-cm-thick, "Bicron-type" (BC-501A) liquid-scintillator detectors placed from 0° to 15° relative to the beam axis at a distance of 15 m from the target. Estimates of the energy resolution and count rate have been made. Distorted wave Born approximation (DWBA) calculations will be used to predict the angular distributions. This project will also require construction and installation on the ion source of a ^{3}He gas-recirculation system (see Sect. 7.2.3.

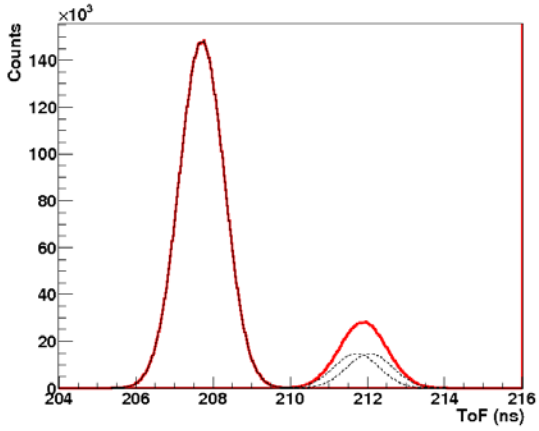

Figure 2.35: (Color Online) Simulated ToF spectra for ^{74}Ge(^{3}He, n)^{76}Se with a beam-pulse FWHM of 1.3 ns and a 10% excited state strength. The dashed black curves show the contributions of the ground state and the first two 0^+ states. The solid red curve is the composite.

An energy resolution of about 1 MeV is required to differentiate between the ground state and the 0^+ excited states of the product nucleus. The neutron energy will be determined by the time-of-flight (ToF) method, which relies on accurate measurements of the target-detector distance and the time between a beam pick-off pulse and a signal in the detector. From these measurements, the neutron energy can be determined with a resolution determined by the timing resolution. There are three sources of time-spread that contribute to the ToF resolution: energy loss in the target, neutron detector thickness, and the width of the ^{3}He beam pulses. A simple Monte-

Carlo code has been developed to predict the ToF spectra produced at 0° by a 1 mg/cm^2 thick target in a 20.0 MeV ^{3}He beam. As seen in Fig. 2.35 the excited states are clearly resolved from the ground state for a beam-pulse FWHM of 1.3 ns. Recent tests with a pulsed α-particle beam (see Sect. 7.2.2) have produced pulse widths down to 1.1 ns.

Count rate estimates were made using a cross section of 1 mb/sr at 0° [Alf79] at a ^{3}He energy of 20.0 MeV. A ^{3}He^{++} beam current of 50 pnA (particle nano-Amperes), an array of 3 Bicron-type detectors at each angle, and a detector efficiency of 0.2 (calculated by the Monte-Carlo code NEFF7 [Die82]) were assumed. The neutron count rate is given by:

$$R_n \approx \frac{d\sigma}{d\Omega} \times \frac{\epsilon t I}{M} \times \Delta\Omega \qquad (2.2)$$

and

$$\Delta\Omega \approx n_{\rm det} \times \frac{\pi\,(D/2)^2}{l^2}, \qquad (2.3)$$

where ϵ is the detector efficiency, t is the target thickness in units of mass per area, I is the beam current, M is the target-nucleus mass, $n_{\rm det}$ is the number of detectors at a given angle, D is the detector diameter, and l is the target-detector distance. The count rate estimates are given in Table 2.3.

Table 2.3: Estimated hourly count rates

Target	counts (hr^{-1})
74Ge	309
76Ge	301

If 100 total counts are desired for each 0$^+$ excited state (10% statistical uncertainty) and if each of these has 1% of the total strength, then a run time of about 30 hours is needed per target to measure the strength to the 0$^+$ excited states.

Backgrounds in the neutron ToF spectra originate from natural radioactivity and beam-induced events uncorrelated with the target. The natural background was measured with a Bicron-type detector to be 40 counts/hr after applying pulse shape discrimination (PSD) at a threshold of 0.5 MeVee This rate will be reduced by a factor of at least 100 in this experiment because of the beam-pulsing duty cycle, with $<$ 4-ns-wide pulses every 400 ns. Beam-related neutron background is reduced by lining the beam-limiting apertures before the scattering chamber with lead and making the target ring and beam stop out of lead. Because the Coulomb barrier for α-particles on lead is nearly 27 MeV, backgrounds due to neutrons from (^{3}He,n) reactions in the lead apertures and beam stop should be very small. Beam-related background from γ-rays will be significantly reduced by ToF and PSD techniques. The Bicron-type-detector γ-ray-rejection ratio has been measured at about 3600:1 at a 0.5 MeVee threshold. Thus on average, of every 3600 detected γ-rays, only one (incorrectly) meets the PSD criteria for neutrons.

A development run is planned for the fall to measure the beam-induced neutron and γ-ray backgrounds using a lead beamstop on the 70° beamline.

[Alf79] W. P. Alford *et al.*, Nucl. Phys., **A323**, 339 (1979).

[Blo10] T. Bloxham *et al.*, Phys. Rev. C, **82**, 027308 (2010).

[Die82] G. Dietze and H. Klein, *NRESP4 and NEFF4 - Monte Carlo codes for the calculation of neutron response functions and detection efficiencies for NE 213 scintillation detectors*, Technical Report PTB-ND-22, Physikalisch-Technische Bundesanstalt, Braunschweig, Germany, 1982.

[Tic11] D. R. Ticehurst *et al.*, TUNL Progress Report, **L**, 148 (2011).

[Vog08] P. Vogel, In *Measurements of Neutrino Mass; Lecture notes for course CLXX*, Varenna, Italy, 2008.

2.2 Tritium β Decay

2.2.1 Commissioning Plans for the KATRIN Main Spectrometer

F.M. Fränkle, T.J. Corona, K.J. Wierman J.F. Wilkerson, *TUNL*; S. Görhardt, S. Groh, B. Leiber, J. Reich, N. Wandkowsky, *Karlsruhe Institute of Technology, Karlsruhe, Germany*; S. Bauer, *University of Münster, Münster, Germany*;

A major component of the KATRIN tritium β-decay experiment is the main spectrometer, which needs to have a background rate less than about 0.01 counts per second. In order to characterize and minimize the main spectrometer background, a series of background measurements were designed for the commissioning phase, which will start in early 2013. Preparations for these measurements and efforts at background minimization are described.

A major component of the KATRIN experiment [KAT05] is the main spectrometer, shown in Fig. 2.36. It is 24 m long, 10 m in diameter, and works as a retarding electrostatic spectrometer. Its purpose is the high precision energy analysis of tritium β-decay electrons. It features an energy resolution of $\Delta E = 0.93$ eV at 18.6 keV for the precise energy analysis of β-decay electrons near the tritium endpoint. This resolution is achieved by using magnetic adiabatic collimation combined with an electrostatic filter, or the MAC-E filter technique. The background rate of the main spectrometer needs to be less than about 0.01 cps in order for KATRIN to reach the planned sensitivity of 200 meV/c^2 on the neutrino mass. In order to characterize and minimize the main spectrometer background, a series of background measurements were designed for the project's commissioning phase, which will start in early 2013.

Figure 2.36: (Color online) The KATRIN main spectrometer and the air coil system.

In general, a MAC-E filter consists of two solenoids, which create a strong guiding magnetic field for electrons, as shown in Fig. 2.37. In this configuration, the guidance of the electrons from the source to the detector is adiabatic, and the magnetic moment μ is constant. Hence, the transverse component of the electron's energy is transformed into longitudinal energy as the electrons move toward the minimum magnetic field B_{min}. The energy analysis is done with an electrostatic retarding potential at B_{min}. The retarding potential is created by an electrode system operated on a (variable) scanning potential U_0. Thus a MAC-E filter acts as an integrating high pass filter with an energy resolution ΔE.

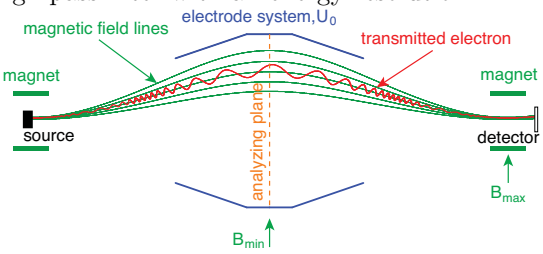

Figure 2.37: (Color online) Schematic of a MAC-E filter with guiding magnetic field lines, source, electrostatic spectrometer and detector.

The background rate of the main spectrometer needs to be less than 0.01 cps to reach the planned KATRIN sensitivity. In principle, a MAC-E filter is able to run background free, due to magnetic shielding. However, there are processes that can generate background electrons, possibly hindering the attainment of the needed measurement sensitivity. These processes are:

- *Penning discharge*: Due to the presence

of strong magnetic and electric fields in a MAC-E filter, Penning traps can be created. If a Penning discharge occurs, it can lead to background rates in excess of 100 cps.

- *Radioactive decays*: Radioactive decays that happen inside the spectrometer volume can produce a large number of secondary electrons, especially if a high-energy electron is magnetically trapped inside the spectrometer [Fra11]. The presence of radon is a particular concern.
- *Magnetic field inhomogeneities*: Inhomogeneities in the magnetic field allow electrons to drift into the volume of the spectrometer.

Different technologies were implemented in the main spectrometer in order to minimize these background effects. Carefully designed and precisely manufactured sets of electrodes are installed in the high-electric-field regions of the spectrometer to avoid Penning traps. A double-layered wire-electrode system was installed, with the wire layers held at an electric potential that is more negative than the spectrometer tank potential, thus rejecting low-energy electrons originating from the tank. Finally, two sets of magnet coils are mounted outside of the spectrometer for fine tuning the magnetic field inside the spectrometer (the LFCS set) and for compensating for the earth's magnetic field (the EMCS set).

The main-spectrometer-commissioning measurements are scheduled to begin early in 2013. In order to characterize the spectrometer background and to optimize the wire-electrode potentials and the air-coil settings, plans for a series of dedicated measurements have been developed:

- *Search for Penning discharges*: An iterative measurement procedure has been defined to check for Penning discharges inside the main spectrometer, while minimizing the risk of damaging sensitive equipment.
- *Optimization of the EMCS*: This measurement will find the optimum settings of the EMCS in order to minimize the spectrometer background.
- *Optimization of the wire electrode potentials and LFCS*: This measurement is aimed at finding the optimum parameters for the wire-electrode screening potentials and the LFCS parameters in order to minimize the spectrometer background.
- *Pressure dependence of the background*: This measurement will study the background behavior of the main spectrometer at different pressures. Assuming that different background processes have characteristic dependences on the pressure, this measurement could be used to discriminate between different background sources, such as radioactive decays, Penning discharges, and cosmic-ray-induced backgrounds.
- *Investigation of electron emission*: This measurement will investigate the electron emission of the spectrometer due to cosmic rays and field emission. In order to reduce field emission, different conditioning strategies for the spectrometer will be tested.
- *Background with an asymmetric magnetic field*: The aim of this measurement is to scan the wall of the main spectrometer for areas of increased rate and to check the integrity of the wire-electrode modules.
- *Background with non-axially symmetric magnetic fields*: The aim of this measurement is to determine the influence of non-axially symmetric field components on the background within the main spectrometer by disturbing the magnetic field in a defined way.
- *Investigation of muon-induced background*: The goal of this measurement is the determination of the expected background rate due to cosmic-ray muons.
- *Investigation of UV-laser-induced background*: The main goal of this measurement is to test the shielding of the wire electrodes and to determine the suppression ratio of the electric and magnetic shielding of the main spectrometer for low energy electrons produced by a UV laser.
- *Investigation of γ-ray-induced background*: The objective of this measurement is to create secondary electrons at the inner surface of the main spectrometer tank by utilizing an external γ-ray source in order to check the magnetic shielding for high energy electrons.

In order to prepare for and interpret the measurements, various simulations will be performed using the simulation code described in Sect. 2.2.3.

[Fra11] F. Fraenkle *et al.*, Astropart. Phys., **35**, 128 (2011).

[KAT05] KATRIN Collaboration, *KATRIN Design Report*, Technical Report FZKA 7090, Forschungszentrum Karlsruhe, 2005.

2.2.2 Field-Induced Background Characterization and Electron Transport Simulation in the KATRIN Focal Plane Detector Region

T.J. Corona, J.F. Wilkerson, *TUNL*

The focal plane detector region of the Karlsruhe Tritium Neutrino experiment contains strongly varying electric and magnetic fields in regions of largely non-axially symmetric components. Software has been developed to precisely simulate these fields, as well as to provide navigation routines through this complicated geometry system. These tools have been successfully applied towards the characterization of field-related phenomena in areas of high vacuum and are currently being implemented by the KATRIN collaboration for the purpose of particle propagation.

The Karlsruhe Tritium Neutrino (KATRIN) experiment is a tritium β-decay measurement designed to measure the neutrino mass by analyzing the tail-end of the tritium decay spectrum. To accomplish this task, the emitted electrons are filtered through an integrating solenoidal retarding electrostatic spectrometer and subsequently detected using a silicon-wafer semiconductor. The region following the spectrometer, where the electron properties are measured, is known as the focal-plane-detector region (see Fig. 2.38). This region has strongly varying electrostatic and magnetostatic fields and has many ports designed for maintaining high vacuum, for electronics feedthroughs, and for calibration systems.

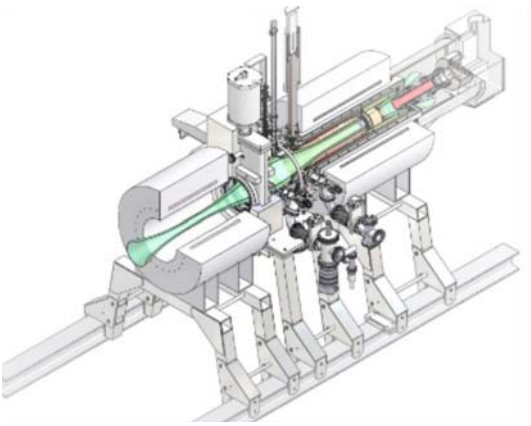

Figure 2.38: (Color online) A CAD representation of KATRIN's focal-plane-detector region.

Prior simulation tools for analyzing the focal-plane-detector region were designed by by F. Glück of Karlsruhe Institute of Technology and made the primary assumption of axial symmetry in order to expedite computation of the electrostatic fields. Recently, we have developed methods for performing field solving and track navigation for a broad set of non-axially symmetric components (see Fig. 2.39). To offset the additional computation time associated with the additional dimension of freedom, these tools have been adapted to take advantage of parallel computing techniques used on both large-scale clusters (such as Killdevil at UNC) and on conventional graphics cards.

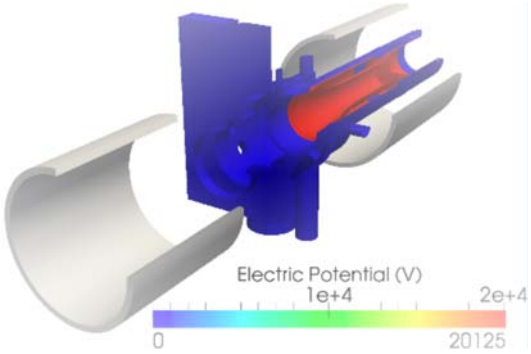

Figure 2.39: (Color online) A model of KATRIN's detector region, comprised of multiple non-axially symmetric components, for use in field simulation and geometry navigation.

We have used these tools to perform a systematic search for Penning traps—potential wells along strong magnetic field lines—within the focal-plane-detector region. Penning traps are an important potential source of background in the KATRIN experiment for several reasons. Dur-

ing Penning discharge, trapped electrons ionize residual gas molecules. If the emitted ions enter the fiducial region of the KATRIN beamline, they can produce an aperiodic background that is difficult to decouple from the true signal. Additionally, arcing due to Penning discharge causes fluctuations in the electrodes' potential, and can damage the experimental apparatus.

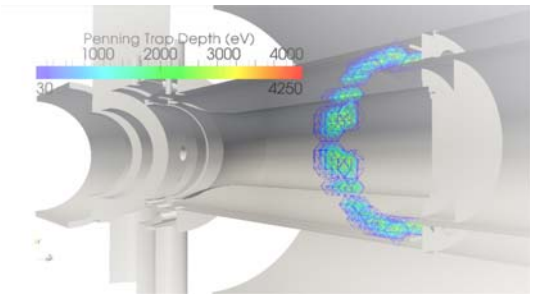

Figure 2.40: (Color online) A computed Penning-trap map of the focal-plane-detector region. Electrode and magnet settings were chosen to reflect production-level conditions.

Figures 2.40 and 2.41 show some of the results of these analyses. In Fig. 2.40, electrode and magnet settings were applied to imitate the optimal settings of the apparatus. Note that, while there is a Penning trap within this configuration, it is physically separated from the focal plane detector housing and is therefore not a potential source of background. In Fig. 2.41, the calibration disk was partially inserted and set to a high negative potential, in order to induce Penning traps within the port housing. These tests have both validated the production-level operation parameters and have verified that the analysis is indeed producing the expected results.

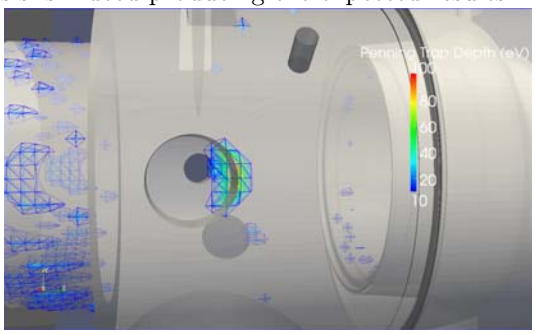

Figure 2.41: (Color online) A computed Penning-trap map of the focal-plane-detector region. Electrode and magnet settings were chosen to induce traps along non-axially symmetric edges (e.g. along the port valves).

Our next goal is to incorporate particle tracking within this model of the focal-plane-detector region. We intend to merge our current software with a package named Kassiopeia, which was developed within the KATRIN collaboration. It computes particle trajectories in electromagnetic fields and simulates the physics processes (such as scattering and electron-silicon interactions) applicable within the KATRIN experiment.

2.2.3 Development of a Large-Scale Electromagnetic Simulation of the KATRIN Main Spectrometer

T.J. Corona, J.F. Wilkerson, *TUNL*

The sensitivity of the Karlsruhe Tritium Neutrino experiment is mainly a function of having a precise understanding of the electrostatic and magnetostatic fields within its largest solenoidal retarding electrostatic spectrometer, known as the "main spectrometer." This spectrometer is the largest of its type and consists of complicated, precisely-defined electrodes that shape the electric potential used to filter electrons. A large-scale simulation of the electrostatic and magnetostatic properties of the main spectrometer is currently underway and will require about 300,000 hours of computation time to complete.

The Karlsruhe Tritium Neutrino (KATRIN) experiment is a large, international tritium-beta-decay experiment designed to make a direct, model-independent measurement of the neutrino mass with a sensitivity of $m_\beta = 0.2$ eV (90% C.L.). This is an order of magnitude lower than the current established limit. This sensitivity is predominantly due to the predicted efficacy of KATRIN's main spectrometer, an integrating solenoidal retarding electrostatic spectrometer with a theoretical filter resolution of < 1 eV. The main spectrometer can be described as a magnetic adiabatic collimation combined with an electrostatic (MAC-E) filter.

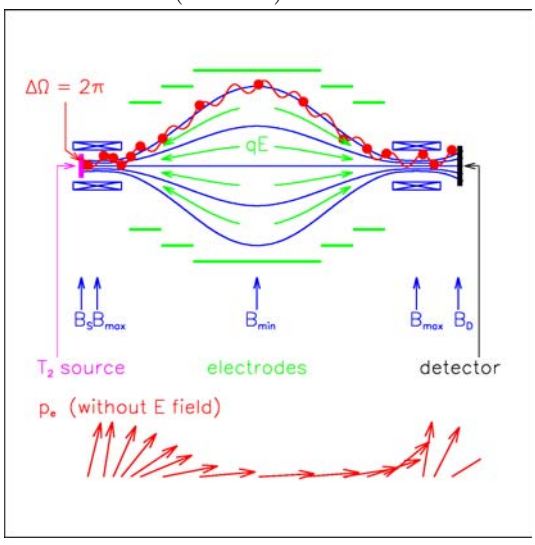

Figure 2.42: (Color online) A diagram of a MAC-E filter. Image taken from [KAT12]

MAC-E filters adiabatically transport electrons from a region of strong magnetic field to a region of weak magnetic field (see Fig. 2.42). Due to the adiabatic invariance of an electron's magnetic moment, this motion effectively rotates an electron's transverse momentum until it is nearly all longitudinal momentum when the particle is at the weakest point in the magnetic field (the center, or "analyzing plane," of the spectrometer). Once the particle reaches the analyzing plane, it encounters an electrostatic potential barrier formed by electrodes within the spectrometer. The resolution of a filter of this type is therefore a function of the relative strengths of the magnetic field at its strongest and weakest points (at the entrance and analyzing plane, respectively), and the electric potential profile at the analyzing plane.

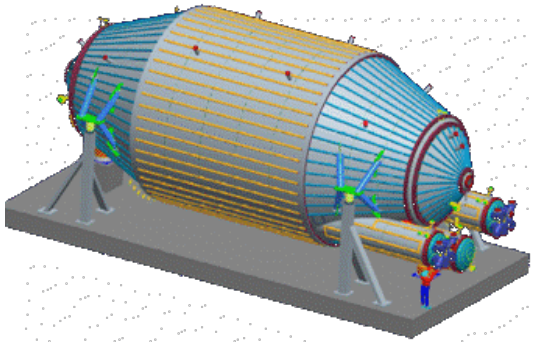

Figure 2.43: (Color online) A rendering of the KATRIN main spectrometer. Image taken from [KAT12]

With a maximum diameter of about 10 m and a length of 23.3 m, the KATRIN main spectrometer is the world's largest MAC-E filter [KAT04]. Along the entire inner surface of the spectrom-

eter, there are approximately 200 comb-shaped wire modules, each housing about 100 wires, providing an inner surface area of roughly 650 m^2. Additionally, there are superconducting magnets at the entrance and exit of the spectrometer, plus many shaping coils and additional current loops to compensate for the earth's magnetic field and to precisely shape the magnetic field throughout the spectrometer.

The size and complicated configuration of the KATRIN main spectrometer provide its ability to precisely define its electrostatic and magnetostatic field configuration but also make an accurate simulation of these fields a daunting task. In order to perform the boundary-element method (BEM) for computing an equivalent-charge-density profile, the inside of the main spectrometer must be discretized into elements that are small enough to allow for the approximation of a constant charge density. However, since the computation of this charge density is proportional to the square of the number of discretized elements, one must strike a balance between accuracy and computational feasibility.

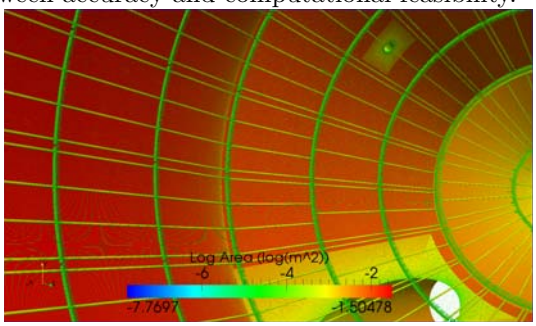

Figure 2.44: (Color online) A simulation of the KATRIN main spectrometer, colored according to discretized element area.

To this end, we are currently constructing a deterministically mesh-able and navigable model of KATRIN's main spectrometer (see Fig. 2.44). The latest model contains about five million discretized elements and is discretized into triangles, rectangles and wires—shapes for which the electric potential and electric field have been analytically determined. We have recently been awarded supercomputing time at the National Energy Research Scientific Computing (NERSC) center to perform this computation. Once the simulation is fully constructed and each component is individually verified (see Fig. 2.45), we hope to run a simulation for about 300,000 hours and obtain the most accurate electromagnetic profile of the main spectrometer to date.

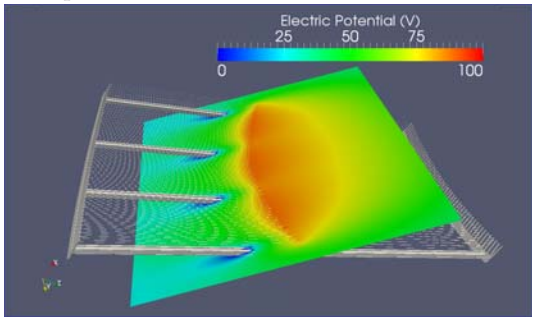

Figure 2.45: (Color online) Verification of one of the wire modules. Dummy potential values are assigned to the wire frame and the inner and outer wire arrays, the charge density profile is computed, and the fields are sampled to ensure consistency of the mesh.

[KAT04] J. Angrik *et al.*, *KATRIN Design Report*, Technical Report 7090, Forschungszentrum Karlsruhe, `http://www-ik.fzk.de/~katrin`, 2004.

[KAT12] The KATRIN collaboration, *The KATRIN homepage*, `http://www.katrin.kit.edu/`, 2012.

2.2.4 Implementation of the KATRIN FPD VETO System

K.J. Wierman, T.J. Corona, F.M. Fränkle, M. Howe, J.F. Wilkerson, *TUNL*; F. Harms, A. Kopmann, M. Steidl, S. Wuestling, *Karlsruhe Institute of Technology, Karlsruhe, Germany*; J. Barrett, J.A. Formaggio, D.L. Furse, N.S. Oblath, *Massachusetts Institute of Technology, Boston, MA*; T.H. Burritt, P.J. Doe, S. Enomoto, G.C. Harper, E.L. Martin, R.G.H. Robertson, T.D. Van Wechel, B.L. Wall, *University of Washington, Seattle, WA*

The KATRIN focal-plane-detector veto system is designed to reduce cosmic-ray backgrounds in the KATRIN experiment. It consists of a passive lead and copper shield and an active scintillator layer read out by wavelength-shifting fibers and multi-pixel photon counters. The system is being utilized by TUNL personnel and their collaborators in Karlsruhe, Germany.

The Karlsruhe Tritium Neutrino (KATRIN) experiment is a model-independent measurement of the kinematic mass of the electron anti-neutrino through the analysis of the spectral shape of the endpoint region of tritium β decay. It uses a next-generation spectrometer coupled to a 148-pixel pin-diode array denoted as the focal-plane detector (FPD) [KAT05].

The desired precision for measuring the neutrino mass is 0.2 eV (90% C.L.). Simulations show that in order to achieve this sensitivity, background events must be suppressed to below 1 mHz. At 49.01° N latitude and 100 m elevation, cosmic-ray-induced events contribute to the overall background rate and require that a cosmic ray veto system be used [Leb10].

The veto system, designed at Massachusetts Institute for Technology (MIT), consists of a passive 3-cm lead and copper shield and an active layer of Bicron-408 plastic scintillator panels. Copper was chosen to line the interior of the lead shield due to its radio-purity and thus its ability to absorb lead X-rays and reduce the shield's intrinsic background. The scintillator panels are formed into a cylinder around the FPD. Figure 2.46 shows the four long panels which form the barrel and the two panels which form the end cap. The panels are covered in reflective Gore ePTFE and Tyvek to reduce light leaks and increase light-collection efficiency. Each of the long panels is read out by six St. Gobain wavelength-shifting (WLS) fibers, while the end caps are each read out by four fibers. The WLS fibers shift the light from 425 nm up to 493 nm, the sensitive region of the detectors [For09].

The light-detection mechanism for the veto system is an array of 32 Hamamatsu multi-pixel photon counters (MPPCs). They consist of a pixelated array of avalanche photo diodes with reverse bias voltage held in the Geiger regime. Simultaneous discharge of the pixels due to photonic excitations allows for signals which indicate the number of photons incident on the detector (see Fig. 2.47).

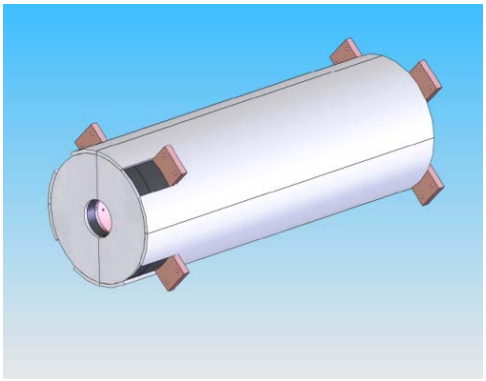

Figure 2.46: Design drawing of the veto system [Ste07].

Electronics were designed at the Karlsruhe Institute of Technology (KIT) for amplification, for the provision of bias voltages for the MPPCs, and for digitization of the output pulses. Data acquisition is performed by custom hardware designed by the Institute of Data Processing (IPE) at KIT. This consists of the IPE DAQ crate with twenty first-level trigger cards. The cards have field-programmable-gate arrays (FPGAs) for the customization of input filtering and processing to cater to the specifications of detector outputs. TUNL personnel worked to identify and implement an FPGA scheme that optimizes detection efficiency. This is essential because MPPC signals have a characteristic width of 50 ns and the

crate has a clock pulse of 20 Mhz, making aliasing between the clock pulse and signals a potential source of efficiency loss.

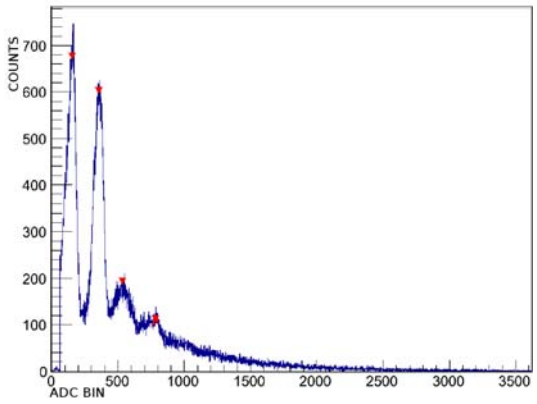

Figure 2.47: Discretized output of the MPPCs. Each peak represents the number of photons impinging on the face of the detector.

The initial veto system was delivered to the University of Washington for detector commissioning. An improved version was implemented and evaluated by TUNL personnel at UNC and delivered to KIT in August 2011. TUNL personnel are currently at KIT to perform further evaluations, train new staff, and integrate the system into the experiment. Plans for improvements in the veto are being made in concert with TUNL staff to produce a more efficient veto system.

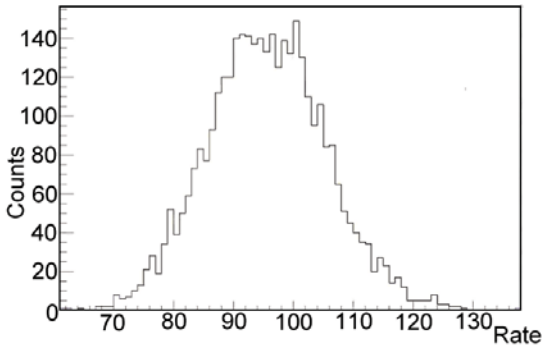

Figure 2.48: Dark Rates for a single MPPC over the course of an hour.

The MPPCs are currently being cooled to -18° C to reduce the system's dark rate (see Fig. 2.48). TUNL personnel worked with MIT and KIT students to perform a protracted study of the rates and spectral stability as a function of time, to determine the long term stability of the system. They have determined that the system is within statistics for summer 2012.

TUNL personnel measured the efficiency of the system by stacking panels in a hodoscope configuration. Coincident-event comparison between panels provided a first-order estimation of panel efficiencies. These were studied as a function of the coincidence windows between fibers in a given panel and between panels (see Fig. 2.49). Because of digitization, the smallest time unit that for providing coincidence between panels is 50 ns. The Mark IV crate FPGAs allow the coincidence time between fibers to be adjusted in these increments and provide a signal indicating that a single panel has fired. This is set by an N-fold coincidence requirement. Additionally, multiple panels firing in coincidence were required to measure an event. This entire parameter space was scanned and analyzed to maximize efficiency and reduce noise due to accidental coincidences. At optimal values, the preliminary system efficiency is at 72.69±0.63%.

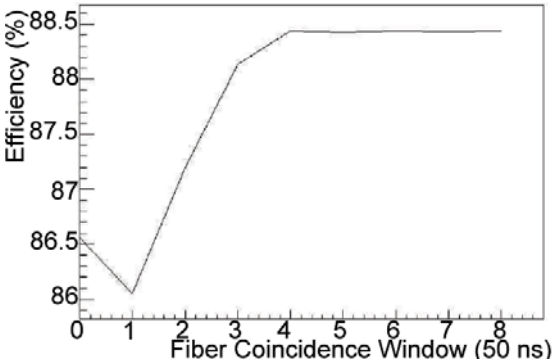

Figure 2.49: Efficiency as a function of coincidence window.

[For09] J. Formaggio, *Test Plans for the KATRIN Active and Passive Shield*, Technical report, Massachusetts Institute of Technology, 2009.

[KAT05] KATRIN Collaboration, *KATRIN Design Report*, Technical Report FZKA 7090, Karlsruhe Institute of Techology, 2005.

[Leb10] M. L. Leber, *Monte Carlo Calculations of the Intrinsic Detector Backgrounds for the Karlsruhe Tritium Neutrino Experiment*, Proquest, Umi Dissertation Publishing, 2010.

[Ste07] M. Steidl *et al.*, *KATRIN Detector Design Document*, Technical report, University of Washington, 2007.

2.3 Dark Matter Search

2.3.1 Optical-Model Analysis for Elastic Scattering of Neutrons from Neon and Argon

S. MacMullin, R. Henning, W. Tornow, C.R. Howell, *TUNL*

Absolute differential cross sections for elastic scattering of neutrons from ^{nat}Ne and ^{nat}Ar were previously measured at the TUNL neutron time-of-flight facility. The data were fit using the spherical optical model. These results will refine Monte Carlo simulations and background estimates for dark-matter experiments.

Several current and next-generation detectors designed to search for weakly-ionizing massive-particle (WIMP) dark matter will use large volumes of noble liquids (neon, argon, xenon). Since neutron-induced nuclear recoils are difficult to distinguish from WIMP events, these experiments rely on Monte Carlo simulations to estimate their neutron background, so it is crucial that neutron-scattering cross sections be well known. The optical model is known to provide an excellent phenomenological description of nucleon-nucleus elastic scattering for nuclei with mass numbers greater than 24 and energies up to 200 MeV [Hod63]. However, global optical model potentials are not reliable for lower mass nuclei where no experimental data exist. This project is designed to measure cross sections relevant to WIMP searches in order to provide a benchmark in regions where the optical model is not well constrained.

Neutron elastic scattering angular distributions were measured at TUNL for ^{nat}Ne at 5.0 and 8.0 MeV and for ^{nat}Ar at 6.0 MeV using the time-of-flight technique. Experimental details are given in Ref. [Mac11]. Those data plus the data from Beach *et al.* [Bea67] at 14.0 MeV were fit with Legendre polynomials, and the total elastic scattering cross sections were determined by integrating the fits. The data were also fit using the spherical optical model. Although global optical-model parameter sets are not generally expected to extend to light nuclei, Dave and Gould [Dav83] were successful in describing measured elastic scattering cross sections for light 1p-shell nuclei from 7 to 15 MeV.

The GENOA code [Per67] was used to determine the optical model parameters that best fit the data. The code searches with up to ten free parameters to define the potential:

$$\begin{aligned} U_{\rm opt}(E_{\rm n},r) = & \\ & - V_{\rm v}(E_{\rm n}) f(r,r_{\rm v},a_{\rm v}) - iW_{\rm v}(E_{\rm n}) f(r,r_{\rm v},a_{\rm v}) \\ & \quad + 4ia_i W_d(E_{\rm n}) \frac{d}{dr} f(r,r_{\rm d},a_{\rm d}) \\ & + V_{\rm s.o.}(E_{\rm n}) \left(\frac{\hbar}{m_\pi c}\right)^2 \frac{\vec{\sigma}\cdot\vec{l}}{r} \frac{d}{dr} f(r,r_{\rm s.o.},a_{\rm s.o.}) \\ & - iW_{\rm s.o.}(E_{\rm n}) \left(\frac{\hbar}{m_\pi c}\right)^2 \frac{\vec{\sigma}\cdot\vec{l}}{r} \frac{d}{dr} f(r,r_{\rm s.o.},a_{\rm s.o.}) \end{aligned} \quad (2.4)$$

where E_n is the laboratory energy and r is the center-of-mass distance between the incident neutron and the target nucleus. The quantities r_i and a_i are the radii and surface diffuseness parameters, respectively. The quantities $V_{\rm v,s.o.}$ and $W_{\rm v,d,s.o.}$ are the real and imaginary components for the volume-central (v), surface-central (d) and spin-orbit (s.o.) potentials. The Woods-Saxon potential, given by

$$f(r,r_j,a_j) = (1 + exp[(r - R_j)/a_j])^{-1}, \quad (2.5)$$

where j = v or d and $R_j = r_j A^{1/3}$, is used to describe the shape of the corresponding part of the optical potential. The GENOA code solves the time-independent Schrödinger equation with numerical fitting based on the generalized least-squares method [Gui00].

Results of the optical-model fits were compared to calculations using existing parameter sets. For the neon data, the optical-model parameters used for comparison were from Dave and Gould [Dav83] and from the Koning-Delaroche global potential [Kon03]. For the argon data, comparisons were made with the ENDF/B-VII.0 parameters and the Koning-Delaroche local potential for ^{40}Ar. Sample

optical-model fits and comparisons to existing datasets are shown in Figs. 2.50 and 2.51.

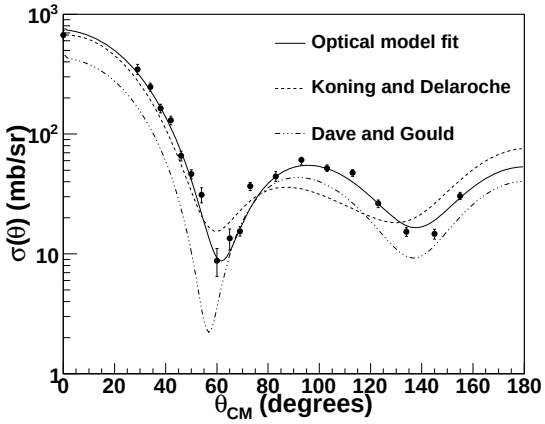

Figure 2.50: The differential elastic scattering cross section of neutrons from ^{nat}Ne at 8.0 MeV.

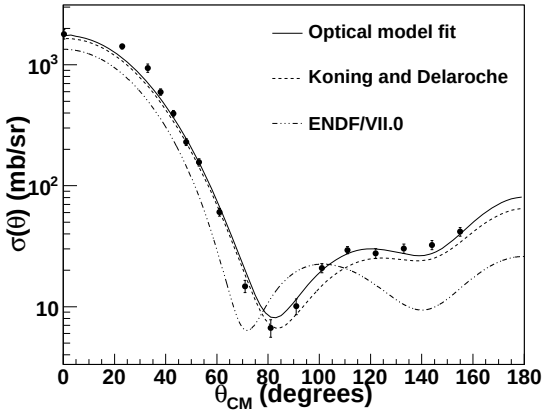

Figure 2.51: The differential elastic scattering cross section of neutrons from ^{nat}Ar at 6.0 MeV.

Using the measured cross sections for neon at 5.0 and 8.0 MeV, a parameter set was determined based on the global optical-model parameters from Koning and Delaroche combined with an extrapolation of the global fits from Dave and Gould. Although the potential well depths are the only energy-dependent terms, in the optical-model potential formulation, good fits to the neon data were not obtained using the radii and surface diffuseness parameters (which should not be energy-dependent) provided by Koning and Delaroche or by Dave and Gould. Therefore, we allowed these parameters to vary in the search. Each parameter was assumed to have a linear energy-dependence. Using this global fit to the data, cross sections were predicted for energies not measured. Although the parameters adequately describe the measured data, we do not expect our global fit to apply outside the $A = 20$ mass range, and it may be limited to the energy range of the current experiment. For these reasons, we restrict our fit to energies between 4 and 9 MeV.

Using the measured cross sections for argon at 6.0 and 14.0 MeV, a parameter set was determined based on the local optical-model parameters of Koning and Delaroche for ^{40}Ar. Only small modifications to the real volume potential ($V_{\rm v}$) and imaginary surface potential ($W_{\rm d}$) were needed to describe the data at 6.0 and 14.0 MeV. Because of the good agreement between the optical-model calculations and the experimental data, we conclude that the available data are consistent with each other and also consistent with the trends of the ^{40}Ar local optical-model potential. Significant disagreement was observed between the experimental data and the cross sections in the ENDF/B-VII.0 database. This disagreement is due to an overestimation of all radius parameters used in the optical-model calculation from which the ENDF/B-VII.0 cross sections were derived.

[Bea67] P. Beach *et al.*, Phys. Rev., **156**, 1201 (1967).

[Dav83] J. Dave and C. Gould, Phys. Rev. C, **28**, 2212 (1983).

[Gui00] F. Guimares and C. Fu, *TNG-GENOA User's Manual*, Technical Report ORNL/TM-2000/252, Oak Ridge National Laboratory, 2000.

[Hod63] P. E. Hodgson, *The Optical Model of Elastic Scattering*, Oxford at the Clarendon Press, 1963.

[Kon03] A. J. Koning and J. P. Delaroche, Nucl. Phys., **A713**, 231 (2003).

[Mac11] S. MacMullin *et al.*, TUNL Progress Report, **L**, 36 (2011).

[Per67] F. Perey, Oak Ridge National Laboratory, unpublished, 1967.

2.3.2 Partial γ-Ray-Production Cross Sections for Neutrons on Argon and Neon

S. MacMullin, R. Henning, *TUNL*; M. Boswell, M. Devlin, S.R. Elliott, N. Fotiades, T. Kawano, B.H. LaRoque, R.O. Nelson, J.M. O'Donnell *Los Alamos National Laboratory, Los Alamos, NM*; V.E. Guiseppe, *University of South Dakota, Vermillion, SD*

Partial γ-ray-production cross sections for $(n, xn\gamma)$ reactions in natural argon and neon were measured for incident neutron energies between 1 and 30 MeV. Measured cross sections were compared to the TALYS and COH$_3$ nuclear reaction codes. These new measurements will help to identify potential backgrounds in neutrinoless double-beta-decay and dark-matter experiments that use argon or neon as a detection medium or for shielding.

Experiments designed to directly detect weakly interacting massive particles (WIMPs) and other rare processes, such as neutrinoless double-beta decay ($0\nu\beta\beta$), are crucial tests for physics beyond the standard model. Neutron-induced backgrounds are a significant concern for these and other experiments that require extremely low levels of radioactive backgrounds. Unmeasured neutron-scattering cross sections are often accounted for incorrectly in Monte Carlo simulations. The measurement of $(n, xn\gamma)$ cross sections for argon and neon, which were previously unavailable, will help to determine neutron-induced backgrounds in dark-matter experiments such as DEAP/CLEAN [Bou04, Bou08] and $0\nu\beta\beta$ experiments such as GERDA, which uses a liquid-argon shield [Sch05].

Data were collected at the Los Alamos Neutron Science Center (LANSCE) Weapons Neutron Research (WNR) facility. A broad-spectrum (roughly 0.2 to 800 MeV) pulsed neutron beam was produced via spallation on a $^{\rm nat}$W target by an 800 MeV proton beam. The neutron beam structure contained 625-μs long "macropulses" driven by two out of every three such macropulses from the linear accelerator, for an average rate of 40 s^{-1}. Each macropulse consisted of "micropulses" spaced every 1.8 μs, each less than 1 ns long. The pulsed beam allowed the incident neutron energy to be determined using the time-of-flight (TOF) technique.

The Germanium Array for Neutron-Induced Excitations (GEANIE) spectrometer comprises twenty HPGe detectors with BGO escape-suppression shields. GEANIE was designed to measure cross sections for $(n, xn\gamma)$ reactions by detecting γ rays from neutron-induced reactions on a target in the center of the array. The neutron flux on target was measured with a $^{235/238}$U fission chamber located about two meters upstream from the center of the array. Data were collected using the MIDAS data-acquisition system. Pulse height and TOF data were collected for each GEANIE event and were written to disk for off-line analysis. A further description of the data analysis techniques is provided in MacMullin et. al. [Mac12].

The gas target cell was a thin-walled aluminum cylinder, 3.81-cm in diameter and 6.35-cm long, with 0.127-mm thick Kapton windows at either end. The gas cell was placed at the center of the GEANIE array, with the neutron beam passing through the Kapton foils. In September and December 2010, data were taken with $^{\rm nat}$Ar. Data with $^{\rm nat}$Ne were taken in February 2012. Part of each data-set was taken with $^{\rm nat}$Fe foils mounted on the ends of the sample cell to provide comparison data with the well-known cross section of ^{56}Fe [Nel05].

Partial γ-ray cross sections for six transitions in ^{40}Ar, two transitions in ^{39}Ar and the first-excited-state transitions in ^{20}Ne and ^{22}Ne were measured from threshold to a neutron energy where the γ-ray yield dropped below the detection sensitivity. The results for the first-excited-state transitions in ^{40}Ar and ^{20}Ne are shown in Figs. 2.52 and 2.53. The results were compared to calculated cross sections obtained from the TALYS and COH$_3$ nuclear reaction codes [Kon05, Kaw10]. The measured ^{40}Ar cross sections are in good agreement with measurements from Mathur and Morgan [Mat65] at $E_n = 3.5$ MeV. Ours are the first available data for neon.

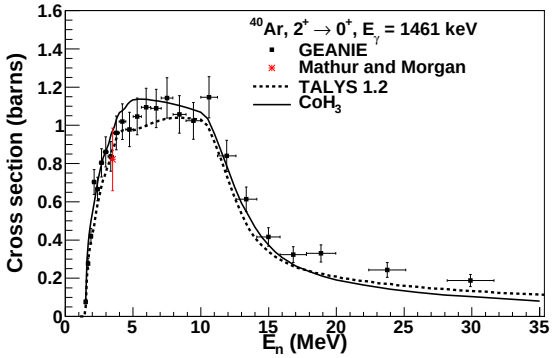

Figure 2.52: (Color online) Partial γ-ray cross-section data for ^{40}Ar$(n,n'\gamma)^{40}$Ar compared to results from the TALYS and COH$_3$ nuclear reaction codes.

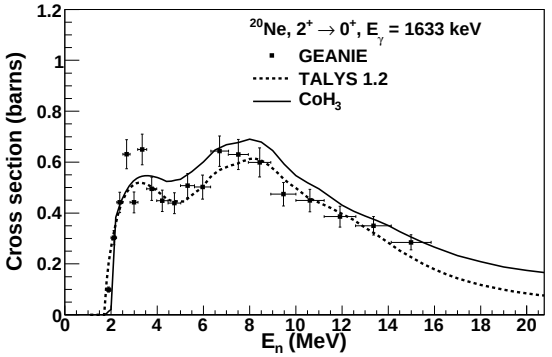

Figure 2.53: Partial γ-ray cross-section data for ^{20}Ne$(n,n'\gamma)^{20}$Ne compared to results from the TALYS and COH$_3$ nuclear reaction codes.

The TALYS reaction code was used to predict the γ-ray production cross sections for the transitions studied in the present work. The TALYS cross sections were calculated using the default settings, which included a direct reaction model using the optical model parameterizations of Koning and Delaroche [Kon03], a pre-equilibrium model, and a compound nucleus reaction model using a Hauser-Feshbach statistical calculation. The TALYS cross sections tend to under-predict the measured cross sections, especially for argon. The difference in the γ-ray production cross section partly comes from the different modeling of the level density [Kaw06], but largely due to the discrete levels included. When some tentative level assignments exist in the evaluated level scheme, it is often assumed that these levels decay to the ground state directly, which results in underestimation of measured γ-ray production cross sections.

These new measured cross sections and upper limits can be included in Monte Carlo simulations combined with the expected neutron spectrum to yield background rates for future low-background experiments using argon or neon as a detector or shield material. The measured cross sections will also aid in the discrimination of neutron backgrounds in WIMP detection experiments which use argon or neon as a detector and where neutrons are the most dangerous source of background.

[Bou04] M. G. Boulay, A. Hime, and J. Lidgard, Arxiv preprint arXiv:0410025, (2004).

[Bou08] M. Boulay *et al.*, J. Phys. Conf. Ser., **136**, 042081 (2008).

[Kaw06] T. Kawano, S. Chiba, and H. Koura, J. Nucl. Sci. Technol., **43**, 1 (2006), Updated parameters based on RIPL-3, (unpublished, 2009).

[Kaw10] T. Kawano *et al.*, J. Nucl. Sci. Technol., **47**, 462 (2010).

[Kon03] A. Koning and J. Delaroche, Nucl. Phys., **A713**, 231 (2003).

[Kon05] A. Koning, S. Hilaire, and M. Duijvestijn, AIP Conf. Proc., **769**, 1154 (2005).

[Mac12] S. MacMullin *et al.*, Phys. Rev. C, **85**, 064614 (2012).

[Mat65] S. Mathur and I. Morgan, Nucl. Phys., **73**, 579 (1965).

[Nel05] R. Nelson *et al.*, AIP Conf. Proc., **769**, 838 (2005).

[Sch05] S. Schönert *et al.*, Nucl. Phys. Proc. Suppl., **145**, 242 (2005).

2.3.3 The ^{40}Ar$(n,p)^{40}$Cl Cross Section between 9 and 15 MeV

C. Bhatia, S.W. Finch, M.E. Gooden, W. Tornow, *TUNL*

For the first time, the ^{40}Ar$(n,p)^{40}$Cl cross section has been measured for neutron energies below 14.5 MeV. This cross section is needed to calculate background events in dark-matter and double-beta decay detectors and to determine the usefulness of liquid argon for detecting core-collapse supernova neutrinos and antineutrinos.

Liquid argon (99.6% ^{40}Ar, 0.3% ^{36}Ar, and 0.06% ^{38}Ar) is a favorite material for detection in dark-matter searches [Dea] and for shielding in double-beta decay searches [Ger]. It is also being considered as the detector medium for a future long-baseline neutrino experiment [Lbn], as well as for core-collapse-supernova neutrino and antineutrino detectors. Although these detectors are (or will be) operated deep underground to provide a low cosmic-ray background environment, they are still exposed to muon-induced spallation neutrons and neutrons from (α,n) reactions. These neutrons can produce background signals that are indistinguishable from the experiment's real signals. Therefore, experimental and theoretical studies are needed to measure and estimate the neutron-induced cross sections on ^{40}Ar in the neutron energy range of interest, which is typically below about 20 MeV. Only then will it be possible to estimate the probability for such background events, assuming that the neutron flux at the experiment's location is known.

Here we present the first comprehensive experimental study of the ^{40}Ar$(n,p)^{40}$Cl cross section ($Q = -6.7$ MeV) between 9 and 15 MeV. The only three existing data points for this reaction [Gra65, Hus68, Ran69] are at around 14.7 MeV, and they differ by a factor of almost two.

To measure the production of ^{40}Cl, which has a half life of 1.35 minutes, we used the activation method. The ^{2}H$(d,n)^{3}$He reaction initiated with pulsed deuteron beams was used to produce pulsed and quasi-monoenergetic neutron beams. Typical deuteron beam currents on target were 1.1 μA. The repetition rate was 2 MHz, with an overall time resolution of 2 ns. A 3-cm-long deuterium gas cell was filled with 6 atm of high-purity deuterium gas. Due to the high, 6.9 MeV threshold of the ^{40}Ar$(n,p)^{40}$Cl reaction, breakup neutrons from the source do not have enough energy to contribute to the production of ^{40}Cl.

High-purity natural argon gas was contained in a high-pressure stainless steel sphere of 20 mm inner diameter and 0.5 mm wall thickness [Rup09], pressurized to about 210 atm. The exact mass of argon (1.585 g) was determined by weighing the cell before and after filling. The center of the sphere was positioned 2.9 cm from the end of the deuterium gas cell. The neutron flux was monitored using a 1.5 in. $\times$ 1.5 in. BC-501A neutron detector of known absolute efficiency, placed at zero degrees relative to the incident deuteron beam and at a distance of 293.5 cm from the end of the deuterium gas cell. Pulse-shape discrimination was applied to reject γ-ray events. The neutron time-of-flight technique allowed for discrimination against breakup neutrons.

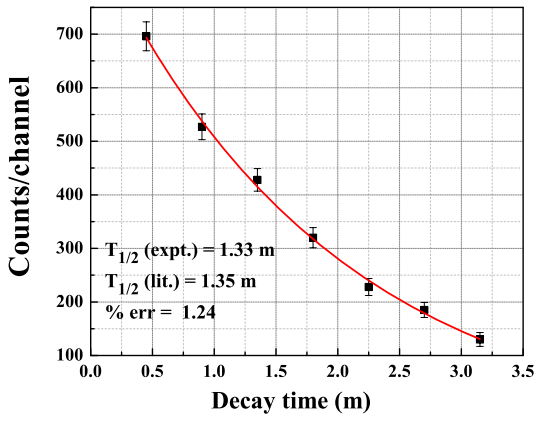

Figure 2.54: (Color online) Measured decay half life of the ^{40}Ar$(n,p)^{40}$Cl reaction. The points show the data, and curve shows the exponential decay fit.

The argon sphere was irradiated for 5.0 min and then, within 10 s, moved to a shielded 60%

HPGe detector to record the yield of the 1461 keV γ rays originating from the β decay of ^{40}Cl to the first excited state of ^{40}Ar.

Calibrated ^{60}Co and ^{133}Ba radioactive sources provided the absolute detection efficiency. The GENIE data-acquisition system was used. Dead time corrections were negligible. As can be seen from Fig. 2.54, we typically followed the decay for about three minutes. Background measurements with an identical, but empty stainless steel cell, also irradiated for 5.0 minutes with neutrons, showed that the 1461 keV yield from the decay of the ^{40}K naturally present in HPGe detector setups was completely negligible compared to the induced ^{40}Ar activity.

A Monte-Carlo code was written to obtain the neutron yield at the position of the argon gas from the yield recorded in the neutron monitor detector. Here, the differential reaction cross section of the ^{2}H$(d,n)^{3}$He reaction and attenuation in the materials between the location of neutron production and points in the neutron detector and/or the argon cell were taken into account. This simulation also provided the mean neutron energy and its spread. Using the neutron yield and the known argon mass, finite-geometry cross-section values were obtained. Finally, these values were deconvoluted to account for the energy dependence and provide the point-geometry cross-section values for the ^{40}Ar$(n,p)^{40}$Cl reaction. These cross sections are shown in Fig. 2.55.

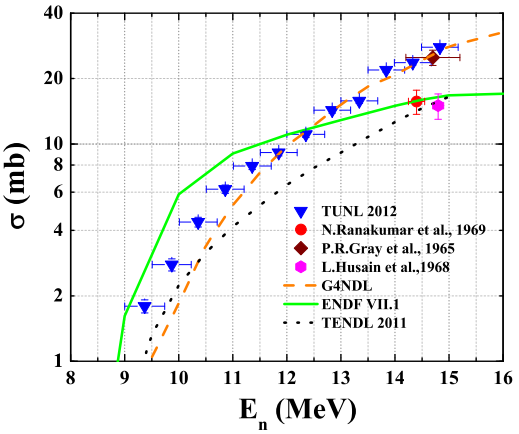

Figure 2.55: (Color online) Measured cross sections for the ^{40}Ar$(n,p)^{40}$Cl reaction.

Clearly, our data support the previous value of [Gra65]. They are in fair agreement with the ENDF-VII.1 evaluation (solid curve) up to about 12.5 MeV. Above this energy, our data follow the trend of the Geant4 library G4NDL3.13 [Gea] (dashed curve), which is based on the ENDF-VI evaluation. Finally, the dotted curve labeled TENDL is the result obtained with the TALYS code [Kon05], which underestimates the data.

Our data for the ^{40}Ar$(n,p)^{40}$Cl cross section will also guide theoretical calculations of this important reaction at higher energies. Our data and the associated calculations are important for estimating potential background effects in the neutrinoless double-beta decay search experiment GERDA [Ger], which uses liquid argon as the coolant and shielding for their enriched (in ^{76}Ge) HPGe detectors. Here, the intensity of the 1461 keV transition could be used to estimate the combined intensity of transitions in ^{40}Cl with γ-ray energies above 2039 keV, the Q-value of the neutrinoless double-beta decay. These γ rays can potentially Compton scatter into the HPGe detectors, producing signals in the energy region of interest. Our data might also be important for the dark-matter-search detector DEEP/CLEAN [Dea], which uses liquid argon as the detection medium. From the number of detected 1461 keV events inside the fiducial volume, the neutron flux can be estimated. From this, the number of fake dark-matter events (neutron-produced recoil nuclei) can be estimated. Finally, our data are expected to guide theoretical calculations to obtain more accurate information on the interaction cross section of antineutrinos with argon. This cross section is important in the development a future large, argon-based neutrino detector.

[Dea] `http://deapclean.org/`.

[Gea] `http://www.geant4.org/geant4/support/`.

[Ger] `http://www.mpi-hd.mpg.de/gerda`.

[Gra65] P. R. Gray *et al.*, Nucl. Phys., **62**, 172 (1965).

[Hus68] L. Husain and P. Kuroda, J. Inorg. Nucl. Chem., **30**, 355 (1968).

[Kon05] A. J. Koning, S. Hilaire, and M. C. Duijvestjin, AIP Conf. Proc., **769**, 1154 (2005).

[Lbn] `http://lbne.fnal.gov/`.

[Ran69] N. Ranakumar *et al.*, Nucl. Phys., **A128**, 333 (1969).

[Rup09] G. Rupp *et al.*, Nucl. Instrum. Methods A, **608**, 152 (2009).

Nuclear Astrophysics

Chapter 3

- **Nucleosynthesis in Hydrostatic and Explosive Environments**
- **^{26}Al in the Interstellar Medium**
- **Thermonuclear Reaction Rates**

3.1 Nucleosynthesis in Hydrostatic and Explosive Environments

3.1.1 New Thermonuclear Reaction Rates for ^{18}O(p,γ)^{19}F

M.Q. Buckner, C. Iliadis, J.M. Cesaratto, C. Howard, T.B. Clegg, A.E. Champagne, S. Daigle, *TUNL*

A new upper limit on the resonance strength of the ^{18}O(p,γ)^{19}F, $E_{\rm R}^{\rm lab}$ = 95 keV resonance was measured at TUNL's Laboratory for Experimental Nuclear Astrophysics. An improved upper limit was also calculated for the astrophysical S-factor at low bombarding energies, and a revised set of reaction rates was determined. From the new reaction rates, it was found that the (p,γ) reaction is not a major contributor to the depletion of ^{18}O at the low stellar-plasma temperatures relevant to "cool-bottom-processing" nucleosynthesis.

3.1.1.1 Introduction

A search for the unobserved 95 keV resonance in the ^{18}O(p,γ)^{19}F reaction was performed at the Laboratory for Experimental Nuclear Astrophysics. Because ^{18}O(p,γ)^{19}F is a process that destroys ^{18}O, we hypothesized that it might contribute to the depletion of ^{18}O observed in low-mass asymptotic giant branch stars and certain presolar oxide grains [Nit08]. This depletion has been attributed to "cool bottom processing" (CBP), an extra-mixing process that occurs by some unknown driving mechanism [Was95]. We were also motivated by evidence that the theoretical stellar plasma temperature regime of this extra-mixing process [Nol03] is in close proximity to the ^{18}O(p,γ)^{19}F, $E_{\rm R}^{\rm lab}$ = 95 keV Gamow peak. The studies reported in Refs. [Wie80, Vog90] were unable to measure the 95 keV resonance directly, and resonance strength upper limits of $\omega\gamma \leq 5.0\times10^{-8}$ eV and $\omega\gamma \leq 4.0\times10^{-8}$ eV were established, respectively.

3.1.1.2 Results

After analyzing 80 C of on-resonance data collected at $E_p^{\rm lab} = 105$ keV with an average proton beam current of 754 μA, we concluded that we had not observed the resonance, but we could constrain the upper limit. To calculate the new upper limit, a relative-resonance-strength calculation was performed by constructing the ratio between the resonance strength of the well known $E_{\rm R}^{\rm lab} = 151$ keV resonance [Bec95] and the unobserved resonance. An analysis Monte Carlo code was written that generated a probability-density function (pdf) for every value that was entered into the relative-resonance-strength calculation. These pdfs where then randomly populated, and the relative-resonance-strength equation was solved to fill a new resonance-strength-upper-limit pdf. This probability-density function was then integrated to the 90%, 95% and 99% confidence levels. Our calculations yielded a new upper limit on the $E_{\rm R}^{\rm lab} = 95$ keV resonance strength of $\omega\gamma \leq 5.4\times10^{-9}$ eV for a rectangular coincidence gate of 4.0MeV $\leq E_\gamma^{\rm NaI(Tl)} \leq$ 10.0 MeV. Our new upper limit is a factor of 8 lower than the previous value [Vog90] .

No direct capture transitions were observed in the accumulated singles or coincidence spectra at $E_{\rm p}^{\rm lab} = 105$ keV. However, an upper limit on the total direct-capture cross section was obtained by assuming a constant S-factor over the target thickness and by integrating numerically with the Monte Carlo analysis code to extract $\sigma(E)$ and $\mathcal{S}(E)$. This set of calculations was performed for the same $\gamma\gamma$-coincidence gate used in the relative-resonance-strength upper-limit calculation. The upper limit we obtained for the astrophysical S-factor is $\mathcal{S}_{\rm total}^{\rm DC} \leq 4.5$ keV b (90% CL), corresponding to a direct-capture-cross-section upper limit of $\sigma_{\rm total}^{\rm DC} \leq 1.0$ pb (90% CL).

Figure 3.1 compares our new reaction rate with the ^{18}O(p,γ)^{19}F reaction rate published in Ref. [Ili10]. The solid lines are the ratios between the present (p,γ) high and low reaction rates and the recommended (p,γ) reaction rate from Ref. [Ili10]. The dotted lines are the same ratios calculated from the high and low rates presented in Ref. [Ili10]. The dashed line at 44.7 MK

represents the highest minimum threshold on CBP stellar plasma temperatures according to Ref. [Nol03]. A second dashed line at 5.5 GK represents the matching temperature calculated from the effective thermonuclear energy range [New08]. Reaction rates corresponding to temperatures beyond this threshold were matched to the Hauser-Feshbach rates [Gor08, Gor09] available through Ref. [Bru11].

Further constraint on the $E_{\rm R}^{\rm lab} = 95$ keV resonance strength has not increased the reaction rates at the CBP stellar plasma temperature threshold. In fact, as Fig. 3.1 shows, the ^{18}O$(p,\gamma)^{19}$F reaction rate calculated from our new upper limit is lower than the recommended rate at CBP temperatures. This further reduces the likelihood that the ^{18}O$(p,\gamma)^{19}$F reaction is a significant contributor to the depletion of ^{18}O seen in stellar atmospheres and presolar grain samples. Based on our calculations, the reaction rate contribution from the $E_{\rm R}^{\rm lab} = 95$ keV resonance is $< 3\%$ in the temperature region relevant to cool bottom processing and can be considered negligible.

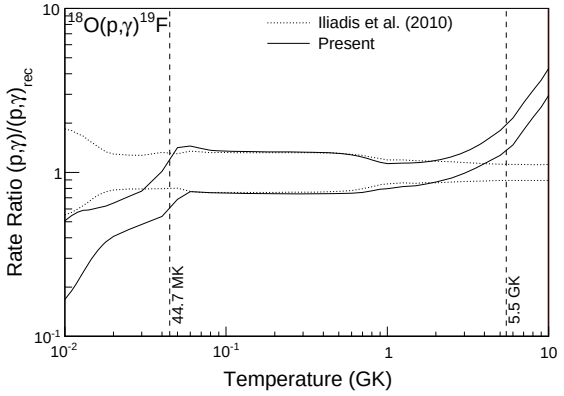

Figure 3.1: The ratio between the (p,γ) reaction rates from the current study and the recommended rates (solid line) are shown. The ratio between the 2010 rates [Ili10] and the recommended rates are shown as dotted lines.

3.1.1.3 Conclusion

A refined upper limit on the ^{18}O$(p,\gamma)^{19}$F astrophysical S-factor was determined at low bombarding energies. Our new upper limit, $\mathcal{S}_{\rm total}^{\rm DC} \leq 4.5$ keV b (90% CL), improves upon the previous value [Wie80] by a factor of 3 at $E_{\rm p}^{\rm lab} = 105$ keV. We were also able to further constrain the upper limit on the strength of the ^{18}O$(p,\gamma)^{19}$F resonance at $E_{\rm R}^{\rm lab} = 95$ keV to $\omega\gamma \leq 5.4\times10^{-9}$ eV—a factor of 8 improvement. Based on our calculations, it is clear that at $E_{\rm R}^{\rm lab} = 95$ keV, the (p,γ) reaction does not contribute significantly to the reaction rate. Therefore, we were able to conclude that ^{18}O$(p,\gamma)^{19}$F is not a major source of ^{18}O depletion during cool bottom processing.

3.1.1.4 Acknowledgments

Additional support for this work was provided for M. Q. Buckner by the National Nuclear Security Administration through a Stewardship Science Graduate Fellowship under Department of Energy grant no. DE-FC52-08NA28752.

[Bec95] H. W. Becker *et al.*, Z. Phys. A, **351**, 453 (1995).

[Bru11] *The Brussels Nuclear Library for Astrophysics Applications*, Technical report, Institute for Astronomy and Astrophysics, Free University of Brussels, 2011, http://www.astro.ulb.ac.be/bruslib.

[Gor08] S. Goriely, S. Hilaire, and A. J. Koning, Astron. Astrophys., **487**, 767 (2008).

[Gor09] S. Goriely *et al.*, Phys. Rev. C, **79**, 024612 (2009).

[Ili10] C. Iliadis *et al.*, Nucl. Phys., **A841**, 323 (2010).

[New08] J. R. Newton, R. Longland, and C. Iliadis, Phys. Rev. C, **78**, 025805 (2008).

[Nit08] L. R. Nittler *et al.*, Astrophys. J., **682**, 1450 (2008).

[Nol03] K. M. Nollett, M. Busso, and G. J. Wasserburg, Astrophys. J., **582**, 1036 (2003).

[Vog90] R. B. Vogelaar *et al.*, Phys. Rev. C, **42**, 753 (1990).

[Was95] G. J. Wasserburg, A. I. Boothroyd, and I.-J. Sackmann, Astrophys. J. Lett., **447**, L37 (1995).

[Wie80] M. Wiescher *et al.*, Nucl. Phys., **A349**, 165 (1980).

3.1.2 Nuclear Thermometers for Classical Novae

L.N. Downen, C. Iliadis, *TUNL*

The effects of thermonuclear reaction-rate variations on classical-novae nucleosynthesis were investigated with an emphasis on elemental and isotopic abundance ratios. Time-temperature-density profiles modeling each nova burning zone were obtained from hydrodynamic calculations. These profiles were used with strategic reaction-rate variations to determine the sensitivity of nucleosynthesis to reaction-rate uncertainties. The goal is to guide future measurements by determining the most sensitive reaction rates.

Classical novae are a type of stellar explosion that occurs in binary systems consisting of a white dwarf and a close companion star [Bod08]. As hydrogen-rich material from the companion star accretes onto the surface of the white dwarf, the accreted material is heated and compressed until a thermonuclear runaway takes place, ejecting material into the interstellar medium. Some of this material can be observed by spectroscopic studies as elemental abundances while other material can be measured as isotopic ratios in presolar grains that have been incorporated into primitive meteorites. Previous research [Dow11] on the importance of elemental ratios has been expanded [Dow], and an exploration of trends in isotopic ratios has begun.

This research utilizes a novel post-processing network to simulate nova nucleosynthesis [Dow11]. This post-processing approach allows for simulations to be completed in significantly less time than hydrodynamic simulations but does so by simplifying the explosion process and ignoring effects such as convection. To better model nova nucleosynthesis, our network has been modified to allow it to occur in all burning zones of the nova and to estimate the convection between these zones.

Roughly 10,000 network calculations have been completed for this work. Each simulation relies on one of four new hydrodynamic profiles, which provide the time, temperature, and density information for each burning zone. These profiles represent ONe classical novae involving 1.15, 1.25, 1.30, and 1.35 $M_\odot$ white dwarfs and span a peak temperature range of 0.228 to 0.313 GK. The recommended reaction rates in this range were supplied by STARLIB, a new reaction rate library derived from a recent evaluation of experimental Monte-Carlo reaction rates [Ili11, Lon10]. The STARLIB recommended rates for 214 reactions were independently varied within their uncertainties and examined for their impact on elemental ratios of interest such as N/O, N/Al, O/S, S/Al, O/Na, Na/Al, O/P, and P/Al. The impact of select reactions on the nucleosynthesis of these ratios is quantified in Table 3.1. The last column in the table gives the factor of uncertainty in the final elemental abundance (mass fraction) ratio caused by varying the rate of the specified reaction within its current uncertainty.

Table 3.1: Uncertainty in Predicted Elemental Abundance Ratios in Neon Novae

Ratio	Reaction	Uncertainty
N/O	^{16}O(p,γ)^{17}F	1.16
N/Al	^{20}Ne(p,γ)^{21}Na	1.29
O/S	^{30}P(p,γ)^{31}S	3.36
S/Al	^{30}P(p,γ)^{31}S	4.62
O/Na	^{16}O(p,γ)^{17}F	1.16
Na/Al	^{23}Na(p,γ)^{24}Mg	1.19
O/P	^{30}P(p,γ)^{31}S	6.44
P/Al	^{30}P(p,γ)^{31}S	6.53

Because of the improvements made to the post-processing network, these results can be directly compared to observational data. Figure 3.2 shows a three-element plot used to compare elemental ratios predicted by post-processing calculations to those from classical nova observations. The thick, solid black line corresponds to the elemental ratios predicted by post-processing calculations using the recommended reaction rates. The thinner lines denote the range of uncertainty in these ratios due to reaction rate uncertainties, such as those in Table 3.1. The data points give the elemental ratios observed in several neon novae.

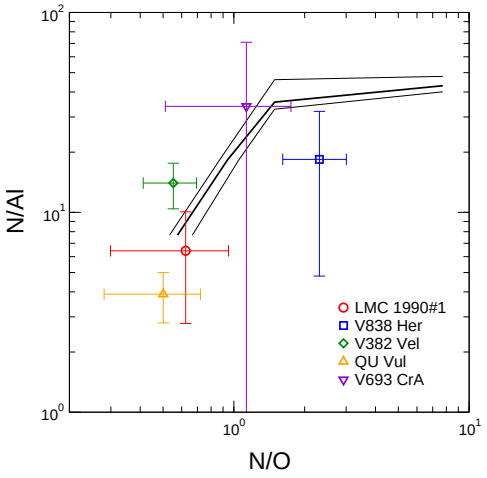

Figure 3.2: (Color online) Three-element plot used to compare elemental ratios predicted by post-processing calculations to those from classical nova observations.

The elemental ratio work presented has been submitted for publication [Dow]. In addition, a full sensitivity study of select isotopic ratios, similar to the elemental ratio study described here, has been completed. Currently these results are being compared to presolar grain observations in order to provide motivation for further laboratory studies of crucial but uncertain nuclear reactions.

[Bod08] M. Bode and A. Evans, *Classical Novae*, Cambridge University Press, 2008.

[Dow] L. N. Downen *et al.*, submitted to Astro. J.

[Dow11] L. N. Downen, C. Iliadis, and A. E. Champagne, TUNL Progress Report, **L**, 58 (2011).

[Ili11] C. Iliadis *et al.*, Astro. J. Suppl. Ser., **193**, 16 (2011).

[Lon10] R. Longland *et al.*, Nucl. Phys., **A841**, 1 (2010).

3.2 ^{26}Al in the Interstellar Medium

3.2.1 Measuring Radioisotopes in the Farmville Meteorite Using $\gamma\gamma$-Coincidence Spectromety

C. Howard, C. Iliadis, *TUNL*; M. Ferm, *Keene State College, Keene, NH*

The LENA γ-ray coincidence spectrometer has been used to measure low levels of radioisotopes in the Farmville meteorite. The data have been measured, and simulations are underway to calculate efficiencies so that the activity can be determined.

Most meteorites are fragments of larger meteoroids that formed at about the same time as our solar system. Because of this, important information about the origin and early history of our solar system can be learned by studying meteoroid fragments that fall to earth as meteorites.

As the meteoroids travel through space they are bombard by cosmic rays that come either from the sun or from galactic sources. These cosmic rays can cause nuclear reactions in the rock, and some of the resulting isotopes are sufficiently long-lived that we can measure their radioactivity when they fall to earth. Knowing when the meteorite fell is a necessary piece of information, as the earth's atmosphere acts as a shield against the cosmic rays, and the activity of the isotope, which could be assumed to be in equilibrium in space, now starts to decay.

Figure 3.3: Farmville meteorite fragment loaned to LENA. It is classified as an H4 chondrite.

In the summer of 2011, the North Carolina Museum of Natural Sciences loaned us the fragment of the Farmville meteorite shown in Fig. 3.3. This meteorite is classified as an ordinary H4 chondrite and has dimensions of approximately $8 \times 9 \times 5$ cm. It has a mass of 0.569 kg, a volume of 152.5 cm^3, and a density of 3.73 g/cm^3. It was observed falling to earth on December 4, 1934.

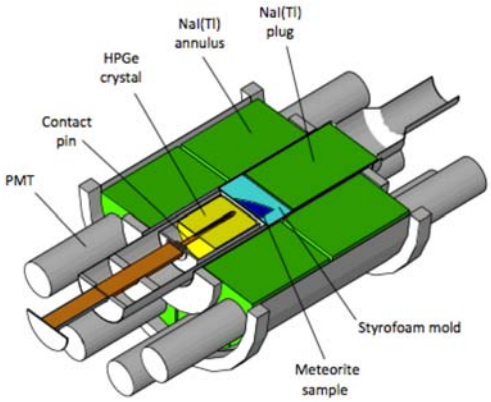

Figure 3.4: (Color online) The coincidence spectrometer used at LENA.

Examples of radioisotopes that can be found in meteorites are ^{26}Al and ^{44}Ti. These isotopes, like many that are of interest to nuclear astrophysics, emit multiple γ-rays simultaneously. In this case, the isotopes are positron emitters, where the positron is in coincidence with a characteristic γ-ray. The positron immediately annihilates creating two 511 keV γ rays.

The Laboratory of Experimental Nuclear Astrophysics (LENA) is designed to measure radioisotopes that decay in a multi-γ-ray decay. This is done by completely surrounding the sample with γ-ray detectors that are segmented to allow detection of individual γ-rays (no summing). This detector has been described in detail in Refs. [Row02, Lon06]. The GEANT4 simulation package [Ago03, All06] has been used to model this detection system, and the details are presented in Ref. [Car10]. Figure 3.4 shows the geometry of the detection system.

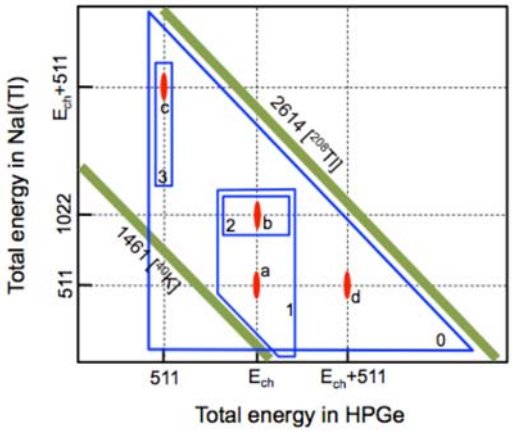

Figure 3.5: (Color online) A simplified version of the analysis energy gating.

The meteorite fragment was placed in the detection system as shown in Fig. 3.4, and data were collected for 12 days of live time. To analyze the data, we a created two-dimensional histogram, with the total energy deposited in all of the NaI(Tl) crystals on the y-axis and all of the energy deposited in the HPGe crystal on the x-axis. We then could see features of the characteristic γ-rays ($E_\gamma = 1157$ keV for ^{44}Ti, $E_\gamma = 1809$ keV for ^{26}Al) and the 511 keV annihilation photons.

Figure 3.5 shows a simplified two-dimensional spectrum, with the signal γ-rays, as well as common γ-rays due to background sources (^{208}Tl and ^{40}K) identified. The labels indicate (a) the characteristic γ-ray at $E_{\rm ch}$ detected in the HPGe and a single 511 keV photon deposited in the NaI(Tl), (b) $E_{\rm ch}$ in the HPGe and both 511 photons in the NaI(Tl), (c) a 511 keV photon in the HPGe and $E_{\rm ch}$ plus a 511 keV photon in the NaI(Tl), and (d) $E_{\rm ch}$ plus a 511 keV photons in the HPGe and a 511 keV photon in the NaI(Tl).

We can use an energy gating scheme to require the peak in the two-dimensional histogram to be located in specific regions. This allows us to select events due only to our signal and greatly reduces our sensitivity to room backgrounds. Region (1) has a wide gate around the $E_{\rm ch}$ in the HPGe and one or both 511 keV photons in the NaI(Tl). We further restrict this in region (2), where we detected $E_{\rm ch}$ in the HPGe and both 511 keV photons in the NaI(Tl). The gate for region (3) selects events with a single 511 keV photon in the HPGe and $E_{\rm ch}$ plus a 511 keV photons in the NaI(Tl).

The efficiency of each of these gates can be determined by using calibration sources and simulations, and this work is nearly complete. We can then determine the measured activity of various radioisotopes in the Farmville meteorite.

[Ago03] S. Agostinelli *et al.*, Nucl. Instrum. Methods A, **506**, 250 (2003).

[All06] J. Allison *et al.*, IEEE Trans. Nucl. Sci., **53**, 270 (2006).

[Car10] S. Carson *et al.*, Nucl. Instrum. Methods A, **618**, 190 (2010).

[Lon06] R. Longland *et al.*, Nucl. Instrum. Methods A, **566**, 452 (2006).

[Row02] C. Rowland *et al.*, Nucl. Instrum. Methods A, **480**, 610 (2002).

3.3 Thermonuclear Reaction Rates

3.3.1 STARLIB: A Next-Generation Reaction-Rate Library for Nuclear Astrophysics

A.L. Sallaska, C. Iliadis *TUNL*

STARLIB is a new stellar reaction-rate library that includes not only rate uncertainties but also the approximate rate probability density functions for a 60 temperature grid. Its structure is based on our Monte-Carlo calculated reaction rates, several of which have been updated over the past year. The library itself has undergone an overhaul of its theoretical rates and input parameters. The website is currently in a completed form and is ready for release upon submission of the library's corresponding publication.

The STARLIB library and its website have both undergone drastic transformations over the past year.

First we consider the library itself. Although the structure of STARLIB emerges naturally from our Monte-Carlo simulation of experimental reaction rates [Lon10, Ili10b, Ili10c, Ili10d], a substantial fraction of the rates is from theoretical calculations. In the previous formulations of STARLIB [Ili10a, Sal11], the Hauser-Feshbach-model code NON-SMOKER, utilized by Rauscher and Thielemann [Rau00], provided STARLIB with its theoretical rates. In addition, laboratory rates must be corrected for stellar conditions by stellar enhancement factors, and calculation of reverse rates includes theoretical partition functions. Reference [Rau00] supplied us with tables of these values as well.

During tests of the library in nucleosynthesis calculations, it became apparent that at least one reaction calculated from theory, ^{18}Ne$(p,n)^{18}$Na, had an incorrect Q-value. Although inspection of the library did not indicate that other Q-values were also incorrect, we decided to replace rates from the NON-SMOKER code with ones calculated from another Hauser-Feshbach code, TALYS [Gor08]. A colleague, Stephane Goriley, not only provided the updated rates in the three-column format of STARLIB but also included many more rates than were available from the previous code. All stellar enhancement factors and partition functions have also been replaced with values from TALYS. In addition to the more robust, modern calculations, our collaborator can update these rates in real time; reformulating the library with new rates takes mere minutes.

In writing the publication to introduce STARLIB to worldwide collaborators, we have sought out new ways to display results from our Monte-Carlo reaction-rate studies. Our previous publication [Ili10b] reports not only the recommended reaction rate but also low and high rates. These values are determined from the 50th, 16th, and 84th quantiles, respectively, of the cumulative rate probability density distribution. However, it seems to be a common misinterpretation of our colleagues to view the low and high rate values as sharp cutoffs. To emphasize that this is not the case, we illustrate the three-dimensional probability density function of a sample reaction rate in Fig. 3.6.

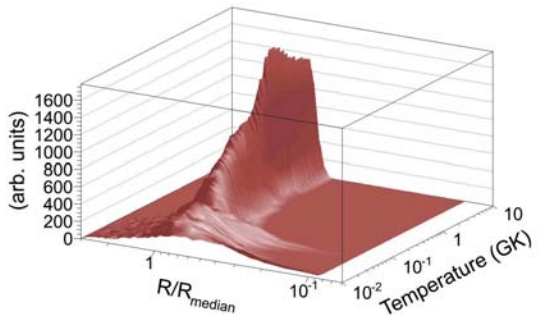

Figure 3.6: (Color online) Rate probability density function, R, for each temperature in our grid, normalized to the median (recommended) rate, $R_{\rm median}$.

A steeper gradient in this figure indicates smaller uncertainties at that specific temperature, and the peak height should occur near a value of $R/R_{\rm median} = 1$. Although we have chosen to associate our "low" and "high" rates with the 16th and 84th quantiles (for a spread of 68%), this choice is rather arbitrary and any number of other quantiles were possible options.

Second, we have completed and upgraded the

STARLIB website (starlib.physics.unc.edu, password protected until its launch). The facade of the site was reimagined with the help of an independent graphic designer. As reported in last year's TUNL report [Sal11], the entire library may be accessed from the web, either to download it or simply to view an individual reaction rate. Previously a security problem arose that concerned uploading a list of nuclei in order to download a subset of the library. This has been circumvented by the use of text boxes, where one may simply copy and paste a list of nuclei to be submitted to our servers. In addition, because of the overhaul of the library, we have added the ability to select which library version is desired. This will be of use in the future, when we upgrade the library while keeping archived versions available for comparison.

Colleagues have also expressed interest in downloading the library with a user-defined temperature grid. This ability has been coded into the website for downloading either the entire library or a subset. However, this feature is not currently available publicly or linked anywhere on the site, because we are still testing our interpolation scheme. A logarithmic interpolation has been chosen as the most accurate to avoid wild variations sometimes associated with spline interpolations. Still, some rates vary by many orders of magnitude, and interpolation over a large range can be problematic. We have attempted to analyze this systematically by removing every other grid point in STARLIB and using our scheme to interpolate the missing points. In comparing what the interpolation routine yields to the original points in STARLIB, we can test the accuracy of the interpolation scheme. Although most interpolated points fall within about 30% of the original points, a non-negligible number fall outside this range due to interpolating over greater than four orders of magnitude. This is, however, a worst-case scenario, because, in practice, twice the number of points can be used as interpolation anchors than in the test. Still, caution should always be exercised when implementing a user-defined grid for our case.

The most drastic updates to the website were for the rate calculator, which was reported as completely non-functional last year [Sal11]. The goal was to allow users to run their own Monte-Carlo simulations on our servers, with access to the simulations' progress and output files. Before beginning a calculation, an input file must be supplied in the same type of text box used for downloading a library subset. The user may either copy and paste a file into the text box or pull up one of our previously defined input files from an online repository. Editing a previous file is encouraged,to ensure accuracy with the specific formatting. Submission to our server requires only a valid email address. We have set up a queue system, which allows filtering of simulations to different queues depending on the input parameters. This facilitates a fast turnover for quick simulations, even if the main queue is filled with longer-duration simulations. Progress during the simulation may be monitored, and an estimate of time remaining is also given. If a mistake was made in an input file, simulations may also be aborted. Upon completion of the simulation, the server sends an automatic alert email to the address provided. The user may then click on the supplied link to download the input file, output file, LaTeX file, histogram file, each tagged with the reaction name and job ID supplied by the queue after submission. The LaTeX file includes the rate formatted in a LaTeX style for ease of copying and pasting into documents, while the histogram file provides the binned reaction rate at each temperature. The user also has the option to delete any of their own files.

Lastly, several Monte-Carlo reaction rates were updated, including ^{22}Ne(α,γ)^{26}Mg and ^{22}Ne(α,n)^{25}Mg [Lon12].

[Gor08] S. Goriely, S. Hilaire, and A. J. Koning, Phys. Rev. C, **78**, 064307 (2008).

[Ili10a] C. Iliadis, TUNL Progress Report, **XLIX**, 72 (2010).

[Ili10b] C. Iliadis *et al.*, Nucl. Phys. A, **841**, 31 (2010).

[Ili10c] C. Iliadis *et al.*, Nucl. Phys. A, **841**, 251 (2010).

[Ili10d] C. Iliadis *et al.*, Nucl. Phys. A, **841**, 323 (2010).

[Lon10] R. Longland *et al.*, Nucl. Phys. A, **841**, 1 (2010).

[Lon12] R. Longland, C. Iliadis, and A. I. Karakas, Phys. Rev. C, **85**, 065809 (2012).

[Rau00] T. Rauscher and F.-K. Thielemann, At. Data Nucl. Data Tables, **75**, 1 (2000).

[Sal11] A. Sallaska and C. Iliadis, TUNL Progress Report, **L**, 66 (2011).

Nuclear Structure and Reactions

Chapter 4

- **Reaction Dynamics of Light Nuclei**
- **Preequilibrium Nuclear Reactions and Random Matrix Theory**
- **Neutron-Induced Reactions**

4.1 Reaction Dynamics of Light Nuclei

4.1.1 Study of the ^{10}B(p,α) Reaction for Proton Energies between 2.0 and 5.8 MeV

A. Kafkarkou, M.W. Ahmed, H.J. Karwowski, I. Mazumdar, J.M. Mueller, L.S. Myers, M.H. Sikora, H.R. Weller, W.R. Zimmerman, *TUNL*; R.M. Prior, M.C. Spraker, *North Georgia College and State University, Dahlonega, GA*

We have collected data to determine the cross section of the ^{10}B(p,α) reaction. Ten silicon surface-barrier detectors were used at angles from 30 to 150 degrees. We have collected spectra for energies between 2.0 and 5.8 MeV with steps of 100 to 200 keV. A sample spectrum is shown, and data analysis continues.

The ^{11}B(p,α) reaction is an important fusion reaction for aneutronic energy production and has previously been studied by our group [Sta11, Spr12]. However, natural boron contains about 20% ^{10}B, and the reaction ^{10}B(p,α)^{7}Be can also take place in the nuclear fuel. The ^{7}Be produced by this reaction is a radioactive isotope with a half life of around 53 days—long enough that large quantities of this isotope can, in principle, pose serious problems. These problems can, of course, be greatly suppressed by using highly enriched ^{11}B, but the accurate measurement of the cross section of this reaction is still of great importance. Several measurements of the ^{10}B(p,α) reaction have been made for various energies and angles [Jen64, Pet75, Cro56, You91]. Our aim is to determine the cross section in the energy region between 2.0 and 5.8 MeV and to compare our values with previous results.

The measurements were performed using the FN tandem accelerator. The incident proton energies were from 2.0 to 4.0 MeV, in steps of 0.1 MeV, and then from 4.0 to 5.8 MeV in steps of 0.2 MeV. Spectra using a gold-foil target were also collected at 2.0 and 4.0 MeV for solid-angle calibration purposes. Our boron target consisted of a thin layer of boron, enriched to about 98% in ^{10}B, and deposited on a thin carbon foil with a nominal thickness of about 40 μg/cm^2. The thickness of the boron layer was about 100 μg/cm^2. The target was placed in the center of the scattering chamber at an angle of approximately 45° with respect to the beam. This target angle facilitated measurements at 90°.

Our detection system consisted of ten silicon surface-barrier detectors—seven with a thickness of 300 μm and three fully depleted detectors with a thickness of 20 μm. Four of the thicker detectors were placed at backward angles from 90° to 150° in increments of 20°. The thinner detectors were placed at the forward angles of 30° to 70°, in increments of 20°, and the remaining thick detectors were placed behind them, using the telescope technique. In that way, alpha particles with the same energy as the protons from elastic or inelastic scattering would stop in the thin detectors, while the protons would pass through and into the thick detectors. Thus the separation between the two types of particles was possible at forward angles. In order to separate the alpha particles from protons with the same energy at backward angles, we placed aluminum foils with a thickness of about 2.5 μm in front of the detectors. Because of the different stopping powers, we were able to "shift" the alpha peaks to lower energies and separate them, in most cases, from the inelastic (p1) peaks. Data without the foils in front of the backward detectors were also collected at some energies, to allow corrections in cases where the shifted alpha peaks were mixed with inelastic (p2) peaks.

The detectors were placed at a distance of approximately 16 cm from the target. We placed collimating slits in front of each detector to define the solid angle. The backward detectors subtended a solid angle of approximately 7×10^{-4} sr at the target, while the solid angle for the forward detectors was about 4.5×10^{-4} sr.

Currently we are analyzing the data, and no cross sections have been calculated yet. A sample spectrum can be seen in Fig. 4.1. An attempt to fit the spectrum with multiple Gaussian functions is also shown. For the future, we are plan-

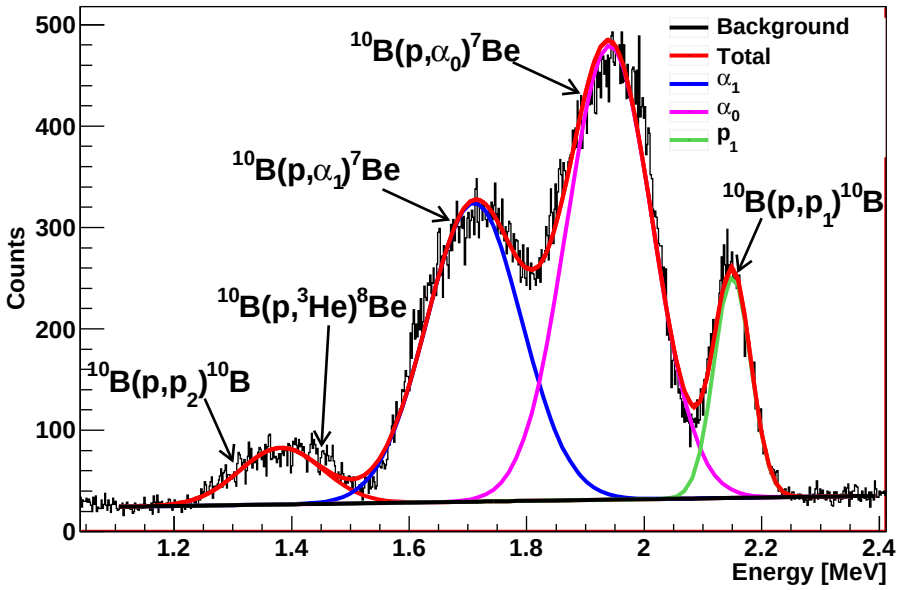

Figure 4.1: (Color online) A sample spectrum taken at 150° for incident protons of 4.0 MeV. The peaks from the ^{10}B(p,α_0) and ^{10}B(p,α_1) reactions, along with some peaks from inelastic proton scattering, are indicated. An attempt to fit the spectrum with multiple Gaussian functions is also shown. The peaks from the elastic scattering on ^{10}B and ^{12}C are off scale. For this spectrum no foils were placed in-front of the detectors.

ning some additional experiments to collect data from 2.0 down to 0.2 MeV, using degrader foils to produce the low-energy beams.

[Cro56] W. J. Cronin, Phys. Rev., **101**, 298 (1956).

[Jen64] J. Jenkin, L. Earwaker, and E. Titterton, Nucl. Phys., **50**, 516 (1964).

[Pet75] R. Peterson *et al.*, Ann. of Nucl. Energy, **2**, 503 (1975).

[Spr12] M. Spraker *et al.*, J. Fus. Energy, **31**, 357 (2012).

[Sta11] S. Stave *et al.*, Phys. Lett., **B696**, 26 (2011).

[You91] M. Youn *et al.*, Nucl. Phys., **A533**, 321 (1991).

4.1.2 Study of the ^{10}B(α,n)^{13}N and ^{11}B(α,n)^{14}N Reactions for Alpha-Particle Energies between 2 and 6 MeV

A. Kafkarkou, M.W. Ahmed, H.J. Karwowski, J.M. Mueller, L.S. Myers, H.R. Weller, W.R. Zimmerman, *TUNL*; R.H. France, III, *Georgia College and State University, Milledgeville, GA*; R.M. Prior, M.C. Spraker, *North Georgia College and State University, Dahlonega, GA*; S.C. Stave, *Pacific Northwest National Laboratory, Richland, WA*

We have studied the ^{10}B(α,n)^{13}N and ^{11}B(α,n)^{14}N reactions using incident α-particle beams with energies between 2 and 6 MeV. The neutrons were detected using nine liquid scintillators. Angular distributions for both reactions were determined, and our results are compared to older data.

As a part of our study of the ^{11}B(p,α) reaction for aneutronic energy production, we measured the cross sections and the angular distributions for the ^{10}B(α,n)^{13}N and ^{11}B(α,n)^{14}N reactions using α-particle with energies of 2 to 6 MeV in increments of 0.25 MeV. These reactions can occur in the nuclear fuel due to the α particles produced, and the released neutrons can pose serious problems. Thus, the accurate measurement of the cross sections of these reactions is of great importance. The setup for this experiment is described in Ref. [Pri11]. The neutrons were detected using nine liquid scintillators with pulse-shape discrimination, and angular distributions were determined.

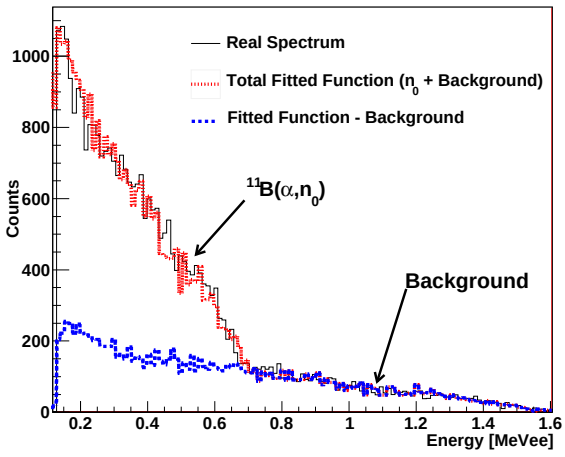

Figure 4.2: (Color online) A sample spectrum for the ^{11}B(α,n)^{14}N reaction at 4.75 MeV taken at 147°. A fit to the spectrum using the response function of the detector is also shown. The x-axis is in MeV-electron-equivalent.

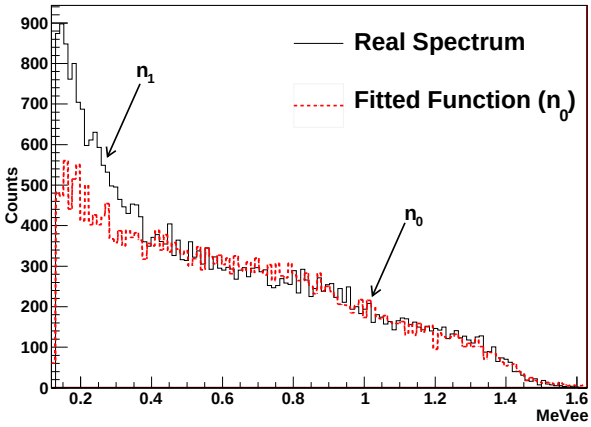

Figure 4.3: (Color online) A sample spectrum for the ^{11}B(α,n)^{14}N reaction at 4.75 MeV taken at 47.9°. In this spectrum no background was observed. However, at this angle the contribution from the n_1 group is obvious.

A sample spectrum for the ^{11}B(α,n)^{14}N reaction at 147° and an α-particle energy of 4.75 MeV is shown in Fig. 4.2. In order to separate the two neutron groups, n_0 and n_1, and subtract the background, we fit our spectra with the detector-response functions. An example of such fitting is also shown in Fig. 4.2. For the selected angle and energy no neutron groups other than the n_0 group are present. In the forward angle detectors, no background was observed, as can be seen in Fig. 4.3. This spectrum was taken at 47.9° for 4.75 MeV α particles. At this angle some neutrons from the n_1 group are also present.

From the collected spectra, the yields for the n_0 group were extracted for each energy and angle by integrating the fitted function and sub-

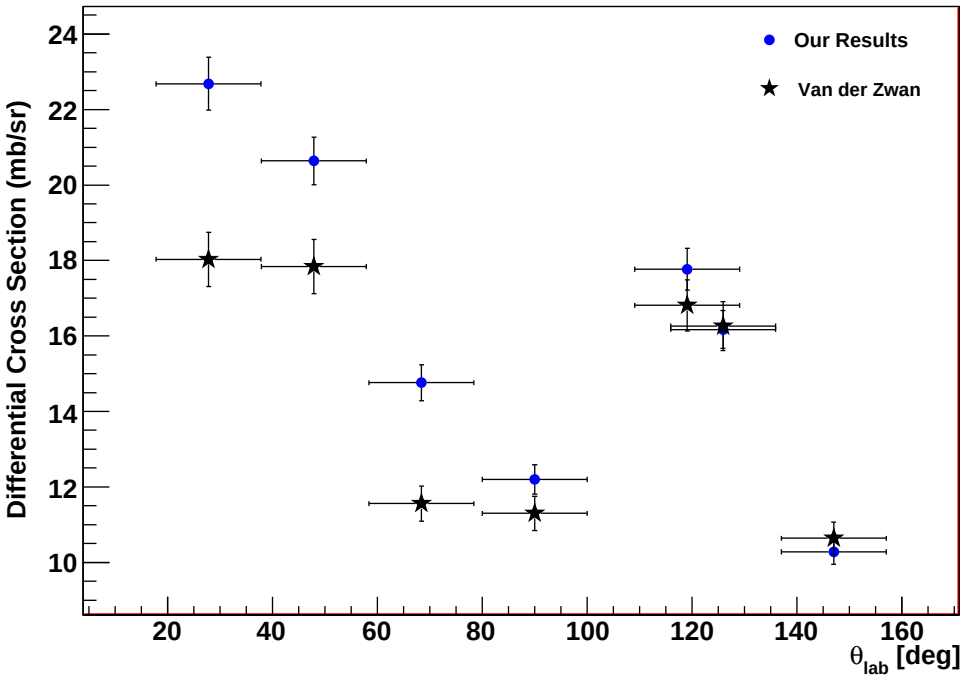

Figure 4.4: (Color online) Angular distribution for the ^{11}B(α,n)^{14}N reaction at 4.75 MeV. Data points from Ref. [VdZ75] are also given for comparison. The cross sections and angles are given in the laboratory frame.

tracting the background where applicable. The yields were then corrected for the detector efficiencies. Using the cross-section values reported in Ref. [VdZ75] for an α-particle energy of 5.5 MeV and our corrected yields for the same energy, we normalized our data for the ^{11}B(α,n)^{14}N reaction. The normalization factors were calculated taking account of target-thickness and solid-angle corrections. These factors were then used to obtain the angular distributions for all the other energies, and they will also be used to determine the angular distributions for the ^{10}B(α,n)^{13}N reaction.

In order to check the validity of our method, we compared our results at 4.75 MeV with those reported in Ref. [VdZ75] for the same energy. This comparison is shown in Fig. 4.4 for the ^{11}B(α,n)^{14}N reaction. Obviously there is a good agreement between the two data sets at backward angles, but the agreement is rather poor at forward angles. The results reported here are preliminary. Better error estimations need to be made, and the differential cross sections for the ^{10}B(α,n)^{13}N reaction are yet to be calculated. Legendre polynomials will be used to fit the angular distributions.

[Pri11] R. M. Prior *et al.*, TUNL Progress Report, **L**, 72 (2011).

[VdZ75] L. Van der Zwan and K. W. Geiger, Nucl. Phys., **A246**, 93 (1975).

4.2 Preequilibrium Nuclear Reactions and Random Matrix Theory

4.2.1 Preequilibrium Reaction Phenomenology

C. Kalbach Walker, *TUNL*

The angular distribution systematics for preequilibrium reactions induced by α particles are being revised. Work this year shows that the multi-step-compound continuum cross section has a smaller "slope parameter" than does the multi-step-direct cross section, which dominates at higher emission energies. Fits to one hundred experimental (α,p) angular distributions were performed, and work to extract revised systematics is continuing.

For light-particle ($A \leq 4$) induced reactions at incident energies of 14 to 200 MeV, the semiclassical exciton model of preequilibrium nuclear reactions provides a simple way to describe the continuum energy and angular distributions of the light particles emitted during energy equilibration. The TUNL code system PRECO is based on the exciton model and has been used (either alone or in Hauser-Feshbach codes) in applied projects and in basic research. Model development uses simple physical concepts and relies on available data to direct choices between alternative model formulations and to provide values for key model parameters. The main area of study this year was revised systematics for describing the continuum angular distributions in α-particle-induced reactions. These are needed for validation of a new projectile-breakup model.

4.2.1.1 Projectile-Breakup Model

A strength of PRECO is its ability to treat complex particles in a reaction's entrance and exit channels, but for d, t, and ^{3}He projectiles and for α particles at incident energies above about 50 MeV, the lack of a model for projectile breakup makes the description incomplete. Because deuteron projectiles were important for the International Atomic Energy Agency's Coordinated Research Project (CRP) to upgrade the Fusion Energy Nuclear Data Library, a phenomenological projectile-breakup model was developed as part of this CRP.

The model gives reasonable agreement with experiment for d- and ^{3}He-induced reactions [Kal10a, Kal10b]. For α-particle-induced reactions, an extra peak in the measured (α,xd) spectra occurs at the energy of the (α,p) breakup peak and was added to the breakup model [Kal11]. The data comparisons needed to verify the breakup model for α-particle-induced reactions were suspended early this year, pending revision to the systematics for the angular distributions of the continuum cross section forming the background under the peaks. The underlying continuum that is drawn in for the comparisons should agree with the new systematics.

4.2.1.2 Angular Distributions for α-Particle-Induced Reactions

A widely used, phenomenological description of continuum angular distributions [Kal88] contains systematics for reactions with incident α particles that are slightly different from those for other light projectiles. The α-particle systematics are now being revised to remove this difference.

The systematics divide the cross section into its multi-step direct (MSD) and multi-step compound (MSC) parts. MSD particle emission occurs when the equilibrating nucleus has passed through a sequence of states having at least one particle degree-of-freedom in an unbound single-particle state [Fes80]. It exhibits a forward-peaked angular distribution described by an exponential in $\cos\theta$. Once the system has passed through at least one configuration in which all the particle degrees-of-freedom are in bound single-particle states, "memory" of the beam direction is assumed to be lost, and the resulting MSC emission is symmetric about 90° in the center-of-mass. It contains exponentials in both $\cos\theta$ and $-\cos\theta$. Most preequilibrium cross section is MSD; equilibrium emission is MSC.

In the systematics, $\cos\theta$ in the exponentials is multiplied by a "slope parameter" $a_{\rm ang}$ that is defined in terms of the energies of the incident and emitted particles. This parameter determines the amount of forward peaking in the MSD part of the angular distribution and the amount of anisotropy in the MSC part. For incident nucleons and deuterons, the equation for $a_{\rm ang}$ has three terms, while for α particles the third term was omitted. New evidence indicates the need for the third term [Kal11]. Forward-angle data points were given reduced weight in the fitting process because of possible projectile-breakup contributions, and the preequilibrium cross section was assumed to be pure MSD, whereas it can have a small MSC component.

The preliminary model for breakup reactions now indicates that the breakup cross section is small, and a correction for it can be applied. Thus it is appropriate to do new fits to the experimental angular distributions from the literature, subtracting the breakup cross section, weighting all angles on the same basis, and varying the fraction of the cross section that is MSD.

The (α,p) channel is expected to be the most favorable, having a fairly large cross section and significant sensitivity to the third term in the slope parameter. The fitting has been carried out on all of the (α,p) data previously analyzed—just over one hundred angular distributions at incident energies of 30 to 172 MeV plus 720 MeV and for emission energies of 6 to 170 MeV. These fits show that extracting slope parameters is not entirely straightforward.

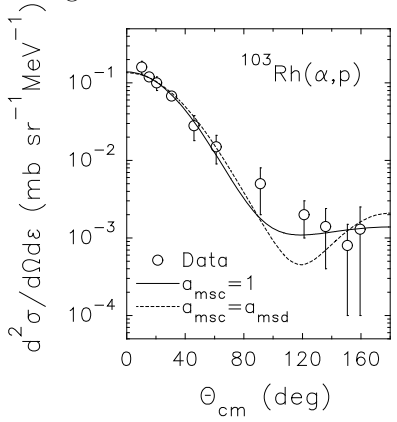

Figure 4.5: Fits to the experimental ^{103}Rh(α,p) angular distribution for an incident energy of 42 MeV and a center-of-mass emission energy of 32 MeV [Wes66].

In the past it was assumed that $a_{\rm ang}$ is the same for the MSD and MSC components, but two new lines of evidence suggest that this is not always the case. First, for angular distributions in the tail of the evaporation peak, it implies an anisotropy that is significantly greater than what emerges from model calculations using angular momentum conservation [Gri11]. Second, using the assumption to fit experimental angular distributions can lead to a dip at 90 to 120 degrees not observed in the data, as shown in Fig. 4.5.

Given these considerations, separate slope parameters, $a_{\rm msd}$ and $a_{\rm msc}$, have been used for the MSD and MSC components in the new fits. Unfortunately, varying both slope parameters plus the fraction of the cross section that is MSD does not yield meaningful results. Because the MSD cross section is dominant at all but the lowest emission energies, the new fits varied $a_{\rm msd}$ while using either $a_{\rm msc} = a_{\rm msd}$ or the limiting option of $a_{\rm msc} = 1.00$.

Fits to the experimental (α,p) angular distributions have been completed, and often the slope-parameter values obtained using the two options for $a_{\rm msc}$ are within ten or twenty percent of each other. Occasionally, however, the fitted slope parameters can differ by up to a factor of 1.5, even when the data are reproduced with comparable accuracy. Apparently, varying the fraction of the cross section that is MSD within reasonable limits can compensate for the change in $a_{\rm msc}$. Such data may have to be eliminated from the search for new slope-parameter systematics. This search will seek a revised description for $a_{\rm msd}$ that has the three-term form used for other projectiles. Then the behavior of $a_{\rm msc}$ will be studied.

[Fes80] H. Feshbach, A. Kerman, and S. Koonin, Ann. Phys., **125**, 429 (1980).

[Gri11] S. M. Grimes and A. Voinov, 2011, Private communication.

[Kal88] C. Kalbach, Phys. Rev. C, **37**, 2350 (1988).

[Kal10a] C. Kalbach Walker, TUNL Progress Report, **XLIX**, 97 (2010).

[Kal10b] C. Kalbach Walker, Report to the 2nd meeting of the FENDL-3 CRP, Vienna, Austria, March 2010, posted at `www-nds.iaea.org/fendl3/vardocs.html`, 2010.

[Kal11] C. Kalbach Walker, TUNL Progress Report, **L**, 80 (2011).

[Wes66] R. W. West, Phys. Rev., **141**, 1033 (1966).

4.3 Neutron-Induced Reactions

4.3.1 The $(n, 2n)$ Cross Sections of ^{181}Ta and ^{64}Zn from 8 to 14.5 MeV

C. Bhatia, M.E. Gooden, W. Tornow, *TUNL*; A.P. Tonchev, *Lawrence Livermore National Laboratory, Livermore, CA*

The cross sections of the reactions ^{181}Ta$(n, 2n)^{180}$Ta and ^{64}Zn$(n, 2n)^{63}$Zn were measured from 8 to 14.5 MeV in small energy steps, in order to resolve inconsistencies in the existing database. This is the first time that the cross section of the $(n, 2n)$ reaction on ^{181}Ta was measured for neutron energies near threshold.

Nuclear data are the backbone of nuclear technology. They are useful in the design and modeling of nuclear energy systems [Cha01, Bha11], radiation safety, activation methods, and interdisciplinary areas, including the production of radioisotopes for medicine and industry, space applications, cancer radiotherapy, radiation damage studies, and environmental monitoring. Precise nuclear data, particularly cross-section measurements, also play an important role in fundamental research to test statistical-model codes and provide insight into the reaction mechanisms in different energy regimes.

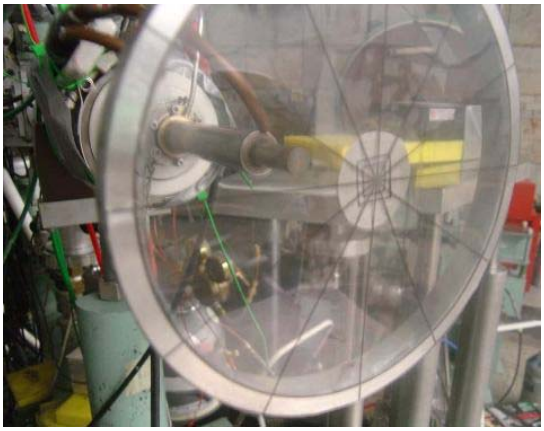

Figure 4.6: (Color online) ^{181}Ta target placed in front of the deuterium gas cell.

^{180}Ta is studied extensively in nuclear physics and is of interest in nuclear astrophysics because it is a natural isomeric target [Ton00]. Furthermore, the ^{181}Ta$(n, 2n)$ reaction was used in underground tests of nuclear devices to assess their performance and for diagnostics at the National Ignition Facility. Zinc is an important element to study because of its extensive use as a structural material and in medical applications.

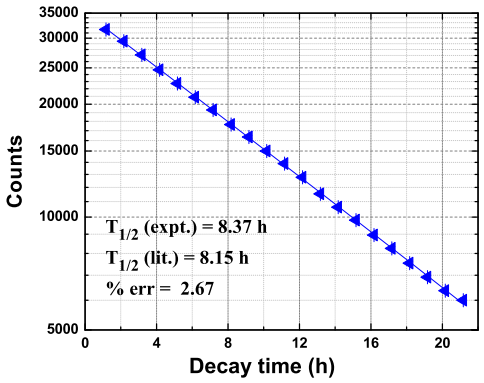

Figure 4.7: (Color online) Measured decay half-life of the ^{181}Ta$(n, 2n)^{180}$Ta reaction.

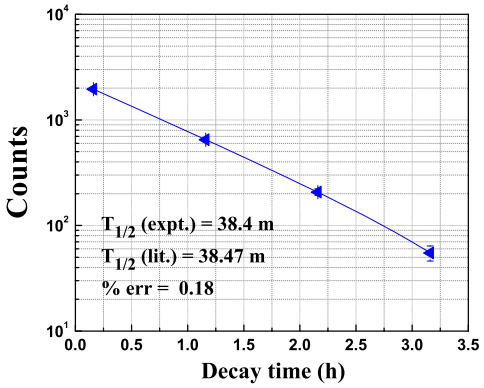

Figure 4.8: (Color online) Measured decay half-life of the ^{64}Zn$(n, 2n)^{63}$Zn reaction.

The cross sections of the ^{181}Ta$(n,2n)^{180}$Ta and ^{64}Zn$(n,2n)^{63}$Zn reactions have been measured at incident neutron energies from 8 to 14.5 MeV in small energy steps using the activation technique. The threshold energies for these reactions on ^{181}Ta and ^{64}Zn are 7.62 MeV and 12.05 MeV, respectively.

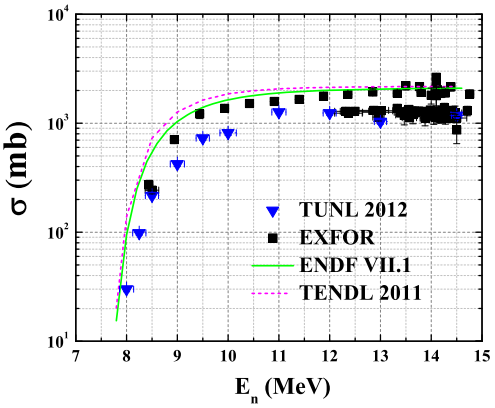

Figure 4.9: (Color online) Measured cross-section data of the ^{181}Ta$(n,2n)^{180}$Ta reaction. Horizontal uncertainties represent the energy spread of the beam.

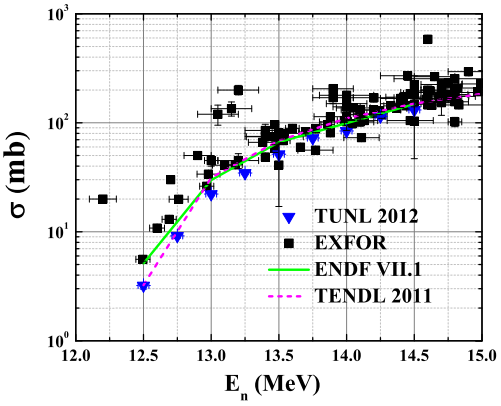

Figure 4.10: (Color online) Measured cross-section data of the ^{64}Zn$(n,2n)^{63}$Zn reaction. Horizontal uncertainties represent the energy spread of the beam.

The targets were foils of ^{181}Ta and $^{\text{nat}}$Zn, 1 cm^2 in area and with masses 229 mg and 263 mg, respectively. The mono-energetic neutron beams were produced using the ^{2}H$(d,n)^3$He reaction, known for its high neutron yield in the present energy region. Deuterium gas was contained in a 3-cm-long cylindrical cell, at a pressure between 1 and 4 atm, depending on the incident deuteron energy. The cell was sealed from the beamline vacuum by a 0.635-μm thin Havar foil. The pressure in the gas cell and the energy loss of the deuteron beam in the Havar foil contributed to the energy spread of the neutron beam. This energy spread was calculated with the program MAGNET [Cro], using the incident deuteron beam energy, the length of the gas cell, the deuterium gas pressure, the thickness of the Havar foil, and the ambient temperature as input. Monte-Carlo simulations were performed to take the gas-cell–target-geometry into account. This further increases the energy spread of the neutron beam and reduces its mean energy. The induced γ-ray activity of ^{180}Ta and ^{63}Zn was measured with high-resolution HPGe detectors. The γ-ray spectra from the offline measurements of the activated samples were analyzed using the software TV [The93] to identify the reaction products and determine the respective peak areas. The cross sections were determined relative to those from aluminum and gold monitor foils measured in the same geometry. The geometry is shown in Fig. 4.6. The details of the method are discussed in Ref. [Ton08].

Half-life plots of ^{180}Ta and ^{63}Zn are shown in Figs. 4.7 and 4.8, respectively. Our cross-section results are shown in Figs. 4.9 and 4.10. Good agreement is obtained for the reaction cross sections with some of the previous measurements. The curves are the existing calculations and evaluations. Clearly, some of the data in the literature need to be revised, and a careful re-evaluation is needed to obtain recommended data sets for those two reactions.

[Bha11] C. Bhatia and V. Kumar, *Role of (n,xn) Reactions in Accelerator Driven Sub-critical Systems*, Lambert Academic Publishing, 2011.

[Cha01] M. B. Chadwick *et al.*, Prog. Nucl. Energy, **38**, 179 (2001).

[Cro] A. S. Crowell, Private communication.

[The93] J. Theuerkauf *et al.*, *Computer code* TV, Technical report, Institute for Nuclear Physics, University of Cologne, 1993, unpublished.

[Ton00] A. P. Tonchev and J. F. Harmon, Appl. Rad. Isotopes., **52**, 873 (2000).

[Ton08] A. P. Tonchev *et al.*, Phys. Rev. C, **77**, 054610 (2008).

4.3.2 Fission-Product-Yield Study of ^{235}U and ^{238}U at 4.6 MeV and 9.0 MeV Using Dual-Fission-Chamber Detectors

C. Bhatia, B.A. Fallin, M.E. Gooden, C.R. Howell, J.H. Kelley, W. Tornow, *TUNL*; C.W. Arnold, E. Bond, T. Bredeweg, M. Fowler, W. Moody, R. Rundberg, G. Rusev, D. Vieira, J. Wilhelmy, *Los Alamos National Laboratory, Los Alamos, NM*; J. Becker, R. Macri, C. Ryan, S. Sheets, M. Stoyer, A. Tonchev, *Lawrence Livermore National Laboratory, Livermore, CA*

The activation method was used to perform high-precision measurements of the fission-product yields for neutron-induced fission of ^{235}U and ^{238}U. Our preliminary results for seven fission fragments are compared to available data at other energies.

In order to resolve long-standing differences between LANL and LLNL regarding the correct fission basis for analysis of nuclear-test data [Cha10, Sel10], a collaboration between TUNL, LANL, and LLNL has been formed to make high-precision measurements of fission-product yields from neutron-induced fission. The goal is to make a definitive statement about the energy dependence of the fission-product yields to an accuracy of better than 2 to 3% for neutron energies between 1 and 15 MeV, where experimental data are very scarce. A series of experiments has been performed utilizing the mono-energetic neutron beams available at TUNL and the dual-fission-chamber detectors described in Sect. 8.2.1.

Neutrons of 4.6 and 9 MeV were produced via the ^{2}H$(d,n)^{3}$He reaction, and targets of ^{235}U and ^{238}U were studied using the activation method. The ^{235}U and ^{238}U monitor targets for the dual-fission-chamber detectors were 100 μg/cm^2 thick, and the thick ^{235}U and ^{238}U target foils had masses of 0.26 g and 0.46 g, respectively. All the foils were one-half inch in diameter. A schematic of the fission-yield experimental setup is shown in Fig. 4.11. Monitor foils of aluminum, indium, gold, and ^{235}U) were used to characterize the neutron field in the vicinity of the dual-fission-chamber detectors. In addition, time-of-flight measurements were performed using a BC-501A neutron monitor and two ^{3}He gas scintillators [Tor11]. A time-of-flight spectrum from the ^{3}He gas scintillator is shown in Fig. 4.12.

After activation, the thick uranium targets were placed in thin aluminum containers. High-resolution HPGe detectors were used to measure the induced γ-ray activity of the fission-products. During the three months of counting, the data-acquisition cycles were gradually increased from thirty minutes during the first day after irradiation to one day after two weeks, and finally to two days after two months. This counting procedure allowed us to follow the experimental half lives of all the fission products of interest very closely and to account for any γ-ray interference between them. In Fig. 4.13, the measured half life for ^{147}Nd is compared to the literature value.

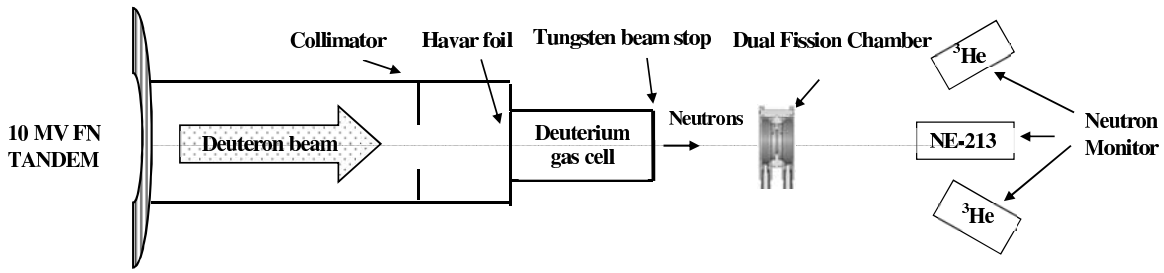

Figure 4.11: Schematic of the experimental setup using a dual-fission-chamber detector.

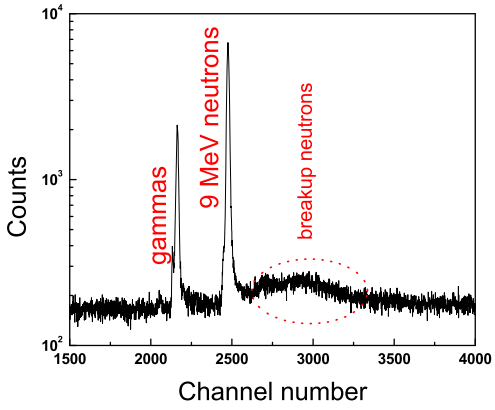

Figure 4.12: (Color online) Time-of-flight spectrum from the ^{3}He gas scintillator.

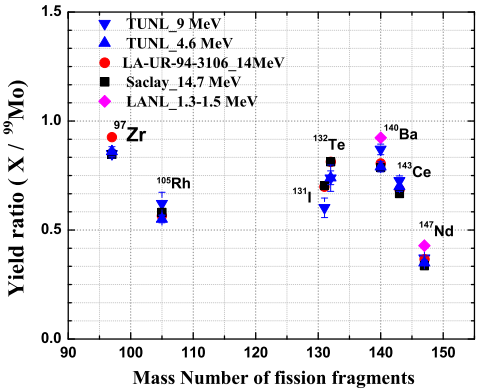

Figure 4.14: (Color online) Fission-product-yield ratios for ^{238}U.

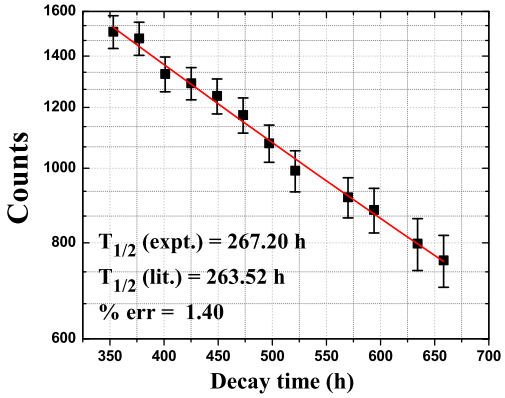

Figure 4.13: (Color online) Measured half life of ^{147}Nd at $E_n = 9$ MeV for ^{238}U target. The points show the data, and the line shows the exponential fit.

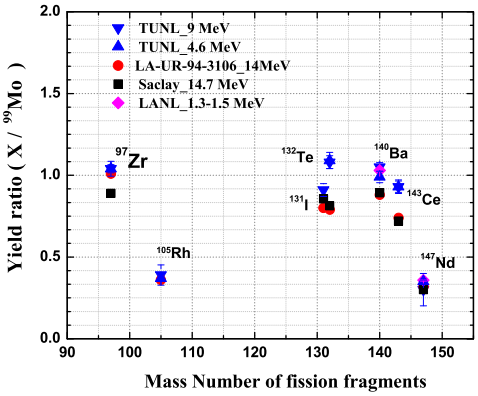

Figure 4.15: (Color online) Fission-product-yield ratios for ^{235}U.

The γ-ray spectra acquired from the off-line measurements of the activated samples were analyzed using the computer code TV [The93] to identify the fission products. In the preliminary analysis, we identified seven fission fragments: ^{97}Zr, ^{105}Rh, ^{131}I, ^{132}Te, ^{140}Ba, ^{143}Ce, and ^{147}Nd. The ratios of the yields for the fission fragments we identified to the yield for ^{99}Mo at neutron energies of 4.6 and 9.0 MeV are shown in Figs. 4.14 and 4.15 along with other available data. These figures show that our fission-product yields are consistent with previously measured data near 1.5 MeV and 14.5 MeV.

[Cha10] M. Chadwick *et al.*, Nucl. Data Sheets, **111**, 2923 (2010).

[Sel10] H. Selby *et al.*, Nucl. Data Sheets, **111**, 2891 (2010).

[The93] J. Theuerkauf *et al.*, *Computer code* TV, Technical report, Institute for Nuclear Physics, University of Cologne, 1993, unpublished.

[Tor11] W. Tornow *et al.*, Nucl. Instrum. Methods A, **647**, 86 (2011).

4.3.3 Fission-Product Yields of ^{239}Pu at 4.6 to 14.8 MeV Using a Dual-Fission-Chamber Detector

C. Bhatia, B.A. Fallin, M.E. Gooden, C.R. Howell, J.H. Kelley, W. Tornow, *TUNL*; C.W. Arnold, E. Bond, T. Bredeweg, M. Fowler, W. Moody, R. Rundberg, G. Rusev, D. Vieira, J. Wilhelmy, *Los Alamos National Laboratory, Los Alamos, NM*; J. Becker, R. Macri, C. Ryan, S. Sheets, M. Stoyer, A. Tonchev, *Lawrence Livermore National Laboratory, Livermore, CA*

The activation method was used to perform high-precision measurements of the neutron-induced fission-product yields of ^{239}Pu. Our preliminary results for seven fission fragments at four neutron energies are presented. This is the first time that results are available for neutron energies between 1.5 and 14 MeV.

A joint Fission Product Review Panel study has identified important issues associated with the possible neutron-energy dependence of the yield from neutron-induced fission [Cha10, Sel10]. In the fission of ^{239}Pu, an energy dependence of 3.7%/MeV was recommended for the yield per fission event of ^{147}Nd at neutron energies from 0.2 to 1.9 MeV. Because, of the renewed interest in fission-product yields, we initiated a program at TUNL to obtain high-precision and self-consistent data for their energy dependence at neutron energies between 1 and 15 MeV for three different actinides. Here we report on the fission-product yields of ^{239}Pu. We used the activation technique and the dual-fission-chamber detector described in Sect. 8.2.1.

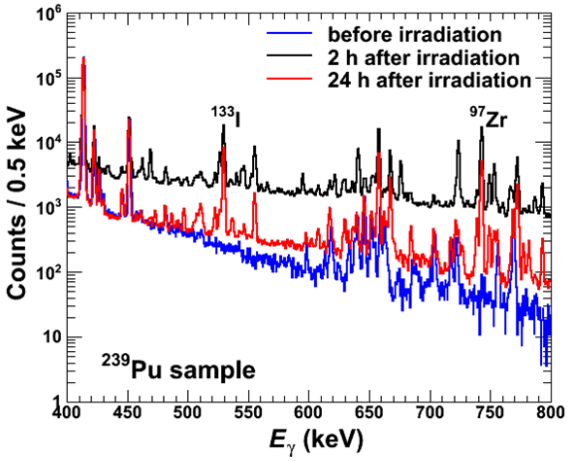

Figure 4.16: (Color online) Portion of a typical γ-ray spectrum at $E_n = 14.5$ MeV.

Neutrons at energies of 4.6, 9.0, and 14.5 MeV were produced via the ^{2}H$(d,n)^3$He reaction, while for neutrons at 14.8 MeV, the ^{3}H$(d,n)^4$He reaction was used. The ^{239}Pu monitor foils for the dual-fission-chamber detector were 10 μg/cm^2, and the two thick ^{239}Pu targets were 0.23 g each. All foils were one-half inch in diameter. A schematic of the experimental setup is shown in Sect. 4.3.2. A typical γ-ray energy spectrum before and after irradiation at $E_n = 14.5$ MeV is shown in Fig. 4.16.

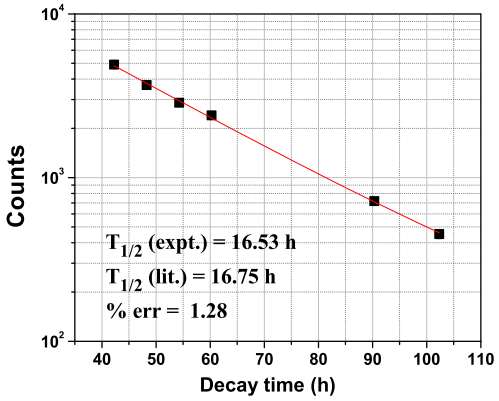

Figure 4.17: (Color online) Measured half life for ^{97}Zr obtained from fission of ^{239}Pu at $E_n = 14.8$ MeV. The points show the data, and the line shows the exponential decay fit.

After activation, the two thick plutonium targets were placed in thin aluminum containers. High-resolution HPGe detectors were used to measure the induced γ-ray activity of the fission

products. To reduce the counting rate in these detectors, a cadmium disk of 1 mm thickness was placed inside the aluminum container facing the HPGe detector. During the three months of counting, the data-acquisition cycles were increased from minutes to days. This made it possible to follow the experimental half lives of all the fission products of interest very closely and to account for any γ-ray interference between them.

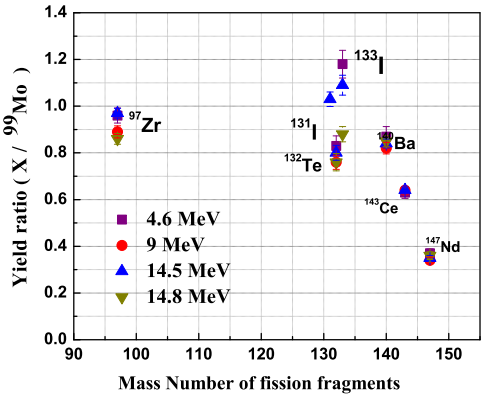

Figure 4.18: (Color online) Fission-product-yield ratios for ^{239}Pu at 4.6, 9.0, 14.5, and 14.8 MeV.

The γ-ray spectra acquired from the off-line measurements of the activated samples were analyzed using the computer code TV [The93] to identify the fission products. In the preliminary analysis of ^{239}Pu, we identified seven fission fragments: ^{97}Zr, ^{105}Rh, ^{131}I, ^{132}Te, ^{140}Ba, ^{143}Ce, and ^{147}Nd. Figure 4.17 shows a comparison of our measured half life for ^{97}Zr with the literature values. The ratios of the yields for the fission fragments we identified to the yield for ^{99}Mo at our four energies are shown in Fig. 4.18.

As can be seen, our preliminary fission-product yields at four different energies are consistent with one another and do not suggest a strong energy dependence. This conclusion is supported by Fig. 4.19, which shows the ^{147}Nd/^{99}Mo ratio as a function of incident neutron energy. Our results at around 14.5 MeV are in agreement with the literature value of Ref. [Eng94] and the measurement of Innes et al. [Inn11].

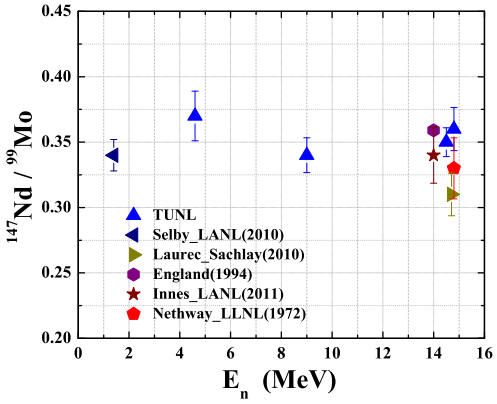

Figure 4.19: (Color online) Measured fission-product-yield ratio of ^{147}Nd compared to available data at neutron energies up to 15 MeV.

[Cha10] M. Chadwick *et al.*, Nucl. Data Sheets, **111**, 2923 (2010).

[Eng94] T. R. England and B. F. Rider, *ENDF-349: Evaluation and Compilation of Fission Product Yields, 1993*, Technical Report LA-UR-94-3106, Los Alamos National Laboratory, 1994.

[Inn11] M. Innes *et al.*, Nucl. Data Sheets, **112**, 3135 (2011).

[Sel10] H. Selby *et al.*, Nucl. Data Sheets, **111**, 2891 (2010).

[The93] J. Theuerkauf *et al.*, *Computer code* TV, Technical report, Institute for Nuclear Physics, University of Cologne, 1993, unpublished.

4.3.4 Neutron-Capture Experiments

G.E. Mitchell, B. Baramsai, E. Batchuluun, A. Chyzh, D. Dashdorj, C.L. Walker, *TUNL*; OTHERS, *Charles University, Prague and Rez Institute of Nuclear Physics, Rez, Czech Republic*; *Los Alamos National Laboratory, Los Alamos, NM*; *Lawrence Livermore National Laboratory, Livermore, CA*

Our measurements of neutron-capture reactions utilize the DANCE array (at LANSCE/Lujan)—a highly efficient calorimeter consisting of 160 BaF_2 detectors. The high degree of segmentation can be used to perform neutron resonance spectroscopy. Several new methods have been developed to determine resonance spins from the multiplicity distributions. The study of the statistical γ-ray cascade from different resonances and for different multiplicities provides unique opportunities to test models of the photon strength function.

Our efforts emphasize neutron-capture reactions measured with the Detector for Advanced Neutron Capture Experiments (DANCE) located at the Los Alamos Neutron Science Center (LANSCE) at LANL. We focus on nuclei that are important for applied science and for nuclear structure interests. Much of the support for this work comes from an NNSA Academic Alliances grant.

DANCE is an array of 160 barium fluoride crystals. This calorimeter identifies capture by the total γ-ray energy. The high efficiency of the calorimeter means that measurements can be made with very small targets. The capture cross sections for specific nuclei are extremely valuable for stewardship science, for advanced-fuel-cycle calculations, and for nuclear astrophysics. The primary nuclear structure interest is in the photon low-energy collective excitations, namely the scissors mode and pygmy resonances. Specifically, we use the properties of the γ-ray cascade from isolated neutron resonances to determine resonance properties and properties of the photon strength function.

We utilize the computer program DICEBOX, developed by our Prague collaborators, to model the γ-ray spectrum for all multiplicities. We vary the photon strength functions in order to obtain the best agreement with experiment.

Thus far we have measured ^{89}Y, ^{94,95,97}Mo, ^{117,119}Sn, ^{151,153}Eu, and ^{152,154,155,156,157,158}Gd and have collaborated on measuring ^{87}Sr. We have finished the analysis of ^{89}Y, ^{94,95}Mo, and the europium and gadolinium isotopes. Preliminary analysis of the other nuclides (^{97}Mo and ^{117,119}Sn) has been completed.

Detailed agreement with the pure statistical model was obtained for neutron capture on ^{95}Mo. Of particular interest is the behavior of the scissors-mode resonance as a function of mass and deformation in the gadolinium isotopes. Analysis of the γ-cascade data in the gadolinium isotopes leads to the clear conclusion that scissors-mode resonances are built not only on the ground state, but also on excited levels in all product nuclei studied.

We have also made arrangements with the neutron time-of-flight group at CERN, who will use their CERN calorimeter to study the same strontium target used for the DANCE measurement. The experimental run has been approved for the near future. This will enable a direct comparison of the relative merits of the two most advanced calorimeters for neutron capture measurements.

In favorable cases, the average multiplicity of the γ-ray decay is sufficient to determine the spin of an s-wave resonance. In general, however, it is necessary to perform a detailed analysis of the multiplicity distribution. One method that we have developed [Bar12] involves pattern recognition theory. This method works for well-isolated resonances but is inconclusive for doublets. In collaboration with our collaborators from Prague, we have developed an alternate method that adopts prototype multiplicity distributions for resonances with known spin, and decomposes the experimental cross section into cross sections for the separate spins. This method [Bec11] works well even for doublets, but provides no quantitative measure of the assignment's correctness. In practice we utilize a combination of the two methods.

[Bar12] B. Baramsai *et al.*, Phys. Rev. C, **85**, 024622 (2012).

[Bec11] F. Becvar, Nucl. Instrum. Methods, **647**, 73 (2011).

Photonuclear Reactions at HIγS

Chapter 5

- **Nuclear Astrophysics**
- **γ-^{3}He Interaction**
- **Study of Many-Body Systems**

5.1 Nuclear Astrophysics

5.1.1 Study of the $^{16}O(\gamma,\alpha)^{12}C$ Reaction with the HIγS O-TPC

W.R. Zimmerman, M.W. Ahmed, S.S. Henshaw, J.M. Mueller, L.S Myers, M.H. Sikora, S. Stave, H.R. Weller, *TUNL*; M. Gai, A.G. Swindell, *University of Connecticut at Avery Point, Groton, CT*

The $^{16}O(\gamma,\alpha)^{12}C$ reaction has been studied at HIγS using an optical time-projection chamber at γ-ray beam energies between 9.1 and 10.7 MeV. Previous data, taken using CO_2 as the target gas, have been fully analyzed, and additional data have been taken using N_2O as the target gas. The measured E1-E2 relative phase angles agree with predictions based on elastic-scattering phase shifts.

Stellar helium burning is driven by two major reactions: $3\alpha \rightarrow ^{12}C$ (the triple-α reaction) and $^{12}C(\alpha,\gamma)^{16}O$. The relative rates of these two reactions determine the carbon-oxygen ratio at the end of helium burning, and this ratio is crucial for predicting all subsequent stages of stellar evolution. The triple-α reaction rate is well-determined for quiescent helium burning, but the $^{12}C(\alpha,\gamma)^{16}O$ reaction rate is highly uncertain.

Previous measurements of the $^{12}C(\alpha,\gamma)^{16}O$ reaction were based on detecting γ-rays [Ass06, Red87] and have been limited by a low cross section and high background. Furthermore, the disagreement between the measured E1-E2 relative phase angle and that predicted by the $^{12}C(\alpha,\alpha')$ elastic scattering phase shifts [Pla87] suggests problems with the measured angular distributions and, as a result, with the extracted E1/E2 ratios. This limits the accuracy of the calculated cross section at around 300 keV—the relevant energy for stellar helium burning—since the E1 and E2 components of the cross section need to be extrapolated separately.

In the present work, the time-reversed reaction $^{16}O(\gamma,\alpha)^{12}C$ was studied using the HIγS optical time-projection chamber (O-TPC) (see Fig. 5.1) with CO_2 and N_2O gas targets at γ-ray beam energies from 9.1 to 10.7 MeV. The HIγS O-TPC can measure the complete angular distributions necessary for accurately extracting the E1 and E2 components of the cross section, as well as their relative phase ϕ_{12} [Gai10].

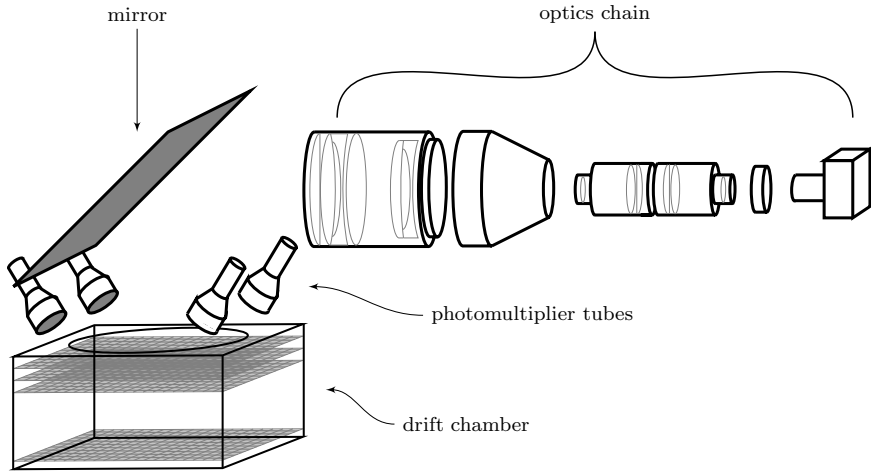

Figure 5.1: The HIγS O-TPC. When a photo-disintegration event occurs in the drift chamber, recoiling particles leave ionization tracks in the gas. Electrons from the ionization drift towards the high-voltage grids, where they are multiplied and produce scintillation light. The scintillation light is detected in the photomultiplier tubes, and the optical chain focuses the image into a camera, which records a photograph of the event.

Apart from the ^{16}O(γ,α)^{12}C events, several types of background events were recorded by the HIγS O-TPC: ^{14}N(γ,p)^{13}C events from the N_2 scintillator and the N_2O target; ^{12}C(γ,α)^{8}Be events from the CO_2 target; ^{18}O(γ,α)^{14}C events from both target gases; and charged particle tracks induced by cosmic rays. The ^{14}N(γ,p)^{13}C, ^{18}O(γ,α)^{14}C, and cosmic-ray events were easily rejected based on the total deposited energy, track length, and position of the tracks.

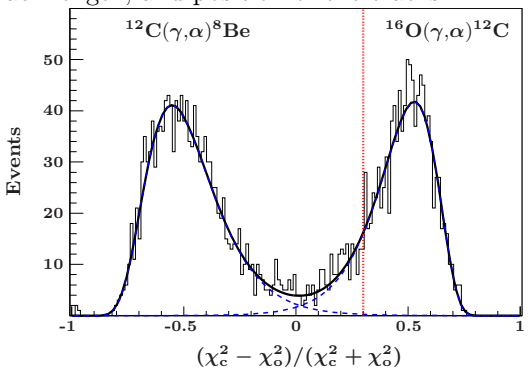

Figure 5.2: (Color online) Discrimination between ^{12}C(γ,α)^{8}Be and ^{16}O(γ,α)^{12}C events. The dotted red line shows the position of the cut; all events to the right were identified as ^{16}O(γ,α)^{12}C. Efficiency of the cut and leakage of ^{12}C(γ,α)^{8}Be events were estimated by fitting the distribution to the sum (solid black line) of two log-normal functions (dashed blue lines).

The ^{12}C(γ,α)^{8}Be events and the ^{16}O(γ,α)^{12}C events have very similar total energies and track lengths, so they were distinguished based on their respective time-projection signals from the photo-multiplier tubes. Simulated time-projection line shapes were calculated by taking the known range and stopping power of the charged particles and simulating the drift of the electrons through the gas. Each of the experimentally measured time-projection signals was fit using both ^{16}O(γ,α)^{12}C and ^{12}C(γ,α)^{8}Be line shapes, and the goodness-of-fit parameters (χ^2) were compared to classify the event. Figure 5.2 shows discrimination between the two event types at a γ-ray beam energy of 9.8 MeV. The quantities χ^2_c and χ^2_o refer to the goodness-of-fit parameters from fitting with the ^{12}C(γ,α)^{8}Be and ^{16}O(γ,α)^{12}C line shapes, respectively. The cut was made so that fewer than 0.1% of the events to the right of the cut were ^{12}C(γ,α)^{8}Be events.

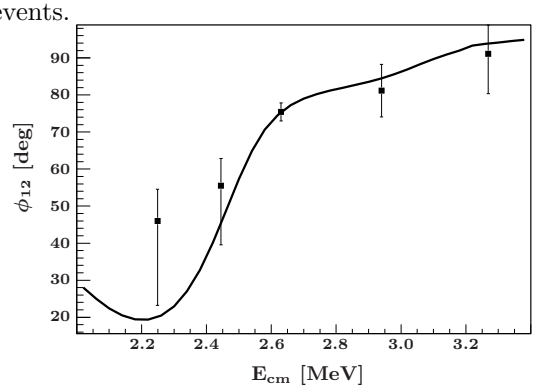

Figure 5.3: E1-E2 relative phase angle ϕ_{12} measured by the HIγS O-TPC, compared with the prediction from elastic scattering [Pla87], averaged over the beam energy distribution and cross section.

Preliminary results from the CO_2 target gas are shown in Fig. 5.3. Good agreement is found between the measured E1-E2 relative phase angle and predictions based on elastic scattering phase shifts. Additional data have been taken with a N_2O target at γ-ray beam energies between 9.3 and 9.8 MeV. These data are currently being analyzed and will help to confirm the results from the CO_2 target, while increasing the statistics to allow for a more accurate measurement of the E1/E2 cross section components and of ϕ_{12}.

[Ass06] Assunção *et al.*, Phys. Rev. C, **73**, 055801 (2006).

[Gai10] M. Gai *et al.*, J. Instrum., **5**, P12004 (2010).

[Pla87] R. Plaga *et al.*, Nucl. Phys. A, **465**, 291 (1987).

[Red87] A. Redder *et al.*, Nucl. Phys. A, **462**, 385 (1987).

5.1.2 Direct Observation of a New 2^+ State in ^{12}C with the HIγS O-TPC

W.R. Zimmerman, M.W. Ahmed, S.S. Henshaw, J.M. Mueller, S. Stave, H.R. Weller, *TUNL*; M. Gai, *University of Connecticut at Avery Point, Groton, CT*

The second $J^\pi = 2^+$ state in ^{12}C, predicted to exist over fifty years ago, has been directly observed in the photo-disintegration of ^{12}C into three α-particles using intense, nearly monoenergetic γ-ray beams available at the HIγS facility and an optical time-projection chamber to detect the outgoing α-particles. Complete angular distributions help to confirm the existence of a 2^+ state in ^{12}C at 10.06(4) MeV with a width of 800(60) keV. This discovery has significant implications for astrophysics and for the structure of the 0^+ "Hoyle" state.

Stellar synthesis of elements heavier than helium is thought to occur through the triple-α process, where two alpha particles fuse together to create a short-lived ^{8}Be nucleus, which fuses with another α-particle to form ^{12}C [Wal97]. Quiescent helium burning occurs at a temperature of 10^8 to 10^9 K, and is completely governed by the Hoyle state [Fow84]. However, during type II supernovae, γ-ray bursts, and other astrophysical phenomena, the temperature rises well above 10^9 K, and higher energy states in ^{12}C can have a significant effect on the triple-α reaction rate [Pru05, Sur11].

The current Nuclear Astrophysics Compilation of Reaction Rates (NACRE) assumes a theoretical 2_2^+ state at 9.12 MeV [Ang99]. However, the JINA REACLIB compilation uses the results of Fynbo *et al.* [Fyn05] and only includes a 2^+ state at 11 MeV. The triple-α reaction rates reported by the two compilations disagree by over a factor of ten at temperatures above 10^9 K.

An experiment to search for a possible 2_2^+ state in ^{12}C was performed at HIγS, using a CO_2 target and nearly monoenergetic γ-ray beams. Recoiling α-particles from the ^{12}C(γ,α)^{8}Be reaction were observed with an optical time-projection chamber (O-TPC) [Gai10]. By using a γ-ray beam, the 2_2^+ state in ^{12}C can be measured without contributions from the 3_1^- state at 9.6 MeV or the 0_3^+ state at 10.3 MeV [AS90], which have plagued previous experiments. Furthermore, this technique allows for a precise measurement of the electromagnetic decay width of the 2_2^+ state. This width is essential for calculating stellar triple-α reaction rates [Ang99].

Yields and angular distributions were measured at seven different γ-ray beam energies between 9.1 and 10.7 MeV. Fig. 5.4a shows the separated E1 and E2 components of the cross section, fit to Breit-Wigner resonances with energy-dependent level shifts and widths [Lan58], convolved with the measured γ-ray beam energy distribution.

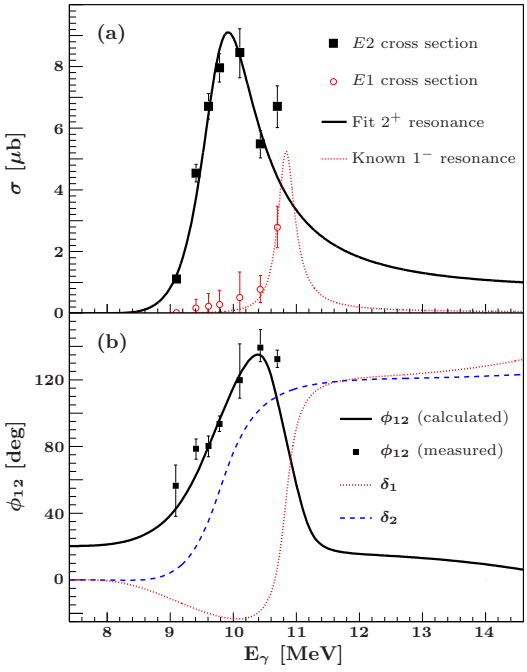

Figure 5.4: (Color online) Measured ^{12}C(γ,α_0)^{8}Be cross section and relative phase angle. The top figure shows the E1 and E2 components of the cross section. The E2 data are fit to a 2^+ resonance, and the E1 data are shown with a 1^- resonance of known width and energy [AS90] and with a strength adjusted to fit the data. The bottom figure shows the measured phase difference ϕ_{12}, along with calculations from a two-resonance model. The error bars include both statistical and systematic uncertainties.

The E1 cross-section data are consistent with the known 1^- resonance at 10.84 MeV [AS90]. The E2 cross-section data demonstrate the existence of a 2^+ state at 10.06(4) MeV with a width of 800(60) keV. Since the highest energy data point suggests a rising E2 cross section, the existence of a possible 2^+ state at higher energy [Fyn05, Hyl10] cannot be excluded.

In addition to the E1 and E2 relative cross sections, the angular distributions also provide measurements of the phase difference ϕ_{12}. Fig. 5.4b shows the measured phase differences, along with a curve representing a calculation of ϕ_{12} using a two-resonance model [Bar91]. Agreement between the measured phase differences and those predicted by the two-resonance model firmly establishes the resonance nature of the 2^+ strength reported here and indicates that there is little or no contribution from other amplitudes, except, perhaps, for the highest-energy data point.

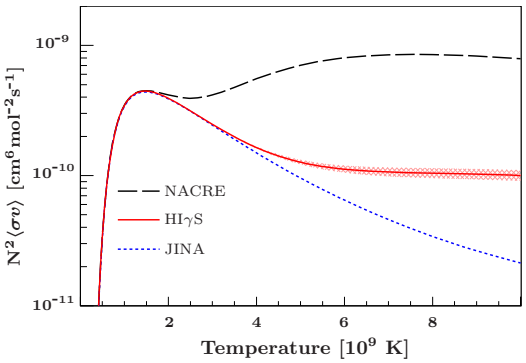

Figure 5.5: (Color online) Triple-α reaction rates, calculated using the 2_2^+ state observed with the HIγS O-TPC. The shaded region represents the propagated uncertainty from the measured state.

The 2_2^+ state at 10.06(4) MeV reported in this work lies 2.41 MeV above the 0^+ Hoyle state. This difference is 0.54 times the excitation energy of the 2_1^+ state above the ground state. Assuming that both 2^+ states are rotational states built on the two respective 0^+ states, this implies that the Hoyle state has a moment of inertia about twice as large as the ground state, or a root-mean-square radius which is around $\sqrt{2}$ times larger than that of the ground state, in agreement with the predictions of the FMD (fermionic molecular dynamics) model [Che07], but inconsistent with the leading-order results from lattice calculations [Epe11]. Future lattice calculations should be able to clarify this conjecture.

Figure 5.5 shows the triple-α reaction rates calculated for temperatures up to 10^{10} K, compared with the rates reported by NACRE [Ang99] and by the JINA REACLIB database [Cyb10]. The NACRE rate includes contributions from the Hoyle state, a 3^- state at 9.64 MeV, and a 2^+ state at 9.12 MeV. The JINA curve is based on the results of Fynbo *et al.* [Fyn05]. The new reaction rates denoted "HIγS" in the figure were calculated using the same states as NACRE, but substituting our measured values in place of NACRE's theoretical values for the second 2^+ state. Astrophysical simulations predict that during explosive burning scenarios, the triple-α reaction rate governs the freeze-out from nuclear statistical equilibrium at temperatures near 5 GK [Sur11]. At this temperature, the results from the present work predict a reaction rate that is 33% higher than that listed in the JINA REACLIB database, and more than five times smaller than that given by NACRE.

[Ang99] C. Angulo *et al.*, Nucl. Phys., **A656**, 3 (1999).

[AS90] F. Ajzenberg-Selove, Nucl. Phys., **A506**, 1 (1990).

[Bar91] F. C. Barker and T. Kajino, Aust. J. Phys., **44**, 369 (1991).

[Che07] M. Chernykh *et al.*, Phys. Rev. Lett., **98**, 032501 (2007).

[Cyb10] R. H. Cyburt *et al.*, Astrophys. J. Suppl. Ser., **189**, 240 (2010).

[Epe11] E. Epelbaum *et al.*, Phys. Rev. Lett., **106**, 192501 (2011).

[Fow84] W. A. Fowler, Rev. Mod. Phys., **56**, 149 (1984).

[Fyn05] H. O. U. Fynbo *et al.*, Nature, **433**, 136 (2005).

[Gai10] M. Gai *et al.*, J. Instrum., **5**, P12004 (2010).

[Hyl10] S. Hyldegaard *et al.*, Phys. Rev. C, **81**, 024303 (2010).

[Lan58] A. M. Lane and R. G. Thomas, Rev. Mod. Phys., **30**, 257 (1958).

[Pru05] J. Pruet *et al.*, Astrophys. J., **623**, 325 (2005).

[Sur11] R. Surman, G. C. McLaughlin, and N. Sabbatino, Astrophys. J., **743**, 155 (2011).

[Wal97] G. Wallerstein *et al.*, Rev. Mod. Phys., **69**, 995 (1997).

5.2 γ-^{3}He Interaction

5.2.1 Three- and Two-Body Photodisintegration of ^{3}He with Double Polarizations

H. Gao, M.W. Ahmed, P. Chu, W. Greene, M. Huang, H.J. Karwowski, G. Laskaris, J.M. Mueller, L.S. Myers, C. Peng, J.R. Tompkins, H.R. Weller, Y.K. Wu, Q.J. Ye, Y. Zhang, W.Z. Zheng, *TUNL*; T. Averett, *College of William and Mary, Williamsburg, VA*; D. Dutta, *Mississippi State University, Starkville, MS*; B. Lalremruata, *Mizoram University, India*; B. Tsang, *Michigan State University, East Lansing, MI*; Q. Ye, *Oak Ridge Associated Universities, Oak Ridge, TN.*

We present preliminary asymmetry results from an experiment on three-body photodisintegration of ^{3}He that took place in 2011 using a circularly polarized photon beam at incident energies of 12.8 and 14.7 MeV. We also present the newly designed apparatus for an experiment on two-body photodisintegration of ^{3}He with double polarizations at 20 MeV.

The goal of the experiments on the three- and two-body photodisintegration of ^{3}He with double polarizations is to test state-of-the-art three-body calculations and carry out studies towards the first investigation of the GDH sum rule [Dre66, Ger66] on ^{3}He below the pion-production threshold.

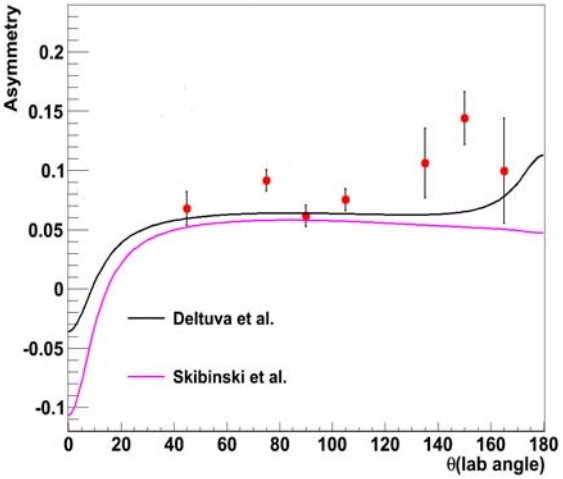

Figure 5.6: (Color online) The physics asymmetry as a function of neutron laboratory angle compared with calculations from Deltuva *et al.* [Del05, Del07] and Skibinski *et al.* [San03, San05]. The measured asymmetry values are for the detectors' $\pm 10^\circ$ angular acceptance. Work on acceptance-corrected values is near completion.

The experiment on the three-body photodisintegration of ^{3}He with double polarizations took data at HIγS from February 21 to March 5, 2011. A total of 150 hours of nearly 100% circularly polarized γ-ray beam with an energy spread of about 3% were used. The photon flux on target at 12.8 MeV and 14.7 MeV was 1.4–1.5×10^8 γ/sec and 1.0–1.1×10^8 γ/sec, respectively, using a 12 mm aperture.

The beam was incident on the hybrid ^{3}He target cell named SPOT. The density of ^{3}He is 6.48 ± 0.1 amagat (amg). Apart from ^{3}He, the pumping chamber contains a mixture of the alkali metals rubidium and potassium, as well as a small quantity (0.108 amg) of N_2. These are vital parts of the spin-exchange–optical-pumping (SEOP) technique [Hap72]. The target polarization throughout the experiment was 40 to 44%. During the experiment, the target-spin direction was flipped to form the spin-dependent asymmetry. To reduce the systematic uncertainties, we also flipped the helicity of the beam.

The neutrons from the $\overrightarrow{^3\mathrm{He}}(\overrightarrow{\gamma},n)pp$ reaction were detected using sixteen liquid-scintillator detectors positioned about one meter from the center of the cell. Each detector was placed inside a mu-metal cylinder to be shielded from the magnetic field. The pulse-height, time-of-flight relative to the beam bunch, and pulse-shape-discrimination signals were recorded for each detector. To subtract the background coming from the target container and from N_2 inside the cell and in the air, data were taken on a N_2 reference cell named Kielbasa. More details about the experiment can be found in [Ahm11]. Fig-

ure 5.6 shows the preliminary results for the physics asymmetries at 14.7 MeV with statistical uncertainties only. The results are displayed as a function of neutron angle in the laboratory frame and are integrated over a neutron kinetic energy range above 1.5 MeV. They are compared with the dynamical inputs based on the CD-Bonn+Δ-isobar [Del05, Del07] and AV18+UIX [San03, San05] models.

The analysis is currently in progress and the results on the partial spin-dependent differential and total cross sections will be available soon.

Although, the dominant contribution in the GDH integral below the pion production threshold is due to the three-body breakup channel, there is an important contribution from the two-body breakup channel as well. This contribution is the focus of the new experiment on the two-body photodisintegration of ^{3}He with double polarizations. The experiment was proposed to the HIγS PAC, and a total time of 60 hours of 100% circularly polarized γ-ray beam at 20 MeV was granted for testing and optimization of the experimental apparatus. The photon flux after the 12 mm collimator is expected to be $6 \times 10^7 \gamma$/sec and the energy spread of the beam will again be about 3%.

A cell similar to the ^{3}He cell used in the three-body breakup experiment will be employed in the new experiment. The main difference is that the wall thickness of the chamber will be a uniform 400 μm. The ^{3}He density of the new cell will be about 4 amg. Cells with such a thin wall have never been constructed before, but Mike Souza from Princeton University is working on constructing such a cell.

The protons from the two-body photodisintegration of polarized ^{3}He will be detected by seventy-two fully depleted Silicon Surface Barrier (SSB) detectors positioned at proton scattering angles of 40, 75, 95, and 120 degrees (eighteen detectors at each angle), each about 8 cm away from the center of the polarized ^{3}He target cell. The active areas of the detectors will vary from 300 to 450 mm^2. The minimum thickness of the detectors is 300μm, and their efficiency for charged particles is about 100%. The detectors will be provided by Michigan State University, and they will be collimated to ensure good angular resolution. Figure 5.7 shows a schematic of the newly designed ellipsoidal detector stand for mounting the detectors around the target chamber of the ^{3}He cell.

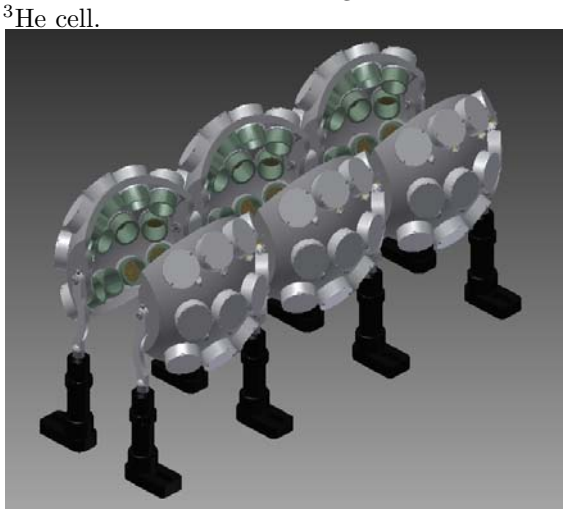

Figure 5.7: (Color online) SSB detectors positioned at 40°, 75°, 95° and 120° degrees scattering angles, 8cm away from the central axis of the target cell. Green color cylinders represent the collimators.

[Ahm11] M. W. Ahmed *et al.*, volume L, p. 98, 2011.

[Del05] A. Deltuva, A. C. Fonseca, and P. U. Sauer, Phys. Rev. C, **71**, 054005 (2005).

[Del07] A. Deltuva, A. Fonseca, and P. Sauer, Nucl. Phys., **A790**, 344c (2007).

[Dre66] S. D. Drell and A. C. Hearn, Phys. Rev. Lett., **16**, 908 (1966).

[Ger66] S. Gerasimov, Sov. J. Nucl. Phys., **2**, 430 (1966).

[Hap72] W. Happer, Rev. Mod. Phys., **44**, 169 (1972).

[San03] R. Skibiński *et al.*, Phys. Rev. C, **67**, 054001 (2003).

[San05] R. Skibiński *et al.*, Phys. Rev. C, **72**, 044002 (2005).

5.3 Study of Many-Body Systems

5.3.1 Compton Scattering on ^{89}Y at $E_\gamma = 23$ to 35 MeV at HIγS

M.H. Sikora, G. Feldman, *George Washington University, Washington DC*; M.W. Ahmed, J.M. Mueller, L.S. Myers, W.R. Zimmerman, H.R. Weller, *TUNL*

We have measured the isovector giant quadrupole resonance (IVGQR) of ^{89}Y via linearly polarized Compton scattering at $E_\gamma = 23$ to 35 MeV. Elastically scattered photons were detected in the eight NaI crystals of the HIγS NaI Detector Array (HINDA). The ratio of out-of-plane to in-plane yields can then be used to extract the IVGQR values. Preliminary results are presented.

In February 2012 a polarized Compton scattering experiment was performed on an ^{89}Y target using the eight-element HINDA NaI detector system in order to extract the IVGQR parameters. Based on the phenomenological model of the Compton scattering amplitude developed by Wright [Wri85], the polarization ratio $R(\theta)$=$\sigma_\perp/\sigma_\parallel$ is predicted to change sign between forward and backward angles, due to the cos(θ) dependence of the E1-E2 interference term. This change can be used to determine the pure E1 contribution, so that any deviation from this line in the observed polarization ratio can be attributed to E2 strength. Simultaneous measurement of $R(\theta)$ at angles symmetric around θ=90° significantly reduces the uncertainty in the extracted IVGQR parameters. This method was first applied in 2010 at HIγS with ^{209}Bi [Hen11], yielding improvements in the reported uncertainties of the IVGQR parameters of up to an order-of-magnitude. A detailed knowledge of the A-dependence of the IVGQR can be used to study the symmetry-energy term in the nuclear equation-of-state, thus providing insight into the properties of nuclear matter in extreme conditions, such as in neutron stars [Pie11].

The setup for the present measurement is shown in Fig. 5.8. Linearly polarized photons impinged on a 100% ^{89}Y target. Four HINDA cores were placed at a polar angles of 55° and four at 125°. At each polar angle two detector cores were placed in a plane parallel to the direction of incident photon polarization and two in a plane perpendicular to the polarization direction.

The run consisted of approximately 70 hours of beam on target at 16 incident photon energies ranging from 23 to 35 MeV. This includes scattering with a circularly polarized beam at 25, 30, and 35 MeV. These data were used to correct for instrumental asymmetries. Typical spectra at forward and backward angles are shown in Fig. 5.9. Compton scattered events are identified cleanly at backward angles, while at forward angles the tail of the large background from atomic interactions extends into the elastic peak.

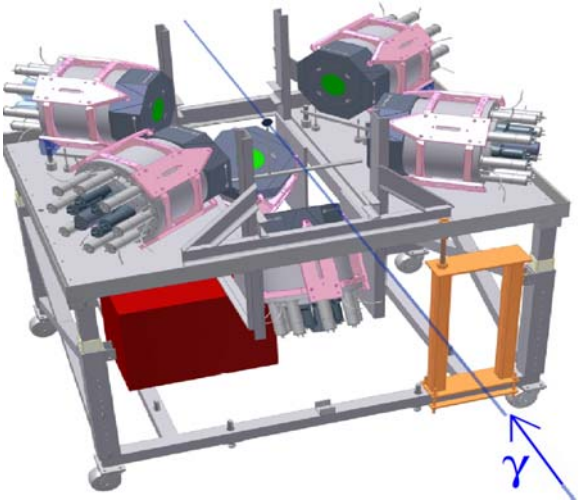

Figure 5.8: (Color online) Illustration of the HINDA and target positions. Two out of plane detectors are not shown for visual clarity.

Yields were extracted using a GEANT4 simulation of the above configuration. Elastic scattering was modeled by generating photons isotropically at the center of the virtual target and recording the energy deposited in the detectors. This generates a response function for elastically

scattered photons in each individual HINDA element. These spectra were then convolved with a Gaussian smearing function to fit the scattering data, where the smearing function accounts for the detector resolution and the beam energy spread. The convolved spectra were then characterized with a Landau distribution that defined a consistent summing window. This procedure was carried out at each measured energy.

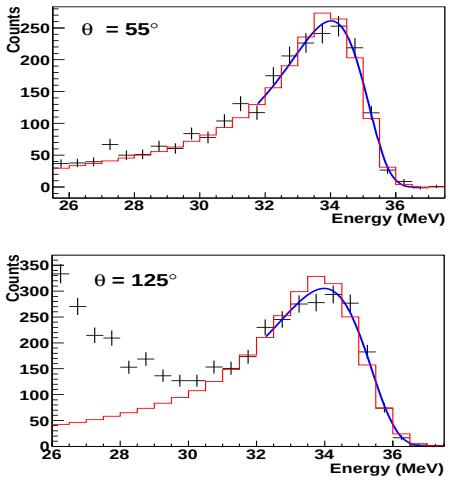

Figure 5.9: (Color online) Sample spectra at forward and backward angles. The points show the data, the solid curve is the Landau distribution, and the dotted histogram is the simulation.

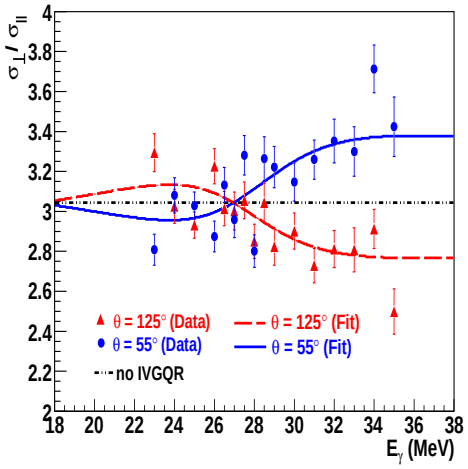

Figure 5.10: (Color online) Preliminary fit of the measured polarization ratios to determine the parameters of the IVGQR in ^{89}Y. The pure E1 contribution is given by the dashed line.

After applying correction factors obtained from the measurements with circular polarization, the ratio of perpendicular to parallel yields was formed at both forward and backward angles (see Fig. 5.10). The IVGQR excitation energy, width, and strength in units of the isovector energy-weighted sum rule (IVEWSR) appear as free parameters in the functional form of the polarization ratio. Preliminary results for the resonance parameters are shown in Fig. 5.11 alongside previous IVGQR measurements listed in [Hen11, Pit80, Zor87].

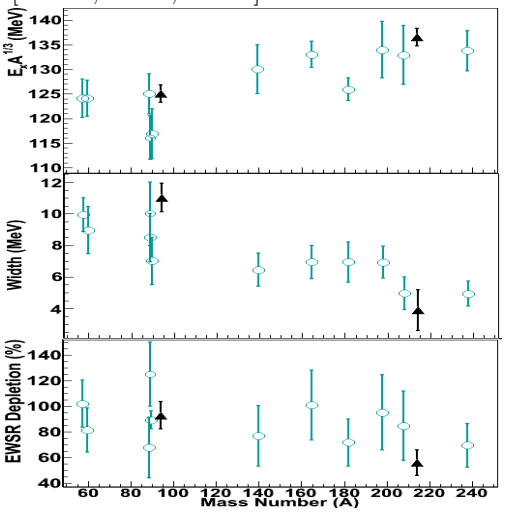

Figure 5.11: (Color online) Extracted IVGQR parameters of previous experiments (open circles) and HIγS results (triangles) for ^{89}Y and ^{209}Bi. The HIγS values have been shifted by five mass units for visual clarity.

The analysis will be finalized in the coming months. This will require determination of the systematic uncertainties and testing the stability of the extraction procedure for the resonance parameters. Future experimental runs are planned in the A=120 mass region.

[Hen11] S. Henshaw *et al.*, Phys. Rev. Lett., **107**, 22501 (2011).

[Pie11] J. Piekarewicz, Phys. Rev. C, **83**, 034319 (2011).

[Pit80] R. Pitthan, In F. Bertrand, editor, *Giant Multipole Resonances: Proceedings of the Giant Multipole Resonance Topical Conference*, Oak Ridge, TN, 1980.

[Wri85] D. Wright *et al.*, Phys. Rev. C, **32**, 1174 (1985).

[Zor87] R. Zorro *et al.*, Nucl. Phy., **A472**, 125 (1987).

5.3.2 Nuclear Resonance Fluorescence of ^{96}Zr

S.W. Finch, C. Bhatia, G. Rusev, W. Tornow, *TUNL*

A nuclear resonance fluorescence (NRF) experiment was carried out on ^{96}Zr at the HIγS facility with beam energies from 3.55 to 7.5 MeV. Several new transitions have been identified, and information on the parity of the states was extracted.

The energy range between about 3.5 and 4.5 MeV is of interest for two-phonon studies, while the energy range centered at around 6 MeV is of importance for establishing the role of the pygmy dipole resonance in ^{96}Zr.

The coupling of two vibrational states is referred to as two-phonon excitations. The coupling of the ^{96}Zr states 3_1^- (1897 keV) and 2_2^+ (2225 keV) leads to a quintuplet of states with $J^\pi = 1^-$ to 5^- and energies close to the sum of the energies of the two states. The two-phonon 1^- state de-excites via E1 radiation to the 0^+ ground state. Spin and parity assignments for the states at 3620, 3700, and 4132 keV were made at Darmstadt [Pie09]. The values are 1^+ (M1) for the first two states and 1^- (E1) for the third. Parity information for other states with excitation energies around 4 MeV is currently unavailable.

The isotope ^{96}Zr consists of 40 protons and 56 neutrons. The proton sub-shell $2p_{1/2}$ and the neutron sub-shell $2d_{5/2}$ are completely filled, making ^{96}Zr comparable to double-magic nuclei. Therefore, ^{96}Zr is ideal for studying the pygmy dipole resonance which has been investigated in the past mainly in magic nuclei or in nuclei in their vicinity. At Darmstadt [Zwe11], the energy region of importance for the pygmy dipole resonance has been studied with bremsstrahlung beams with endpoint energy of 5 and 7.7 MeV, but parity assignments could not be made. States belonging to the pygmy dipole resonance should be of E1 character.

Data were taken at the HIγS facility using linearly polarized γ rays. Twenty-two different beam energies, ranging from 3.55 to 7.5 MeV, were chosen such that all transitions from 3620 to 7629 keV could be studied when the 4-5% photon beam width was factored in. The energies were below ^{96}Zr's neutron separation energy of 7.855 MeV. The target consisted of 7.28 g of ZrO_2 enriched to 91.39% in ^{96}Zr. The sample was housed in a plastic disk with a thickness of 10.22 mm, a diameter of 31.75 mm, and a wall thickness of 1.4 mm.

The detector array consisted of six high-purity germanium (HPGe) detectors. Two 60% HPGe detectors were horizontally mounted in the plane of beam polarization. One 60% and one 25% detector were vertically mounted, perpendicular to the beam polarization. Another 25% detector was placed at a backward angle of 135° from the beam line, in the plane of polarization. The final detector was used for beam energy and flux measurements. Since the HIγS beam is 100% linearly polarized, an in plane/out of plane asymmetry in our detectors may be used to characterize the transition as either an E1 or M1 excitation. Figure 5.12 illustrates the degree of asymmetry in three transitions observed with our ^{96}Zr target. As can be seen, the 4132 keV state has E1 character, as assigned by [Pie09]. The states at 3947 and 4038 keV are 1^+ (M1) states. Previously these parities were unknown.

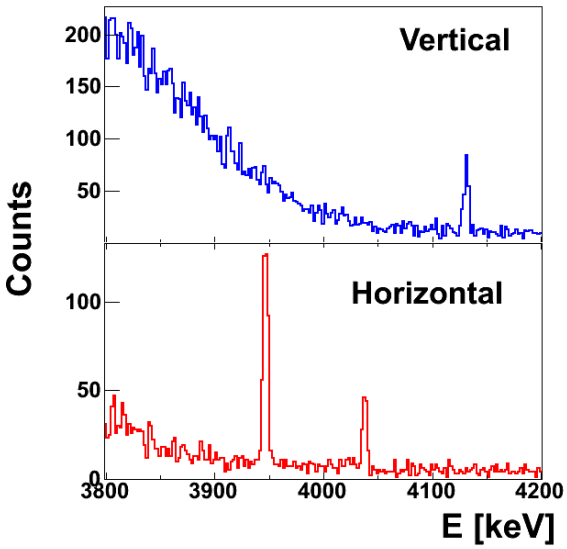

Figure 5.12: (Color online) Typical energy spectrum showing the in plane and out of plane detectors. The asymmetry is used to determine state parity.

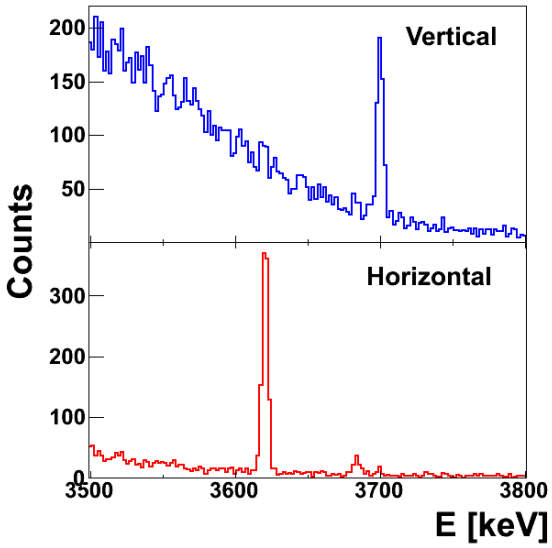

Figure 5.13: (Color online) The 3620 and 3700 keV states, M1 and E1 transitions respectively.

In all, 62 transitions were observed and a parity assigned for each. Of these, 35 transitions are not currently listed in the NNDC database and 13 were not seen by Ref. [Zwe11]. Furthermore, the parity assigned to the 3700 keV transition by Ref. [Pie09] was found to be inconsistent with our data. Figure 5.13 shows the 3620 and 3700 keV transitions, which were both assigned $\pi = +1$ by Ref. [Pie09]. Our data indicates the 3620 keV state is indeed 1^+, but the 3700 keV state is actually 1^-. No M1 transitions were observed above an incident photon energy of 5 MeV, supporting recent findings that the pygmy dipole resonance is comprised of E1 excitations. Currently, work is being done to extract cross-section information for the stronger transitions.

[Pie09] N. Pietralla *et al.*, In *Proceedings of the International Conference on Nuclear Structure and Related Topics, Joint Institute for Nuclear Research, Dubna, Russia*, 2009.

[Zwe11] M. Zweidinger, Master's thesis, Technische Universitaet Darmstadt, 2011.

5.3.3 Study of the Spin-Flip M1 Resonance in ^{206}Pb

C. Bhatia, C.W. Arnold, G. Rusev, R. Raut, J.H. Kelley, A.P. Tonchev, W. Tornow, S.L. Hammond, C.R. Howell, *TUNL*

The spins, parities, branching ratios and decay widths of excited states in ^{206}Pb have been measured from 5 to 9 MeV, using nuclear resonance florescence in conjunction with 100% linearly polarized photon beams from the HIγS facility. Data analysis is underway.

The strength and the location of the M1 giant resonance in medium- and heavy-mass nuclei has been a long-standing problem in nuclear structure physics because of the large discrepancies between experimental and theoretical results. The small size of the measured M1 strength relative to the predicted strength is often called quenching. Predicting the magnitude and distribution of the M1 strength is a major problem for theory, since there is no model-independent sum-role. In general, the total M1 strength depends on the properties of the ground-state wave function.

Most of the experimental and theoretical investigations of the M1 spin-flip resonance have been devoted to the doubly magic ^{208}Pb nucleus [Shi08]. ^{206}Pb has only two neutrons less than ^{208}Pb, but the excitation spectra of these two nuclei differ significantly. Moving from the magic ^{208}Pb nucleus to its neighbors results in a much higher density of complex configurations at the same excitation energies. Hence, there is an expectation of strong fragmentation of the M1 strength in ^{206}Pb compared to ^{208}Pb. For ^{208}Pb, the neutron separation energy is 7.4 MeV, and very close to the energy where the isovector M1 resonance should be located [Pon87]. For ^{206}Pb the neutron separation energy is 8.1 MeV, significantly higher than for ^{208}Pb. Therefore a larger part of the total M1 strength can be observed with real photon beams for ^{206}Pb.

The spin-flip M1 strength in ^{206}Pb has been measured in photon scattering experiments with quasi-monochromatic and 100% linearly polarized photon beams at the HIγS facility. Details of the experiment are presented in Ref. [Arn11]. The HIγS beam, in combination with high-resolution HPGe detectors, was used to precisely deduce the strength and location of the individual M1 transitions that make up the giant M1 resonance. The HPGe detectors were positioned at specific angles relative to the incident photon beam to unambiguously distinguish M1 transitions from E1 and E2 de-excitations.

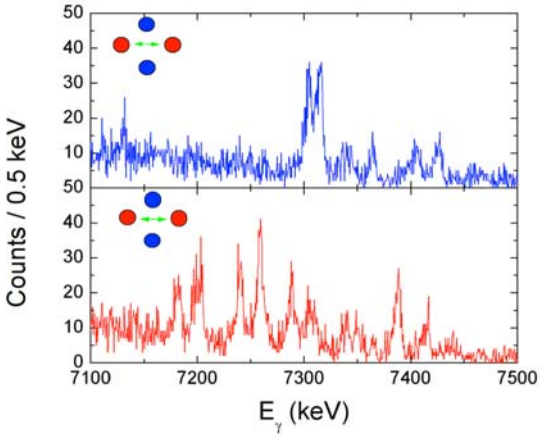

Figure 5.14: Spectra obtained with a photon beam of 7.25 MeV mean energy. The top panel shows results for the vertical detectors indicating E1 transitions. The bottom panel corresponds to the horizontal detectors implying M1 transitions.

A portion of the γ-ray spectra obtained with a photon beam of energy 7.25 MeV is shown in Fig. 5.14. In the preliminary data analysis, we have observed about 93 E1 transitions, of which 40 are newly discovered and 35 M1 transitions, of which 23 are newly discovered.

[Arn11] C. W. Arnold *et al.*, TUNL Progress Report, **L**, 106 (2011).

[Pon87] V. Ponomarev *et al.*, J. Phys. G: Nucl. Phys., **13**, 1523 (1987).

[Shi08] T. Shizuma *et al.*, Phys. Rev. C, **78**, 061303(R) (2008).

Applications of Nuclear Physics and Nuclear Data Evaluation

Chapter 6

- **Homeland and National Nuclear Security**
- **Pyroelectric Research**
- **Public Health Research**
- **Nuclear Data Evaluation**

6.1 Homeland and National Nuclear Security

6.1.1 Photofission Fragment Asymmetry Studies on ^{232}Th and ^{238}U

J.R. Tompkins, M.W. Ahmed, A. Collins, A. Hill, H.J. Karwowski, L.S. Myers, J.M. Mueller, G.C. Rich, J. Silano, *TUNL*; B.J. Davis *North Carolina Central University, Durham, NC*

The first ever measurements of fission fragment angular distributions induced with 100% linearly-polarized, monoenergetic photon beams for ^{238}U and ^{232}Th have been completed at near-barrier energies. The observed angular anisotropies are important for understanding recently observed anisotropies in the accompanying prompt-fission neutrons produced with similar beams. The fragment anisotropy is substantial and observed to decrease with increasing photon energy.

Photofission-fragment angular distributions (PFADs) have been the subject of many studies since they were discovered by Winhold, Demos, and Halpern in 1952 [Win52]. These studies have revealed systematics in the anisotropy that provide insight into the fission barrier and into the states of minimal spin through which photofission occurs [Van73]. However, prior to the present work, all PFAD studies have employed beams with minimal to no polarization or were characterized by a continuous energy spectrum. This lack of PFAD data obtained with 100% linearly-polarized photon beams of well-defined energy is not ideal for understanding the recently observed angular anisotropies of the accompanying prompt-fission neutrons [Mue12]. The simplest explanation for the existence of a prompt-fission neutron anisotropy is that it is merely a reflection of an underlying fragment anisotropy. Though investigations of this hypothesis using the previous data have been fruitful, the clearest investigation would be based on PFAD data obtained with similar beams.

The first ever measurements of PFADs using beams of 100% linear polarization and energy spreads of approximately 3% have been made. The characteristics of the photon beams produced at HIγS for this work are listed in Table 6.1. The beams induced fission on targets of ^{238}U and ^{232}Th with thicknesses of 0.09 cm and 0.10 cm, respectively.

Fission fragments were detected using four Micron Semiconductor YY1 silicon strip detectors (SSDs) used in previous work [Mit98, Kel02]. These were paired together and positioned using a previously designed mounting system [Tom11]. Each detector pair was sensitive to anisotropies with respect to rotation about the beam axis, characterized by the azimuthal angle ϕ. This was accomplished by positioning the detectors such that one detector lay in the plane of beam polarization and the other in the plane perpendicular to it. The geometry of the strip contacts on each SSD provided further sensitivity to anisotropies with respect to the polar angle, θ, which was measured from the beam axis. Each SSD contained sixteen strip contacts. Individual contacts were sensitive to a spread of θ that varied from strip to strip. These were between 6° and 20° and differed as a result of relative target-to-strip distances. The paired detectors were aligned so that the matching strip contacts were sensitive to the same fractional solid angle.

Table 6.1: List of the photon beam characteristics produced by HIγS during this experiment, including the flux on target.

Energy (MeV)	Polarization	Flux (γ/s)	Target
5.7	Linear	1.3×10^7	^{238}U
5.9	Linear	2.2×10^7	^{232}Th
6.2	Linear	1.1×10^7	^{232}Th,^{238}U
6.2	Circular	1.5×10^7	^{238}U
6.7	Linear	2.5×10^7	^{232}Th
6.7	Circular	2.3×10^7	^{232}Th
7.2	Linear	2.7×10^7	^{232}Th
7.6	Linear	2.6×10^7	^{232}Th
7.6	Circular	2.5×10^7	^{232}Th

Ratios of the fragment yields measured by paired strip contacts were formed at each angle θ. These yield ratios are plotted in Fig. 6.1. It is

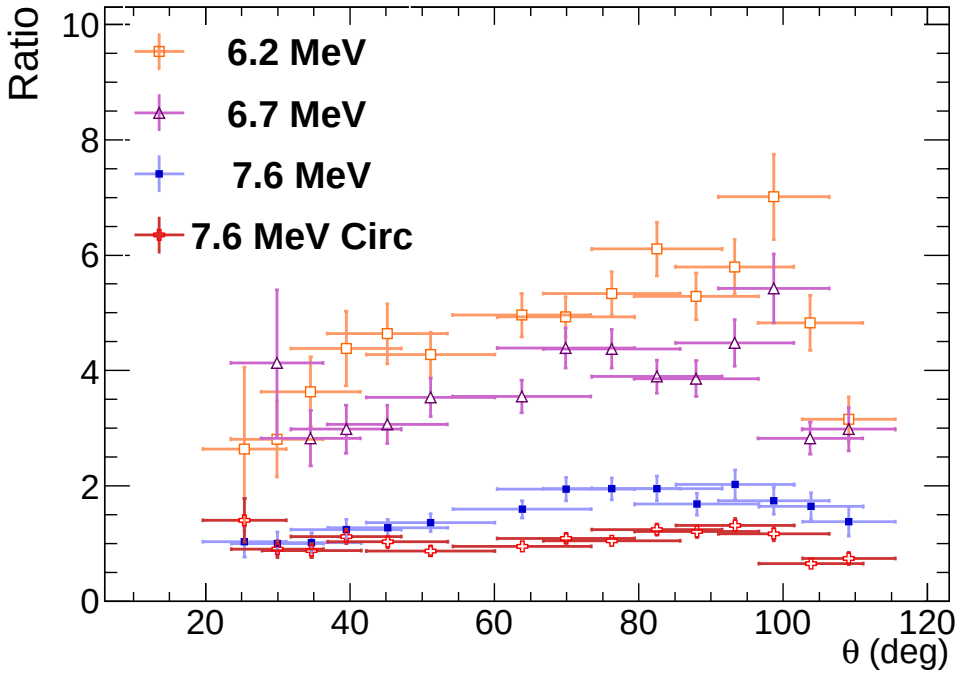

Figure 6.1: (Color online) Yield ratios from ^{232}Th as a function of polar angle. Only points corresponding to the forward angles have been plotted. All of the datasets shown were produced with 100% linearly-polarized photon beams, unless otherwise indicated.

clear that the anistropy diminishes with increasing energy. Further, the ratio peaks at angles slightly less than 90°. There is no reason to expect a ratio that is asymmetric about $\theta = 90°$ based on the formalism of Bohr [Boh55]. However, the detection of events with respect to ϕ is biased as a result of the rotation of the target and the straggling of fragments within it prior to detection. Substantial modeling efforts employing the GEANT4 toolkit [Ago03] have corroborated this fact. Fitting is underway to extract parameters that characterize the angular distributions.

[Ago03] S. Agostinelli *et al.*, Nucl. Instrum Methods A, **506**, 250 (2003).

[Boh55] A. Bohr, In *International Conf. on Peaceful Uses of Atomic Energy*, volume 2, p. 151, New York, 1955. United Nations.

[Kel02] J. H. Kelley *et al.*, TUNL Progress Report, **XLI**, 136 (2002).

[Mit98] G. E. Mitchell *et al.*, TUNL Progress Report, **XXXVII**, 5 (1998).

[Mue12] J. M. Mueller *et al.*, Phys. Rev. C, **85**, 014605 (2012).

[Tom11] J. R. Tompkins *et al.*, TUNL Progress Report, **L**, 112 (2011).

[Van73] R. Vandenbosch and J. R. Huizenga, *Nuclear Fission*, Academic Press, New York, 1973.

[Win52] E. J. Winhold, P. T. Demos, and I. Halpern, Phys. Rev., **87**, 1139 (1952).

6.1.2 Measurements of Neutron-Polarization Asymmetries in Photofission of ^{235,238}U, ^{239}Pu, and ^{232}Th

J.M. Mueller, M.W. Ahmed, S.S. Henshaw, H.J. Karwowski, L.S. Myers, B.A. Perdue, S. Stave, J.R. Tompkins, H.R. Weller, *TUNL*; B.J. Davis, D.M. Markoff, *North Carolina Central University, Durham, NC*;

Photofission experiments were performed on ^{235,238}U, ^{239}Pu, and ^{232}Th using linearly polarized, high intensity, and nearly-monoenergetic γ rays with energies between 5.6 and 7.3 MeV. Eighteen liquid scintillating detectors were used to measure prompt-fission-neutron angular distributions. The measured ratio of yields parallel and perpendicular to the plane of beam polarization is near unity for ^{235}U and ^{239}Pu, while a ratio of about three was found for ^{238}U and ^{232}Th. A phenomenological model of near-threshold photofission has been developed to explain this large difference.

This contribution summarizes recently published measurements of prompt neutron polarization asymmetries in photofission [Mue12]. Previous measurements using unpolarized bremsstrahlung beams have indicated large anisotropies in fission fragment angular distributions [Rab70]. These anisotropies are largest for beam energies of 5 to 10 MeV in even-even actinide targets. If a linearly polarized beam were applied, these anisotropies in θ would become anisotropies in ϕ. Shortly after a target nucleus fissions, each fission fragment emits one or several prompt neutrons. Because these neutrons are emitted after the fragments have fully accelerated, the expected polarization asymmetries in the fission fragments could produce polarization asymmetries in the prompt neutrons. Potential applications of polarization asymmetries in prompt neutrons include a novel method of interrogation for special nuclear materials.

Experiments were performed at HIγS to investigate prompt-neutron-polarization asymmetries resulting from photofission of ^{235,238}U, ^{239}Pu, and ^{232}Th. Eighteen liquid scintillator detectors, placed at angles of 55°, 72°, 90°, 107°, 125°, and 142° in θ and 0°, 90°, 180°, and 270° in ϕ, were used to measure prompt-fission neutrons. A nearly 100% linearly polarized beam with an intensity of about $10^7\gamma/s$ was used to investigate polarization effects in these neutrons. Neutron spectra from the photofission of ^{235,238}U are shown in Fig. 6.2. A circularly polarized beam was then used to correct for small instrumental asymmetries.

In the case of photofission of ^{235}U and ^{239}Pu, approximately equal prompt-neutron yields were measured parallel and perpendicular to the plane of beam polarization, as shown in Fig. 6.3. However, in photofission of ^{238}U or ^{232}Th, a factor of about three more prompt neutrons was detected parallel to the plane of beam polarization than perpendicular to it. This polarization ratio in the prompt neutrons peaked at 90° in θ, and prompt neutrons with more energy were found to have a larger polarization ratio than neutrons with less energy as shown in Fig. 6.4.

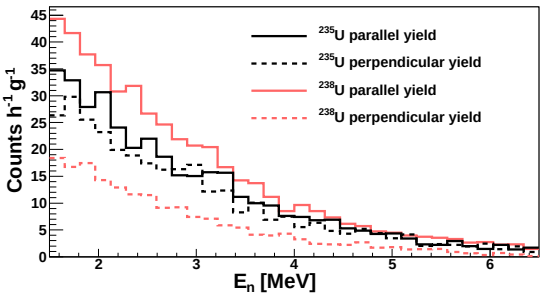

Figure 6.2: (Color online) Comparison of the raw neutron spectra for ^{235,238}U, parallel and perpendicular to the plane of beam polarization, at 90° in θ with beam energies of 5.8 to 6.2 MeV and $\sim 5 \times 10^6\gamma/s$ on target.

A simulation of prompt-neutron angular distributions has been developed to interpret these experimental results. For the simulation, it was assumed that the fission-fragment angular distributions from the photofission of ^{238}U, ^{239}Pu, and

^{232}Th were well determined in previous experiments [Rab70, Sol70]. A simulation was not performed for ^{235}U because the fission-fragment angular distribution has been measured to be consistent with isotropy [Zhu78], implying a polarization ratio equal to 1.0.

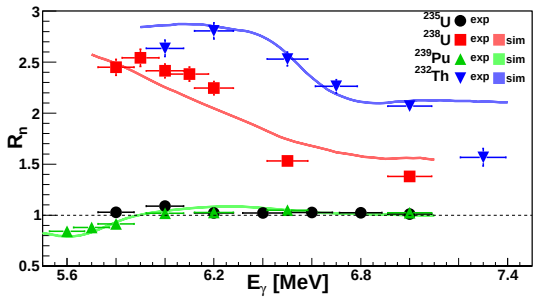

Figure 6.3: (Color online) Comparison of the experimental and simulated prompt neutron polarization ratios as a function of γ-ray beam energy. Only prompt neutrons at 90° in θ with energies greater than 1.5 MeV are shown.

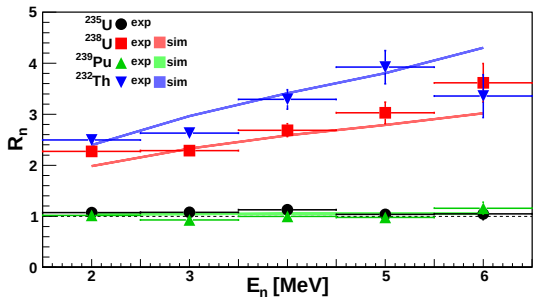

Figure 6.4: (Color online) Comparison of the experimental and simulated prompt neutron polarization ratios as a function of neutron energy. Only the results at 90° in θ at beam energies between 5.8 and 6.2 MeV are shown.

.

In the simulation, two fission fragments are generated according to the fragment angular distribution for that beam energy, modified to account for the linearly polarized beam used at HIγS assuming only electric photoabsorption. The masses of the fragments are randomly selected from the asymmetric fragment mass distribution, and the total kinetic energy of the fragments is fixed to equal the measured average total kinetic energy [Eng92, Van74]. Then, after the fragments' momentum vectors are calculated, each fragment is assumed to emit exactly one prompt neutron. The prompt neutron is emitted with no preferred direction in the rest frame of the fragment, and the kinetic energy of the neutron in this frame is chosen from a modified evaporation spectrum [Fra52]. Then the neutron is boosted into the laboratory frame, and its laboratory momentum vector is calculated. Finally, the neutron is allowed to propagate in a straight line, and a hit is recorded if its path intersects a detector.

Good agreement is found between the simulated and experimental results, as shown in Figs. 6.3 and 6.4. The simulation reproduces the trend of increasing ratio with increasing neutron energy, and it accurately models the decreasing ratio with increasing beam energy. This agreement suggests that the prompt neutron emission mechanism is accurately described by the simulation. Future work will investigate potential improvements in the simulation. Additional experimental measurements of prompt neutron polarization ratios from photofission of ^{233}U, ^{237}Np, and ^{240}Pu will be performed.

[Eng92] T. England and B. Rider, *Evaluation and Compilation of Fission Yields*, 1992, ENDF-349, LA-UR-94-3106, Extracted from ENDF.

[Fra52] J. S. Fraser, Phys. Rev., **88**, 536 (1952).

[Mue12] J. M. Mueller *et al.*, Phys. Rev. C, **85**, 014605 (2012).

[Rab70] N. S. Rabotnov *et al.*, Yad. Fiz., **11**, 508 (1970).

[Sol70] A. S. Soldatov, Yu. M. Tsipenyuk, and G. N. Smirenkin, Sov. J. Nucl. Phys., **11**, 552 (1970).

[Van74] R. Vandenbosch and J. R. Huizenga, *Nuclear Fission*, Academic Press Inc., 1974.

[Zhu78] V. E. Zhuchko *et al.*, Sov. J. Nucl. Phys., **27**, 746 (1978).

6.1.3 Linearly Polarized Beam-Induced Photoneutron Yield Ratios in ^{9}Be

D.M. Markoff, B.J. Davis, *North Carolina Central University, Durham, NC*; M.W. Ahmed, H.J. Karwowski, J.M. Mueller, L.S. Myers, S.C. Stave, J.R. Tompkins, H.R. Weller, W. Zimmerman, *TUNL*

The ratio of photoneutron yields parallel and perpendicular to the plane of polarization of the γ-ray beam has been measured for the ^{9}Be(γ,n)^{8}Be reaction. The data were taken for γ-ray energies between 5.5 and 15.5 MeV. The lower energy range is of interest for interrogation of special nuclear materials. The higher energy data includes regions near the resonances at 11.3, 11.8 and 13.8 MeV plus one energy below these resonances and one above them. The photoneutron yield ratio is found to increase from about 2.5 to 6.5 as the γ-ray energy increases from 5.5 to 15.5 MeV.

Photoneutron yields from the ^{9}Be(γ,n)^{8}Be reaction were measured to determine the ratio of the yields parallel and perpendicular to the plane of γ-ray-beam polarization. This effort is part of the DNDO program at TUNL to measure the neutron yield ratios using polarized γ rays for cargo interrogation of special nuclear materials. A 2.54 cm thick ^{9}Be cylindrical target of diameter 1.9 cm was placed axially in the beam. The array of 18 neutron detectors used for these measurements has a half-meter flight path and is described in detail in Ref. [Tom10].

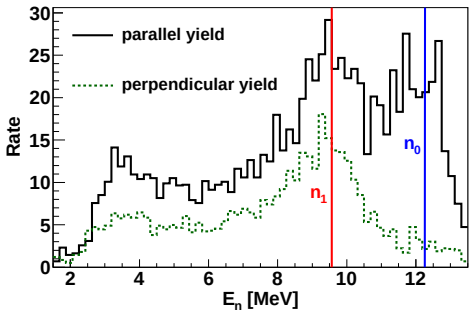

Figure 6.5: (Color online) Photoneutron rates in counts/(hr g) at a polar angle of 90° for 15.5 MeV linearly polarized γ rays. The total rates from the 90° detectors parallel and perpendicular to the plane of γ-ray polarization are shown separately. The γ-ray intensity is about $10^{7}\gamma$/s.

An example of the differences in the neutron yields parallel and perpendicular to the plane of γ-ray-beam polarization is shown in Fig. 6.5. The data are for a linearly polarized beam of 15.5 MeV γ rays and detectors located at 90° in polar angle relative to the beam axis. The high yield ratios measured at this energy are clearly seen in the large difference in rates between the two spectra. The spectra also show structure around the energies associated with decays through the ground and first excited states in ^{8}Be. The expected energies of the neutrons emitted in the decays to the ground state (n_0) and the first excited state (n_1) are indicated in Fig. 6.5 at 12.3 and 9.6 MeV, respectively. Note that the indicated energies include the recoil energy loss and the transformation to the laboratory frame.

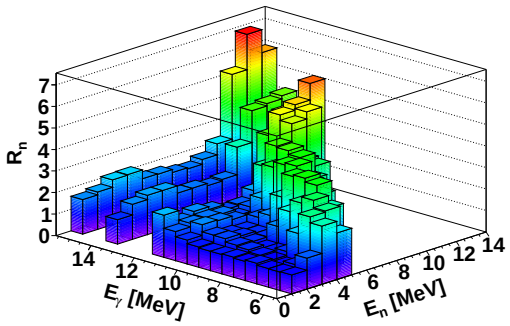

Figure 6.6: (Color online) Photoneutron yield ratios as a function of outgoing neutron energy for linearly polarized γ rays at energies between 5.5 and 15.5 MeV and at a laboratory angle of 90°.

We measured the ratio of the parallel and perpendicular yields $R_n = (I_{par}/I_{perp})$ for five incident energies between 10.5 and 15.5 MeV and at energies in 0.5 MeV steps between 5.5 and 10.0 MeV. The photoneutron yield ratios for 90° are presented in Fig. 6.6 as a function of outgo-

ing neutron energy for each incident γ-ray energy. In Fig. 6.7, the ratios for the expected n_0 and n_1 neutrons emitted at 90° are plotted as a function of incoming γ-ray energy. The ratios are nearly one for the n_1 neutrons, indicating that the larger overall asymmetries arise from neutrons that decay from the ground state. For the n_0 yields, the ratios initially increase as a function of γ-ray energy from a value of about 2.5 at 5.5 MeV to a value of about 4 at 10 MeV. Then the ratio becomes nearly constant with energy until a jump to a relatively large ratio of 6.5 at 15.5 MeV. An effort has been initiated to compare the measured ratios to calculations based on a direct-capture model including resonances.

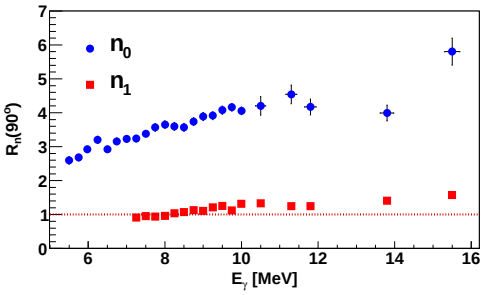

Figure 6.7: (Color online) Photoneutron yield ratios from neutrons emitted to the ground state (n_0) and to the first excited state (n_1) as a function of incoming linearly polarized γ-ray beam energy between 5.5 and 15.5 MeV and at a laboratory angle of 90°.

We note that Fig. 6.5 contains a peak around 3.3 MeV in the parallel-yield γ-ray spectrum. This peak seen in the 15.5 MeV data corresponds to the series of rising ratios in Fig. 6.6 at γ-ray energies above 10 MeV and at low neutron energies. These ratios are located at energies consistent with the γ-ray-induced decay of ^{9}Be to ^{5}He and an α particle, with the ^{5}He decaying in flight to produce the detected neutron.

The measured ratios from ^{9}Be shown in Fig. 6.6 are typically larger than the ratios for nuclei we have studied—Cd, Sn, Ta—that are common in structural materials [Mye11]. The beryllium ratios between 5 and 6 MeV are slightly smaller than those measured at 90° from a ^{238}U target [Mue11]. Although the asymmetries are comparable to those of ^{238}U, the emitted neutron energies are very different, which may provide a means to distinguish beryllium from the uranium isotope in a composite material.

[Mue11] J. M. Mueller *et al.*, TUNL Progress Report, **L**, 114 (2011).

[Mye11] L. S. Myers *et al.*, TUNL Progress Report, **L**, 118 (2011).

[Tom10] J. R. Tompkins *et al.*, TUNL Progress Report, **XLIX**, 140 (2010).

6.1.4 Photoneutron Polarization Ratios of ^{nat}Ce, ^{139}La, ^{nat}Dy, and ^{nat}Hg

L.S. Myers, M.W. Ahmed, J.M. Mueller, H.R. Weller, W.R. Zimmerman, *TUNL*; C.S. Whisnant, J.H. Devilbiss, W.R. Henderson, R.K. Thrasher, *James Madison University, Harrisonburg, VA*; D. Markoff, B.J. Davis, *North Carolina Central University, Durham, NC*; R.M. Prior, M.C. Spraker, *North Georgia College & State University, Dahlonega, GA*; R.H. France *Georgia College & State University, Macon, GA*

Photoneutron emission was studied using targets of natural cerium, lanthanum, dysprosium and mercury with a beam of linearly polarized γ rays at energies of 11 to 15 MeV. Eighteen liquid-scintillator neutron detectors, covering the angular range of 55° to 142°, were employed. The ratio of the neutron yield in the plane of beam polarization versus that perpendicular to the plane was measured.

6.1.4.1 Motivation

The photoneutron polarization ratios of several elements in the lanthanide series and of natural mercury were measured using linearly polarized γ rays. These data are part of the larger DNDO-funded research being conducted at the HIγS facility. The aim is to determine if neutron polarization ratios (the ratio of the neutron yield in the plane of beam polarization versus those perpendicular to that plane) can be used to uniquely identify fissile materials. The data discussed here are important for baseline comparisons.

6.1.4.2 Detector Array

The neutron detectors used in this experiment were arranged on a mount consisting of two rings. One ring was oriented perpendicular to the plane of the beam polarization and was centered over the target. The other ring was oriented parallel to the plane of polarization. Four detectors were placed at each of the scattering angles of 55°, 90° and 125° (two in the plane and two perpendicular to the plane). The remaining six detectors were placed at angles of 72°, 107° and 142°, with one of each pair in the plane of polarization and the other in the perpendicular plane. All the detectors have a diameter of 12.7 cm and were positioned approximately 50 cm from the target.

6.1.4.3 Target Information

The ^{nat}Ce, ^{nat}La(natural lanthanum is 99.9% ^{139}La), and ^{nat}Dy targets all had the same physical dimensions. Each target measured 5.08 cm x 5.08 cm x 3.18 mm and was positioned with the large faces perpendicular to the γ-ray beam and then rotated 45° in θ and 45° in ϕ. The masses of these targets were 50 g (^{139}La), 55 g (^{nat}Ce), and 70 g (^{nat}Dy). The ^{nat}Hg target was housed in a sealed lexan cylinder. The target diameter was 7.62 cm and its thickness was 4.76 mm with a mass of 227 g. The circular face of the target was placed perpendicular to the beam direction. All targets were located at the center of the detector array. Each target was sufficiently large to subtend the γ-ray beam spot.

6.1.4.4 Measurement and Analysis

The neutron detectors used in this experiment were filled with BC-501A liquid scintillator. The scintillator response to γ rays is different from its response to neutrons which allows for pulse-shape discrimination (PSD) to be used to distinguish the two particles. In addition, the γ rays serve as a reference time, so that time-of-flight (TOF) measurements can be made to determine the neutron energy accurately. As a result, neutron yields can be determined as a function of neutron energy with little to no γ-ray background.

Prior to production running, ^{137}Cs and AmBe sources were used to determine the detector threshold and gain and to set PSD cuts. Next, a D_2O target was used to get the TOF-to-energy conversion for the neutrons, using a circularly polarized beam. Finally, the target was installed and data were collected with a 15 MeV circularly polarized beam to measure any instrumental asymmetries. Following that measurement, data were then collected using linearly polarized γ rays at several energies between 11 MeV and 15 MeV. The polarization ratios were investigated as

a function of γ-ray energy, neutron energy, and target material.

Particle-identification cuts using PSD were applied in order to distinguish neutrons from Compton-scattered photons. As seen in Fig. 6.8, a clear distinction can be made. The energy of the scattered neutron was determined using TOF.

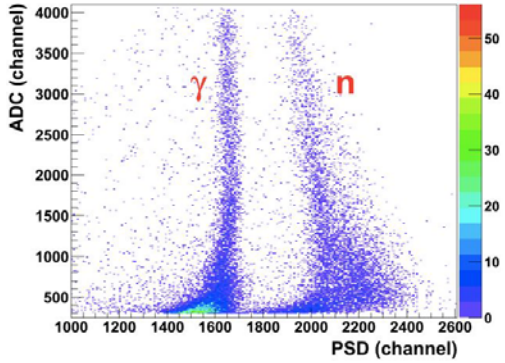

Figure 6.8: (Color online) Typical plot of pulse height versus PSD signal. The bands of photons and neutrons are indicated.

6.1.4.5 Results

The polarization ratios were extracted from the data sets and are shown in Fig. 6.9. Baker and McNeil [Bak61] measured the unpolarized angular distribution coefficient, a_2, for these targets. The ratio at 90° is related to a_2 by

$$R_n = \frac{1 - 2a_2}{1 + a_2}. \tag{6.1}$$

Because of the precision of our measurements, the uncertainties of the extracted anisotropy coefficients a_2 for ^{139}La, ^{nat}Ce, ^{nat}Dy, and ^{nat}Hg are only about 1%, significantly lower than those obtained by Baker and McNeil [Bak61]. For instance, for ^{nat}Hg the ratio as determined by Baker and McNeil for all photoneutrons above 5 MeV is $R_n = 2.35 \pm 0.25$ and for this experiment it is $R_n = 2.57 \pm 0.03$).

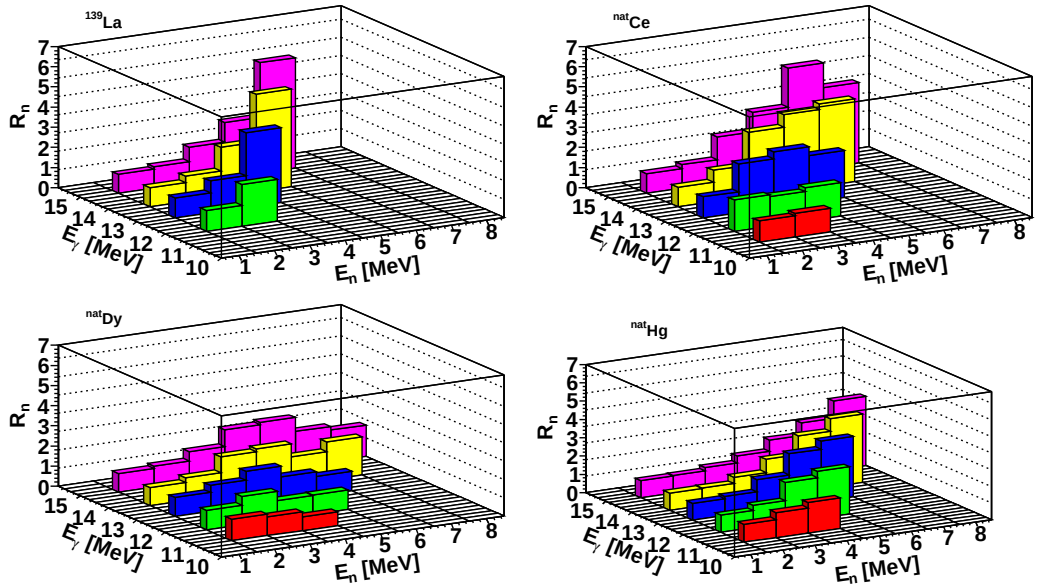

Figure 6.9: (Color online) Clockwise from upper left, the ratios (R_n) as measured for ^{139}La, ^{nat}Ce, ^{nat}Hg, and ^{nat}Dy as a function of γ-ray and neutron energies at $\theta = 90°$.

[Bak61] R. G. Baker and K. G. McNeil, Can. J. Phys., **39**, 1158 (1961).

6.1.5 Measurement of Airborne Fission Products in Chapel Hill, NC, from the Fukushima Dai-ichi Reactor Accident

S. MacMullin, G.K. Giovanetti, M.P. Green, R. Henning, K. Vorren, J.F. Wilkerson, *TUNL*; R. Holmes, *University of North Carolina, Chapel Hill, NC*;

Activity concentrations of airborne fission products were measured in Chapel Hill, NC, USA for 62 days following the March 11, 2011 accident at the Fukushima Dai-ichi nuclear power plant. Airborne particle samples were collected and radio-assayed with two high-purity germanium detectors. The activities of the fission products ^{131}I and ^{137}Cs were below the limits set by the EPA. Additional activity from ^{131,132}I, ^{134,136,137}Cs and ^{132}Te was measured underground using a low-background HPGe detector.

On March 11, 2011, reactors at the Fukushima Dai-ichi nuclear power plant in Japan (37°45' N, 141°27' E) were shut down following a 9.0 magnitude earthquake. Emergency diesel generators were activated to power the water pumps needed to cool the reactors and prevent intensely radioactive nuclear fuel from overheating and damaging the reactor containment vessels. Shortly after the earthquake, the plant was struck by a 14-meter tsunami which flooded the electrical building, disabling the emergency generators. Fires, explosions, and possible partial core meltdowns released radioactive fission products into the atmosphere. A limited amount of information and few measurements relevant to the release of radioactive material were available. Considering global interest in possible public health effects and the local impact on our physics program, which relies on ultra-low radioactive background detectors, we began collecting airborne particle samples and monitoring for fission products on March 17, 2011.

An air sampling pump and filter assembly were housed on the roof of Phillips Hall at the University of North Carolina at Chapel Hill (35°55'N, 79°2' W, 150 m elevation). Air filters collected airborne particles for approximately 24 hours, then were removed, folded into 5 cm × 10 cm rectangles and sealed in nylon bags. A total of 38 air filters were collected over the 62 days immediately following the March 11, 2011 earthquake.

Two 5% relative efficiency compared to NaI (R.E.) high-purity germanium (HPGe) detectors were used to identify characteristic γ rays from radioactive fission products. The detectors were setup horizontally with a 10 mm separation between their end caps. Bagged filters were placed between the end caps of the detectors for assay. The detectors were surrounded by a lead shield, 5 to 10 cm thick, to reduce backgrounds from cosmic rays and natural radiation.

The first filter was placed in the air sampler on March 17, 2011 and collected particles for 24 hours. No fission products were detected in this filter and all visible γ-ray peaks could be attributed to known background sources. Filters from subsequent days produced clear peaks attributable to ^{131}I and ^{137}Cs. A plot of the measured the ^{131}I and ^{137}Cs activity concentrations is shown in Fig. 6.10. Local weather had a significant impact on measured activities. In particular, sharp decreases in both ^{131}I and ^{137}Cs activity, seen in Fig. 6.10, can be correlated with rain events. The maximum activity concentration of ^{131}I was 4.2 ± 0.6 mBq/m^3, sampled on March 30, 2011. The measured ^{131}I activity concentrations did not include a correction for the volatile iodine components. If the volatile components were included, the maximum measured activity concentration may have been comparable to the limit of 7.8 mBq/m^3 set by the Environmental Protection Agency (EPA) although it was well below the limit of 7.4 Bq/m^3 set by the Nuclear Regulatory Commission (NRC). The NRC limit is intended to limit public dosage to less than 1 mSv effective dose.

Ten filters which had already been measured using the setup described above were then assayed at the Kimballton Underground Research Facility (KURF) in order to search for more exotic, long-lived fission products. KURF is located in the Kimballton mine near Ripplemead, VA, which provides shielding from cosmic-ray induced

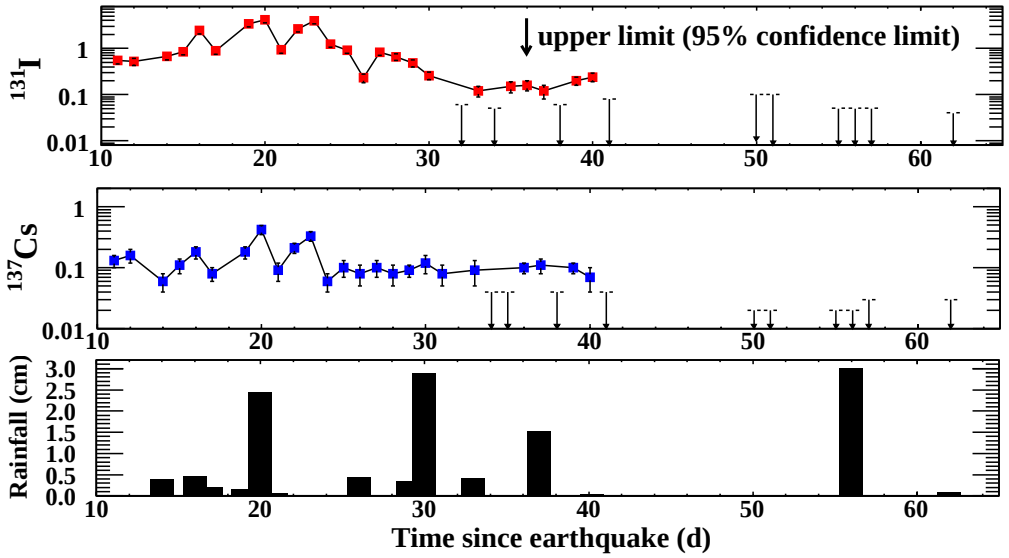

Figure 6.10: (Color online) The time dependence of the ^{131}I and ^{137}Cs activity concentrations in mBq/m^3 and of the local rainfall. Time is shown in days after the March 11 earthquake, rounded to the nearest day. Each activity measurement corresponds to the day the filter was removed from the air sampler. Days when the fission product activity was below the detection sensitivity are reported as upper limits (95% confidence limit).

backgrounds that is equivalent to 1450 meters of water. The detectors in this counting facility have a background rate for γ rays with energies in the region from 40 to 2700 keV that is about 40 times less than the above-ground detectors. All 10 filters were tightly fit into a Marinelli beaker and were assayed simultaneously in the "VT-1" detector, which is a 35% R.E. coaxial HPGe detector with very low background (ORTEC LLB). For technical specifications on the counting systems and facility see Ref. [Fin11]. Peaks from the isotopes ^{132}Te, ^{132}I and ^{134,136}Cs, which could not be seen in the above-ground detectors, were visible.

Fallout from the reactor accident is not expected to have any health implications for the people living in North Carolina. The maximum measured ^{131}I activity concentration is below limits set by the EPA and NRC and also below many sources of natural background radiation, including radon. After April 20, 2011, the radioactivity in the air fell below our detection limits. The measurements reported here are part of the larger global effort to quantify the transport of fallout from the Fukushima accident. We hope they will contribute to future models of the atmospheric transport of fission products. This project was the basis for an undergraduate senior project, with a significant contribution from the student in setup, data acquisition, and analysis. Further descriptions of the experimental details and results can be found in Ref. [Mac12].

[Fin11] P. Finnerty *et al.*, Nucl. Instrum. Methods A, **642**, 65 (2011).

[Mac12] S. MacMullin *et al.*, J. Environ. Radioact., **112**, 165 (2012).

6.2 Pyroelectric Research

6.2.1 Reconverting Solar Energy into Nuclear Fusion Energy

W. Tornow, *TUNL*

By changing the temperature of a pyroelectric double-crystal arrangement in a deuterium gas environment, deuterium ions were produced and accelerated towards a tritiated-titanium target, producing 14.7 MeV neutrons via the ^{3}H(d,n)^{4}He reaction.

In continuation of our previous work, which focused on initiating the reaction ^{2}H(d,n)^{3}He with a pyroelectric double-crystal arrangement [Tor10], we recently turned to the reaction ^{3}H(d,n)^{4}He with the goal of producing 14.7 MeV neutrons. At first glance this task seems easier than the one involving the reaction ^{2}H(d,n)^{3}He, with its relatively small reaction cross section of 16 mb at 100 keV, compared to almost 5000 mb for the ^{3}H(d,n)^{4}He reaction. Furthermore, the large Q-value of +17.56 MeV for the reaction on tritium compared to +3.26 MeV for the reaction ^{2}H(d,n)^{3}He makes neutron detection in the presence of background somewhat easier. However, the safety requirements associated with the use of tritium, combined with another tritium-target-related issue, posed severe constraints on operating our standard pyroelectric crystal apparatus.

A schematic view of our experimental setup is shown in Fig. 6.11. It consists of a cylindrical chamber made of aluminum, which houses the pyroelectric two-crystal arrangement. The 1 in. diameter and 1 in. long $LiTaO_3$ crystals and their heating/cooling devices were glued onto a copper frame. The distance between the crystals was 6 cm. A tritiated-titanium target was attached to the z^- face of the left crystal, facing the z^+ face of the right crystal. The tritiated-titanium target consisted of a 19 mm diameter and 0.4 mm thick disk of copper with a titanium layer evaporated onto it. The thickness of the titanium layer was 2.2 mg/cm^2, and its diameter was 16 mm. It was loaded with 1.6 Ci of tritium. A teflon ring kept the tritiated-titanium target in place. A Geiger counter was placed above the chamber to monitor the x-ray radiation produced. In addition, a planar HPGe detector, positioned adjacent to the Geiger counter, was used to determine the maximum x-ray energy, which is a measure of the acceleration potential between the two crystals. Two 5 in. diameter and 2 in. thick BC-501A neutron detectors, each enclosed by a 1/4 in. thick lead housing, were positioned outside of the chamber (see the lower portion of Fig. 6.11). The entire apparatus was operated in TUNL's NTOF target room, which provided the necessary infrastructure to vent fore-pump exhaust gases from beam lines containing tritiated targets.

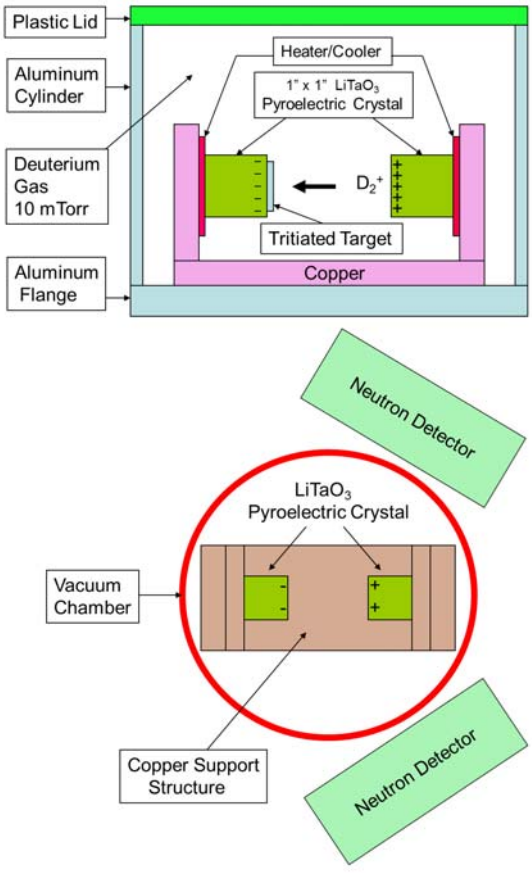

Figure 6.11: (Color online) Schematic side view (upper drawing) and top view (lower drawing) of the experimental setup.

In our previous work involving the ^{2}H(d,n)^{3}He reaction, we heated the $LiTaO_3$ crystals, including their deuterated polyethylene coated front faces, up to 130 °C and subsequently cooled them to about 0 °C in a deuterium gas environment of a few mTorr. Although tritiated-titanium targets are known not to release substantial amounts of tritium at temperatures below 220 °C [MF60], we limited our maximum temperature to 80 °C to provide a comfortable safety margin. Because the electric potential achievable with pyroelectric crystals depends on $\Delta T/\Delta t$, the temperature change over the time interval, we suffered a considerable loss of acceleration potential; the existing heating/cooling system could not make up for the reduced ΔT by reducing Δt as well. Therefore, the maximum acceleration potential was only 170 kV.

The neutron production cross section of the reaction ^{3}H(d,n)^{4}He has a very pronounced maximum at a deuteron energy of about 100 keV. The deuterium ions produced in our work consist of D_2^+ ions, as was shown in Ref. [Tor11] by employing the magnetic-field deflection technique. Therefore, the maximum energy available for neutron production is only 85 keV. This available energy was reduced still further by a dead layer that developed on the tritiated-titanium target surface, beginning with the first heating/cooling cycle. After ten heating/cooling cycles, the dead layer had turned the color on the surface from gray to deep black, though it remains of unknown thickness. In addition, once the deuterium ions reach the active target layer, their energy loss within this layer results in a small reaction cross section and a very small useful target thickness. We estimate that our effective deuteron energy is more than a factor of three lower than the 100 keV needed to be on top of the ^{3}H(d,n)^{4}He resonance.

However, even with such a low effective deuteron energy and small useful target thickness, neutrons were produced via the ^{3}H(d,n)^{4}He reaction. The solid histogram in Fig. 6.12(a) shows the neutron energy spectrum obtained with one of the two neutron detectors when the neutron yield produced in eleven cool-down runs of the pyroelectric crystals from 80 °C to 0 °C were combined. In each individual run, neutron events were observed during two or three time intervals lasting about two to three minutes each. In Fig. 6.12 the total neutron production time was 74.3 minutes. For comparison, the dashed histogram in Fig. 6.12(a) shows the associated cosmic-ray-induced neutron background measured in between cool-down runs for the same total time. Finally, Fig. 6.12 (b) represents the difference spectrum, resulting in 1.94 neutrons per minute above background.

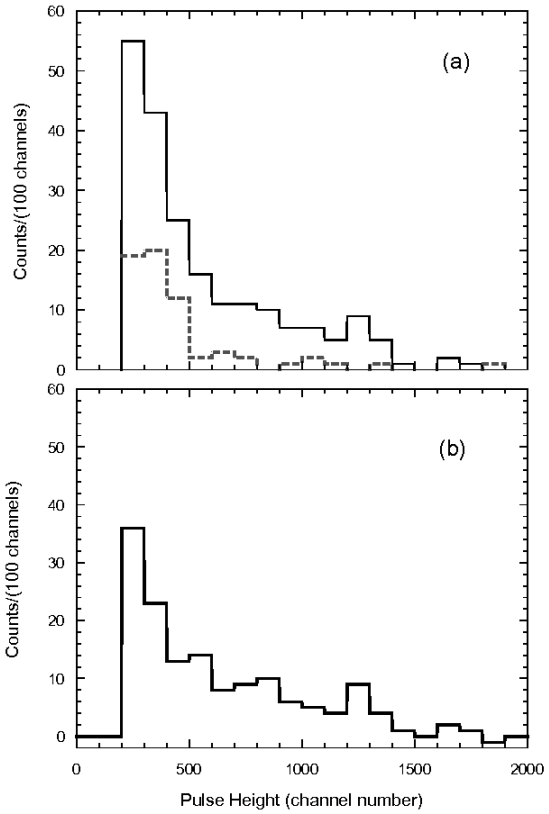

Figure 6.12: (a) Measured neutron pulse-height distribution of ^{3}H(d,n)^{4}He reaction (solid line) and background pulse-height distribution (dashed line). (b) Difference spectrum (note slight change of the y-axis scale)

.

Taking the efficiency and solid angle of our two neutron detectors into account, the number of neutrons produced in our work via the reaction ^{3}H(d,n)^{4}He is about 3 s^{-1}, with an uncertainty of 15%. The uncertainty is mostly due to counting statistics and the 4% uncertainty in the neutron detection efficiency.

We conclude from our first attempt at producing 14.7 MeV neutrons that future work with a more suitable tritiated target should increase the neutron yield by several orders of magnitude.

[MF60] J. Marion and J. Fowler, editors, *Fast Neutron Physics*, Interscience Publ. Inc., 1960.

[Tor10] W. Tornow *et al.*, Nucl. Instrum. Methods, **624**, 699 (2010).

[Tor11] W. Tornow *et al.*, TUNL Progress Report, **L**, 122 (2011).

6.3 Public Health Research

6.3.1 Degradation Studies of Water Purification Membranes During Alpha-Particle Irradiation

E.S. Meyer, L. Lin, O.Coronell, *University of North Carolina, Chapel Hill, NC*; T.B. Clegg, *TUNL*

We have studied the degradation of polymeric membranes during irradiation with a 2-MeV beam of α particles. Of the three most important membrane support materials, polysulfone had the highest fluence of irradiation at which changes in the oxygen-to-carbon ratio start to occur. For membranes having heavy-metal-ion content, the concentration of metal ion did not vary significantly with increasing fluence of irradiation, even at fluences one order-of-magnitude higher than those at which the oxygen-to-carbon ratio changed.

The degradation behavior of reverse osmosis (RO) and nanofiltration (NF) membranes during Rutherford backscattering spectrometry (RBS) and elastic recoil detection (ERD) was studied. These membranes are able, in one step, to remove a broad range of contaminants from water without adding chemicals, making them attractive technologies for water treatment applications. RO and NF membranes usually have a three-layer structure: an ultra-thin, 50-200 nm, fully aromatic polyamide active layer; a 20-50 μm thick polysulfone or polyethersulfone support; and a backing layer of polyester fibers approximately 300 μm thick. Several physicochemical properties of these membranes, including elemental composition and charge density [Cor11, Cor10], are characterized by RBS and ERD analysis, during which the membrane active and support layers are susceptible to molecular degradation due to the irradiation with α particles [Mi07]. Because polymer damage to a given material can be avoided below a fluence (α-particles/cm^2) threshold, the thresholds must be well understood to ensure accurate data from RBS and ERD analyses.

In this study, membrane support materials were tested, because polysulfone supports have been reported to suffer damage during RBS at a lower fluence than polyamide supports [Mi07]. Testing of polysulfone and polyethersulfone supports was performed using RBS analysis at different intensities of a 2-MeV α-particle beam. The change in the concentration of heavy ions in the active membrane layer was also evaluated.

Figure 6.13 presents the normalized cumulative oxygen-to-carbon (O:C) ratios for two polysulfone membranes (PS-H and PS-20), a polyethersulfone membrane (PES-2), a polysulfone membrane with a coating of insolubilized polyvinyl alcohol (PS+PVA-INS), and a polysulfone membrane with a coating of crosslinked polyvinyl alcohol (PS+PVA-CL). Polyvinyl alcohol is commonly used as a coating material in membranes [Pet93]. A second PES membrane was also tested and the results (not shown) were similar to those presented for PES-2. For PES-2, for example, the results indicate that the maximum fluence $F_{\max}$ at which no change in the O:C ratio is detected is between 6×10^{13} and 1.2×10^{14} He^{2+}/cm^2. In order to ensure that damage, as defined by a change in the O:C ratio, does not occur during RBS analysis, the lower end of this fluence range should be taken as the maximum fluence for the corresponding membrane.

Comparing the different membrane materials tested, Fig. 6.13 indicates that changes in the membrane elemental composition were detected at different fluences of irradiation for different materials, with the membrane with a coating of insolubilized polyvinyl alcohol degrading much faster than all other membranes. The results for $F_{\max}$ are given in Table 6.2.

Some membrane properties are determined by probing membrane samples with metals ions, such as barium, and evaluating the metal content in the membrane. Accordingly, we used barium ions to probe the active layer of NTR-7450 NF membranes and evaluated the change in barium content beyond the fluence of irradiation at which changes in the O:C ratio were detected. Figure 6.14 shows that by a fluence of 3×10^{15} He^{2+}/cm^2, the concentration of barium only changed by ap-

proximately 5%.

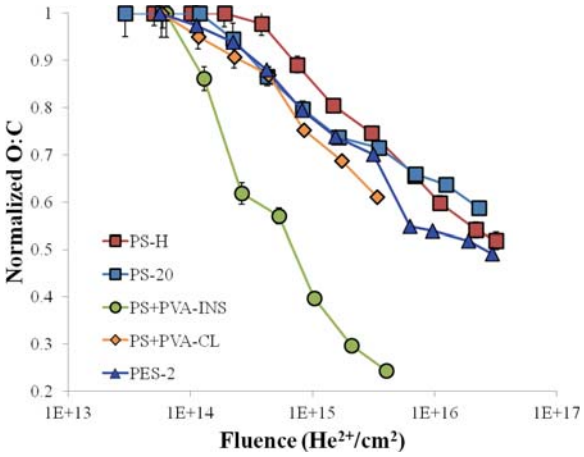

Figure 6.13: (Color online) Normalized cumulative O:C ratios as a function of fluence of irradiation for discretely scanned samples of five commercial membrane materials identified in the text.

Table 6.2: Maximum fluences for different membrane supports.

Material	$F_{\max}$ (He^{2+}/cm^2)
PS-H	1.90×10^{14}
PS-20	1.20×10^{14}
PS+PVA-INS	6.36×10^{13}
PS+PVA-CL	5.81×10^{13}
PES-2	6×10^{13}

The results indicate that the elemental content of the heavy ion probe (barium) did not change significantly even at a fluence more than one order-of-magnitude higher than that at which changes in the O:C ratio of the polysulfone support were detected. As a result, if the properties of interest during RBS and ERD analysis are related to the heavy-ion content, then the $F_{\max}$ values obtained in Fig. 6.13 can be exceeded, and a membrane sample that is more than ten times smaller can be used. The spectra shown in Fig. 6.14 can be obtained by analyzing a sample of approximately one square centimeter.

The degradation of membrane support materials of RO and NF membranes upon helium beam irradiation during RBS/ERD analysis showed that the elemental composition of polysulfone and polyethersulfone is compromised at helium fluences of approximately 5×10^{13} He^{2+}/cm^2 and 10^{14} He^{2+}/cm^2. It was also found that polyvinyl alcohol degrades faster than polysulfone and polyethersulfone, but that when polyvinyl alcohol is crosslinked, a fluence of 5×10^{13} He^{2+}/cm^2will not result in polymer degradation. Finally, the elemental content of heavy ion probes was found to remain approximately constant up to fluences of 3×10^{15} He^{2+}/cm^2.

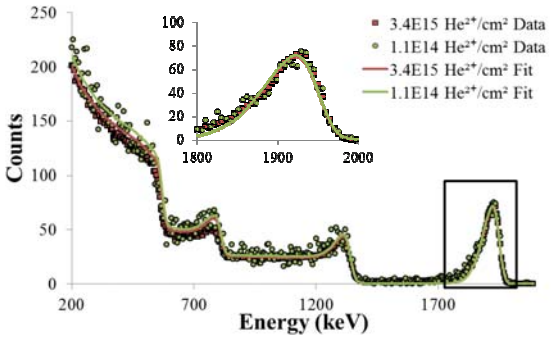

Figure 6.14: (Color online) RBS spectra for NTR-7450 NF membrane probed with barium ions.

[Cor10] O. Coronell *et al.*, Environ. Sci. Tech., **44**, 6808 (2010).

[Cor11] O. Coronell, B. Mariñas, and D. Cahill, Environ. Sci. Tech., **45**, 4513 (2011).

[Mi07] B. Mi, D. Cahill, and B. Mariñas, J. Membrane Sci., **291**, 77 (2007).

[Pet93] R. J. Petersen, J. Membrane Sci., **83**, 81 (1993).

6.4 Nuclear Data Evaluation

6.4.1 Nuclear Data Evaluation Activities

J.H. Kelley, C.G. Sheu, H.R. Weller, *TUNL*; J.E. Purcell, *Georgia State University, Atlanta, GA*

The Nuclear Data Evaluation Group at TUNL is part of the United States Nuclear Data Program and the International Nuclear Structure and Decay Data network. After the retirement of Fay Ajzenberg-Selove in 1990, TUNL assumed responsibility for evaluation of nuclides in the mass range $A = 3$ to 20. The status of the published evaluations and preliminary reviews is presented.

Along with producing evaluations of the $A = 3$ to 20 nuclei in the "Energy Levels of Light Nuclei" series that is published in Nuclear Physics A, the Nuclear Data Evaluation Group has been charged with providing the corresponding updates to the Evaluated Nuclear Structure Data Files (ENSDF) database that is maintained at the National Nuclear Data Center (NNDC) at Brookhaven National Laboratory. We also provide a web-based service for the nuclear science and applications communities at http://www.tunl.duke.edu/nucldata/.

6.4.1.1 Publications

Table 6.3 displays the status of our most recent published evaluations and preliminary reviews. A new evaluation for $A = 11$ was published in April 2012.

Table 6.3: Current publication status.

Nuclear Mass	Publication	Institution
Published:		
$A = 3$	Nucl. Phys. A848 (2010) 1	TUNL
$A = 4$	Nucl. Phys. A541 (1992) 1	TUNL [a]
$A = 5$ to 7	Nucl. Phys. A708 (2002) 3	TUNL [a,b]
$A = 8$ to 10	Nucl. Phys. A745 (2004) 155	TUNL [c]
$A = 11$	Nucl. Phys. A880 (2012) 88	TUNL
$A = 11$, 12	Nucl. Phys. A506 (1990) 1	Penn [d]
$A = 13$ to 15	Nucl. Phys. A523 (1991) 1	Penn [d]
$A = 16$, 17	Nucl. Phys. A564 (1993) 1	TUNL
$A = 18$, 19	Nucl. Phys. A595 (1995) 1	TUNL
$A = 20$	Nucl. Phys. A636 (1998) 247	TUNL [e]
Reviews in Progress:		
$A = 12$, 13	Expected 2013	TUNL

[a] Co-authored with G.M. Hale, LANL.
[b] Co-authored with H.M. Hofmann, Universität Erlangen-Nürnberg, Germany.
[c] Co-authored with D.J. Millener, BNL.
[d] F. Ajzenberg-Selove, University of Pennsylvania.
[e] Co-authored with S. Raman, ORNL.

6.4.1.2 Evaluated Nuclear Structure Data Files

The ENSDF files contain concise nuclear structure information such as tables of adopted level energies and tables of properties for levels that have been observed in various nuclear reactions and decays. The ENSDF files are updated concurrently with the last published reviews in the "Energy Levels of Light Nuclei" series.

Work on the $A = 12$, 13 ENSDF files is presently underway.

6.4.1.3 Experimental Unevaluated Nuclear Data List

TUNL has taken responsibility for creating the $A = 2$ to 20 data sets for the Experimental Unevaluated Nuclear Data List (XUNDL) beginning in April 2009. This activity was developed at McMaster University by Dr. Balraj Singh, who aimed to quickly provide the most current data to users in the high-spin community. The nuclear structure data in recent references is compiled in XUNDL with minimal evaluation effort. Since becoming involved, TUNL has prepared roughly 200 data sets, a rate of 5 per month on average. The data sets are reviewed by Dr. Singh and then added to the database at NNDC.

6.4.1.4 World Wide Web Services

Our group continues to develop web-based services for the nuclear science and applications communities. The website layout and contents are constantly revised and kept up to date to ensure high-quality service and accurate information. Figure 6.15 displays the usage of our website from the nuclear science communities since

April 2002.

The following items are currently available:

- Ground-State Decay Data to provide evaluated data from recent work on ground-state β decays and charged-particle decays, as well as compiled data from earlier measurements, has been completed for nuclides with $A = 3$ to 20.

  We have begun to review and evaluate β-delayed–particle-emission data and will add relevant data sets to the ENSDF database.

- Thermal Neutron Capture Data on $A = 2$ to 20 nuclei is provided based on compiled data.

- Excitation Function Data to provide compiled data related to the level parameters for $A = 3$ to 20 nuclei populated in proton- and α-particle-induced reactions.

- PDF and HTML documents are online for TUNL's and Fay Ajzenberg-Selove's reviews from 1959 to the present. The PDF versions include hyperlinks for references, Tables of Recommended Level Energies, Electromagnetic Transitions Tables, General Tables, Energy Level Diagrams, and Erratum to the Publications. The HTML documents are more comprehensive than the PDF documents, as they include hyperlinks to tables in the PDF and PS formats, reactions and reaction discussions, TUNL and NNDC references, Energy Level Diagrams, and General Tables.

  We have essentially completed the recreation of PDF files for our publications, in order to provide the most current NNDC reference keys and to correct all errors found since the articles went to press. We will continue to work on the corresponding HTML and table/PS/PDF files.

- Energy Level Diagrams for publication years from 1959 to the present are provided in GIF, PDF and EPS/PS formats.

- Tables of Energy Levels provides a brief listing of the tables of recommended energy levels (in PDF and PS formats) from the most recent publications for nuclides with $A = 4$ to 20.

- General Tables that reference theoretical work related to TUNL's most recent reviews are available on our website for the masses $A = 5$ to 10. The tables include dynamic links to the NSR (Nuclear Science References) database.

- ENSDF information for $A = 3$ to 20 nuclides is available through the NNDC site.

- A link to NuDat (Nuclear Structure and Decay Data), which allows users to search and plot nuclear-structure and nuclear-decay data interactively, is available through the NNDC site.

- Links to the National Nuclear Data Center and other useful sites, as well as to the online journals that the nuclear science communities use most often, are provided. There is also a sitemap with a complete listing and links to everything on the website.

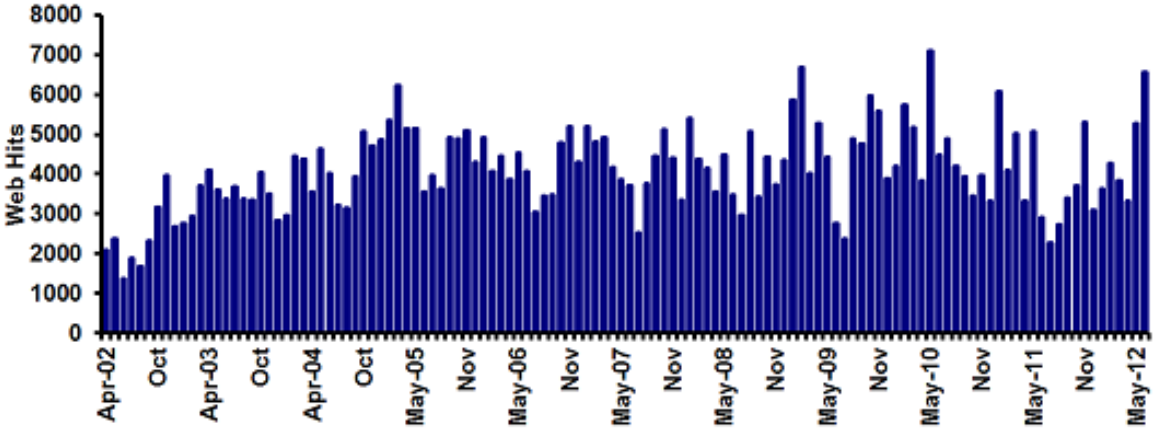

Figure 6.15: (Color online) Overview of web usage deduced from the Analog Web Analysis Package

Accelerator Physics

Chapter 7

- **The High Intensity γ-Ray Source (HIγS)**
- **The FN Tandem Accelerator and Ion Source**
- **The LENA Accelerator and Ion Sources**

7.1 The High-Intensity γ-Ray Source (HIγS)

7.1.1 Operation of the HIγS Facility

Y.K. Wu, P. Wallace, S.F. Mikhailov, *TUNL*

From August 1, 2011 through February 24, 2012, the HIγS accelerator facility was operated for 1593 hours for a variety of research programs and accelerator-related activities, with a reliability of about 93%. A total of 1134 hours of on-target γ-ray beamtime was delivered to the HIγS user-research program.

7.1.1.1 HIγS Operation

During the present reporting period, theHIγS accelerators were operated for nuclear physics research for the first seven months, before being shut down for a major upgrade to install the FEL wiggler switchyard system. Between August 1, 2011 and February 24, 2012, the HIγS facility operated for 130 days, providing 1593 hours of beamtime for a variety of research programs and accelerator-related activities. Operation was carried out with a two-shift, five-day schedule, except for eight days of specially arranged 24-hour operation. In this period, the reliability of the HIγS accelerators and light sources was 93.1%. A detailed breakdown of accelerator operation hours is summarized in Table 7.1 and Fig. 7.1.

During this seven-month operation period, we delivered 1134 hours of γ-ray beamtime to basic and applied nuclear physics research programs. Accelerator research and development used 179 hours. Much of this was spent on developing new accelerator capabilities in various areas, including (1) the optimization of the longitudinal and transverse bunch-by-bunch feedback systems; (2) the development of betatron-tune measurement techniques using the transverse feedback system; (3) the study of the effect of longitudinal and transverse feedback systems on the beam current threshold in the two-bunch and four-bunch modes of operation; (4) the study of beam instabilities; and (5) the development of a soft orbit bump at the end of the FEL straight section to reduce dipole radiation on the FEL mirror.

A substantial amount of time (281 hours) was used for the setup and tuning of the accelerators, FELs, and Compton γ-ray source, plus other related activities. The HIγS users program in this period demanded frequent changes of γ-ray beam parameters, including beam energy, flux, and polarization. This led to frequent changes of the FEL mirrors, with each requiring time spent on conditioning and aligning the mirrors and on setting up the accelerators, FELs, and Compton γ-ray source. However, since no new accelerator operation modes were developed in this reporting period, the time spent on setup (see Table 7.1) was a smaller percentage of the total time than the 22.2% in the previous reporting period.

Table 7.1: Summary of the accelerator beamtime from Aug. 1, 2011 to Feb. 24, 2012.

Activities	Hours	%
HIγS user research	1134	66.2%
Accelerator R&D	179	10.5%
Setup and tuning	281	16.4%
Unscheduled downtime	119	6.9%
Total scheduled beamtime	1712	100%

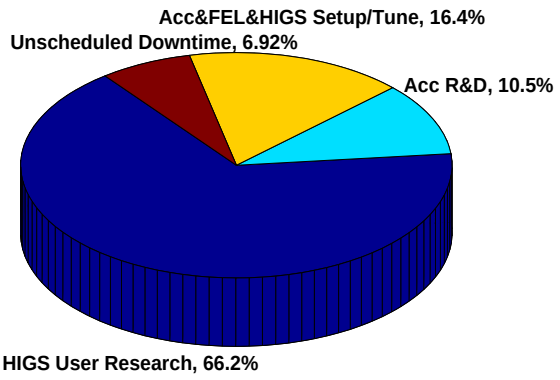

Figure 7.1: (Color online). Beamtime distribution from August 1, 2011 to February 24, 2012.

The monthly HIγS user beamtime is shown in Fig. 7.2 and averaged about 162 hours per month, or about 10 hours higher than in the previous reporting period. In January 2012, two weeks of

three-shift operations were carried out for two experiments. This increased the HIγS beamtime on target in this month to 286 hours. In November and December 2011, fewer operation hours were scheduled for user experiments, due to holidays and maintenance activities.

7.1.1.2 Accelerator Reliability Issues

Within the 1712 hours of planned accelerator operation, unscheduled downtime was 119 hours, or 6.9%. This is higher than the 4 to 5% seen in previous years. The major accelerator failures were failures of the booster and ring RF systems and problems with the linac modulators.

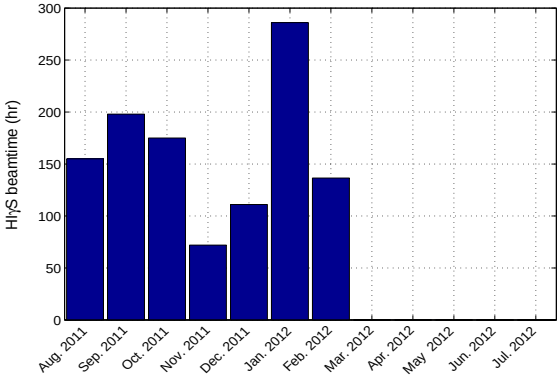

Figure 7.2: (Color online) Monthly distribution of γ-ray beamtime delivered to the HIγS experimental program.

The longest unscheduled downtime (39 hours) was due to the failure of multiple RF tubes in the ring RF generator in November 2011. The first tube failed after 10,712 hours of operation and caused damage to the fast protection system within the anode power supply (APS). A new spare tube was installed after repairing the APS. However, this tube failed during conditioning at relatively low RF power. A decision was made to try to repair the first RF tube, which had been removed from the system in May 2008 due to a short between the grid and filament. A high voltage capacitor bank, capable of storing about 50 J of energy, was assembled to "zap" the shorts while heating up the cathode. It took three discharges to eliminate the shorts completely. This tube was installed and has been operational since November 18, 2011, giving an additional 1,000+ hours of operation. In all, several weeks of accelerator operation, including a number of scheduled user shifts, were lost. Fortunately, some user shifts could be rescheduled.

The second longest downtime (18 hours) was a failure of the booster RF tube. A spare was shipped overnight from the vendor, and installed the next day. The most frequently encountered accelerator problems were multiple brief trips of the ring RF systems, due to instabilities. The stability of the storage-ring and booster-kicker systems was improved in 2012, with kicker problems accounting for only 6 hours of unscheduled downtime.

Despite the hardware problems with the RF and other accelerator systems, a reasonably high reliability of the accelerators operation was realized. This can be attributed to successful preventive maintenance. Over the years, we have established a maintenance schedule for critical hardware systems using the projected mean time to failure. We also schedule semi-annual maintenance in the fall and spring, to evaluate all systems and prepare for the coming change in outdoor temperature. In addition, we continuously monitor hardware systems for any sign of degraded performance and perform additional checks on any questionable systems. Ideally, maintenance activities would be performed every two to three weeks. In the past three years, frequent FEL mirror changes have been helpful in increasing our flexibility to schedule maintenance tasks. The failure of the amplifier tubes for the storage-ring RF system in 2011 demonstrated that the reliability of accelerators and light sources depends on the availability of replacement critical hardware components in-house. Timely procurement of expensive but critical hardware will remain a challenge, as we push to operate the accelerators with higher energy and beam current and for longer durations.

7.1.1.3 FEL Wiggler-Switchyard Upgrade

To extend high γ-ray flux operation into higher energy regions (first above 60 MeV, then above 100 MeV), an FEL wiggler switchyard system was developed to host up to four helical OK-5 wigglers. The accelerator shutdown for the wiggler switchyard upgrade started on February 27, 2012. After about three and half months of intensive work by the DFELL staff, the wiggler switchyard system was installed and hardware systems reconnected. Electrical power was restored to the accelerator equipment on June 8, and the first electron beam was stored in the storage ring on June 14, 2012. Details about the wiggler switchyard upgrade and accelerator commissioning are found in Sects. 7.1.2 and 7.1.3.

7.1.2 HIγS Upgrade with FEL Wiggler Switchyard

Y.K. Wu, M. Emamian, M. Busch, J. Faircloth, H. Hao, J.Y. Li, S.F. Mikhailov, V.G. Popov, G. Swift, P. Wallace, *TUNL*

The HIγS accelerator facility was shut down for about three months to install the FEL wiggler switchyard, enabling a significant increase in the laser gain for UV-VUV FEL operation. The switchyard system will preserve previous γ-ray beam capabilities with linear and circular polarizations below 100 MeV and enable the development of new γ-ray beams with circular polarization at higher energies, aiming to exceed the pion-threshold.

7.1.2.1 Upgraded HIγS with Wiggler Switchyard

To extend HIγS operation above 100 MeV and then above 150 MeV (beyond the pion-threshold energy), the FEL gain for VUV-lasing below 200 nm must be increased through a longer FEL system with up to four helical OK-5 wigglers. To preserve the HIγS capabilities with linear polarization, associated with the planar OK-4 FEL, a wiggler switchyard system was developed to allow either the two OK-4 wigglers or two additional helical OK-5 wigglers to be placed in the middle of the FEL straight section. The wiggler switchyard is the most cost-effective solution for extending the energy range, since it employs the existing straight section and FEL cavity system, and uses the existing γ-ray beamline and downstream target rooms.

With the wiggler switchyard, the Duke FEL and HIγS can be operated in two significantly different configurations: (1) the mixed-wiggler configuration of two planar OK-4 wigglers and two helical OK-5 wigglers; and (2) the configuration with four helical OK-5 wigglers. The switchyard facilitates a rapid transition between these configurations, as shown in Fig. 7.3.

In the mixed-wiggler configuration, two OK-4 wigglers are brought to the middle of the FEL straight section, so the wiggler setup is almost identical to the earlier one, but with small changes in the location of the quadrupoles adjacent to the OK-4 wigglers. All γ-ray beam capabilities from before the switchyard upgrade are retained, and HIγS can be operated to produce γ-ray beams in either linear or circular polarization in the energy range below 100 MeV, as before.

In the helical-wiggler configuration, two additional OK-5 wigglers are brought to the middle of the straight section to replace the OK-4 wigglers. The OK-5 FEL can be operated with different numbers of wigglers. For example, for operation at 240 nm or 190 nm, the two middle wigglers can be used. To produce γ-rays with energies of 100 to 150 MeV, either the first three or all four OK-5 wigglers can be used, producing FEL lasing at 175 or even 150 nm.

7.1.2.2 Wiggler-Switchyard System Installation

The final design of the wiggler switchyard was completed in late fall 2011. During the same period, the mechanical components were procured, fabricated, and tested. New vacuum chambers were welded, assembled, and processed for use in ultra-high vacuum (UHV). The shutdown for the wiggler-switchyard upgrade started on February 27, 2012. Over the next three and a half months, we carried out the following major tasks: (1) dismantling the old OK-4 beamline, a 15 m long section of the FEL beamline with two OK-4 wigglers, a number of quadrupoles and correctors, and modifying cooling-water and electrical infrastructure; (2) setting up new hardback supports, and installing a series of linear sliding tracks topped by a sliding wiggler platform; (3) installing and aligning a pair of OK-4 wigglers, a pair of OK-5 wigglers, and two buncher magnets on the sliding platform; (4) installing adjacent quadrupole magnets, and restoring cooling water to all magnets; (5) installing new vacuum chambers to connect the OK-5-wiggler vacuum chambers with the rest of the storage ring; and (6) connecting power bus-bars to the OK-5 wigglers and cables to various magnets.

The main equipment of the storage ring was first powered up on June 8, 2012. The storage ring with two new OK-5 wigglers (see Fig. 7.4) was commissioned on June 14, 2012, storing the

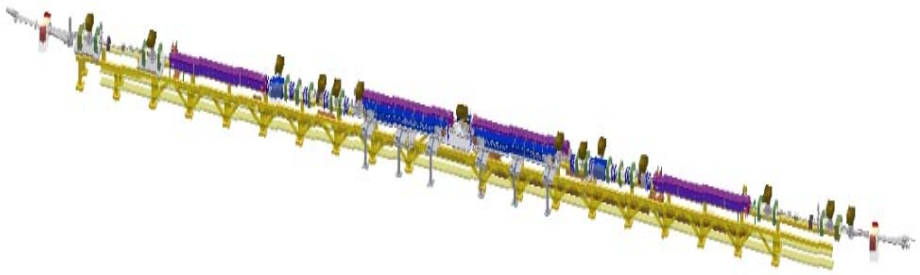

Figure 7.3: (Color online) The layout of the FEL straight section with the wiggler-switchyard system in the middle. The electron beam travels from left to right.

first electron beam in only a few hours.

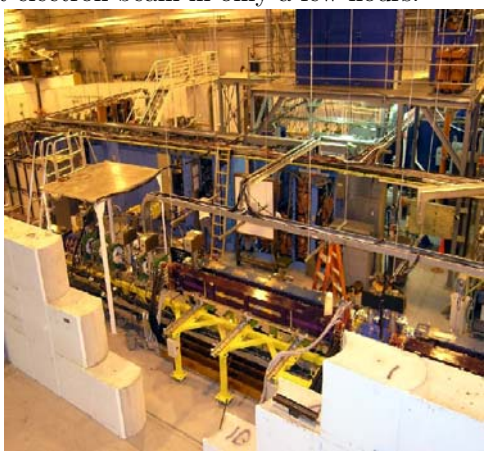

Figure 7.4: (Color online) The completed wiggler-switchyard system in early June 2012, before the shielding wall was fully restored.

The initial mechanical work was a major undertaking, but the DFELL team was able to complete these tasks very efficiently and move the project ahead of schedule by two to three weeks.

Following the installation and alignment of the support structure, the wiggler platform was installed. It consists of two long aluminum plates, each supporting one OK-4 and one OK-5 wiggler. A third aluminum plate, bolted between the wiggler plates, supports two buncher magnets. The precise alignment of the wigglers was one of the most challenging project tasks and was accomplished in several steps: (1) two OK5 wigglers were first installed on the platform and several sliding tests with each of the two aluminum plates were performed to ensure ease of motion and check the reproducibility of the wiggler position; (2) two OK4 wigglers were added to the system, followed by the same sliding tests; (3) the entire wiggler platform with two plates bolted together was moved and tested, and finally the OK5 wigglers were pre-aligned with the rest of the beamline. The supporting platform was then bolted and stabilized, and fine alignment of the OK5 wigglers was carried out.

A rapid recovery of user operation after shutdown demands high quality work on the new vacuum chambers. For the chambers to meet strict UHV requirements, exposure of all vacuum surfaces to air was minimized. The vacuum system was designed to keep the adjacent vacuum chambers vented and under dry nitrogen purge for only a short duration—for example, about 1 hour of nitrogen purge during a typical OK5/OK4 wiggler exchange. Overall, we modified four existing chambers, fabricated eighteen new chambers, and added four new vacuum gauges.

The new configuration of four OK-5 wigglers required a re-working of all bus bars along the straight section. The sections under the center wiggler pairs were shifted to new supports on the south side of the hardback supports. All connections between the bus-bar sections and to the wiggler-lugs were custom-made with new groups of five parallel 535 MCM cables. A third (unused) wiggler power supply was first brought online. Two wiggler power supplies were connected in series to provide sufficient voltage and flexibility to power all eight OK-5 wiggler coils or any subset of coils. Full cooling protection for high-current operation was put in place on the center OK-5 wiggler pair. The two OK-4 wigglers and all other straight-section magnets were also recabled and tested for proper operation.

7.1.3 New Storage Ring Lattices for FEL Wiggler Switchyard System

H. Hao, J. Li, Y.K. Wu, *TUNL*

With the addition of two more helical OK-5 wigglers and the installation of a wiggler switchyard system that allows either two planar OK-4 or two helical OK-5 wigglers to be placed in the middle of the FEL straight section, a new magnetic lattice was needed. The design of this lattice for the operation of the wiggler switchyard system is described.

In order to operate HIγS at γ-ray energies above 100 MeV, stable FEL operation below 190 nm is required (see Sect. 7.1.2). This can be achieved by increasing the FEL gain using a long OK-5 FEL system with a maximum of four helical wigglers, including two new wigglers in the middle of the Duke-storage-ring south-straight-section (SSS). To preserve the capability of producing linearly polarized photons using planar OK-4 wigglers, a wiggler switchyard system has been developed as described in Sect. 7.1.2. This allows operation of the FEL using several wiggler configurations [YWu06], with the switching between the OK-4 and OK-5 wigglers expected to take only a few days. Storage ring operation with this new wiggler configuration requires a redesign of the SSS magnetic optics. This report uses the configuration of two OK-5 wigglers as an example to introduce the new SSS lattice.

All hardware changes for installation of the wiggler switchyard need to take place in the SSS, requiring a redesign of the SSS lattice. Fortunately, many important characteristics of the original storage ring lattice, such as the betatron tunes and injection scheme, can be preserved. This reduces the overall design and commissioning effort. We also expect that the nonlinear aspects of the new storage ring lattice will be similar to those of the old ring.

For efficient interaction between the FEL and electron beams, whether for FEL lasing or γ-ray production, the transverse sizes of the two beams should be matched. In our design, β_x at the center of the SSS is kept at 4.5 m, which is optimal for operating the two central wigglers. To allow for the longer OK-5 wigglers, two pairs of doublets at the middle of the SSS had to be moved outward by about 20 cm. This change is small enough that the design of the new lattice can be similar to that of the old one. HIγS operation requires changing between different wiggler configurations by turning some of the wigglers on or off within several minutes, without causing significant beam loss. To enable these changes, we need to design a special lattice with all wigglers turned off (the 0-lattice), to be shared by all wiggler configurations in the new SSS lattice. In addition, the lattice should be designed for a wide range of wiggler settings and beam energies.

The OK-5 wiggler is a 30-period, 4.08-m-long electromagnetic helical wiggler, used for producing the circularly polarized FEL and γ-ray beams. Theoretically, the lattice perturbation caused by a wiggler is related to the square of the energy normalized by the wiggler strength, $(E_0/K_\mathrm{w})^2$, where E_0 is the electron energy. Thus we can write the change of the quadrupole strength for wiggler compensation as $\Delta K_{1,\mathrm{cmps}}(k)$ where $k = (0.1\,K_\mathrm{w}/E_0)^2$ and E_0 is in GeV. It is known that a general-case solution for $\Delta K_{1,\mathrm{cmps}}(k)$ cannot be obtained, but $\Delta K_{1,\mathrm{cmps}}(k)$ should be a well-behaved function varying smoothly with k. Thus it can be approximated by a low-order polynomial of k,

$$\Delta K_{1,\mathrm{cmps}}(k) = a_1 k + a_2 k^2 + \cdots , \qquad (7.1)$$

where $a_{1,2,\cdots}$ are coefficients for different orders of k.

For the lattices with two OK-5 wigglers, we use 6th-order polynomials to represent the functions $\Delta K_{1,\mathrm{cmps}}(k)$ for all 18 quadrupoles. Fig. 7.5 shows the SSS lattices for values of k from 0 to 0.7 GeV^{-2}. This shows that the lattice variations needed for wiggler compensation can be confined inside the SSS. The β-functions represented by thick black and red lines in Fig. 7.5 are for $k = 0$. Starting from this 0-lattice, the SSS lattices for non-zero wiggler strength vary smoothly as the strength increases. Meanwhile, the phase advances of the SSS are kept fixed, with $\mu_x = 1.302 \times 2\pi$ rad and $\mu_y = 1.030 \times 2\pi$ rad. The quantities $\beta_{x,y}$ at the center of the SSS are kept at 4.5 m.

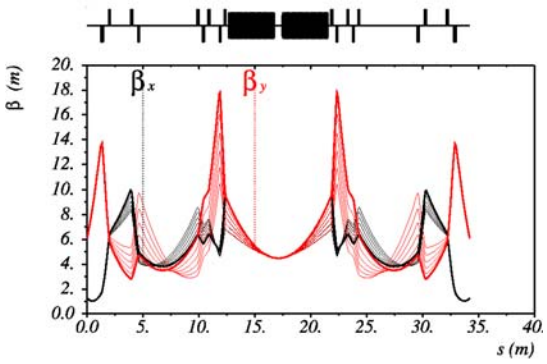

Figure 7.5: (Color online) SSS lattices with varying wiggler strength for a lattice with two OK-5 wigglers (shown as rectangles in the top portion of the figure). The positions of the eighteen quadrupoles are also shown.

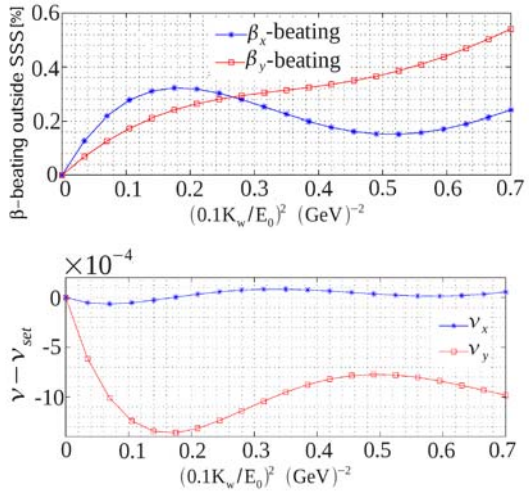

Figure 7.6: (Color online) Lattice deviations using the fitted K_1 of Eq. (7.1) for the same lattice as in Fig. 7.5. Upper plot: relative β-beating outside the SSS; Lower plot: global tune deviation.

The coefficients in Eq. (7.1) are extracted by fitting the discrete K_1 data from the lattices designed using MAD-8. Figure 7.6 shows the differences between the lattices with the fitted K_1 values and those with values obtained directly from MAD-8. Here the maximum relative β-beating outside the SSS due to the wiggler compensation schemes is $\leq 0.5\%$, much smaller than the allowed amount of β-beating for the operation of the Duke storage ring. Figure 7.6 also shows that the differences for ν_x and ν_y are small—on the order of 10^{-4} and 10^{-3}, respectively—which can be easily compensated by using tune knobs.

A storage ring needs a set of tune knobs to provide flexibility for its commissioning and operation. Once the 0-lattice is determined, the additional quadrupole strength $\Delta K_{1,\mathrm{knob}}$ for the tune knob is a function of the tune deviations $\Delta\nu_{x,y}$ and the wiggler strength k. We can approximate this focusing change using a low-order polynomial of $\Delta\nu_{x,y}$. To make the fitting formula simpler, we assume that there is no coupling between the x and y directions for a small tuning range. The fitting formula can then be written as

$$\Delta K_{1,\mathrm{knob}} = b_1(k)\Delta\nu_x + b_2(k)(\Delta\nu_x)^2 + \cdots + c_1(k)\Delta\nu_y + c_2(k)(\Delta\nu_y)^2 + \cdots \quad (7.2)$$

where the tune knob coefficients $b_{1,2}(k)$ and $c_{1,2}(k)$ are functions of wiggler strength. These coefficients can be obtained by fitting the quadrupole-strength data obtained from the designs of the lattices with tune changes. For the configuration with two OK-5 wigglers, 3rd-order polynomials of $\Delta\nu_{x,y}$ and 6th-order polynomials of k for the coefficients are used. Figure 7.7 shows the effectiveness of the tune knob for the configuration lattice with two OK-5 wigglers and a tuning range $\Delta\nu_{x,y}$ from -0.1 to $+0.1$. We can see that, for much of the tuning region, the tune difference between the calculated values using Eq. (7.2) and the specified values $\Delta\nu_{\mathrm{set}}$ is smaller than 10^{-3}, which is quite adequate for operation.

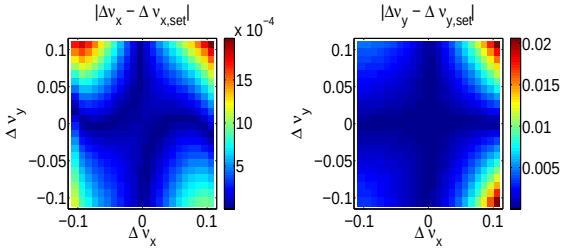

Figure 7.7: (Color online) Tune deviations due to lattice tuning.

To summarize, we have successfully developed a series of new magnetic lattices for the Duke storage ring with the wiggler switchyard system. These include a set of sophisticated wiggler compensation schemes and tune knobs.

[YWu06] Y. K. Wu *et al.*, Phys. Rev. Lett., **96**, 224801 (2006).

7.1.4 Betatron-Tune Measurement System Based on Bunch-by-Bunch Transverse Feedback

W. Xu, W.Z. Wu, J. Li, Y.K. Wu, *TUNL*

A digital bunch-by-bunch transverse-feedback (TFB) system to combat electron-beam instabilities has been developed for the Duke storage ring. We have used the TFB to develop beam-diagnostic techniques, especially the TFB-based tune-measurement techniques. This system has been used to measure the betatron tune amd chromaticity and to study vacuum-chamber impedance effects.

A system to measure the betatron oscillations (betatron tunes) of the electron beam in a storage ring is one of the most important beam diagnostics. The basic approach is to excite the electron beam and measure its response. At the Duke FEL laboratory, tune-measurement systems using a network analyzer and an optical detector were previously developed for both the storage ring and booster injector [YWu07]. However, the measurement of betatron tunes can also be realized using a bunch-by-bunch transverse-feedback (TFB) system, since the TFB can generate signals to both drive the beam and detect its response. Unlike conventional techniques, the TFB-based system can selectively drive electron bunches, thus performing the tune measurements for individual bunches during multi-bunch operation.

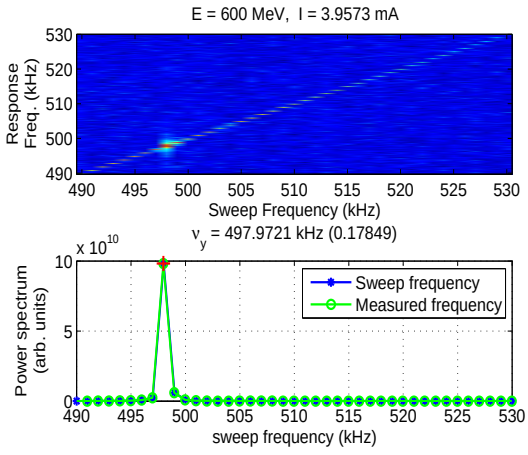

Figure 7.8: (Color online). A vertical tune measurement using the TFB-based slow-tune measurement technique ($\nu_y = 0.1785$). The frequency span and bandwidth are set to 40 and 1 kHz, respectively.

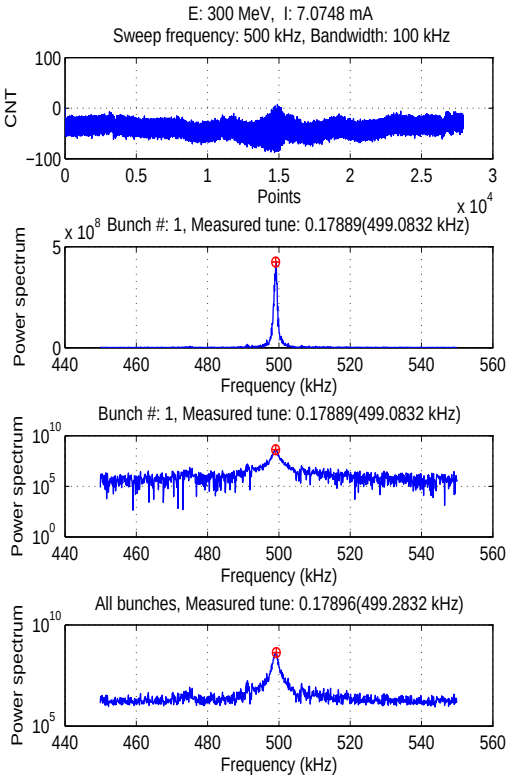

Figure 7.9: (Color online) A vertical tune measurement using the fast-tune technique ($\nu_y = 0.1789$). The electron beam is excited by a broadband (100 kHz) drive signal. Upper plot: the overall beam signal in the time domain. Bottom plot: the same signal in the frequency domain. Middle plots: the power spectrum of the signal from bunch #1 (linear and logarithmic scales).

Using the TFB, we have developed two

distinct ways to measure the betatron tunes [WXu12]. The slow-tune technique slowly scans the drive frequency in a preset region and records the beam response at each frequency. Figure 7.8 shows the measurement of the vertical tune of a 3.96 mA beam at 600 MeV. Using this technique, it typically takes three to four minutes to measure the tune.

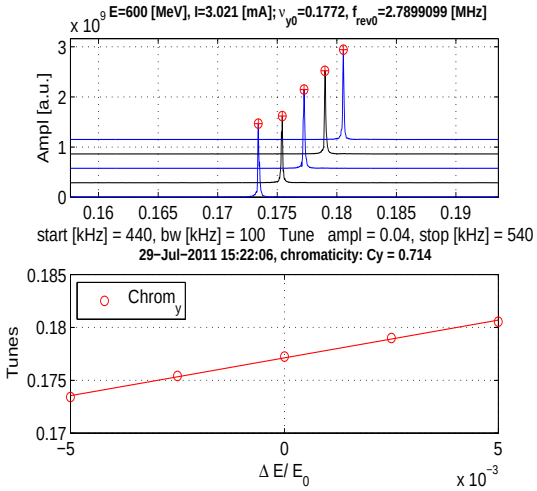

Figure 7.10: (Color online) A measurement of the vertical chromaticity using the TFB-based tune-measurement system. The upper plot shows the measured tunes for the electron beam at different energies. The lower plot shows a linear fit to the measured tunes; the slope of the fitted line is the measured chromaticity ($\xi_y = 0.714$).

A much faster tune-measurement technique was also developed by driving the electron beam with a broadband signal and recording the beam response. To determine the betatron tune, the time-domain beam-response signal is analyzed using fast Fourier transforms. Using this technique, the betatron tune of all bunches can be measured in a few seconds. A vertical-tune measurement using the fast-tune measurement technique is shown in Fig. 7.9.

Chromaticity is an important parameter of a storage ring, describing the variation of tunes with beam energy. The chromaticity is defined to lowest order as:

$$\xi = \frac{d\nu}{d\,(\Delta E/E)}, \tag{7.3}$$

where ν is the tune and E is the beam energy. Thus a direct way to determine the chromaticity is by measuring the tune shift with the beam energy. The change in beam energy can be achieved by tuning the RF frequency of the storage ring:

$$\frac{\Delta E}{E} = -\alpha_c \frac{\Delta f}{f_0}, \tag{7.4}$$

where α_c is the momentum compaction factor of the storage ring, f_0 is the RF frequency, and Δf is the change in the RF frequency. For a typical chromaticity measurement, the energy change is chosen to be in the range -0.5% to $+0.5\%$. To have a good linear fit to the measured tunes, at least five measurements are performed. Figure 7.10 shows the results of a typical chromaticity measurement using the TFB-based fast-tune measurement method.

Using the TFB-based tune-measurement tool, we also performed a calibration for the tune-and-chromaticity knob [YWu97]. The tune-knob-calibration result is shown in Fig. 7.11. For a small tune change, $\Delta\nu_y \leq 0.08$, the response to the vertical-tune-knob setting is quite linear, with a slope of 1.01. Beyond this point, the measured tune starts to deviate from the tune-knob set value, indicating a finite, but still adequate, linear range of this knob.

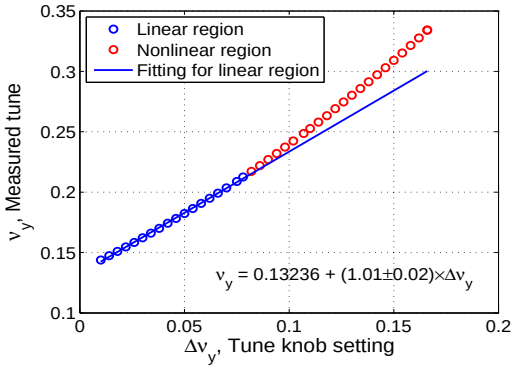

Figure 7.11: (Color online) Calibration of the vertical-tune knob for the Duke storage ring.

The TFB-based tune-measurement system has also been used successfully in several other research projects, including the measurement of the betatron tune for individual bunches in multi-bunch operation, the measurement of the vertical tune change with the beam current, and the study of the impedance of the vacuum chambers of the OK-4 FEL wigglers.

[WXu12] W. Xu *et al.*, In *Proceedings of the International Particle Accelerator Conference*, p. 849, 2012.

[YWu97] Y. Wu *et al.*, IEEE Trans. Nucl. Sci., **44**, 1753 (1997).

[YWu07] Y. Wu *et al.*, In *Proceedings of Particle Accelerator Conference, PAC07*, p. 4063, 2007.

7.1.5 Improving Performance and Reliability of the Duke Storage Ring and Booster Kickers with Cold-Cathode Thyratrons

V.G. Popov, S.F. Mikhailov, J.Y. Li, P.W. Wallace, Y.K. Wu, *TUNL*

The performance of HIγS critically depends on the injection/extraction kicker systems of the booster injector and storage ring. The kicker systems employ cold-cathode thyratrons, a new type of fast switch with very low time-jitter. After more than six years of operation, we recently tested next-generation cold-cathode thyratrons.

Since 2007, the operation of HIγS has benefited greatly from a full-energy, top-off booster injector (0.18 – 1.2 GeV), allowing fixed energy operation of the Duke storage ring [Mik07]. The injection/extraction kicker system is a key component of the accelerator facility, determing the efficiency and reliability of operation. Pseudo-spark switches (PSS), also known as cold-cathode thyratrons, are the critical components of the high-voltage pulse generators for the kickers, and we have now had six or seven years to study their stability and lifetime.

Pseudo-spark switches with low time-jitter are still considered to be new technology for accelerators. Table 7.2 shows the main specifications of the three types of PSS currently used in the Duke accelerator kicker systems [Vic09].

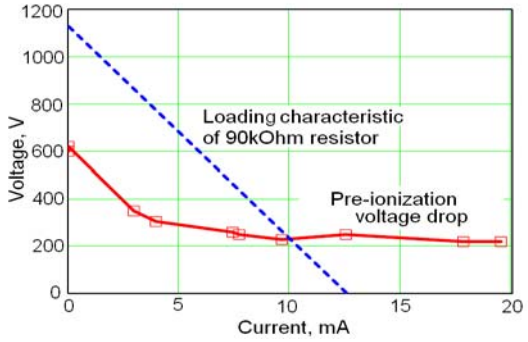

Figure 7.12: (Color online). Voltage-current characteristic of the discharge power supply.

The unique performance characteristics of a PSS, compared with a conventional thyroton, are provided by a complex firing process using a glow discharge created and sustained by a discharge power supply [Boc01]. Any instabilities in the discharge can interfere with reliable operation of the high-voltage generator. For example, mismatch between the voltage-current characteristics of the discharge power supply (see Fig. 7.12) and substantially nonlinear characteristics of the gas discharge can provoke instability and even self-oscillation (see Fig. 7.13).

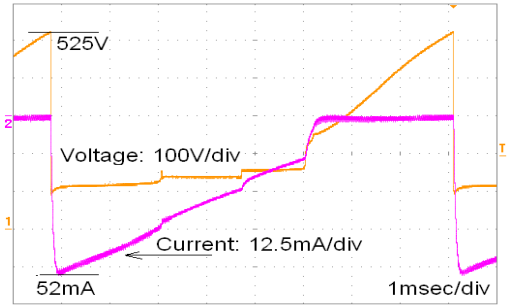

Figure 7.13: (Color online). Self-oscillating discharge with a TPI1-10k/20. The pre-ionization power supply uses current control feedback and a 5 kΩ limiting resistor.

Such a mismatch can also cause a long recovery time, thus limiting the maximum repetition rate of the kicker system. Even when the voltage drop on the pre-ionization electrode is stable, the electrode can settle to a different level after an initial discharge. In this case, the initial conditions for the next triggering of the thyratron will be different from those of the previous one. The use of a discharge power supply with a high output impedance does not guarantee a fast and repeatable recovery of the glow discharge (see Fig. 7.14).

Another important factor for the glow discharge process is the internal hydrogen pressure. Lowering the pressure increases the voltage drop on the pre-ionization electrode, eventually making it impossible to even initiate a discharge. It also reduces the lifetime of the thyratron. It is well-known [E2V02] that a negative bias voltage at the control grid helps to prevent self-

Table 7.2: Specifications of TPI-type thyratrons.

Specification	TPI1-1k	TPI1-10k and TPI3-10k
Peak forward anode voltage (max), kV	22	28
Peak forward anode current (max), kA	3	10
Average anode current, A	0.15	0.3
Max. anode current rise-rate, A/sec	5×10^{11}	1×10^{12}
Anode current pulse duration, μs	0.01–5	0.01–5/10
Time jitter, ns	< 1	< 1
Operating resource (switched charge), C	10^6	5×10^5

firing of the thyratron and increase the operational hydrogen pressure. We found that the original negative-bias power supply did not provide enough current to compensate the electrons coming to the anode-grid region. The elimination of this issue has allowed us to reduce the voltage drop at the pre-ionization electrode by 20 to 60 V.

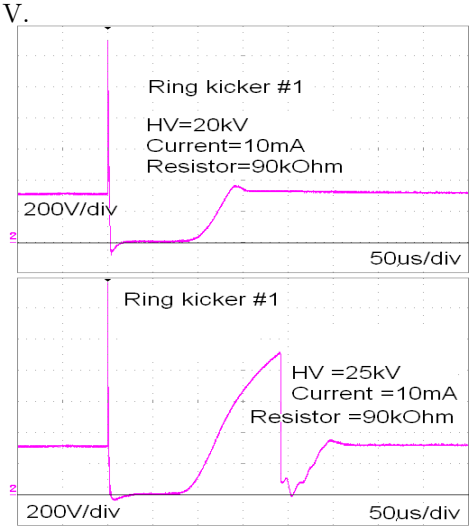

Figure 7.14: Upper: The well optimized recovery process after firing the new-generation thyratron TPI1-10k/20 with a 1300 V power supply and 90 kΩ resistor. Lower: The recovery process of the same thyratron when the voltage setting is increased from 20 to 25 kV.

The most difficult factor to control is the aging of the thyratrons. The exhaustion of the cathode emitting element is accompanied by a growth of the voltage drop. The next generation TPI1-10k/20 thyratrons feature an embedded getter. According to the manufacturer, this new device has better cathode performance and, therefore, improved lifetime. We have already installed and tested one in storage-ring kicker-generator #1. While it is too early to judge any change in lifetime, we have found that this thyratron is more sensitive to the negative bias voltage at the control grid and requires better matching with the pre-ionization power supply.

We have observed evident widening of the booster extraction pulses. The growth of the pulse voltage has two parts: an initial slow rise followed by rapid growth. Fig. 7.15 shows the evolution of this pulse distortion for the two extraction generators. Note that the full width at half-height of the pulse is unchanged. Also, when operating at a higher voltage setting, this pulse deformation is less noticeable.

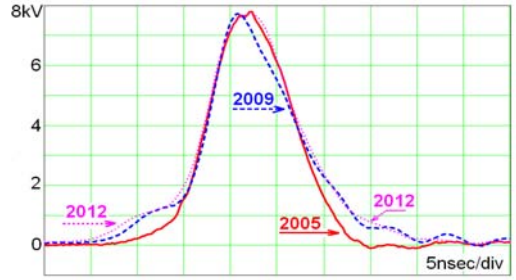

Figure 7.15: (Color online). Evolution of the booster-extraction negative pulse at HV = 15 kV from 2005 to the present.

Another issue as thyratrons age is the well-known problem of grid spikes. Here we do not have an ultimate solution, but we employ spark-gap arresters to suppress spikes. This has the advantage that the shape of the trigger pulse remains undistorted. Failed arresters need replacing approximately every few months.

[Boc01] V. D. Bochkov *et al.*, IEEE Trans. Plasma Sci., **29**, 802 (2001).

[E2V02] *A1A-Hydrogen Thyratrons Preamble Issue 3*, Technical report, E2V Technologies Limited, 2002.

[Mik07] S. F. Mikhailov *et al.*, In *Proceedings of Particle Accelerator Conference, PAC07*, p. 1238, 2007.

[Vic09] V. Popov *et al.*, In *Proceedings of Particle Accelerator Conference, PAC09*, p. 1736, 2009.

7.1.6 Soft Orbit Bump for Duke-Storage-Ring VUV FEL Operation

S.F. Mikhailov, J.Y. Li, V.G. Popov, P.W. Wallace, Y.K. Wu, *TUNL*

The production of intense, high-energy γ-ray beams at HIγS requires a high-current electron beam with energies around 1 GeV. Using such electron beams, the dominant cause of damage to the downstream FEL mirror is radiation from the end-of-arc dipole magnet, not from the helical FEL wigglers. The concept of a "soft" orbit bump to significantly reduce the radiation from this dipole toward the FEL mirror has been developed and tested.

The Duke storage ring is designed as a dedicated FEL driver and a host for several FEL wigglers in a thirty-four-meter-long FEL straight section. The straight section was recently upgraded to accommodate either four OK-5 helical wigglers (see Fig. 7.16) or a mixture of the WIG01 and WIG04 OK-5 wigglers and two planar OK-4 wigglers in the middle of the straight section. In 2010, before this upgrade, the two side wigglers WIG01 and WIG04, were used to demonstrate the production of a substantial flux of nearly 100 MeV γ-rays using 190 nm FEL mirrors [YWu11]. Table 7.3 shows the prospective conditions for the OK-5 vacuum-ultra-violet (VUV) FEL/HIγS high-energy operations, including future FEL operation at 150 nm. The number of OK5 wigglers to be used is determined by the available FEL gain compared to the optical cavity loss and by seeking the optimum intensity for the γ-ray beam while minimizing radiation damage to the downstream FEL mirror. Extending the FEL operation toward 150 nm using VUV mirrors with increasing loss requires a high FEL gain and, therefore, more FEL wigglers.

Table 7.3: Prospective OK-5 VUV FEL/HIγS high energy operations.

$\lambda_{\mathrm{mirror}}$ (nm)	$E_{e,\mathrm{max}}$ (GeV)	$E_{\gamma,\mathrm{max}}$ (MeV)	λ_{c} (nm)	# of OK5 wigglers
250	0.925	60	1.5	2
190	1.060	100	1.0	2–3
150	1.200	158	0.7	3–4

High-energy, high-flux HIγS operation with the OK-5 FEL was possible with the help of in-vacuum mirror-protection apertures to block much of the off-axis wiggler harmonic radiation [Hua09]. The aperture full-gap opening is tunable from 5 mm to about 36 mm.

In producing γ-ray beams with energies above 55 to 60 MeV (electron beam energy above 0.9 GeV), the corner bending magnets and other magnetic elements of the FEL straight section are also significant sources of radiation. For VUV FEL operation we are trying to eliminate as much as possible of all other sources of radiation harmful to the downstream FEL mirror. The most powerful hard-photon source is the corner bending magnet adjacent to the downstream mirror (E01B in Fig. 7.16). To reduce its radiation to the mirror, we are developing an orbit bump using designated orbit correctors. In order not to introduce additional sources of radiation, the magnetic field of the correctors is limited so as to produce extremely soft radiation, with a critical wavelength close to or below that of the FEL mirror. The negative bump deflects the beam orbit at the entrance of E01B, thereby steering the dipole edge radiation away from the axis of the mirror (see Fig. 7.17). Though we cannot fully eliminate the dipole edge radiation, we can significantly reduce its power.

The properties of the edge radiation (ER) are fundamentally different from those of classical synchrotron radiation from a uniform magnetic field [Chu93]. For example, there is no ER in the forward direction. The ER power emitted from the magnet entrance was evaluated using a model with a step-function edge to the magnetic field. This makes the angular distribution of the ER in the long wavelength region independent of the wavelength. The ER power density for both σ and π modes peaks at a horizontal and vertical angle $1/\gamma$ off the radiation axis. However, the π mode is symmetric with respect to the vertical angle, while the σ mode is asymmetric, as shown in the right-hand portion of Fig. 7.17.

The wiggler and non-wiggler-related radiation was measured using a VUV Hamamatsu R7400-09 photo-multiplier tube (PMT), with a spectral response extending from 170 to 290 nm. The ex-

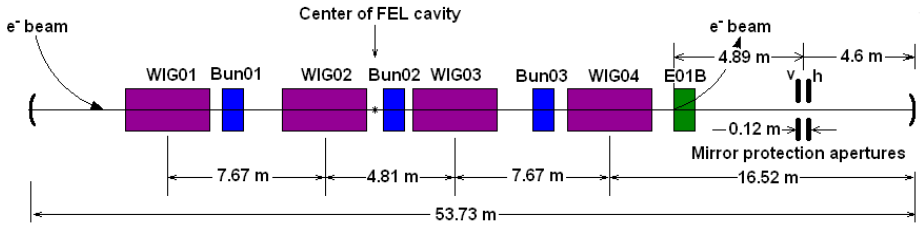

Figure 7.16: (Color online) Configuration of the OK5 FEL.

periment was performed at $E_e = 0.926$ GeV, so that the PMT response was also a good match for the wiggler radiation (around 190 to 250 nm for the conditions of producing 60 MeV γ-rays). The purpose of the measurements were (1) to evaluate the effect of the soft orbit bump on the non-wiggler radiation; (2) to confirm that the dominant source of non-wiggler radiation is the ER from the E01B bending magnet and verify that the simplified model used for the ER power calculation is adequate; and (3) to compare the non-wiggler-related radiation with the wiggler radiation in the wavelength range of the PMT.

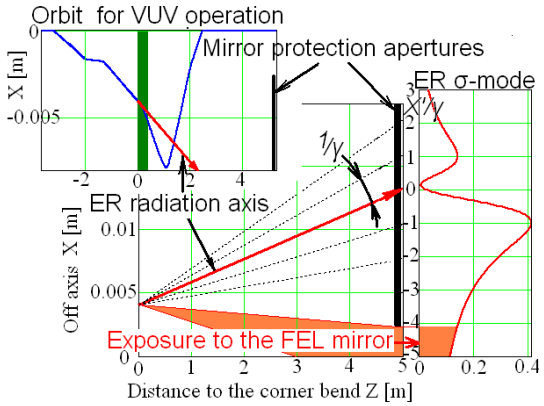

Figure 7.17: (Color online). Using an orbit bump to protect the FEL mirror from radiation of the corner bending magnet. The amplitude of the bump when the kick of the corrector is set to $x'_{\rm cor} = -1.4$ mrad is shown. The horizontal full opening of the mirror-protection apertures is 5 mm.

All the calculations and measurements have the protection apertures with half-gap openings of $\Delta x_{\rm aper} \approx 2.5$ mm and $\Delta y_{\rm aper} \approx 4.5$ mm. These values are typical for VUV FEL/HIγS high-energy operation. Only the WIG01 upstream wiggler was energized. Figure 7.18 shows the power of the E01B ER integrated over $\pm\Delta x_{\rm aper}$, $\pm\Delta y_{\rm aper}$, and $\Delta\lambda = 170$ to 290 nm, calculated as a function of the amplitude of the soft orbit bump. The calculated and experimental evaluation shows that, with the soft orbit bump set at $|x'_{\rm cor}| = 2.1$ to 2.8 mrad, the power of the ER, and therefore the mirror damage effect, can be reduced by a factor of three to four.

For a typical storage-ring energy of 0.925 GeV, the total ER power integrated through the entire bandwidth is about a factor of 20, 4, and 2 greater than the total wiggler-harmonics radiation using WIG01, WIG02+WIG03, and all four wigglers, respectively. All these estimates for the ER radiation are conservative, since the actual dipole edge field is "softer" than the step function.

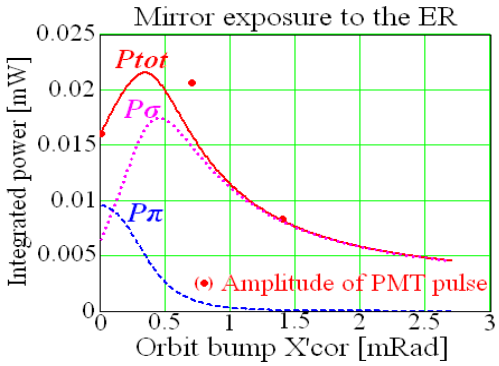

Figure 7.18: (Color online). The power from the corner dipole magnet in $\Delta\lambda = 170 - 290$ nm, with $E_e = 0.926$ GeV and $I_e = 5$ mA. The PMT pulse height is normalized using the calculated power with $x'_{\rm cor} = 0$.

In a real VUV FEL/HIγS high-energy operation, the soft orbit bump allows us to reduce the power of the ER from the E01B magnet down to at least about the same level as the total power of the wiggler-harmonics radiation. Additional development is planned to further improve the soft-bump scheme.

[Chu93] O. V. Chubar and N. V. Smolykov, In *Proceedings of Particle Accelerator Conference*, p. 1626, 1993.

[Hua09] S. Huang *et al.*, Nucl. Instrum. Methods A, **606**, 762 (2009).

[YWu11] Y. K. Wu *et al.*, In *Proceedings of Particle Accelerator Conference PAC11*, p. 778, 2011.

7.2 The FN Tandem Accelerator and Ion Sources

7.2.1 Tandem Accelerator Operation

C.R. Westerfeldt, J.H. Addison, E.P. Carter, J.D. Dunham, R. O'Quinn, B. Walsh, *TUNL*

The operation, maintenance, and improvements at the TUNL FN tandem accelerator over the last year are summarized.

7.2.1.1 Tandem Operation

During the period September 1, 2011 to August 31, 2012, the TUNL FN tandem accelerator was operated 235 days for 3166 hours at terminal potentials ranging from 0.5 MV to just over 8.5 MV. Beams accelerated during this period include unpolarized protons, deuterons, and ^{4}He. The terminal operating potential during the reporting period is shown graphically in Fig. 7.19.

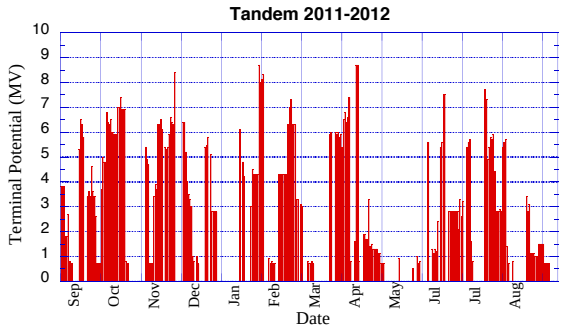

Figure 7.19: (Color online) The TUNL FN Tandem Operating Potential during the present reporting period.

The tandem was opened on May 4, 2012 for routine maintenance. No bad column resistors were found at this opening. The foil stripper box was opened and cleaned. The terminal steerer plates were removed and polished and a new set of 75 stripper foils was installed. These were mostly thin, 1 to 1.5 μgm/cm^2 foils for Rutherford backscattering measurements. The Pelletron charging system received minor maintenance. The chain motors were greased, the tension on the high-energy drive belt was adjusted, and the terminal alternator belt was replaced. New hardware was installed to permit proper tensioning and alignment of the alternator drive belt. The corona needles were cleaned and the corona shield was replaced. A slow-start module was installed in the Pelletron motor control center for the high-energy chain. This was done to the low-energy chain drive last year to reduce the stress on the chain during startups. The low-energy chain which is quite old was found to be in good condition and was simply cleaned instead of being replaced as was planned. The tandem was closed on May 18. Tandem operations resumed the next day.

7.2.1.2 Laboratory Projects

The off-axis direct-extraction negative-ion source (DENIS) continues to be the most utilized of our three ion sources, with 3700 hours logged (beam available but not necessarily accelerated) during this reporting period. No significant changes were made to the source this past year. A new regulated arc-current power supply was installed, but it failed almost immediately and was removed. Stable operations at 25 to 30 μA of analyzed beam on the low energy cup are normal. These intensities are required for pulsed operation. Typical dc beam currents for dc operation are 5 μA (protons and deuterons).

The TUNL helium exchange source was operated for over 500 hours this past year, delivering 1 to 2 μA of ^{4}He beam to the tandem low-energy cup using a sodium charge-exchange canal. A parallel-plate chopper was installed this year at the exit of the ion-source box. It is described elsewhere in Sect. 7.2.2. A recirculation system is being designed for this source to capture the ^{3}He gas pumped by the diffusion pump, purify it, and compress it into a ballast container to be reused (see Sect. 7.2.3). Actual construction and testing of this system will occur this fall.

Several changes were made to safety systems in the tandem accelerator laboratory this year. A neutron area monitor was installed in the corri-

dor outside of the neutron time-of-flight (NTOF) room. Two local readouts were also installed to permit personnel entering the building at the end of this corridor and those leaving the building to observe the neutron radiation level in this area. Additionally, a polyethylene sliding seal was fabricated and installed on the NTOF shielding door to reduce the measured neutron radiation escaping through the exiting gap. Measurements confirm that this seal has reduced the neutron dose rate in the corridor.

7.2.2 Optimization of the Beam-Pulsing System for the Helium-Ion Source at TUNL

D.R. Ticehurst, D. Combs, C.R. Howell, A.R. Young, *TUNL*

A beam-pulsing system for the helium-ion source has been developed and characterized. It has been shown to produce a pulsed ^{4}He beam with a 1.1±0.2 ns pulse FWHM. This capability was developed to carry out measurements of the (^{3}He,n) transfer reaction using neutron time-of-flight spectroscopy on nuclei relevant to neutrinoless double-beta decay. An experiment was done this year to measure the pulse width and to optimize the ion-source operating parameters to obtain the minimum pulse width.

A pulsed ^{3}He beam is needed to make cross-section measurements of the (^{3}He,n) two-nucleon transfer reaction. The goal of these measurements is to test models of nucleon pairing in calculations of nuclear matrix elements for neutrinoless double-beta decay (see Sect. 2.1.14). The measurements require that the energy of the emitted neutrons be determined with a resolution of better than a few hundred keV. Time-of-flight spectroscopy will be used to measure the energy of the emitted neutrons. The beam-pulsing system used for the proton and deuteron beams from the direct-extraction negative-ion source has been expanded to serve the helium-ion source.

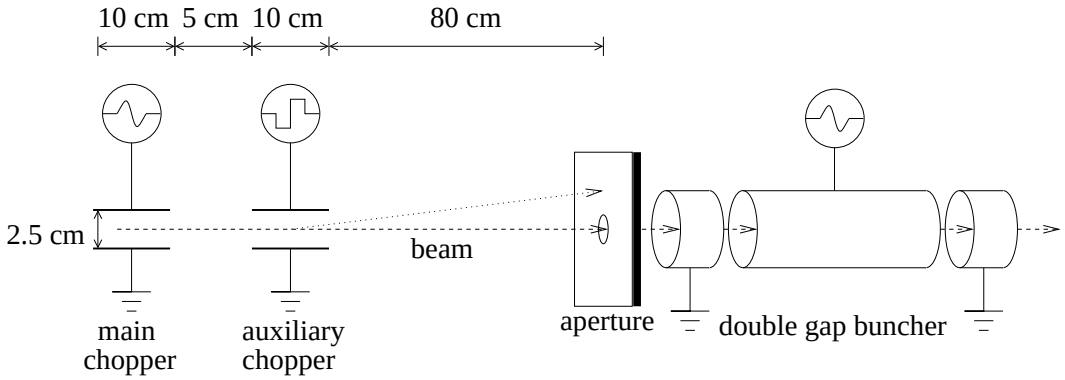

Figure 7.20: Schematic diagram of the chopper/buncher pulsing system

A schematic diagram of the beam pulsing system is shown in Fig. 7.20. The pulsing system consists of two components that alter the time structure of the ion beam: an adjustable frequency "chopper" and a fixed-frequency double-gap "buncher." The buncher electrode is an ungridded cylindrical tube located in the tandem injection beam line and is common to all ion sources. A 5-MHz sine-wave voltage is applied to the tube creating a time-dependent electric field across the gap between the tube and the ground electrode on each end. As seen in Fig. 7.20, the chopper consists of two sets of parallel plates through which the helium ions pass. When brought to different potentials, the transverse electric field between a set of plates deflects the ions and prevents them from passing through the aperture. In the current design, the plates of the main chopper are driven by a 2.5 MHz sine-wave voltage, while an adjustable frequency square-wave voltage is applied to the plates of the auxiliary chopper. The auxiliary chopper serves to sharpen the pulse edges and discard m of every n pulses from the main chopper, where $m < n$. With this system the frequency and width of the beam pulses that are passed to the buncher are adjustable [Mil79, Moa64].

The beam pulse FWHM was measured with

a 22 MeV pulsed ^{4}He beam on the 20° port off the bending magnet on the 59° beamline in the tandem laboratory. The beam passed through a capacitive pickoff before impacting a tantalum beamstop. A 5 cm diameter, 5 cm thick CsF scintillator detector was placed about 15 cm from the beamstop, at an angle of about 90° from the beam axis to record γ-rays produced by the beam. The detector was carefully shielded with lead and tungsten to ensure that it could only view the beamstop. A time-to-amplitude converter, started by the CsF detector and stopped by the delayed beam-pickoff signal, provided a measurement of the pulse width. A minimum FWHM of 1.1 ns was achieved (see Fig. 7.21) with an average beam current on target of 650 pnA (particle nanoamperes).

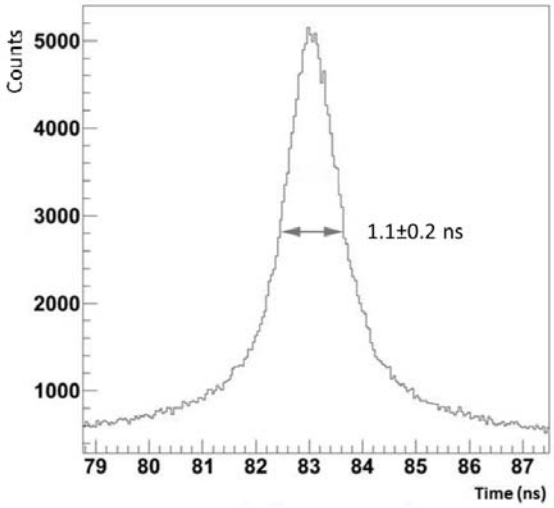

Figure 7.21: A measurement of the beam pulse time profile obtained with a 22 MeV ^{4}He beam using the beam pulsing system.

The minimum width of the beam pulse is limited by the energy spread of the ions emerging from the source. The main source of the energy spread is thought to be in the duoplasmatron (see Fig. 7.22), where a helium plasma is created by thermionic electrons emitted from the filament and is accelerated towards a biased probe. The plasma is magnetically confined, and helium ions are extracted using a high-voltage electrode. Decreasing the probe bias lowers the plasma temperature and consequently reduces the energy spread. Operating the source at a significantly lower probe bias requires increasing the gas pressure, magnetic field, and filament heating current well outside their normal operating values to obtain a nominal beam current. In addition, the source accelerating voltage was increased from 15 kV (30 keV beam) to 24 kV (48 keV beam) to improve the relative energy spread (ΔE/E). The source parameters for both standard- and low-plasma-temperature operating modes are given in Table 7.4.

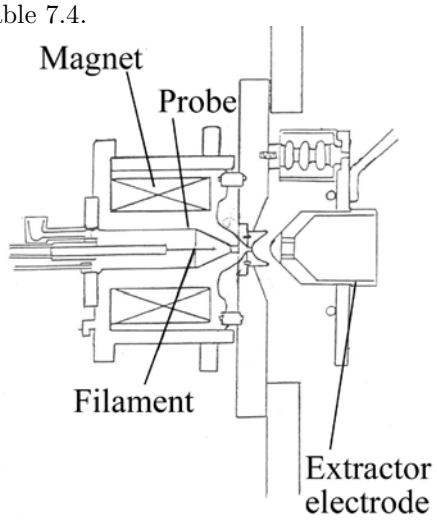

Figure 7.22: A schematic of the helium ion source duoplasmatron and extractor

Table 7.4: Comparison of Helium source parameters between normal and low plasma temperature modes. Probe bias is relative to filament.

Parameter	Normal	Low-T
Probe bias (V)	55	1
Filament current (A)	64	75 (max)
Magnet current (A)	1.5	1.68 (max)
Acceleration potential (kV)	15	24
Gas pressure (Torr)	0.25	4
Beam on target (pnA)	900	650
Pulse FWHM (ns)	3.3	1.1

[Mil79] W. T. Milner, IEEE Trans. Nucl. Sci., **NS-26**, 1445 (1979).

[Moa64] C. D. Moak *et al.*, Rev. Sci. Instrum., **35**, 672 (1964).

7.2.3 A ^{3}He Gas-Recirculation System for the Helium Ion Source

D.C. Combs, C.R. Howell, D.R. Ticehurst, A.R. Young, *TUNL*

A system for recovering and storing ^{3}He gas from the helium ion source on the tandem accelerator at TUNL has been designed. The design of the system is discussed.

Neutrinoless double-beta-decay ($0\nu\beta\beta$) experiments have the ability to probe the absolute mass scale of the neutrino, provided the nuclear matrix element associated with the decay is accurately known. Unfortunately, results from calculations of the $0\nu\beta\beta$ matrix element for a given isotope vary considerably depending on the model used [Ell04]. In an effort to constrain the calculated value of the ^{76}Ge $0\nu\beta\beta$-decay nuclear matrix element, a series of experiments to study the two-nucleon-transfer reaction (^{3}He,n) on isotopes of germanium will be carried out using the TUNL tandem accelerator. Given the scarcity and high cost of ^{3}He [Ade10], a system to recover and recirculate the gas in the helium ion source has been designed.

The helium ion source uses a diffusion pump backed by a mechanical pump to evacuate the source chamber. In the existing system the mechanical pump exhausts to atmosphere. The new recirculation system is shown in Fig. 7.23. To keep from introducing pump oil into the recirculating gas, a dry scroll pump with a molecular sieve on the inlet is used to back the diffusion pump. The gas then passes through a liquid nitrogen trap and an adsorber to further reduce contaminants. A diaphragm compressor is used to refill and pressurize the helium reservoir. The reservoir can also be refilled from a ^{3}He gas cylinder. Gas from the reservoir is fed to the source chamber through a flow controller. The adsorber and liquid nitrogen trap can be isolated with a set of valves and recharged using a second mechanical pump.

Vendors for most of the major system components have been identified, and the purchase of the system will happen in the coming months. Testing and construction of the system will follow as soon as the parts arrive at TUNL.

[Ade10] S. Adee, IEEE Spectrum, **47**, 16 (2010).

[Ell04] S. R. Elliott and J. Engel, J. Phys. G, **30**, R183 (2004).

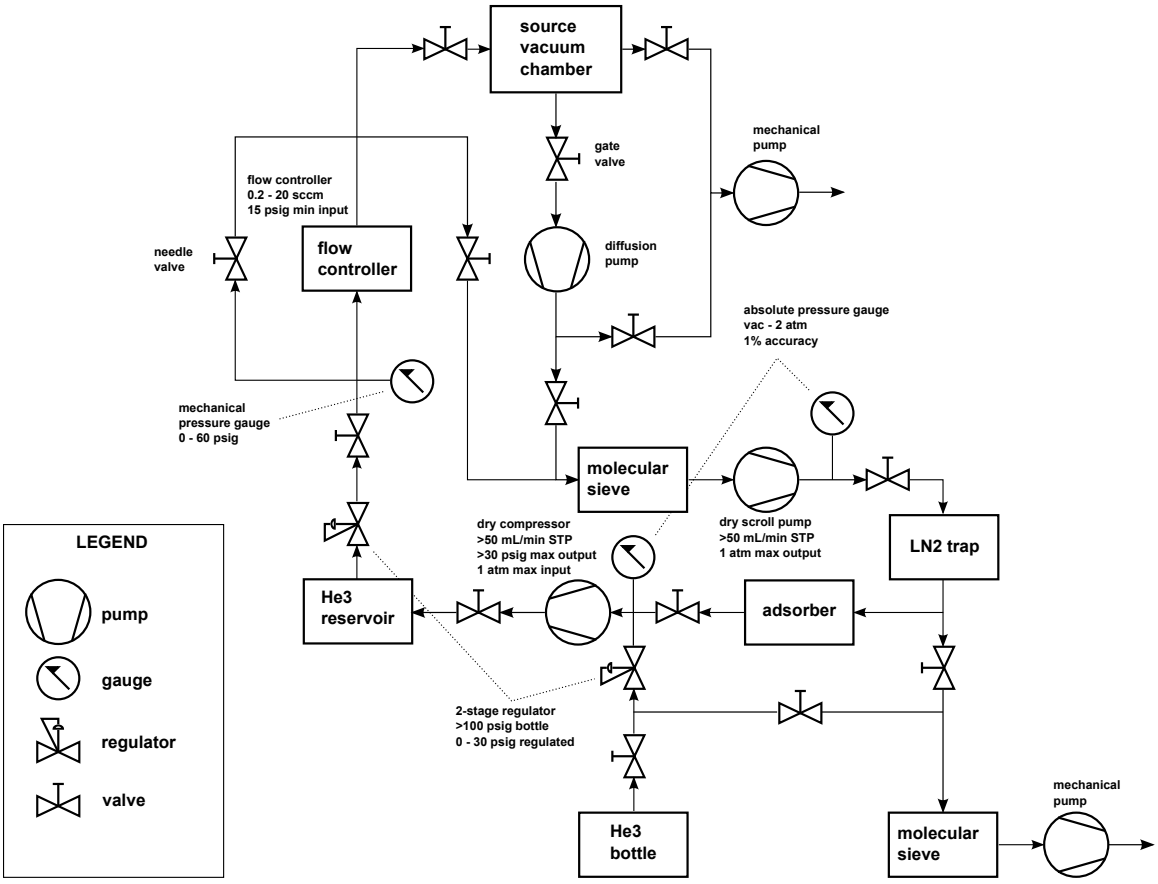

Figure 7.23: Schematic diagram of the proposed ^{3}He recirculation system. Specifications for key components are given.

7.3 The LENA Accelerator and Ion Sources

7.3.1 New LENA JN-Ion-Source Test Stand

S.M. Hunt, T.B. Clegg, A.E. Champagne, C.R. Westerfeldt, J.D. Dunham, *TUNL*

We have constructed a model JN ion source at LENA for testing electronic components and for the development of a He^+ beam for future experiments.

The LENA JN Van de Graaff accelerator is heavily used for nuclear astrophysics experiments, and many of its ion-source electrical components are currently operating very close to their technical design limits. Typical H^+ currents extracted from the accelerator are 100 to 300 μA, but electrical discharges or component overheating can cause failures or reduce the extracted beam. When failures have occurred, considerable time has often been expended in trying to find the cause.

Figure 7.24: (Color online) The new ion-source test stand with its protective cover in place.

Because of the heavy experimental use and the difficulty of testing and modifying the RF ion source without interrupting routine data collection, we constructed a separate ion-source test bench for off-line studies and component testing. Our first efforts with this new ion source will benchmark all key components and parameters for its RF oscillator circuits.

Another intended use of this new system is for identifying the operating parameters needed for intense He^+ beams for future (α,γ) and (α,n) experiments. Such development and testing can proceed without removing the JN accelerator from regular operation.

Figure 7.25: (Color online) Ion-source test stand with its cover removed to show the accelerator tube, electronics, and metering gauges.

This new ion-source test bench for offline component testing and He^+ beam exploration is shown in Figs. 7.24 and 7.25. It consists of a pumping system utilizing a 400 l/s turbopump and a backing pump mounted below a small section of acceleration tube. The RF-ion-source bottle attached to its gas sources is located on top of the tube. In the foreground are the metering gauges for ion-source parameters and extracted beam current, while the vertical plate on the right contains electrical components for the RF-oscillator circuit, extraction-electrode bias volt-

age, and variable-components tuning. The oscillator box and tubes, which have the greatest tendency to fail and which require the most testing, can be seen mounted at the upper right of the vertical plate.

A stable hydrogen discharge was obtained on the first day of testing, and we have begun to identify and select reliable oscillator-circuit components. After the most essential electrical components have been tested, work to obtain a He^+ beam will begin.

Nuclear Instrumentation and Methods

Chapter 8

- **Targets**
- **Detector Development and Characterization**
- **Facilities**
- **Data Acquisition Hardware and Software Development**

8.1 Targets

8.1.1 Development of the HIγS Frozen-Spin Target at TUNL

P.-N. Seo, D.G. Crabb, R. Duve, B. Norum, S. Tkachenko, *University of Virginia, Charlottesville, VA*; R. Miskimen, *University of Massachusetts, Amherst, MA*; C.R. Howell, H.R. Weller, *TUNL*

The HIγS Frozen-Spin-Target is under development for measurement of the GDH sum rule on the deuteron. The cryostat/refrigerator has been extensively tested at UVa, and the other subsystems are being tested at TUNL. We report progress.

The HIγS Frozen-Spin-Target (HIFROST) system consists of several major subsystems: the cryostat/refrigerator, pumping, 70-GHz microwave, NMR, polarizable material, and superconducting magnet systems. In July 2011, the complete frozen-target system, except for a 2.5-T iron magnet and its power supply, arrived at UVa from Helmholtz-Zentrum-Geesthacht, Germany. After initial checking, all the equipment, except for the cryostat/refrigerator and roots pumps, was brought to TUNL. The manuals and operation documents came with the equipment but were written in German. Translations of the necessary manuals were performed, but the resulting hand-written documents are still difficult to understand. A lot of the equipment is useful, but testing, repair, modification, and the purchase of missing parts will be necessary before it can be used in HIFROST. We report on progress in the construction of HIFROST, which is proceeding in parallel at UVa and TUNL.

Work at UVa consisted of modifying the mixing chamber, reconfiguring and testing the thermal sensors around the target area, and extensive leak tests of the cryostat/refrigerator at room temperature (see Figs. 8.1 and 8.2). Leaks found in the ^{3}He path of the dilution refrigerator (DR) were repaired, and the leak tests were repeated. Currently the cryostat is being prepared for an extensive cryo-cooling test at UVa. A pump for a separator on the dilution refrigerator was repaired. ^{3,4}He pipes were leak-tested and connected to the UVa system. A target stand was fabricated just for this test. During the cooling test, we will be able to test this newly-designed mixing chamber and the target holder (both tested with LN_2 and microwaves), as well as the cryostat. After the cryo-cooling test, the system will be shipped to TUNL. We plan to have a target stand ready at HIγS to support the cryostat on the beam line, both horizontally for operation and vertically for target changes. The stand is under construction.

Figure 8.1: (Color online) A newly developed, LN_2-tested mixing chamber mounted to a dilution refrigerator.

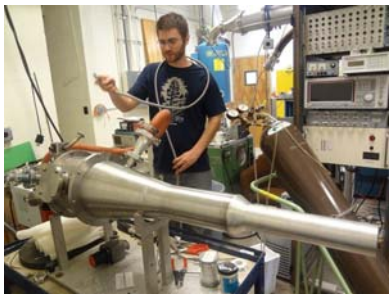

Figure 8.2: (Color online) Leak-testing the DR at room temperature.

The pumping system consists of the ^{3,4}He pumping systems and the gas-handling system. Two completed pumping systems were periodically run overnight for longer hours, and they performed as expected. The HIFROST gas-handling system, part of which is shown in Fig. 8.3, uses a 100-L liquid helium (LHe) buffer Dewar for continuous feeding of the refrigerator, plus a 500-L storage Dewar. The buffer Dewar is located close to the cryostat, while the storage Dewar is located outside the experimental setup area. We have completed the design of the LHe transfer line from the storage Dewar to the buffer Dewar and to a polarizing superconducting magnet. The lines use a combination of flexible parts and rigid lines with vacuum- and super-insulated technology for efficient transfer. Cryofab, Inc. in New Jersey is fabricating the LHe transfer lines with a lead time of seven weeks. The other parts of the gas-handling system are the main vacuum system, the IVC vacuum system, the ^{3}He circulation system, and the ^{4}He venting system. The main vacuum system was tested, and the vacuum reached 2.3×10^{-8} mbar. The cold-trap in the ^{3}He circulation system is being tested; the ^{4}He venting system is under construction; and the piping for ^{3,4}He is currently being designed.

Figure 8.3: (Color online) Racks holding a gas tank and a cold trap.

HIFROST has two sets of microwave systems to generate 70 GHz in a 2.5-T magnetic field using the dynamic-nuclear-polarization technique. One option (see Fig. 8.4) is an extensive-interaction oscillator (EIO) driven by a Cober power supply. The other (see Fig. 8.5) is a carcinotron driven by a Siemel power supply. The EIO was purchased a few years ago, and a Cober power supply was recently refurbished and tested at TUNL. Each power supply was tested with energy distributors (dummy loads) and then connected to the corresponding microwave generator. Both generators are water-cooled. In order to monitor modulation of the RF frequency, we scanned the line voltages for different anode voltages. Results from each microwave system agreed with the test data given by the manufacturers. The EIO and Cober power supply will be our main microwave system, and the other system will be used as a backup. The Cober will be manually tuned during an experiment.

Figure 8.4: (Color online) Photo of microwave system test; EIO powered by Cober.

Figure 8.5: (Color online) Photo of microwave system test; carcinotron powered by Siemel.

Three NMR Q-meters were also obtained from Germany, and two of them were tested. Two proton Q-meters and one deuteron Q-meter are available. The LabVIEW-operated DAQ was tested at TUNL and is being upgraded at UVa.

In developing and constructing the frozen-spin-target system for HIγS, a lot of progress has been made on the DR, the microwave system, the gas-handling system, and on the design of several critical components. Our efforts for HIFROST are aimed at commissioning the system in the next six to seven months. Installation of gas piping and the LHe transfer lines is planned for October. In December, we will start to install the HIFROST equipment in the experimental area, with testing of the system as a whole scheduled for February 2013.

8.1.2 Status of the Polarized ^{3}He Compton Target at TUNL

H. Gao, M.W. Ahmed, C.W. Arnold, C.R. Howell, T. Clegg, M. Huang, S.S. Jawalkar, H. Karwowski, G. Laskaris, H.R. Weller, Y. Wu, X. Yan, Q.J. Ye, A. Young, *TUNL*; T. Averett, *College of William and Mary, Williamsburg, VA*; J.R. Calarco, *University of New Hampshire, Durham, NH*; J.P. Chen, *Thomas Jefferson National Accelerator Facility, Newport News, VA*; D. Dutta, *Mississippi State University, Starkville, MS*; A. Nathan, *University of Illinois, Urbana-Champaign, IL*; X. Qian, *California Institute of Technology, Pasadena, CA*; Q. Ye, *Oak Ridge Associated Universities, Oak Ridge, TN*

A high-pressure ^{3}He cell has been polarized inside a single layer solenoid using the spin-exchange optical-pumping technique. This target system is under development for double-polarized Compton-scattering experiments. The initial report is delineated here.

Nucleon spin polarizabilities describe the stiffness of the nucleon spin to changing external electric and magnetic fields. Compared to the nucleon's electric and magnetic polarizabilities, very little is known about the nucleon's spin polarizabilities. The only quantities that have been determined experimentally are the forward and backward spin polarizabilities. Recently, double-polarized elastic Compton scattering from polarized ^{3}He has been investigated theoretically, and sensitivity to the neutron's spin polarizabilities has been demonstrated [OdL01]. The double-polarized Compton experiment requires circularly polarized photons and a polarized ^{3}He target.

The ^{3}He target for this experiment is under development and consists of four sub-systems: the solenoid magnet to provide the magnetic holding field, the oven and heating system to maintain the temperature required for spin-exchange optical pumping (SEOP), the laser and optics to generate circularly polarized light for SEOP, and the nuclear magnetic resonance (NMR) and electron paramagnetic resonance (EPR) system for polarimetry.

A single-layer solenoid has been developed to provide the holding field for the polarized ^{3}He target. It provides a uniform magnetic field along the cylindrical axis of the target chamber for maintaining the ^{3}He polarization and defining the polarization vector. The heating system funnels hot air into the oven that holds the glass cell containing ^{3}He and a small quantity of rubidium (and potassium in the case of a hybrid cell). A temperature sensor inside the oven monitors the temperature, and the highest temperature reached is typically 240°C. Laser light at 795 nm is circularly polarized using the standard optics arrangement, and the NMR and EPR systems are similar to the ones used in Ref. [Ye08]. A schematic of the oven inside the solenoid is shown in Fig. 8.6.

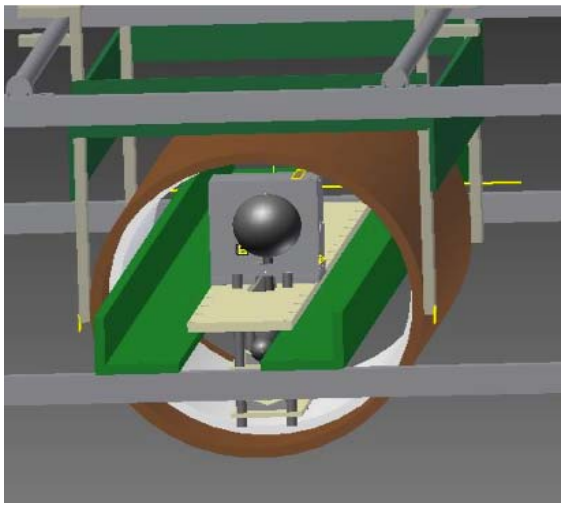

Figure 8.6: (Color online) Schematic of the oven inside the single layer solenoid. The oven and pumping chamber of the cell (gray) are placed at the center of the cylindrical solenoid magnet (brown).

The new target system was used to polarize ^{3}He for the first time in March 2012 with about 60W of laser power. The NMR system is functional, and signal height from the NMR signal is proportional to target polarization.

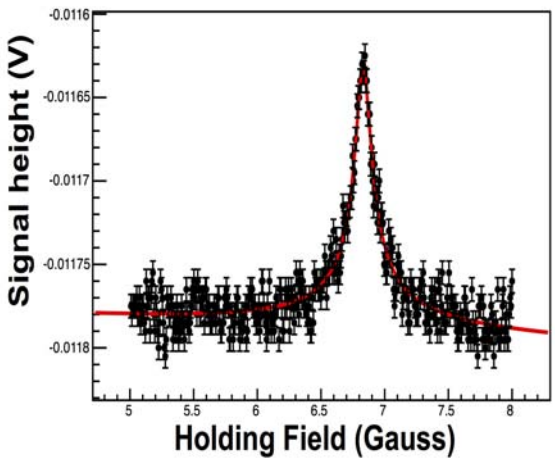

Figure 8.7: (Color online) NMR scan as a function of the holding field of the solenoid. The signal height is proportional to the ^{3}He target polarization.

An example of a good NMR scan is shown in Fig. 8.7. The system was tested using two cells named "Pablum" and "Yu." We are in the process of increasing laser power so as to achieve higher polarization and perform a successful EPR measurement. This target system will be used in the gamma vault at HIGS to measure double-polarized Compton scattering. The details for installing the entire target system are in the research-and-development stage.

[OdL01] V. Olmos de Leon *et al.*, Eur. Phys. J. A, **10**, 207 (2001).

[Ye08] Q. Ye, Ph.D. thesis, Duke University, 2008.

8.2 Detector Development and Characterization

8.2.1 Commissioning of Dual-Fission-Chamber Detectors to Study Fission Product Yields

C. Bhatia, B.A. Fallin, M.E. Gooden, C.R. Howell, J.H. Kelley, W. Tornow, *TUNL*; C.W. Arnold, E. Bond, T. Bredeweg, M. Fowler, W. Moody, R. Rundberg, G. Rusev, D. Vieira, J. Wilhelmy, *Los Alamos National Laboratory, Los Alamos, NM*; J. Becker, R. Macri, C. Ryan, S. Sheets, M. Stoyer, A.P. Tonchev, *Lawrence Livermore National Laboratory, Livermore, CA*

The design, fabrication, and testing of three dual-fission-chamber detectors were completed. The chambers will be used to study the energy dependence of the fission-product yields of ^{235}U, ^{238}U, and ^{239}Pu. They measure the fission-product activity relative to the total fission activity, and are used for high precision, absolute fission-yield measurements.

A joint TUNL-LANL-LLNL program was initiated to provide a modern, accurate, self-consistent approach to systematically investigate the energy dependence of the cumulative fission yields. For these measurements, we have fabricated three dual-fission-chamber detectors and used one for each of the three fissile targets: ^{235}U, ^{238}U, and ^{239}Pu. The detectors were basically a copy of the design developed by D. Gilliam at NIST [Gru75]. A cut-away view of a dual-fission-chamber detector is shown in Fig. 8.8.

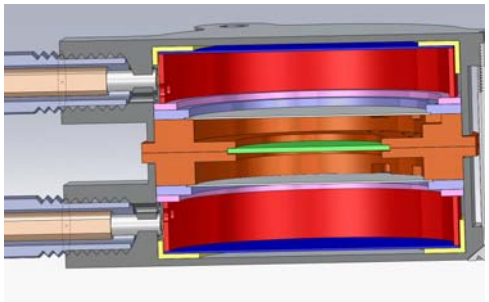

Figure 8.8: (Color online) Cut-away view of a dual-fission-chamber detector.

The dimensions of the active gas volume (2.21 cm diameter, 0.43 cm thick) are the same as in the original NIST chamber. The body of the detector has an outside diameter of 2.50 cm and is 1.73 cm thick. The thin beam-monitoring targets were prepared by electroplating onto 5 mil thick Ti, and the active deposits were a half inch in diameter. For the ^{235}U and ^{238}U detectors, the monitor targets were about 100 μg/cm^2, while for the ^{239}Pu target the monitor foils were about 10 μg/cm^2. The thicker activation foils were also a half inch in diameter. The masses of the target foils were 0.46 g for ^{238}U, 0.26 g for ^{235}U, and 0.23 g for ^{239}Pu.

We improved the design to facilitate the insertion and removal of the thick activation target between the two fission chambers. This was done by making the two fission chambers mirror images of each other, as shown in Fig. 8.9. This separation required a gas connection to each fission chamber and a separate signal connection for each chamber. When the two chambers are mounted together, there are passages between them for gas to flow from one to the other. For normal operation, the gas connection on one chamber is the gas supply and the gas connection on the second chamber is the gas return (see also Fig. 8.8).The mating faces of the two chambers are carefully machined and then lapped so that the assembled detector is leak free, even without a gasket between the two chambers. Likewise, the holder for the thin fission target in each chamber is designed to be a press fit into the chamber body and is also leak tight. Gas connections to the fission chambers are made with SS tubing. The gas lines terminate in a manifold that has connections for the gas supply or return, as well as connections for the chamber signals. The signals from each of the fission chambers are connected to the manifold via UT-085 semi-rigid coax that runs inside the gas lines.

P-10 counting gas (90% argon and 10% methane) is used for the detector fill gas. The total volume of the detector is about 3.5 cm^3. The

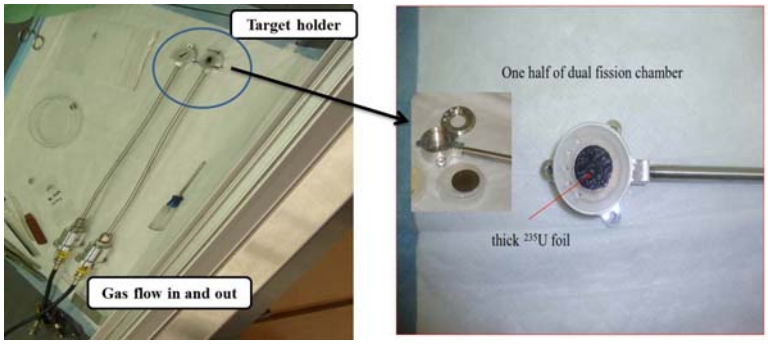

Figure 8.9: (Color online) Complete view of dual-fission-chamber detector showing the target-holder and gas-flow systems.

gas return from the detector flows through a 0.5 μm filter to prevent loss of any particulate material that might be formed in the fission chambers. After the filter, the gas is passed through an oil filled bubbler to allow visual monitoring of the gas flow (a few cc/min). After the bubbler, the gas is vented to ambient atmosphere.

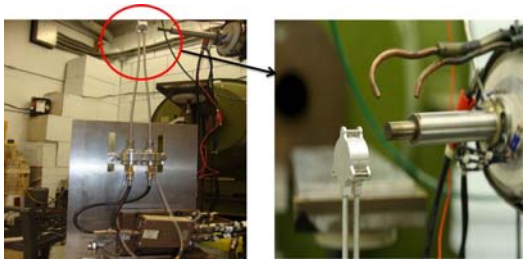

Figure 8.10: (Color online) Dual-fission-chamber detector in front of the deuterium gas cell.

The detectors, with their thick target foils and thin monitor foils, were exposed to neutron beams produced via the ^{2}H$(d,n)^3$He and ^{3}H$(d,n)^4$He reactions, as shown in Fig. 8.10. The chambers were biased with +150 V on the collector, although in a few runs the bias was +200 V. The signals from the chambers were fed to Ortec 142-PC preamplifiers. The energy signals from the preamplifiers were then amplified, shaped, and digitized. The timing signals from the preamplifiers were used to provide system triggers. The acquisition signal logic was set up so that signals from either chamber could trigger the acquisition system. In cases where we used a pulsed beam, there was also a TAC that was started by the beam pulse and stopped by signals from the fission chamber or the neutron flux monitor. We used these data to investigate the energy distribution of the neutrons as measured via time-of-flight. The timing resolution measured between the fission detector and the beam pulse was 6 ns FWHM with a beam pulse of about 2 ns duration. Excellent separation between α-particles and fission events is observed, as shown in Fig. 8.11.

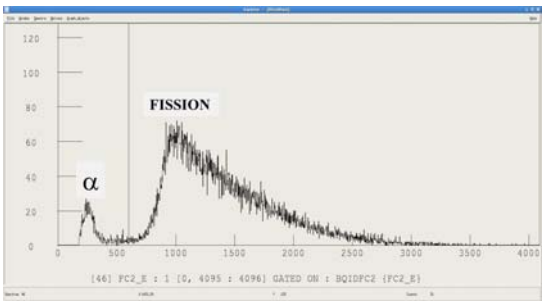

Figure 8.11: (Color online) Fission spectrum at E_n = 9 MeV, showing excellent α-fission separation.

The fission detection efficiency (counts/fission) was reported [Gru75] to be greater than 0.985. We also measured the efficiency by preparing ^{252}Cf sources with the same configuration as the monitor foils and whose fission rates were determined by alpha counting. These measurements gave detection efficiencies of 1.00 ± 0.02. In addition, we measured the neutron flux with activation foils and estimated the detection efficiency based on the observed fission rate. We estimated the difference in the neutron flux at the positions of the two monitor foils due to geometrical differences and found that the observed differences in fission counting rate (upstream/downstream = 1.23) agreed with the calculated values. We also replaced the monitor foils with activation foils to determine the flux at the monitor foil positions and the measured activities agreed with calculated values.

[Gru75] J. Grundl *et al.*, Nucl. Technol., **25**, 237 (1975).

8.2.2 Development of a Lithium-Glass-Based Composite Neutron Detector for ^{3}He Replacement

G.C. Rich, *Lawrence Livermore National Laboratory, Livermore, CA and TUNL*; K. Kazkaz, *Lawrence Livermore National Laboratory*

We are fabricating two cylindrical lithium-glass-based composite neutron detectors. One is 2 in. in diameter, 3 in. in height and another 5 in. by 5 in., each made of dye-loaded polyvinyltoluene embedded with 1.5-mm lithium-glass cubes. Initial simulations of a ^{252}Cf source suggest that the 2 in. x 3 in. and 5 in. x 5 in. detectors will be roughly 1% and 10% efficient, respectively, for detection of unmoderated fission neutrons. Experimental evaluation of the detectors will be carried out in late summer 2012.

The idea of composite scintillators was explored by Knoll in the late 1980's [Kno87], but there has been a renewed interest in their development and optimization, with numerous groups exploring composites based on lithium gadolinium borate (LGB) crystals for capture-gated neutron spectroscopy [Men09], anti-neutrino detection [Nel11], and helium-3 replacement [Kaz11]. Motivated by the well-established ^{3}He shortage, we have sought to improve upon previous efforts exploring composite scintillators as neutron detectors by selecting an alternative neutron-sensitive, embedded scintillator material and optimizing the dimensions of the pieces of this material to enable more reliable γ-ray-rejection capabilities through pulse-shape discrimination or PSD.

Kazkaz *et al.* [Kaz11] showed that only signals produced by neutron capture on ^{6}Li could be reliably distinguished from γ-ray events, encouraging selection of a different inorganic scintillator to optimize neutron detection efficiency. There are numerous factors to consider when selecting an appropriate replacement for LGB in this application. These include the scintillation light decay constant, which must be sufficiently long relative to that of the acrylic matrix to facilitate reliable PSD and γ-ray rejection; the chemical composition and, specifically, the number of ^{6}Li nuclei per molecule, which should be high to maximize effective use of detector volume; the scintillation light output; and the material's index of refraction. Numerous alternative scintillators were considered, and KG2-type, ^{6}Li-enriched glass was selected for its closely matched index of refraction with the acrylic matrix, its desirable scintillation decay time, and its relatively high number of ^{6}Li nuclei per molecule.

Extensive Monte Carlo simulations have been carried out using the GEANT4 simulation toolkit. To analyze the simulation outputs, a 9% Gaussian spreading is applied to the raw, unbinned energy depositions in both the plastic and the ^{6}Li-glass cubes. This 9% resolution is based on experimental findings for an LGB detector [Kaz11]. Included in these simulations is the quenching of light from energy depositions in the lithium glass by the α particle and triton resulting from neutron capture on ^{6}Li. Relative to light output from electron energy deposition, the neutron capture peak occurs at an electron-equivalent energy of 1.6 MeV (or 1.6 MeVee) [Fir61]. Figure 8.12 illustrates the procedure for determining the number of neutron events.

Simulations suggest that a 2-in.-diameter, 3-in.-tall cylindrical detector with 7% Li-glass by mass will have an intrinsic detection efficiency for fission neutrons from ^{252}Cf of about 1 %. Menaa *et al.* [Men09] performed experiments using 2 in. x 2 in. cylindrical detector loaded with approximately 20 % LGB by mass and found its intrinsic detection efficiency for ^{252}Cf neutrons to be (0.28 ± 0.03) %. Similarly, simulations predict an intrinsic unmoderated fission neutron detection efficiency of about 10% for a 5 in. x 5 in. cylindrical Li-glass composite detector (again 7% Li-glass by mass), which can be compared to the experimental results of Kazkaz *et al.* who found a comparably sized, LGB-based detector, with 1% LGB by mass, to have an intrinsic efficiency of (0.416 ± 0.007) %.

Selection of small dimensions for the Li-glass cubes helps to minimize the number of γ-ray-induced counts that occur inside the neutron-peak region-of-interest (NPR). According to the ESTAR library provided by NIST [Ber05], the range of a 1.5 MeV electrons in lithium glass is calculated to be about 3.5 mm—over twice

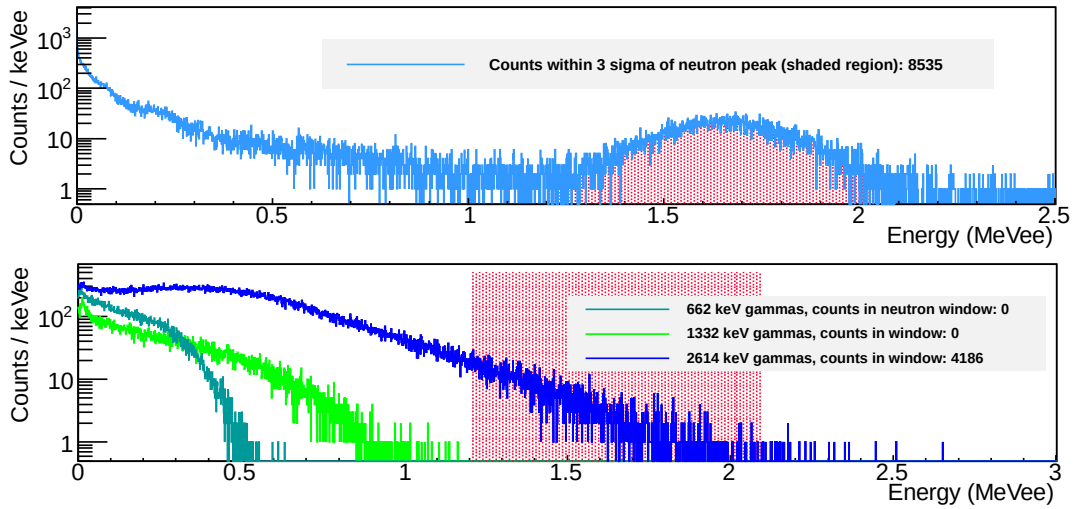

Figure 8.12: (Color online) Plot of the simulation output for a 2-in.-diameter by 3-in.-tall cylindrical, Li-glass based composite detector with 9% Li-glass by mass. (Top) The number of neutron counts is determined by fitting a Gaussian to the neutron peak centered around 1.6 MeVee and integrating the histogram to $\pm 3\sigma$, defining the NPR (shaded). The simulation used ten million primary decay events of a ^{252}Cf source, emitting isotropically, located 16.2 cm from the circular face of the detector. (Bottom) The energy spectra in the glass cubes for various γ-ray energies; the shaded region represents the NPR. In each simulation, there were one million γ rays of the designated energy, all generated 16.2 cm from and directed towards the center of the circular face of the detector.

the length of the side of a face of our cubes. Neglecting potential pile-up events, our detector should have no sensitivity to typical γ-ray backgrounds, such as those from ^{137}Cs, ^{60}Co, and ^{40}K. However, γ rays with an energy over about 1.6 MeV could deposit sufficient energy in a Li-glass cube to appear in the NPR (see bottom panel of Fig. 8.12). Current simulations do not consider the PSD capabilities of this composite material. Using PSD techniques, LGB detectors have achieved levels of gamma sensitivity on the one-part-per-billion scale [Kaz11].

Experimental results from the first 2 in. x 3 in. detector are expected in early August 2012, with results of the 5 in. x 5 in. model following soon thereafter. The detectors will initially be characterized using various neutron and γ-ray sources and will be compared directly to new measurements using an LGB-based composite detector and moderated ^{3}He tubes. Further studies may be undertaken using neutrons generated by the ^{7}Li(p,n)^{7}Be reaction.

This work supported by the U.S. Department of Energy under Lawrence Livermore National Laboratory contract DE-AC52-07NA27344. LLNL-TR-566674.

[Ber05] M. Berger *et al.*, *Stopping-Power and Range Tables for Electrons, Protons, and Helium Ions*, Technical Report NISTIR 4999, NIST, Physical Measurement Laboratory, http://physics.nist.gov/Star, 2005.

[Fir61] F. Firk and G. Slaughter, Nucl. Instrum. Methods, **13**, 313 (1961).

[Kaz11] K. Kazkaz, N. Bowden, and M. Pedretti, arXiv/nucl-ex, **1109** (2011).

[Kno87] G. Knoll, T. Henderson, and W. Felmlee, IEEE Trans. Nucl. Sci., **NS-34**, 470 (1987).

[Men09] N. Menaa *et al.*, IEEE Trans. Nucl. Sci., **56**, 911 (2009).

[Nel11] P. Nelson and N. Bowden, Nucl. Instrum. Methods A, **660**, 77 (2011).

8.3 Facilities

8.3.1 Development of an Ultracold-Neutron Source at the NC State PULSTAR Reactor Facility

R. Golub, P.R. Huffman, G. Medlin, G. Palmquist, A.R. Young, *TUNL*; A. Cook, A. Hawari, E. Korobkina, B. Wehring, *North Carolina State University, Raleigh, NC*

We are in the early stages of commissioning a next-generation ultracold-neutron source at the PULSTAR reactor facility on the campus of NC State University. We envision using the source for performing neutron β-decay measurements as well as systematic studies for the neutron-electric-dipole-moment experiment as described in a separate contribution.

Ultracold neutrons (UCNs) play an important role in nuclear-physics investigations that seek to test the Standard Model of particle physics and characterize the weak interaction. UCN-source technology is advancing rapidly, and the numerous techniques presently being implemented should permit a gain of several orders of magnitude in useful UCN densities. Such higher densities of UCNs will not only permit improved measurements of quantities such as the neutron electric dipole moment (nEDM) and neutron β-decay lifetime, where measurements utilizing UCNs already provide the most precise experimental values, but will also play a role in neutron-angular-correlation measurements, neutron-antineutron-oscillation searches, spectroscopic studies of neutron decay, fundamental tests of quantum mechanics, and, potentially, cutting-edge neutron-scattering applications.

The PULSTAR ultracold-neutron source is designed to be a next-generation UCN source that utilizes solid deuterium (SD_2) at a temperature of 5 K to moderate thermal neutrons to UCN energies. The high leakage of fast/thermal neutrons from the reactor core makes it possible to couple efficiently the neutron flux to the D_2O thermal moderator and the solid methane CH_4 cold moderator that surrounds the deuterium.

The concept for our facility is to place the UCN source in a tank of D_2O positioned in the former thermal column of the PULSTAR reactor. Neutrons leaving the face of the reactor core are channeled into the D_2O tank by a 45 cm × 45 cm × 70 cm long void in a graphite assembly called the nose port. The source consists of a UCN converter of solid ortho deuterium, 17 cm in diameter and 4.5 cm thick, held at a temperature below 5 K. The converter is surrounded by a 1-cm-thick, cup-shaped cold source of solid methane held at a temperature of about 25 K. This configuration was optimized for maximum cold-neutron flux using detailed MCNP calculations. Measurements of the thermal neutron flux inside the D_2O volume are presently being used to benchmark these calculations and to predict the useful experimental UCN population using a Monte Carlo transport code developed at NCSU. The basic geometry of the source is shown in Fig. 8.13.

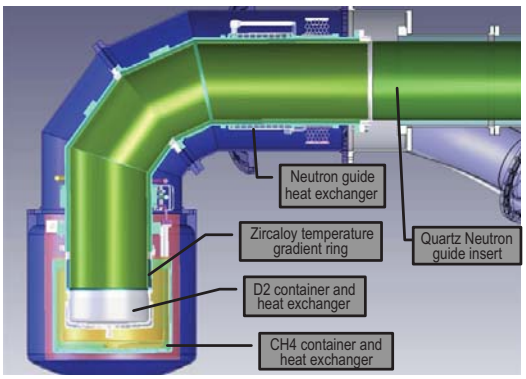

Figure 8.13: (Color online) Schematic of the UCN source and guide system. A D_2O thermal moderator surrounds the entire assembly.

As discussed in previous progress reports, the installation of the nose port/shielding box in the reactor is complete. The heavy-water tanks and circulation system as well as modifications to the thermal-column door assembly are in place. The liquid-helium liquefier and circulation system are installed and have been tested. A photograph of the assembled source and guide housing is

shown in Fig. 8.14; a photograph of the source within the thermal moderator housing is shown in Fig. 8.15. Photographs of the ^{58}Ni coated neutron guides and the gas-handling system are shown in Figs. 8.16 and 8.17, respectively.

The source is fully constructed, and initial testing and characterization have begun. The system is leak-tight and has been successfully cooled with liquid nitrogen.

Figure 8.14: (Color online) Photograph of the assembled UCN source.

Figure 8.15: (Color online) Photograph of the large aluminum container that houses the D_2O thermal moderator surrounding the UCN source assembly. The UCN source is located within this container.

Initial cryogenic tests of the system are in progress using non-flammable gasses. Specifically, we have cooled the cryogenic methane-moderator container and solidified argon into the region. We first filled the room-temperature ballast tank with 1100 mbar of argon. The cryostat was cooled with liquid nitrogen and the argon liquefied into the methane container. The temperature was then lowered, and the argon froze into a solid. This allowed us both to verify the functionality of the system and to confirm that the temperatures and pressures at which argon begins to condense and/or solidify are consistent with our estimates.

Figure 8.16: (Color online) Photograph of a ^{58}Ni-coated neutron guide that resides in the UCN source assembly.

Figure 8.17: (Color online) Photograph of the methane and deuterium gas-handling systems.

The next step is to repeat this system test with neon substituting for the deuterium moderator. Once these two tests are performed and additional safety approvals are in place, we will repeat these tests with methane and deuterium. Upon completion, we will move the entire assembly into the thermal column of the reactor and begin producing ultracold neutrons.

8.4 Data Acquisition Hardware and Software Development

8.4.1 Status of the ORCA Data Acquisition Software

M.A. Howe, J.F. Wilkerson, *TUNL*; T. Bergmann, A. Kopmann, *Karlsruhe Institute of Technology, Karlsruhe, Germany*

We describe additions and improvements to ORCA, an object-oriented real-time control-and-acquisition system. ORCA is in use at a number of laboratories in the US, Canada, and Germany and is under continuous development. Over the last year, a number of new VME, ethernet, and serial devices were added to the list of supported hardware. In addition, new features were added to some of ORCA's subsystems.

The ORCA (object-oriented real-time control-and-acquisition) software system [How11] is designed for dynamically building flexible and robust data-acquisition systems. ORCA is being used at UNC, TUNL, University of Washington's Center for Experimental Nuclear Physics and Astrophysics, SNOLAB, Karlsruhe Institute of Technology, LANL, LBNL, and MIT. It is being used in the development of the KATRIN, MAJORANA, SNO+, and HALO experiments. ORCA-based slow-control systems are monitoring the environmental conditions for the MAJORANA project at the Sanford Underground Research Facility.

ORCA is under continuous development. New features are added as requested, and the catalog of supported objects continues to grow. In the last year, a number of new serial devices were added:

- TPG256A. A four-channel measurement and control unit for Pfeiffer compact pressure gauges.
- TM700. A controller for a Pfeiffer turbo pump.
- RGA300. A residual-gas analyzer from Stanford Research Systems.
- CP8. A cryopump controller.
- MKS651c. A single-channel pressure gauge with five set points for valve control.
- Met 237. A two-channel particle counter.
- Met 837. A six-channel particle counter.
- MKS660B. A baratron pressure gauge from MKS.
- ProXR16. A sixteen-channel relay control card useful for controlling valves.

One new VME card was added:

- V830. A 32-channel multi-event latching scaler.

The list of newly supported IP devices includes:

- LabJack UE9. A data-acquisition box with fourteen 12-bit analog inputs, two 12-bit analog outputs, twenty-three digital I/O lines, two counters, and six timers.
- Labjack Mux80 AIN Board. This board expands the number of ADC inputs of the UE9 to 80.

A few objects were developed specifically for the MAJORANA experiment:

- MAJORANA Preamp Controller. This is the detector preamp which is controlled from ORCA via a serial peripheral interface bus connection from a GRETINA card.
- Vacuum Status. A dialog showing an overview of the MAJORANA vacuum system, including enunciation of any existing operation constraints.
- Two-Bit Callback Object. This object is used in ORCA process controllers to dynamically map MAJORANA vacuum-system gate-valve limit switches to digital I/O channels.
- One-Bit Callback Object. This object is used in ORCA process controllers to dynamically map a MAJORANA vacuum-system gate-valve limit switch to a digital I/O channel.

- Object-Callback Processor. This object is used in ORCA process controllers to dynamically map a MAJORANA gate-valve actuator to a relay controller like the ProXR16.

New generic objects include:

- Custom 2D Plotter. This object can be used by ORCA scripts for plotting 2D data sets.

- Remote Socket Object. This is an interface object that allows a script to retrieve arbitrary information from another ORCA running on a remote machine. It can also be used to control remote ORCA operations.

Some objects had major improvements:

- KATRIN Power-and-Control (PAC) Board. The PAC board object was integrated into ORCA's process control system. The user interface was rewritten to be easier to use.

- VXM Stepper-Motor Controller. This object was rewritten to be easier to use via scripts. A motion-sequence system was added so that a large number of motion commands can be executed one after another, automatically.

- Scripts. Simple file I/O was added. A global variable pool was added for inter-script communication. A very large self-test script was developed to verify script syntax and functionality.

- SIS3302. This Struck card had a new firmware update to make readout of long waveforms more efficient.

- KATRIN First Level Trigger (FLT) Cards. The FLT cards now support direct-memory-access block transfers, which increases their maximum data rate by an order of magnitude.

The release of a new compiler (XCode 4) and MacOS operating system (10.7) required a large sweep of the ORCA code base to eliminate new compiler warnings and to take advantage of some of the new Objective-C language features. One such feature, Blocks, allows a more functional programming style for user interface elements like Open/Save dialogs through the elimination of callbacks. All ORCA code using callbacks was rewritten to take advantage of Blocks.

Another major change was the wide-spread adoption in ORCA of a new framework for launching concurrent operations. Now many operations in ORCA that were previously handled in the main thread using timers and other tricks have been moved into separate threads, which makes the code more efficient and easier to read. Previously threaded operations that were prone to deadlocks and thread safety issues are much more robust under the new framework. In addition, in the new framework, inter-operation dependencies that provide an absolute execution order for operations can be specified, even if those operations are located in different operation queues.

A new version of the mobile remote-monitoring application (IORCA) [How10] for ORCA was released. The new version now runs on iPhones as well as iPads. This required reworking all of the dialogs so they would fit on the smaller iPhone display. In addition, a number of improvements were added. Previously only one database could be monitored at a time. In the new version, the user can now enter a list of databases, and the database query code was completely rewritten to allow the monitoring of all of the ORCA databases in the list to be monitored simultaneously. In addition, the dialog showing the list of all available data now uses a hierarchical and collapsible list, which makes it much easier to navigate large data sets.

A secondary application to ORCA, called ORCAROOT, provides a tool kit to build analysis programs that can decode raw ORCA data streams. As new objects are added to ORCA, new decoders are also added to ORCAROOT to fully support ROOT analysis of data from the new objects.

[How10] Howe, M. A. *et al.*, TUNL Progress Report, **XLIX**, 214 (2010).

[How11] Howe, M. A. *et al.*, TUNL Progress Report, **L**, 182 (2011).

8.4.2 Status of the KATRIN Data Acquisition System

M.A. Howe, J.F. Wilkerson, *TUNL*; T. Bergmann, A. Kopmann , *Karlsruhe Institute of Technology, Karlsruhe, Germany*; S. Enomoto, *University of Washington, Seattle*

We describe the status of the KATRIN data acquisition system. Over the last year, the main focal-plane detector and the veto-system hardware have been installed in the detector hall at KIT. The data acquisition software ORCA and the slow-control systems have been running stably during the integration and testing of the system.

Data acquisition for the KATRIN detector requires a complex chain of software consisting of the main data-acquisition software, the slow-controls monitoring system, databases to hold all operational parameters, and a data-analysis chain. All of the software in this chain is now in place and is being commissioned at the experiment's site at Karlsruhe Institute of Technology (KIT) in Karlsruhe, Germany.

The main data-acquisition-system software is the object-oriented real-time control-and-acquisition (ORCA) system, developed and supported by UNC (See Sect. 8.4.1). ORCA is responsible for controlling and reading out the KATRIN main focal-plane detector (FPD), the veto system, and the KATRIN monitor spectrometer.

The FPD is a 148-pixel detector that produces data at rates that vary from mHz (normal running) to MHz (during calibration). The FPD was originally assembled and tested at the University of Washington (UW). Last year the system was shipped from UW to KIT and reassembled on site. The signals from the detector are digitized using the first-level-trigger (FLT) cards developed at the Institute of Data Processing and Electronics (IPE). The design of the FTL electronics allows for data readout to be done in either an event-by-event mode or a fast histogramming mode. One major change in the FLT cards in the last year was the development of direct-memory-access (DMA) readout modes. DMA increases the maximum readout rate by an order of magnitude. All readout modes are supported by ORCA.

The veto system was developed at MIT and was shipped to KIT last summer. The veto system has 32-channels and runs at hundreds of Hz. In the past year, we worked closely with our KIT collaborators at IPE to provide ORCA support of the new FLT card field-programmable gate array firmware that is used by the KATRIN veto system. The veto firmware has a run-time option that allows one IPE crate to support a mixed set of FLT cards, some running in the veto mode and the others running in the regular readout mode. The ORCA FLT software and dialogs were expanded to show the veto parameters as panel groups, with options to set the number of channels required to be in coincidence for an event. Extensive verification of the veto firmware at the University of Washington, UNC, and KIT included the analysis of output from pulser, scintillator, and silicon-photomultiplier (SiPM) electronics in the configuration intended for use in the KATRIN experiment. The testing uncovered synchronization issues within the system's readout, dropped events, and trigger jitter. The problem was caused because the crate's internal clock and the veto signals coincidently had the same characteristic time of 50ns. This caused a timing disparity in the digitization of the signals that led to signal degradation and occasional loss of events. To improve the efficiency of the system as a whole, TUNL personnel are working to configure the input filtering of the Mark IV crate to resolve this.

To help operators monitor both the FPD and the veto systems simultaneously, an integrated status dialog in ORCA was developed. As seen in Fig. 8.18, a representation of the FPD and the veto channels can show each channel's thresholds, gains, event rate, or total event counts. Double-clicking on a pixel element opens the control dialog for that channel's FLT card. A panel for run control is included for convenience. This dialog, along with ORCA's other on-line data monitoring capabilities, is being extensively used during the commissioning phase of the project to verify that the entire system is working as designed.

The monitor spectrometer is a five-pixel detector that will be used to monitor the main spectrometer's voltage potential. The scripting

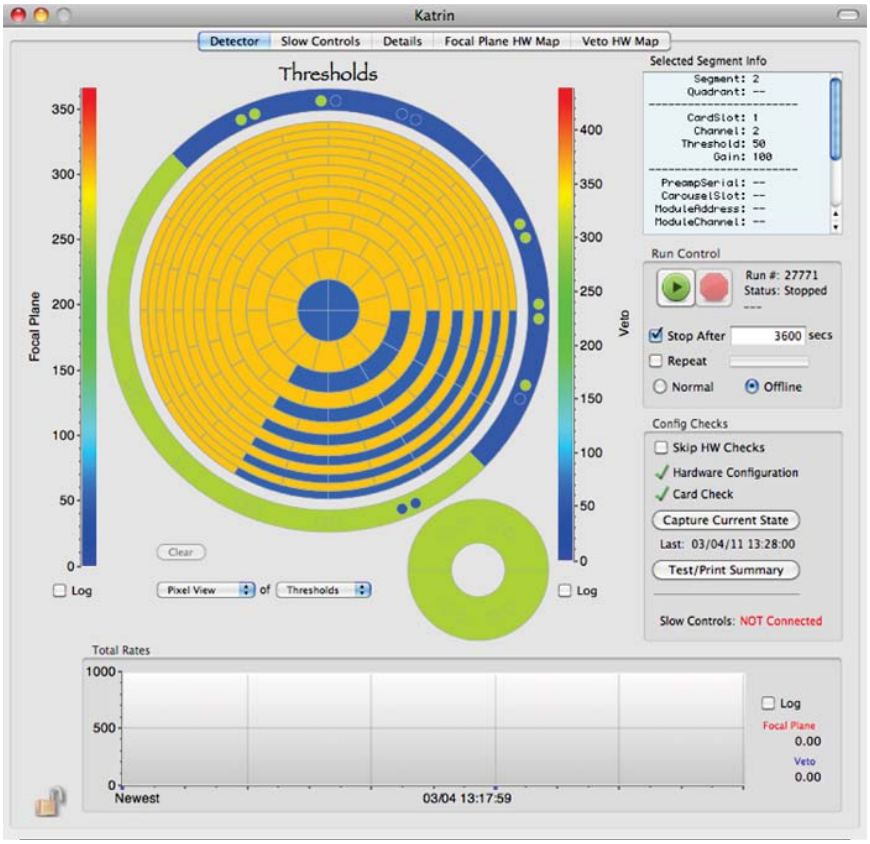

Figure 8.18: (Color online) A screen shot of the main KATRIN-status dialog in ORCA.

capabilities of ORCA have been used extensively in the development of run-control procedures for the monitor spectrometer. To facilitate remote monitoring of the monitor spectrometer, IORCA [How10] was expanded to include support for it. ORCA has been running the monitor spectrometer virtually continuously for more than a year. A number of enhancements were made to ORCA's run-control system to help the monitor spectrometer run autonomously. One such improvement was the addition of run lists, so that operators can specify a long list of runs and run lengths with free parameters that could be used by scripts to make changes to hardware parameters at the start of every run.

The KATRIN slow-control system ZEUS, developed by collaborators at KIT, is implemented in LabVIEW and integrates various PC-based controllers. The thousands of parameters monitored by ZEUS are stored in a database and made available on a website created by the Advanced Data-Extraction Infrastructure system (ADEI), which was developed by collaborators at KIT. ORCA has been successfully integrated with ADEI and can extract monitor parameters from ADEI, posting custom alarms as needed. Since ADEI also has the ability to send commands to ZEUS for execution, ORCA can use that command channel to control a selected set of hardware that is normally controlled by slow controls. This allows ORCA to use scripts to ramp hardware parameter settings. This is needed to automate data collection, for example for calculating transmission functions.

ORCA has been successfully integrated with the Katrin Libraries (KaLi) for data conversion and in-line processing. Automated checks have been developed for checking that data integrity is maintained throughout the analysis chain.

[How10] Howe, M. A. *et al.*, TUNL Progress Report, **XLIX**, 214 (2010).

8.4.3 Validation Suite for the MaGe Monte Carlo Package

F.M. Fränkle, R. Henning, C. Johnson, *TUNL*

The MaGe Monte-Carlo package is a GEANT4- and ROOT-based simulation package used by the Majorana and Gerda collaborations. In order to test the underlying physics relevant for MaGe simulations, a validation suite is being developed.

The Gerda and Majorana projects are both searching for the neutrinoless double-β decay of ^{76}Ge and are developing a joint Monte-Carlo simulation framework called MaGe [Bau06], based on the GEANT4 simulation and ROOT analysis packages.

New releases of simulation software such as GEANT4 may contain bugs that change the physics results. However, the Majorana collaboration needs reliable simulations in order to generate, for example, specifications on the radiopurity of materials. Therefore a validation of the physics of the underlying simulation code (especially GEANT4) is needed. Because a manual check is time consuming, a validation suite that is able to perform the diagnostic tests of the important physics in an automated fashion is being developed.

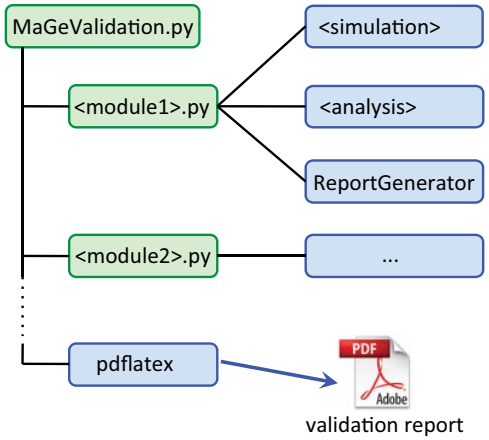

Figure 8.19: (Color online) Structure of the validation framework.

The execution of the validation suite is controlled by a single PYTHON script that calls the individual diagnostic modules, as shown in Fig. 8.19. A diagnostic module typically consists of a simulation program to generate simulated data and an analysis program to compare the simulated data with either literature values or the results obtained from theoretical models. After the diagnostic tests are executed, a pdf file containing all the results of the validation tests is automatically created. The validation report contains plots and tables of the validation results and a short description of the validation test.

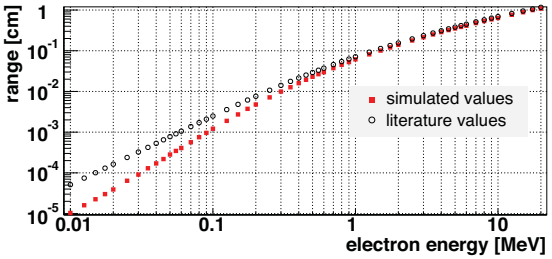

Figure 8.20: (Color online) Comparison between simulated and calculated electron ranges in copper.

The validation framework contains methods to compare values and to color code the difference, in order to make the report easier to read. It is also possible to compare the results of different versions of the simulation code with each other, in order to check for relative changes.

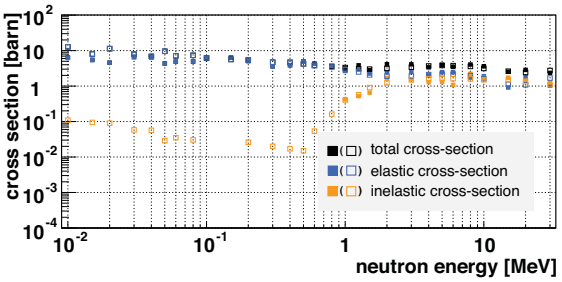

Figure 8.21: (Color online) Comparison between simulated neutron cross sections in copper (solid points) and the corresponding literature values (open points).

In addition to the existing diagnostic mod-

ules for radioactive decays and the interaction of γ rays with matter, new diagnostic modules have been implemented.

The first new module is designed to check the interactions of electrons with matter. The range of electrons of different starting energies is simulated, and the values are compared with calculated values using the continuous slowing down approximation (CSDA). Figure 8.20 shows an example of simulated and CSDA ranges in copper. The agreement is remarkably good, although the simulated values seem to underestimate the electron ranges at lower energies.

The diagnostic check of the interactions of α particles with matter is done in a way similar to that used for electron interactions. The range of α-particles in matter is simulated and then compared with calculated CSDA values.

A major new diagnostic module is designed to check neutron interactions. Because neutron cross sections can vary by several orders of magnitude within a small energy interval, a continuous energy spectrum is used for the simulation. The neutron cross sections (total, elastic and inelastic) are then averaged over a given energy interval and compared with averaged literature data for the same interval. Figure 8.21 shows a comparison between simulated cross sections for neutron interactions in copper and values from the literature.

The MaGe validation suite now covers diagnostic modules for most of the important physics needed for MaGe simulations. The execution of the validation suite is part of the tagging procedure for new releases of MaGe.

[Bau06] M. Bauer *et al.*, J. Phys.: Conf. Ser., **39**, 362 (2006).

Appendices

- **Graduate Degrees Awarded**
- **Publications**
- **Invited Talks, Seminars, and Colloquia**
- **Professional Service Activities**

A.1 Graduate Degrees Awarded

Ph.D. Degrees

1. Samantha L. Hammond, *Dipole Response of ^{238}U to Polarized Photons Below the Neutron-Separation Energy*,
University of North Carolina at Chapel Hill, November 2011
Supervisor: H. J. Karwowski

2. Leah J. Broussard, *High Precision Measurement of the ^{19}Ne Lifetime*,
Duke University, May 2012
Supervisors: A. R. Young and C. R. Howell

3. James H. Esterline, *Measurements of the Analyzing Power of n-^{3}He Elastic Scattering Between 1.60 and 5.54 MeV*,
Duke University, May 2012
Supervisor: W. Tornow

4. Wangzhi Zheng, *Experiments of Search for Neutron Electric Dipole Moment and Spin-Dependent Short-Range Force*,
Duke University, May 2012
Supervisor: H. Gao

5. Wenzhong Wu, *Feedback Systems for Control of Coupled-Bunch Instabilities in the Duke Storage Ring*,
Duke University, May 2012
Supervisor: Y. K. Wu

6. Adam T. Holley, *Ultracold Neutron Polarimetry in a Measurement of the Beta-Asymmetry*,
North Carolina State University, May 2012
Supervisor: A. R. Young

7. Christopher A. Swank, *An Investigation in the Dynamics of Polarized Helium-3 in Superfuid Helium-4 for the Spallation Neutron Source (SNS) neutron-Electric-Dipole-Moment (nEDM) Experiment*,
North Carolina State University, July 2012
Supervisor: P. R. Huffman and R. Golub

M.S. and M.A. Degrees

1. Brent Fallin, *Neutron Dosimetry of Mice Using Monoenergetic Neutron Beams*,
Duke University, December 2011
Supervisor: C. R. Howell

2. Jacqueline Strain, *Creating an Efficient Muon Veto for an Underground Low-Background Modified Broad-Energy Germanium Detector*,
University of North Carolina at Chapel Hill, December 2011
Supervisor: J. F. Wilkerson

3. Sean W. Finch, *Search for $2\nu\beta\beta$ and ECEC Decays to Excited Final States*,
Duke University, May 2012
Supervisor: W. Tornow

A.2 Publications

The publications co-authored by members of TUNL research groups between September 2011 and August 2012 are tabulated in Table A.1. The papers in refereed journals by TUNL research groups are listed below in chronological order.

Type	No.
Refereed Journal Articles	48
Conference Proceeding Papers	28

Table A.1: Summary of TUNL publications from September 2011 through August 2012. Among the 48 refereed journal papers, 6 were letters.

Journal Articles Published

1. *Astroparticle Physics With a Customized Low-Background Broad Energy Germanium Detector*, C. E. Aalseth *et al.* (The Majorana Collaboration, including R. Henning, W. Tornow, J. F. Wilkerson, and A. R. Young), Nucl. Instrum. Methods A, **652**, 692 (2011).

2. *Asymmetry Dependence of Nucleon Correlations in Spherical Nuclei Extracted from a Dispersive-Optical-Model Analysis*, J. M. Mueller *et al.* (including A. S. Crowell, J. H. Esterline, B. Fallin, C. R. Howell, and C. Westerfeldt), Phys. Rev. C, **83**, 064605 (2011).

3. *Calibration of Muon Reconstruction Algorithms Using an External Muon Tracking System at the Sudbury Neutrino Observatory*, T. J. Sonley *et al.* (including J. F. Wilkerson), Nucl. Instrum. Methods, **648**, 92 (2011).

4. *Discovery of Low-lying E-1 and M-1 Strengths in ^{232}Th*, A. S. Adekola, C. T. Angell, S. L. Hammond, A. Hill, C. R. Howell, H. J. Karwowski, J. H. Kelley, and E. Kwan, Phys. Rev. C, **83**, 034615 (2011).

5. *Discrete Deexcitations in ^{235}U Below 3 MeV from Nuclear Resonance Fluorescence*, E. Kwan, G. Rusev, A. S. Adekola, F. Donau, S. L. Hammond, C. R. Howell, H. J. Karwowski, J. H. Kelley, R. S. Pedroni, R. Raut, A. P. Tonchev, and W. Tornow, Phys. Rev. C, **83**, 041601 (2011).

6. *Extracting the Photoproduction Cross Section off the Neutron, via the $\gamma n \to \pi^- p$ Reaction, from Deuteron Data with Final-State Interaction Effects*, V. E. Tarasov, W. J. Briscoe, H. Gao, A. E. Kudryavtsev, and I. I. Strakovsky, Phys. Rev. C, **84**, 035203 (2011).

7. *Full Simulation of the Sudbury Neutrino Observatory Proportional Counters*, B. Beltran *et al.* (including J. F. Wilkerson), New J. Phys., **13**, 073006 (2011).

8. *General Solution to Gradient-Induced Transverse and Longitudinal Relaxation of Spins Undergoing Restricted Diffusion*, W. Zheng, H. Gao, J.-G. Liu, Y. Zhang, and C. Swank, Phys. Rev. A, **84**, 053411 (2011).

9. *Limits on Possible New Nucleon Monopole-Dipole Interactions from the Spin Relaxation Rate of Polarized ^3He Gas*, A. K. Petukhov, G. Pignol, and R. Golub, Phys. Rev. D, **84**, 058501 (2011).

10. *Measurement of the Absolute and Differential Cross Sections for ^7Li (γ,n_0) ^6Li*, W. A. Wurtz, R. E. Pywell, B. E. Norum, S. Kucuker, B. D. Sawatzky, H. R. Weller, M. W. Ahmed, and S. Stave, Phys. Rev. C, **84**, 044601 (2011).

11. *Measurement of the ^8B Solar Neutrino Flux with the KamLAND Liquid Scintillator Detector*, S. Abe *et al.* (The KamLAND Collaboration, including H. J. Karwowski, D. M. Markoff, and W. Tornow), Phys. Rev. C, **84**, 035804 (2011).

12. *Measurements of the $^{48}Ca(\gamma, n)$ Reaction*, J. R. Tompkins, C. W. Arnold, H. J. Karwowski, G. C. Rich, L. G. Sobotka, and C. R. Howell, Phys. Rev. C, **84**, 044331 (2011).

13. *New Limit on Time-Reversal Violation in Beta Decay*, H. P. Mumm *et al.* (including J. F. Wilkerson), Phys. Rev. Lett., **107**, 102301 (2011).

14. *New Method for Precise Determination of the Isovector Giant Quadrupole Resonances in Nuclei*, S. S. Henshaw, M. W. Ahmed, G. Feldman, A. M. Nathan, and H. R. Weller, Phys. Rev. Lett., **107**, 222501 (2011).

15. *Precise Measurement of Deuteron Tensor Analyzing Powers with BLAST*, C. Zhang *et al.* (The BLAST Collaboration, including H. Gao and W. Xu), Phys. Rev. Lett., **107**, 252501 (2011).

16. *Radon Induced Background Processes in the KATRIN Pre-Spectrometer*, F. M. Frankle *et al.*, Astropart. Phys., **35**, 128 (2011).

17. *Search for an Annual Modulation in a p-Type Point Contact Germanium Dark Matter Detector*, C. E. Aalseth *et al.* (including J. F. Wilkerson), Phys. Rev. Lett., **107**, 141301 (2011).

18. *Spin-Dependent Electron Scattering from Polarized Protons and Deuterons with the BLAST Experiment at MIT-Bates*, D. K. Hasell, R. G. Milner, R. P. Redwine, R. Alarcon, H. Gao, M. Kohl, and J. R. Calarco, Ann. Rev. Nucl. Part. Sci., **61**, 409 (2011).

19. *The Effects of Thermonuclear Reaction-Rate Variations on ^{26}Al Production in Massive Stars: A Sensitivity Study*, C. Iliadis, A. E. Champagne, A. Chieffi, and M. Limongi, Astrophys. J. Suppl., **193**, 16 (2011).

20. *The Majorana Experiment*, Majorana Collaboration, J. Esterline *et al.* (The Majorana Collaboration, including J. Kephart, M. Kidd, R. Henning, W. Tornow, and J. F. Wilkerson), Nucl. Phys. B Proc. Suppl., **221**, 364 (2011).

21. *A High-Field Adiabatic Fast Passage Ultracold Neutron Spin Flipper for the UCNA Experiment*, A. T. Holley *et al.* (including L. J. Broussard, R. W. Pattie, and A. R. Young), Rev. Sci. Instrum., **83**, 073505, (2012).

22. *Alpha Backgrounds for HPGe Detectors in Neutrinoless Double-Beta Decay Experiments*, R. A. Johnson, T. H. Burritt, S. R. Elliott, V. M. Gehman, V. E. Guiseppe, and J. F. Wilkerson, Nucl. Instrum. Methods A, **693**, 51 (2012).

23. *A Course to Prepare Physics Students for the Research Laboratory*, D. G. Haase, H. Hallen, and D. P. Kendellen, Spring 2012 Newsletter of the Forum on Education of the American Physical Society, p. 13 (2012).

24. *Amplitude Analysis of $\gamma n \to \pi^- p$ Data Above 1 GeV*, W. Chen *et al.* (including H. Gao), Phys. Rev. C, **86**, 015206 (2012).

25. *A Remotely-Controlled, Semi-Automatic Target System for Rutherford Backscattering Spectrometry and Elastic Recoil Detection Analyses of Polymeric Membrane Samples*, P. J. Attayek, E. S. Meyer, L. Lin, G. C. Rich, T. B. Clegg, and O. Coronell, Nucl. Instrum. Methods A, **676**, 21 (2012).

26. *Beam-Target Double Spin Asymmetry A_{LT} in Charged Pion Production from Deep Inelastic Scattering on a Transversely Polarized ^3He Target at $1.4 < Q^2 < 2.7$ GeV^2*, J. Huang *et al.* (The Jefferson Lab Hall A Collaboration, including X. Qian, W. Chen, H. Gao, Y. Qiang, X. Zhu, and X. Zong), Phys. Rev. Lett., **108**, 052001 (2012).

27. *Compton Scattering from ^6Li at 60 MeV*, L. S. Myers *et al.* (including M. W. Ahmed, S. S. Henshaw, J. M. Mueller, and H. R. Weller), Phys. Rev. C, **86**, 044614 (2012).

28. *Cross Section Measurement of $^9Be(\gamma, n)^8Be$ and Implications for $\alpha + \alpha + n \to {}^9Be$ in the r-Process*, C. W. Arnold, T. B. Clegg, C. Iliadis, H. J. Karwowski, G. C. Rich, J. R. Tompkins, and C. R. Howell, Phys. Rev. C, **85**, 044605 (2012).

29. *Cross-Section Measurements of ^{2}H(n,np)n in Symmetric Star Configurations*, A. H. Couture, T. B. Clegg, S. Tajima, C. R. Howell, B. Fallin, J. H. Esterline, A. S. Crowell, B. J. Crowe, D. M. Markoff, L. C. Cumberbatch, R. S. Pedroni, and H. Witala, Phys. Rev. C, **85**, 054004 (2012).

30. *Dipole Response of ^{238}U to Polarized Photons Below the Neutron Separation Energy*, S. L. Hammond, A. S. Adekola, C. T. Angell, H. J. Karwowski, E. Kwan, G. Rusev, A. P. Tonchev, W. Tornow, C. R. Howell, J. H. Kelley, Phys. Rev. C, **85**, 044302 (2012).

31. *Electromagnetic Dipole Strength of ^{136}Ba Below the Neutron Separation Energy*, R. Massarczyk *et al.* (including G. Rusev, J. H. Kelley, E. Kwan, R. Raut, A. P. Tonchev, and W. Tornow), Phys. Rev. C, **86**, 014319 (2012).

32. *Energy Levels of Light Nuclei A=11*, J. H. Kelley, E. Kwan, J. E. Purcell, C. G. Sheu, and H. R. Weller, Nucl. Phys. A, **880**, 88 (2012).

33. *La138/139 Isotopic Data and Neutron Fluences for Oklo RZ10 Reactor*, C. R. Gould and E. I. Sharapov, Phys. Rev. C, **86**, 027601 (2012).

34. *Limits on Majoron-Emitting Double-Beta Decays of ^{136}Xe in the KamLAND-Zen Experiment*, A. Gando *et al.* (The KamLAND-Zen Collaboration, including W. Tornow, H. J. Karwowski, and D. M. Markoff), Phys. Rev. C, **86**, 021601 (2012).

35. *Lutetium Thermometry for Oklo Natural Reactors: A New Examination of Old Data*, C. R. Gould and E. I. Sharapov, Phys. Rev. C, **85**, 024610 (2012).

36. *Measurement of Prompt Neutron Polarization Asymmetries in Photofission of ^{235}U, ^{238}U, ^{239}Pu, and ^{232}Th*, J. M. Mueller *et al.* (including M. W. Ahmed, S. S. Henshaw, H. J. Karwowski, D. Markoff, L. S. Myers, and B. A. Perdue), Phys. Rev. C, **85**, 014605 (2012).

37. *Neutron Resonance Parameters in ^{155}Gd measured with the DANCE γ-ray Calorimeter*, B. Baramsai *et al.* (including G. E. Mitchell, A. Chyzh, and C. L. Walker), Phys. Rev. C, **85**, 024622 (2012).

38. *Partial Gamma-Ray Production Cross Sections for (n,xnγ) Reactions in Natural Argon from 1–30 MeV*, S. MacMullin, *et al.* (including R. Henning), Phys. Rev. C, **85**, 064614 (2012).

39. *Photodisintegration Cross Section of the Reaction $^{4}He(\gamma, n)^{3}He$ at the Giant Dipole Resonance Peak*, W. Tornow, J. H. Kelley, R. Raut, G. Rusev, A. P. Tonchev, M. W. Ahmed, A. S. Crowell, and S. C. Stave, Phys. Rev. C, **85**, 061001 (2012).

40. *Photodisintegration Cross Section of the Reaction $^{4}He(\gamma,p)^{3}H$ between 22 and 30 MeV*, R. Raut, W. Tornow, M. W. Ahmed, A. S. Crowell, J. H. Kelley, G. Rusev, S. C. Stave, and A. P. Tonchev, Phys. Rev. Lett., **108**, 042502 (2012).

41. *PhytoBeta Imager: A Positron Imager for Plant Biology*, A. G. Weisenberger *et al.* (including A. S. Crowell and C. R. Howell), Phys. Med. Biol., **57**, 4195 (2012).

42. *Pressure Dependence of Wall Relaxation in Polarized ^{3}He Gaseous Cells*, B. Saam, A. K. Petukhov, J. Chastagnier, T. R. Gentile, R. Golub, and C. M. Swank, Phys. Rev. A, **85**, 047401 (2012).

43. *Reaction Rates for the s-Process Neutron Source $^{22}Ne+\alpha$*, R. Longland, C. Iliadis, and A. I. Karakas, Phys. Rev. C, **85**, 065809 (2012).

44. *Recommended Cross Section of the $^{16}O(p,\gamma)^{17}F$ Reaction Below 2.5 MeV: A Potential Tool for Quantitative Analysis and Depth Profiling of Oxygen*, P. Mohr and C. Iliadis, Nucl. Instrum. Methods A, **688**, 62 (2012).

45. *Search for Spin-Dependent Short-Range Force Between Nucleons Using Optically Polarized ^{3}He Gas*, W. Zheng, H. Gao, B. Lalremruata, Y. Zhang, G. Laskaris, W. M. Snow, and C. B. Fu, Phys. Rev. D, **85**, 031505 (2012).

46. *Semi-Inclusive Charged-Pion Electroproduction off Protons and Deuterons: Cross Sections, Ratios and Access to the Quark-Parton Model at Low Energies*, R. Asaturyan *et al.* (including D. Dutta), Phys. Rev. C, **85**, 015202 (2012).

47. *The Production of K+K- pairs in Proton-Proton Collisions at 2.83 GeV*, Q. J. Ye *et al.* (including H. Gao), Phys. Rev. C, **85**, 035211 (2012).

48. *Virtual Compton Scattering and the Generalized Polarizabilities of the Proton at Q^2=0.92 and 1.76 GeV^2*, H. Fonvieille *et al.* (The Jefferson Lab Hall A Collaboration, including H. Gao and C. Howell), Phys. Rev. C, **86**, 015210 (2012).

Journal Articles Accepted

1. *Design and Optimization of Longitudinal Feedback Kicker Cavity for HLS-II Storage Ring*, X. Wei, W. Z. Wu, H. Due-Hui, and Y. K. Wu, accepted for publication, Chinese Phys. C, (May, 2012).

2. *Measurement of Airborne Fission Products in Chapel Hill, NC, USA From the Fukushima Daiichi Reactor Accident*, S. MacMullin, G. K. Giovanetti, M. P. Green, R. Henning, R. Holmes, K. Vorren, and J. F. Wilkerson, J. Environ. Radioactivity, now published in **112**, 165, (2012).

3. *Measurement of the Neutron β-Asymmetry Parameter A_o with Ultracold Neutrons*, B. Plaster *et al.* (including H. O. Back, L. J. Broussard, J. Hoagland, A. T. Holley, R. W. Pattie, Jr., and A. R. Young), Phys. Rev. C **86**, 055501 (2012).

4. *Measurement of n-n Scattering – the Gamma Ray-Induced Outgassing Complication*, S. L. Stephenson, B. E. Crawford, W. I. Furman, E. V. Lychagin, A. Yu Muzuchka, G. V. Nekhaev, E. I. Sharapov, V. N. Shetsov, A. V. Strelkov, B. G. Levakov, A. C. Lyzhin, Y. I. Chernukhin, C. R. Howell, G. E. Mitchell, and W. Tornow, accepted for publication, Nucl. Phys. A (2012).

5. *Performance of the Los Alamos National Laboratory Spallation-Driven Solid-Deuterium Ultra-Cold Neutron Source*, H. O. Back, *et al.* (including L. J. Broussard, B. Filippone, A. Holley, A. R. Young, and A. Sallaska), accepted for publication, Rev. Sci. Instrum. (2012).

6. *Proposal for the Simultaneous Measurement of the NeutronNeutron and NeutronProton Quasi-Free Scattering Cross Section via the NeutronDeuteron Breakup Reaction at E_n = 19 MeV*, W. Tornow, C. R. Howell, and A. S. Crowell, to be published in Few-Body Systems (2012).

7. *Search for a T-Odd, P-Even Triple Correlation in Neutron Decay*, T. E. Chupp, R. L. Cooper, K. P. Coulter, S. J. Freedman, B. K. Fujikawa, A. Garcia, G. L. Jones, H. P. Mumm, J. S. Nico, A. K. Thompson, C. A. Trull, F. E. Wietfeldt, and J. F. Wilkerson, Phys. Rev. C, now published in **86**, 035505 (2012).

Journal Articles Submitted

1. *Characteristics of Signals Originating Near the Lithium-Diffused N+ Contact of High Purity Germanium P-Type Point Contact Detectors*, E. Aguayo *et. al.* (including A. R. Young, R. Henning, J. F. Wilkerson, J. Esterline, and W. Tornow), submitted to Nucl. Instrum. Methods A.

2. *Compton Scattering from ^{6}Li at 60 MeV*, L. S. Myers, *et al.*, submitted to Phys. Rev. C.

3. *Combined Analysis of all Three Phases of Solar Neutrino Data from the Sudbury Neutrino Observatory*, B. Aharmim *et. al* (including J. F. Wilkerson), submitted to Phys. Rec. C.

4. *Gamma Ray Fluxes in Oklo Natural Reactors*, C. R. Gould, A. A. Sonzogni, and E. I. Sharapov, submitted to Phys. Rev. C (now published in **86** 054602).

5. *Nuclear Thermometers for Classical Novae*, L. Downen, C. Iliadis, J. Jose, and S. Starrfield, submitted to Astrophys. J.

6. *Nucleosynthesis in Type I X-Ray Bursts*, A. Parikh, J. Jose, G. Sala, and C. Iliadis, submitted to Prog. Part. Nucl. Phys.

7. *Oklo Phenomenon and Nuclear Data*, E. I. Sharapov, C. R. Gould, and A. A. Sonzogni, submitted to Phys. Rev. C (now accepted).

8. *Performance of the Los Alamos National Laboratory Spallation-Driven Solid-Deuterium Ultracold Neutron Source*, A. Saunders *et al.* (including L. J. Broussard and A. R. Young), submitted to Rev. Sci. Instrum.

9. *Photon Strength Functions of ^{155}Gd from Radiative Capture of Resonance Neutrons*, B. Baramsai, J. Kroll, G. E. Mitchell, U. Agvaanluvsan, F. Becvar, T. A. Bredeweg, A. Chyzh, A. Couture, D. Dashdorj, R. C. Haight, M. Jandel, A. L. Keksis, M. Krticka, J. M. O'Donnell, R. S. Rundberg, J. L. Ullmann, D. J. Vieira, and C. L. Walker, submitted to Phys. Rev. C.

Special Reports and Books

1. *Journal Musings*, C. Gould, Magazine of the Society of Physics Students, SPS Observer, **XLV**, Issue 3, 3-5, (2011).

2. *Light Sterile Neutrinos: A White Paper*, K.N. Abazajian *et. al.* (including J. F. Wilkerson), http://arxiv.org/abs/1204.5379 (April 2012).

3. *Missing Levels with Two Superimposed Sequences*, J. F. Shriner, Jr. and G. E. Mitchell, International Atomic Energy Agency, INDC(NDS)0598 (2011).

4. *Nuclear Astrophysics: The Unfinished Quest for the Origin of the Elements*, J. Jose and C. Iliadis, Rept. Prog. Phys., **74**, 096901 (2011).

Conference Reports and Articles in Conference Proceedings

1. *A New Limit on Time-Reversal Violation in Beta Decay: Results of the Emit-II Experiment*, T. E. Chupp *et. al.* (including J. F. Wilkerson), Proceedings of the PANIC11 Conference, AIP Conf. Proc., **1441**, 585–589, (2012), PANIC11 conference.

2. *A New Limit on Time-Reversal-Invariance Violation in Beta Decay: Results of the EmiT-II Experiment*, H. P. Mumm *et. al.* (including J. F. Wilkerson), PoS, vol. EPS-HEP2011, 134, (2011), European Physical Society.

3. *Cross Section Measurements of Neutron Induced Reactions on GaAs Using Monoenergetic Beams from 7.5-MeV to 15-MeV*, R. Raut, A. S. Crowell, B. Fallin, C. R. Howell, C. Huibregtse, J. H. Kelley, T. Kawano, E. Kwan, G. Rusev, A. P. Tonchev, W. Tornow, D. J. Viera, and J. B. Wilhelmy, J. Phys. Conf. Ser., **312**, 062008 (2011).

4. *Development of PhytoPET: A Plant Imaging PET System*, A. G. Weisenberger, H. Dong, B. Kross, S. J. Lee, J. McKisson, J. E. McKisson, W. Xi, C. Zorn, C. R. Howell, A. S. Crowell, L. Cumberbatch, C. D. Reid, M. F. Smith, and A. Stolin, Nucl. Sci. Symp., Med. Imaging Conf. (NSS/MIC), 275 (2011 IEEE).

5. *Future (Transverse) Spin Physics at Jefferson Lab*, H. Gao, J. P. Chen, M. Huang, and X. Qian, J. Phys. Conf. Ser., **295**, 012019 (2011).

6. *Hadron Physics at Low Energies*, H. Gao, Eur. Phys. J. ST **198**, 3 (2011).

7. *Hydrodynamic Studies of the Evolution of Recurrent Novae to Supernova Ia Explosions*, Proceedings of the IAU Symposium 281 on Binary Paths to Supernova Ia Explosions, (Cambridge University Press, 2011) in print.

8. *Neutron Capture Experiments with 4π DANCE Calorimeter*, B. Baramsai *et al.* (including G. E. Mitchell), Workshop on Compound Nuclear Reactions and Related Topics, EPJ Web of Conferences **21**, 03002 (2012).

9. *Scissors Mode in Gd Nuclei*, J. Kroll *et al.* (including G. E. Mitchell), Workshop on Compound Nuclear Reactions and Related Topics, EPJ Web of Conferences **21**, 04005 (2012).

10. *Search for the Neutron Electric Dipole Moment: Contributions from the Triangle Universities Nuclear Laboratory*, P. R. Huffman, R. Golub, C. R Gould, D. G. Haase, D. P. Kendellen, E. Korobkina, C. M. Swank, A. R. Young, M. W. Ahmed, and M. Busch, Proceedings of the DPF-2011 Conference (2011).

11. *Stellar Helium Burning Studied with an Optical Readout TPC (O-TPC) at HIγS*, Moshe Gai for the UConn-Yale-Duke-Weizmann-PTB-UCL Collaboration, J. Phys. Conf. Ser., **316**, 012033 (2011).

12. *The Majorana Demonstrator*, E. Aguayo *et al.* (including J. F. Wilkerson, presented by F.T. Avignone III), Proceedings of the DPF-2011 Conference (2011).

13. *The MAJORANA DEMONSTRATOR: A Search for Neutrinoless Double-Beta Decay of Germanium-76*, A. Schubert *et al.* (including J. F. Wilkerson, presented by A. G. Schubert), Proceedings of the PANIC11 Conference, AIP Conf. Proc., **1441**, 480 (2012).

14. *The Majorana Experiment*, E. Aguayo *et. al.* (presented by R. Henning), Proceedings of the Matrix Elements for the Double-Beta Decay Experiments (MEDEX11) Conference, AIP Conf. Proc., **1417**, 95 (2011).

15. *Cold Cathode Thyratron Based High-Voltage Kicker Generators at the Duke Accelerators: Six Year Experience*, V. Popov, S. F. Mikhailov, P. W. Wallace, and Y. K. Wu, Proceedings of the 2012 International Particle Accelerator Conference (IPAC'12), 3698, (2012).

16. *Cross-Section Measurements of the $^{86}Kr(\gamma,n)$ Reaction to Probe the s-Process Branching at ^{85}Kr*, R. Raut, A. Banu, C. Iliadis, J. H. Kelley, G. Rusev, R. Schwenger, A. P. Tonchev, and W. Tornow, Proceedings of the Conference on Nuclear Physics in Astrophysics V, J. Phys. Conf. Ser. **337**, 012048, (2012).

17. *Current Status of the $^{22}Ne+\alpha$ s-process Neutron Source*, R. Longland and C. Iliadis, Proceedings of the Conference on Nuclear Physics in Astrophysics V, J. Phys. Conf. Ser. **337**, 012047, (2012).

18. *Dark Matter Sensitivities of the MAJORANA Demonstrator*, G. K. Giovanetti *et al.*, J. Phys. Conf. Ser., **375**, 012014 (2012).

19. *Electron Beam Diagnostics Based on Transverse Feedback System at Duke Storage Ring*, W. Xu, D. He, W. Z. Wu, J. Li, and Y. K. Wu, Proceedings of the 2012 International Particle Accelerator Conference (IPAC'12), 849, (2012).

20. *Fundamental Physics at the Intensity Frontier*, J. Hewett *et al.* (including A. R. Young and J. F. Wilkerson), Report of the 2011 Workshop on Fundamental Physics at the Intensity Frontier, (2012).

21. *Hydrodynamic Studies of the Evolution of Recurrent, Symbiotic and Dwarf Novae: The White Dwarfs are Growing in Mass*, S. Starrfield, F. X. Timmes, C. Iliadis, W. R. Hix, W. D. Arnett, C. Meakin, and W. M. Sparks, Proceedings of the 1^{st} Asiago Meeting on Symbiotic Stars, Baltic Astronomy **21**, 75 (2012).

22. *Neutron Resonance Spin Determination Using Multi-Segmented Detector DANCE*, B. Baramsai, G. E. Mitchell, U. Agvaanluvsan, F. Becvar, T. A. Bredeweg, A. Couture, A. Chyzh, D. Dashdorj, R. C. Haight, M. Jandel, A. L. Keksis, M. Krticka, J. M. O'Donnell, R. S. Rundberg, J. L. Ullmann, D. J. Vieira, C. Walker, and J. M. Wouters, Application of Accelerators in Research and Industry, AIP Conf. Proc. **1336**, 581 (2011).

23. *New Storage Ring Lattice for the Duke FEL Wiggler Switchyard System*, H. Hao, J. Li, Y. K. Wu, Proceedings of the 2012 International Particle Accelerator Conference (IPAC'12), 1272 (2012).

24. *Soft Orbit Bump for Duke Storage Ring VUV FEL Operation*, S. F. Mikhailov, J. Y. Li, V. G. Popov, P. W. Wallace, and Y. K. Wu, Proceedings of the 2012 International Particle Accelerator Conference (IPAC'12), 1774 (2012).

25. *The Radial Structure of the Proton and Its Constituents*, H. Gao, AIP Conf. Proc. **1441**, 21-28 (2012).

26. *The Majorana Experiment: An Ultra-Low Background Search for Neutrinoless Double-Beta Decay*, D. G. Phillips, II *et. al.* (including J. F. Wilkerson), Proceedings of the Rutherford Centennial Conference on Nuclear Physics, J. Phys. Conf. Ser., **381**, 012044 (2012).

27. *The Majorana Demonstrator: A Search for Neutrinoless Double-Beta Decay of Germanium-76*, J. F. Wilkerson *et. al.*, Proceedings of the 12^{th} International Conference on Topics in Astroparticle and Underground Physics, TAUP2011, J. Phys. Conf. Ser.,**375**, 042010 (2012).

28. *UCNB Experiment: Neutrino Asymmetry From the Decay of Polarized Ultracold Neutrons*, L. J. Broussard et al. (including A. R. Young, R. W. Pattie, A. T. Holley), Conference on the Intersections of Particle and Nuclear Physics, Tampa, FL, June 2012.

Abstracts to Meetings and Conferences

1. *A Personal Perspective on Triangle Universities Nuclear Laboratory Development*, T. B. Clegg, http://meetings.aps.org/link/BAPS.2011.SES.GD.2

2. *A Study of the Ionization of Deuterium Gas by Pyroelectric Crystals*, B. Taylor, S. Shafroth, and W. Tornow, http://meetings.aps.org/link/BAPS.2011.SES.BC.1

3. *$^{nat}Dy(\gamma, n)$ Asymmetry Measurements with Linearly Polarized γ-Rays between 11 and 15 MeV*, R. K. Trasher, J. Hauver, W. R. Henderson, C. S. Whisnant, M. W. Ahmed, H. J. Karwowski, J. M. Mueller, L. S. Myers, J. Silano, J. R. Tompkins, H. R. Weller, and W. R. Zimmerman, http://meetings.aps.org/link/BAPS.2011.SES.LA.28

4. *Exploring the Cosmos from the Ground: Nuclear Astrophysics at UNC/TUNL*, A. L. Sallaska, http://meetings.aps.org/link/BAPS.2011.SES.CA.3

5. *Neutron Photoproduction from ^{139}La Using 12–15 MeV Linearly Polarized γ-Rays*, R. K. Trasher, J. Hauver, W. R. Henderson, C. S. Whisnant, M. W. Ahmed, H. J. Karwowski, J. M. Mueller, L. S. Myers, J. Silano, J. R. Tompkins, H. R. Weller, W. R. Zimmerman, B. J. Davis, D. M. Markoff, M. Spraker, R. M. Prior, and R. H. France, http://meetings.aps.org/link/BAPS.2011.SES.LA.26

6. *Neutron Photoproduction from ^{Nat}Hg Using 11–15 MeV Linearly Polarized γ-Rays*, R. K. Trasher, J. Hauver, W. R. Henderson, C. S. Whisnant, M. W. Ahmed, H. J. Karwowski, J. M. Mueller, L. S. Myers, J. Silano, J. R. Tompkins, H. R. Weller, and W. R. Zimmerman, http://meetings.aps.org/link/BAPS.2011.SES.LA.27

7. *A Measurement of Neutron Polarization Asymmetries in Photofission of Actinides Using Polarized Gamma Rays at HIγS*, J. M. Mueller, M. W. Ahmed, S. S. Henshaw, H. J. Karwowski, L. Myers, B. A. Perdue, S. Stave, J. R. Tompkins, H. R. Weller, B. Davis, and D. Markoff, http://meetings.aps.org/link/BAPS.2011.DNP.NF.7

8. *A Next-Generation Reaction-Rate Library for Nuclear Astrophysics*, A. L. Sallaska, C. Iliadis, A. E. Champagne, F. X. Timmes, and S. Starrfield, http://meetings.aps.org/link/BAPS.2011.DNP.NA.1

9. *A Study of the Ionization of Deuterium Gas by Pyroelectric Crystals*, B. Taylor, S. Shafroth, and W. Tornow, http://meetings.aps.org/link/BAPS.2011.DNP.EA.126

10. *An Improved Apparatus for $2\nu\beta\beta$ and ECEC Studies to Excited Final States*, S. Finch, R. Raut, and W. Tornow, http://meetings.aps.org/link/BAPS.2011.DNP.CC.7

11. *Compton Scattering on ^{6}Li at 60 MeV*, L. S. Myers, M. W. Ahmed, S. S. Henshaw, J. M. Mueller, H. R. Weller, G. Feldman, T. Balint, K. Sykora, and M. A. Kovash, http://meetings.aps.org/link/BAPS.2011.DNP.GE.2

12. *First Measurement of Statistical Gamma-Ray Transitions in ^{88}Sr at TUNL via Inelastic Neutron Scattering*, S. Carter, G. Rusev, C. Arnold, W. Tornow, M. Gooden, J. H. Kelley, S. L. Hammond, and L. Stevens, http://meetings.aps.org/link/BAPS.2011.DNP.EA.25

13. *High Precision Measurement of the ^{19}Ne Lifetime*, L. J. Broussard, http://meetings.aps.org/link/BAPS.2011.DNP.FE.5

14. *Results from UCNA 2010*, Robert Pattie, http://meetings.aps.org/link/DNP.2011.GC.6

15. *Full Distribution of Dipole States below 9 MeV in ^{76}Se*, N. Cooper *et al.* (including J. Kelley, R. Raut, G. Rusev, A. P. Tonchev, and W. Tornow), http://meetings.aps.org/link/BAPS.2011.DNP.JF.7

16. *Internal Conversion Electron Study of Excited States in ^{76}As*, F. M. Prados-Estévez, S. W. Yates, B. P. Crider, E. E. Peters, T. Kibèdi, G. D. Dracoulis, R. F. Leslie, A. E. Stuchbery, N. M. Cooper, V. Werner, T. Williams, and A. P. Tonchev, http://meetings.aps.org/link/BAPS.2011.DNP.MF.5

17. *Locating a Radioactive High Voltage Nut for the MAJORANA Project*, B. Rose, http://meetings.aps.org/link/BAPS.2011.DNP.EA.115

18. *Neutron Capture from ^{87}Sr*, G. Rusev, R. Raut, A. P. Tonchev, W. Tornow, B. Baramsai, J. H. Kelley, G. Mitchell, T. Bredeweg, A. Couture, M. Jandel, J. O'Donnell, R. Rundberg, J. L. Ullmann, A. Chyzh, and E. Kwan, http://meetings.aps.org/link/BAPS.2011.DNP.GG.2

19. *Precision Polarimetry with UCN in the UCNA Experiment*, A. T. Holley, http://meetings.aps.org/linkBAPS.2011.DNP.GC.8

20. *Update on The MAJORANA Neutrinoless Double-Beta Decay Experiment*, R. Henning for the Majorana Collaboration, SSP 2012, Groningen, The Netherlands (2012).

21. *Characterization of Large Area, Thick, and Segmented Silicon Detector for Electron and Proton Detection from Neutron Beta Decay Experiments in the Cold and Ultracold Energies*, A. S. Bacci *et al.* (including L. Broussard, R. Pattie, S. Hoedl, A. R. Young, and B. Zeck), http://meetings.aps.org/link/BAPS.2012.DNP.NC.3

22. *Cryogenic Design for the nEDM Experiment*, D. Kendellen, D. Haase, and P. Huffman, http://meetings.aps.org/link/BAPS.2012.APR.D11.5

23. *Lu Thermometry for Oklo Natural Reactors: A New Look at Old Data*, C. Gould and E. Sharapov, http://meetings.aps.org/link/BAPS.2012.APR.H11.7

24. *Oklo Phenomemon and Nuclear Data*, E. I. Sharapov, C. R. Gould, and A. A. Sonzogni, ISINN20, Alushta, Ukraine, May 2012.

25. *Overview of Measurements Related to Three-Nucleon Force*, W. Tornow, http://meetings.aps.org/link/BAPS.2012.APR.C4.3

26. *$^{18}O(p,\gamma)^{19}F$ Resonance Strength Measurement at Low Energies*, M. Buckner, C. Iliadis, J. Cesaratto, C. Howard, T. Clegg, A. Champagne, and S. Daigle, http://meetings.aps.org/link/BAPS.2012.APR.H11.2

27. *Recent Progress Towards a Measurement of the Neutron Lifetime Using Magnetically Trapped Ultracold Neutrons*, K. W. Schelhammer *et al.* (including C. R. Huffer, P. R. Huffman, and D. E. Marley), http://meetings.aps.org/link/BAPS.2012.APR.C10.6

28. *Ultracold Neutron Source Technology: Status in 2012*, A. R. Young, http://meetings.aps.org/link/BAPS.2012.DNP.1WC.2

29. *Thermonuclear Reaction Rates From Rare Oxygen Isotope Radiative Proton Capture*, M. Q. Buckner, C. Iliadis, J. M. Cesaratto, C. Howard, T. B. Clegg, A. E. Champagne, and S. Daigle, Poster presentation at DOE Stewardship Science Annual Conference, 2012.

30. *Thermonuclear Reaction Rate for $^{18}O(p,\gamma)^{19}F$*, M. Q. Buckner, C. Iliadis, J. M. Cesaratto, C. Howard, T. B. Clegg, A. E. Champagne, and S. Daigle, Poster presentation at 12^{th} International Symposium on Nuclei in the Cosmos, 2012.

A.3 Invited Talks, Seminars, and Colloquia

Invited Talks, Seminars, and Colloquia

1. *Homeland Security and Photofission*, M. W. Ahmed, Ohio University, Athens, OH, November 2011.

2. *Studies of Nuclei at TUNL/HIGS: From Hadron Structure to Exploding Stars*, M. W. Ahmed, Thomas Jefferson National Accelerator Facility, Chiral Dynamics, August 2012.

3. *A Next Generation Neutron-Antineutron Oscillations Experiment Using Very Cold and Ultracold Neutrons*, R. W. Pattie, Conference on the Intersections of Particle and Nuclear Physics, St. Petersburg, FL, June 2012.

4. *UCNB experiment: Neutrino Asymmetry from the Decay of Polarized Ultracold Neutrons*, L. J. Broussard, Conference on the Intersections of Particle and Nuclear Physics, St. Petersburg, FL, June 2012.

5. *High Precision Measurement of the ^{19}Ne Lifetime*, L. J. Broussard, Los Alamos National Laboratory, Group P-25 seminar, Los Alamos, NM, January 2011.

6. *A Personal Perspective on Triangle Universities Nuclear Laboratory Development*, T. B. Clegg, invited talk, Southeastern Section of the American Physical Society Meeting on the occasion of the 100^{th} Anniversary of the Discovery of the Atomic Nucleus, http://meetings.aps.org/link/BAPS.2011.SES.GD.2.

7. *TMD Experimental Overview*, Haiyan Gao, invited talk, International Workshop on Physics Opportunities at an Electron Ion Collider, Bloomington, IN, August 2012.

8. *New Results from HIGS*, Haiyan Gao, invited talk, Gordon Research Conference on Photonuclear Reactions, August 2012, Holderness, NH.

9. *TMD Physics at 12-GeV Jefferson Lab*, Haiyan Gao, invited talk, Fourth Workshop on Hadron Physics in China and Opportunities in US, KITPC, Beijing, China, July 2012.

10. *QCD Physics at EIC*, Haiyan Gao, invited talk, From Nucleon Structure to Nuclear Structure and Compact Astrophysical Objects, KITPC, Beijing, China, July 2012.

11. *Probing the Three-Dimensional Structure of the Nucleon at 12-GeV Jefferson Lab and Beyond*, Haiyan Gao, invited talk, US-Korea Workshop: International Cooperation on Particle, Nuclear and Astrophysics, KAIST, Dae Jeon, South Korea, April 2012.

12. *Subthreshold Photoproduction of ϕ Mesons*, Haiyan Gao, invited talk, Workshop on Non-Perturbative Color Forces in QCD, Temple University, Philadelphia, PA, March 2012.

13. *The Story of Polarized ^{3}He: from Form Factors to Search for New Forces*, Haiyan Gao, invited talk, Symposium on Electroweak Nuclear Physics in honor of R. D. McKeown's 60th birthday, Duke University, Durham, NC, March 2012.

14. *New Searches on the Neutron Electric Dipole Moment and Spin-Dependent Short-Range Forces*, Haiyan Gao, seminar, Joint Center for Particle Nuclear Physics and Cosmology, Nanjing University, China, June 2012.

15. *Frontiers in Experimental Nuclear Physics and Personal Research Experience*, Haiyan Gao, public lecture, Beijing University of Posts and Communications, May 2012, Beijing, China.

16. *Frontier Research at Jefferson Lab and China-US Collaborations*, Haiyan Gao, colloquium, China Institute of Atomic Energy, Beijing, China, May 2012.

17. *New Searches on the Neutron Electric Dipole Moment and Spin-Dependent Short-Range Forces*, Haiyan Gao, seminar, Kyungpook National University, Korea, April 2012.

18. *The Latest on Proton Charge Radius*, Haiyan Gao, Nuclear Physics seminar, Haiyan Gao, University of Virginia, November 2011.

19. *Latest results from JLab on Neutron TMDs and Future Program*, Haiyan Gao, Nuclear Physics seminar, George Washington University, October 2011.

20. *How Well Do We Build the Foundation of Physics? The Report of the National Task Force on Physics Teacher Preparation*, D. Haase, invited paper, APS Spring Meeting, Atlanta, GA, April 2012.

21. *The nEDM Project: A New Cryogenic Measurement of the Electric Dipole Moment of the Neutron*, D. Haase, Nuclear Physics seminar, University of Virginia, Charlottesville, VA, March 2012.

22. *Why is Time a One-Way Street?*, D. Haase, Keynote Speaker, North Carolina Student Academy of Science State Meeting at NC School of Science and Mathematics, Durham, NC, March 2012.

23. *Neutron-Deuteron Breakup: A Probe of the Neutron-Neutron Interaction*, C. R. Howell, The 7^{th} International Workshop on Chiral Dynamics, Newport News, VA, August 2012.

24. *Measuring Plant-Environment Feedback Dynamics for Resource Allocation Using Short-lived Radioisotopes*, C. R. Howell, Physics seminar, Duke University, Durham, NC, November 2011.

25. *My Personal Path and Research*, C. R. Howell, invited talk, Symposium on Blazing Trails: African Americans in Science, Technology, Engineering and Mathematics, the SciWorks Science Center and Environmental Park, Winston-Salem, NC, February 2012.

26. *Nuclear Data Measurements Using Gamma Rays and Radiation Detector Development*, C. R. Howell, DNDO ARI Grantees Conference, Leesburg, VA, July 2012.

27. *A Search for the Electric Dipole Moment of the Neutron*, P. R. Huffman, invited talk, Meeting of the Division of Particles and Fields of the American Physical Society, Brown University, Providence, RI, August 2011.

28. *Monte Carlo Charged-Particle Reaction Rates: A New Frontier*, C. Iliadis, invited talk, Workshop on Thermonuclear Reaction Rates for Astrophysics Applications (THERRAA), Athens, Greece, November 2011.

29. *Nuclear Astrophysics: Underground Versus Sea Level*, C. Iliadis, International Workshop on Nuclear Astrophysics at the Canfranc Underground Laboratory, Canfranc Estacion, Spain, March 2012.

30. *Nuclear Fusion in Stars: Origin of the Elements*, C. Iliadis, public lecture, North Carolina Museum of Natural Sciences, Raleigh, NC, May 2012.

31. *Exploding Stars in the Laboratory*, C. Iliadis, colloquium, Helmholtz-Zentrum Dresden-Rossendorf, Dresden, Germany, July 2012.

32. *Cross Sections, Level Densities and Strength Functions*, G. E. Mitchell, Stockpile Stewardship Academic Alliance Symposium, Washington DC, 2012.

33. *Neutron Capture Experiments with 4π DANCE Calorimeter*, B. Baramsai, Workshop on Compound Nuclear Reactions and Related Topics, Prague, 2011.

34. *Applications of Random Matrix Theory*, G. E. Mitchell, Helmholz Zentrum Rossendorf Dresden, 2012.

35. *Analyzing Power of ^{3}He(n,n)^{3}He Between 1.60 and 5.54 MeV*, W. Tornow, invited talk, 20^{th} International Conference on Few Body Problems in Physics, Fukuoka, Japan, August 2012.

36. *A New Method for the Precise Determination of the Isovector Giant Quadrupole Resonance in Nuclei*, H. R. Weller, Zakopane Conference on Nuclear Physics 2012, Zakopane, Poland, August-September 2012.

37. *Compton Scattering at the HIGS Facility*, H. R. Weller, Chiral Dynamics Workshop 2012, Newport News, VA, August 2012.

38. *Unambiguous Observation of the Second 2^+ State in ^{12}C*, H. R. Weller, seminar, Argonne National Laboratory, Argonne, IL, October 2012.

39. *A New Method for Identifying Special Nuclear Materials Using Polarized Gamma Rays*, H. R. Weller, invited talk, ARI Grantees Conference, Leesburg, VA, July 2012.

40. *New Tri-Alpha Structures in ^{12}C*, H. R. Weller, Institute for Nuclear Theory Workshop on Light Nuclei from First Principles, Seattle, WA, October 2012.

41. *The Majorana Demonstrator: A Search for Neutrinoless Double-Beta Decay of ^{76}Ge*, J. F. Wilkerson, invited presentation, 12th International Conference on Topics in Astroparticle and Underground Physics, Munich, Germany, September 2011.

42. *The Neutrino at Eighty*, J. F. Wilkerson, seminar, National Superconducting Cyclotron Laboratory, Michigan State University, East Lansing, MI, September 2011.

43. *The Majorana Demonstrator: A Search for Neutrinoless Double-Beta Decay of ^{76}Ge*, J. F. Wilkerson, seminar, University of Michigan, Ann Arbor, MI, September 2011.

44. *Dark Matter and Neutrinoless Double Beta Decay Searches with High Purity Ge Detectors*, J. F. Wilkerson, seminar, Shanghai Jiao Tong, Shangahi, China, December 2011.

45. *Searching for Neutrinoless Double Beta Decay and Dark Matter with High Purity Ge Detectors*, J. F. Wilkerson, seminar, Tsinghua University, Beijing, China, December 2011.

46. *The Majorana Demonstrator ^{76}Ge Neutrinoless Double Beta Decay Experiment*, J. F. Wilkerson, seminar, Institute of High Energy Physics, Chinese Academy of Sciences, Beijing, China, December 2011.

47. *The Neutrino at Eighty*, J. F. Wilkerson, Physics Colloquium, University of Wisconsin, Madison, WI, April 2012.

48. *A Review of Direct Neutrino Mass Experiments*, J. F. Wilkerson, invited talk, Neutrinos 2012 Conference, Koyoto, Japan, June 2012.

49. *The Majorana Demonstrator Overview*, J. F. Wilkerson, Joint GERDA-MAJORANA Workshop, Munich, Germany, June 2012.

50. *Experimental Study of FEL Power Scaling in the Storage Ring FEL*, Y. K. Wu, The 33^{st} International Free Electron Laser Conference (FEL2011), Shanghai, China, August 2011.

51. *Overview of Present and Future Compton Photon Sources*, Y. K. Wu, International Particle Accelerator Conference (IPAC'12), New Orleans, LA, May 2012.

52. *From Lasers to Compton Gamma-Ray Sources*, Y. K. Wu, Physics colloquium Talk, George Washington University, Washington, DC, April 2012.

53. *Beta-Decay Angular Correlation Measurments at Los Alamos National Laboratory*, A. R. Young, 8^{th} UCN Workshop, St. Petersburg, Russia, June 2011.

54. *UCN as Probes of Neutron-Antineutron Oscillations*, A. R. Young, NANO Workshop on Neutron-Antineutron Oscillations, VECC, Calcutta, India, July 2011.

55. *Experimental Searches for Neutron-Antineutron Oscillations using Ultracold Neutrons*, A. R. Young, Workshop on Baryon and Lepton Number Violation, Gatlinburg, TN, September 2011.

56. *High Intensity Frontier: Physics Opportunities with Neutron Beta-Decay*, A. R. Young, Workshop on the High Intensity Frontier, Rockville, MD, November 2011.

57. *LANL Test Facilities*, A. R. Young, Workshop on Project X Spallation Targets, Fermilab, Batavia, IL, March 2012.

58. *Angular Correlations Measurements in Neutron Beta-Decay*, A. R. Young, TRIUMF Nuclear Summer School, Vancouver, BC, Canada, August 2012.

59. *Improved Experimental Searches for Neutron-Antineutron Oscillations*, A. R. Young for the NNbarX Collaboration, NNN-2012 Conference, Fermi National Accelerator Laboratory, September 2012.

60. *Direct Observation of a New 2^+ State in ^{12}C Through the $^{12}C + \gamma \rightarrow 3\alpha$ Reaction*, W. Zimmerman, Conference: Chiral Dynamics Workshop, Thomas Jefferson National Accelerator Facility, August 2012.

Seminars at TUNL

1. Peter Fielinger, Technical University Munich, (September 20, 2011)
   Electric Dipole Moments

2. Moshe Gai, Yale and University of Connecticut, (October 6, 2011)
   Scientists and Home Land Security

3. Patrizia Rossi, Laboratori Nazionali di Frascati-INFN, (October 20, 2011)
   Studies of the 3D Structure of the Nucleon with Pion and Kaon Production in Hard Processes

4. Deniz Savran, GSI ExtreMe Matter Institute EMMI, (November 1, 2011)
   On the Nature of the Pygmy Dipole Resonance

5. Lixin Chen, Cyclotron Institute Texas A& M, (November 2, 2011)
   Probing Fundamental Electroweak Physics with Precision Superallowed Beta-Decay Experiments

6. Matthias Schindler, Department of Physics & Astronomy University of South Carolina (November 15, 2011)
   Effective-Field-Theory Approach to Hadronic Parity Violation

7. Kareem Kazkaz, Lawrence Livermore National Laboratory,(January 19, 2012)
   Detecting Anti-Neutrinos and Neutrons with Composite Scintillators

8. Richard Cyburt, Michigan State University,(February 24, 2012)
   How to Get the Most Bang for Your Buck!

9. Aron Bernstein, Massachusetts Institute of Technology,(March 22, 2012)
   New Experimental Tests of QCD Symmetries

10. Alain Coc, Centre de Spectrométrie Nucléaire et de Spectrométrie de Masse, Orsay, (April 26, 2012)
    Variations of Constants Probed by Nuclear Physics

11. Mitzi Boswell, Los Alamos National Laboratory,(May 3, 2012)
    Gamma-Ray and Neutron Induced Reactions Pertinent to Neutrino Physics

12. Jorgen Randrup, Lawrence Berkeley Laboratory,(May 24, 2012)
    Fission Fragment Mass Distributions from Strongly Damped Shape Evolution

13. Josh Klein, University of Pennsylvania, (May 31, 2012)
    Neutrino and Neutrinoless Physics with SNO+

14. Walter Greiner, Frankfurt Institute for Advanced Studies (June 6, 2012)
    There Are No Black Holes

Advances in Physics Lectures and Seminars

1. Mohammad Ahmed, North Carolina Central University and Duke University, (May 30, 2012)
   Building Blocks of Nuclei
2. Mohammad Ahmed, North Carolina Central University and Duke University, (May 30, 2012)
   NN Interactions and Local Accelerators
3. Indranil Mazumdar, Duke University, (June 1, 2012)
   Nuclear Structure
4. Constance Kalbach Walker, Duke University, (June 7, 2012)
   Scientific Writing Part I: Its Not About You!
   Scientific Writing Part II: Making it Clear and Easy
5. Mohammad Ahmed, North Carolina Central University and Duke University, (June 8, 2012)
   Nuclear Instrumentation
6. Calvin Howell, Duke University, (June 8, 2012)
   Nuclear Scattering and Reactions
7. Paul Huffman, North Carolina State University, (June 14, 2012)
   Fundamental Physics with Neutrons
8. Tom Clegg, University of North Carolina at Chapel Hill, (June 21, 2012)
   Electron, Photon, Ion, and Neutron Sourcery: Beam Production for Nuclear Physics Experiments at TUNL
9. Haiyan Gao, Duke University, (June 28, 2012)
   The QCD Internal Landscape of the Nucleon
10. Ying Wu, Duke University, (July 5, 2012)
    Compton X-Ray and Gamma-Ray Sources
11. Ed Kearns, Boston University, (July 26, 2012)
    Underground Physics

A.4 Professional Service Activities

Advisory/Fellowship/Review Committees

1. Member, LUX Davis Campus Safety Readiness Review Committee, *M. Busch*
2. General Councillor, American Physical Society, 2011, *H. Gao*
3. President of International Organization of Chinese Physicists and Astronomers, January 1, 2011–December 31, 2012, *H. Gao*
4. Member, AIP/AAPT/APS Task Force on Teacher Preparation in Physics, *D. Haase*
5. Member, Program Committee for the Forum on Education of the APS, *D. Haase*
6. Member, Executive Committee, Neutron Electric Dipole Moment Experiment, *R. Golub*
7. Reviewer, DOE Science Graduate Fellowship Program, *R. Henning*
8. Chair line, Executive Committee of the Few-Body Topical Group, American Physical Society (APS), 2010-2014, *C. R. Howell*
9. Member, Stockpile Stewardship Graduate Fellowship Program Selection Committee, 2010-present, *C. R. Howell*
10. Member, Selection Committee for the Mellon Mays Dissertation Grant, 2000-present, *C. R. Howell*
11. Member, Majorana Senior Advisory Committee, 2007 - present, *C. R. Howell*
12. Member of the PRC Editorial Board (2011 - present), *C. R. Howell*
13. Member, Executive Committee for the SNS Fundamental Neutron Physics Beam Line Instrument Development Team, *P. R. Huffman*
14. Member, Executive Committee for the Neutron Electric Dipole Moment Experiment, *P. R. Huffman*
15. Member, International Review Committee of Centro Fisica Nuclear da Universidade de Lisboa (CFNUL), Lisbon, Portugal, December 2011, *W. Tornow*
16. Member, NA-22 LANL Review Panel *Plutonium Isotopics Projects* for the Non-Proliferation agency of DOE, Los Alamos National Laboratory, October 25, 2012, *H. R. Weller*
17. Chair, HIGS PAC Committee, July 2011 and November 2012, *H. R. Weller*
18. Member, NSAC Sub-Committee on Implementation of the 2007 Long Range Plan, 2012, *J. F. Wilkerson*
19. Member, International Neutrino Physics Summer School Organizing Committee, 2012, *J. F. Wilkerson*
20. Member, International CUORE Review Committee, 2011, 2012, *J. F. Wilkerson*
21. Co-organizer, National Nuclear Physics Summer School 2011, *J. F. Wilkerson*
22. Faculty coordinator, 2013 U.S. Particle Accelerator School at Duke (January 14–25, 2013), *Y. K. Wu*
23. Reviewer, Center grant proposal, National Nuclear Security Administration (NNSA), DoE, 2012, *Y. K. Wu*

24. Co-PI UCNA Experiment LANSCE User Group Executive Committee Convener: Project X Physics Study, Fermilab, June 2012, *A. R. Young*

25. Convener, Project X Physics Study, Fermilab, Batavia, IL, 2012, *A. R. Young*

26. Member, LANSCE User Group Executive Committee, 2011-2012, *A. R. Young*

27. Co-spokesman, UCNA experiment, *A. R. Young*

Conferences, APS Meetings and Workshops

1. Member, International Advisory Committee, STORI11 Frascati, Laboratori Nazionali di Frascati dell'INFN, October 9–14, 2011, Frascati, Italy, *H. Gao*
2. Member, International Advisory Committee, Partons in Nucleons and Nuclei, September 26–30, 2011, Marrakesh, Morocco, *H. Gao*
3. Member, International Advisory Committee, Chiral Dynamics 2012 Workshop, August 6–10, 2012, Jefferson Laboratory, Newport News, VA, *H. Gao*
4. Member, International Advisory Committee, the 20^{th} International Conference on Few-Body Physics, Fukuoka, Japan, August 20–25, 2012, *H. Gao*
5. Member, International Advisory Committee, 12^{th} International Workshop on Meson Production, Properties and Interaction, Krakow, Poland, May 31–June 5, 2012, *H. Gao*
6. Member, International Advisory Committee, 5^{th} Symposium on Symmetries and Subatomic Physics (SSP2012), Groningen, Netherland, June 18–22, 2012, *H. Gao*
7. Co-chair, Symposium on Electroweak Nuclear Physics, Duke University, Durham, NC, March 7–9, 2012 *H. Gao*
8. Co-Chair, 4^{th} Workshop on Hadron Physics in China and Opportunities in US, KITPC, Beijing, China, July 2012, *H. Gao*
9. Member, Review panel, SFB 1044, Deutsche Forschungsgemeinschaft, September 26 -27, 2011, *H. Gao*
10. Member, International Program Committee ND2013, International Conference on Nuclear Data and Technology, March 2013, *C. Gould*
11. Member, AAPT Book Publications Five-Year Review Committee, *D. Haase*
12. Member, International Advisory Committee, 11^{th} Conference on the Intersections of Particle and Nuclear Physics, 2011–2012, *C. R. Howell*
13. Member, International Advisory Committee, International Nuclear Physics Conference INPC 2013, Florence, Italy, *W. Tornow*
14. Vice Chair (2011) and Chair (2012), APS Division of Nuclear Physics, 2012 Tom Bonner Prize Committee, *J. F. Wilkerson*
15. Member, Scientific Program Committee, the 34th International FEL Conference (FEL2012), August 26–31, 2012, Nara, Japan, *Y. K. Wu*
16. Member, International Advisory Committee, 8^{th} UCN Workshop, St. Petersburg, Russia, June 2011, *A. R. Young*
17. Co-organizer, Workshop on Baryon and Lepton Number Violation, Gaitlinburg, TN, September 2011, *A. R. Young*

Other Service

1. Steering Committee for Whitepaper for Electron-Ion Collider Science in US for NSAC Long Range Plan, 2011–2012, *H. Gao*
2. Member, 2012 NSAC Subcommittee on the Implementation of the Long Range Plan, *H. Gao*
3. Jefferson Lab Program Advisory Committee, January 2010 to present, *H. Gao*

Glossary of Acronyms

Laboratories, Facilities, Experiments and Programs

ANL	Argonne National Laboratory
BNL	Brookhaven National Laboratory
DFELL	Duke Free-Electron Laser Laboratory
DNDO	Domestic Nuclear Detection Office
FNPB	Fundamental Neutron Physics Beam Line
GV	Gamma-Vault at HIGS
HIFROST	HIGS Frozen Spin Target
HIγS	High Intensity Gamma-Ray Source
JLAB	Thomas Jefferson Lab National Accelerator Facility
KURF	Kimballton Underground Research Facility
LANL	Los Alamos National Laboratory
LENA	Laboratory for Experimental Nuclear Astrophysics
LLNL	Lawrence Livermore National Laboratory
nEDM	Neutron Electric Dipole Moment
NNSA	National Nuclear Security Administration
ORNL	Oak Ridge National Laboratory
PNNL	Pacific Northwest National Laboratory
REU	Research Experience for Undergraduates
UTR	Upstream Target Room at HIGS

Detectors, Material, Particles, Electronics, Acquisition and Software

DAQ	Data Acquisition
HINDA	HIGS NaI Detector Array
HPGe	High Purity Ge Detector
MCNP	Monte Carlo N-Particle
NaI	Sodium Iodide
ORCA	Object-Oriented Real-Time Control and Acquisition
OTPC	Optical Time Projection Chamber
PSD	Pulse Shape Discrmination
SBC	Single Board Computer
SNM	Special Nuclear Material
VME	VERSA module Eurocard

Calculations, Reactions, and Techniques

3NF	3-Nucleon Force
4NF	4-Nucleon Force
DWIA	Distorted Wave Impulse Approximation
EFT	Effective Field Theory
FWHM	Full Width at Half Maximum
GDR	Giant Dipole Resonance
LIT	Lorentz Integral Transform
MEC	Meson Exchange Current
NRF	Nuclear Resonance Fluorescence
QCD	Quantum Chromodynamics
QRPA	Quasiparticle Random Phase Approximation
xPT	Chiral Perturbation Theory

Triangle Universities Nuclear Laboratory

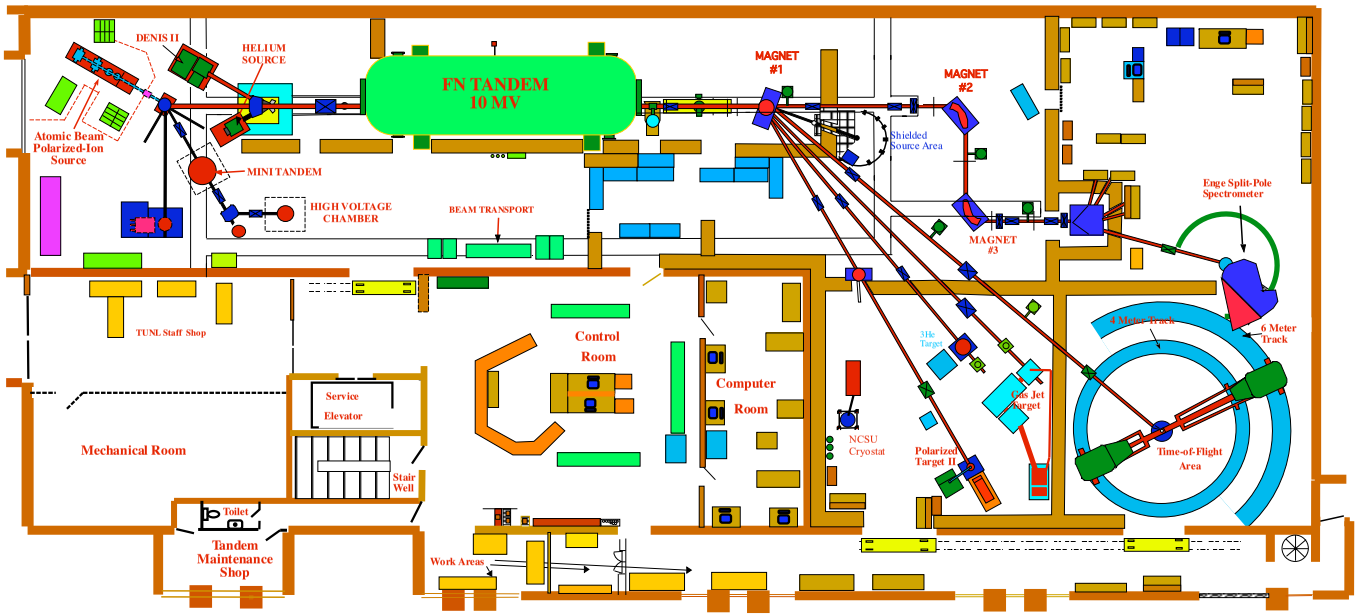

TUNL/801